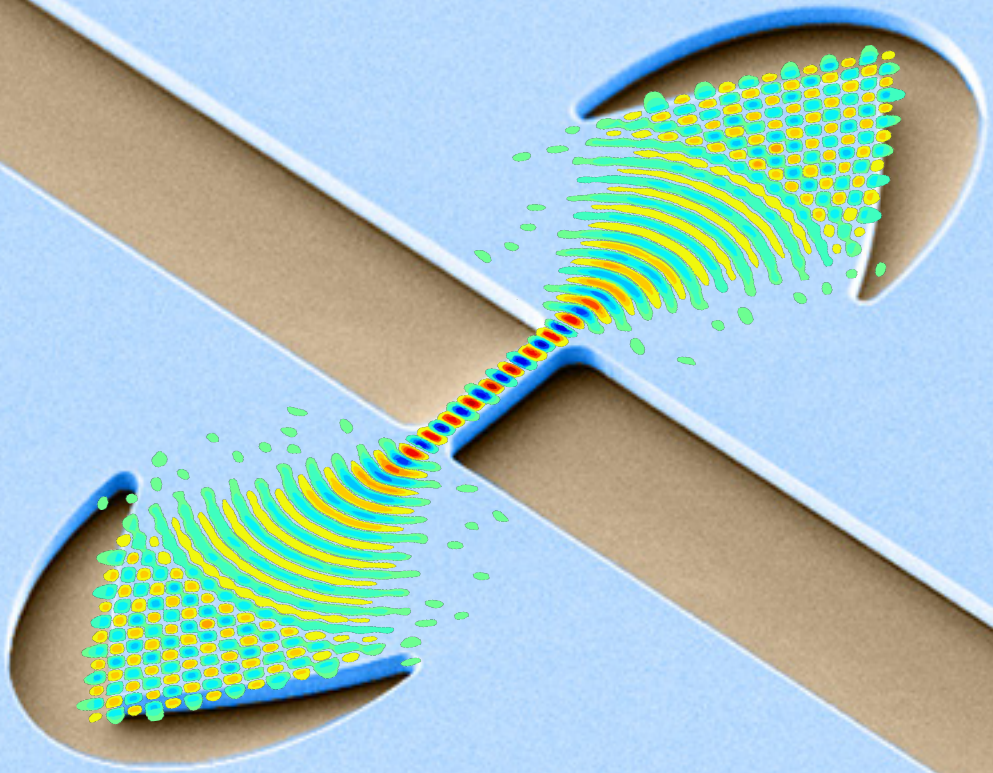


Strained Germanium Laser



Francesco Taro Armand Pilon
2021

DISS. ETH NO. 27531

Strained Germanium Laser

A thesis submitted to attain the degree of
DOCTOR OF SCIENCES of ETH ZÜRICH
(Dr. sc. ETH Zürich)

presented by
FRANCESCO TARO ARMAND PILON
M.Sc. in Physics, Università degli Studi di Milano

born on 21.07.1988
citizen of Italy

accepted on the recommendation of
Prof. Dr. Jérôme Faist, examiner
Prof. Dr. James Harris, co-examiner
Dr. Alexei Tchelnokov, co-examiner
Dr. Hans Sigg, co-examiner

2021

Abstract

Silicon technology shaped the digital world surrounding us in just a few decades. Our electronic devices' astonishing power and functionalities stem from the continuous development of the complementary metal-oxide-semiconductor (CMOS) technology and the integrated circuits' miniaturization. However, the emergence of quantum effects naturally limits this scaling approach. Silicon is thus foreseen to become a major host material for quantum technology applications. An alternative vision aims to use silicon as a platform to control, guide, and manipulate light. The idea of silicon photonics (SiPh) is to provide silicon with novel functionalities in the fields of sensing, processing, and communicating optical data.

Silicon photonics' last bottleneck on becoming a complete platform is the development of an efficient, low-cost, and fully silicon-compatible laser source. Nowadays, the integration of mature laser technology based on the III-V materials on silicon sets the bar in terms of performance. However, this approach brings intrinsic technical hurdles and, thus, high costs. A long-standing wish is the development of a group-IV-based laser. Using materials that are naturally compatible with silicon and thus with the CMOS technology would unlock cost-effective mass production.

Among the group-IV elements, germanium (Ge) is the primary candidate because its band structure is already near to direct. The energy difference between the band that can provide strong optical transitions - at the center of the Brillouin zone - and the fundamental band - at the Brillouin zone's edge - is only about 140 meV. By straining Ge along particular directions or alloying it with tin (Sn), the electronic bands appropriately move to reach a direct bandgap configuration enabling light generation and eventually lasing. The past years witnessed many efforts to implement both these approaches. The first demonstration of lasing in direct band gap GeSn succeeded in 2015. This important breakthrough triggered a fascinating race towards the first room temperature and electrically injected all-group-IV laser source. However, the strained Ge approach revealed to be more challenging, demanding further studies of fundamental nature, like the bands' alignment dependence on the strain.

Thus, this thesis's goal is thus twofold: (i) demonstrate the feasibility of the tensile strain approach to achieve lasing in Ge and (ii) study the fundamentals of group-IV lasing. The first part of the dissertation describes the technology developed at the Paul Scherrer Institut to induce high tensile strain in Ge microstructures routinely on a wafer level. We then discuss the strained germanium's radiative properties as a function of the bands' alignment and present the modeling of the optical cavity.

The second part presents the experimental results. Via photoluminescence spectroscopy, we characterize the strained germanium microstructures integrated into an optical cavity. Then, we show the first lasing in strained germanium upon pulsed excitation at low temperature and demonstrate the typical lasing fingerprints. In the final part, we unravel steady state lasing upon continuous wave excitation and benchmark the optical gain and loss models, allowing us to gather in-depth information about the bands' alignment and the build-up of loss as a function of the strain and temperature. In conclusion, this thesis reports on the realization of the strained germanium laser and reflects our understanding of the physical principles for the fabrication of group-IV lasers.

Riassunto

La tecnologia del silicio ha modellato il mondo digitale che ci circonda in pochi decenni. La incredibile capacità computazionali e le funzionalità dei nostri dispositivi elettronici derivano dal continuo miglioramento delle tecnologia *complementary metal-oxide-semiconductor* (CMOS) e dalla miniaturizzazione dei circuiti integrati. Tuttavia, la strategia di ridurre le dimensioni dei componenti elettronici è intrinsecamente limitata dall'emergere di effetti quantistici. In futuro, gli scienziati prevedono quindi di usare il silicio come materiale adatto ad ospitare applicazioni basate su tecnologie quantistiche. Una visione alternativa mira a controllare, guidare e manipolare la luce direttamente sul silicio. L'idea della fotonica del silicio è quella di ampliarne lo spettro delle funzionalità, aggiungendo la possibilità di rilevare, processare e comunicare dati ottici.

L'ultimo ostacolo della fotonica del silicio è rappresentato dallo sviluppo di un laser che sia efficiente, a basso costo e totalmente compatibile con il silicio. Oggigiorno, è l'integrazione su silicio dei laser basati sulle leghe III-V ad impostare il livello delle prestazioni. Tuttavia, questo approccio è intrinsecamente limitato da ostacoli tecnici e, quindi, da costi alti. Lo sviluppo di un laser basato sugli elementi del gruppo IV rappresenta quindi una soluzione molto ambita. Usare materiali che siano naturalmente compatibile con il silicio, e quindi con la tecnologia CMOS, permetterebbe una produzione su larga scala e a basso costo.

Tra gli elementi del gruppo IV, il germanio è il candidato principale grazie alla sua struttura a bande quasi diretta. La differenza di energia tra la banda al centro della zona di Brillouin, responsabile delle transizioni ottiche, e la banda all'esterno della zona di Brillouin è di soli 140 meV. La deformazione del germanio lungo specifiche direzioni cristallografiche o la lega del germanio con lo stagno (Sn) fanno sì che le bande elettroniche si modifichino fino a raggiungere la configurazione di semiconduttore a *band gap* diretto, aumentando così la possibilità di generare luce. Gli scorsi anni hanno visto molti gruppi di ricerca impegnati a dimostrare queste strategie. La prima dimostrazione di un laser basato sulla lega GeSn a *band gap* è avvenuta nel 2015. Questo importante risultato ha iniziato tra i ricercatori la corsa verso lo sviluppo del primo laser basato interamente su materiali del gruppo IV funzionante a temperatura ambiente e ad iniezione elettrica costante. La strategia di deformare il germanio si è rivelata al contrario più difficile del previsto, rendendo necessari ulteriori studi di natura fondamentale, come l'evoluzione delle bande elettroniche in funzione della deformazione.

L'obiettivo di questa tesi è quindi doppio: dimostrare la fattibilità della strategia di ottenere un laser basato unicamente sul germanio deformandolo e studiare i fondamenti fisici

dei laser basati sul gruppo IV. La prima parte della dissertazione descrive la tecnologia sviluppata presso il Paul Scherrer Institut per indurre alti livelli di deformazione in microstrutture di germanio. Successivamente, discuteremo le proprietà ottiche del germanio deformato in funzione dell'allineamento delle bande e svilupperemo un modello per comprendere le proprietà della cavità ottica.

La seconda parte espone i risultati sperimentali. Investigheremo le proprietà del germanio deformato e integrato in una cavità ottica tramite spettroscopia a fotoluminescenza. Dimostreremo il primo laser al germanio, ottenuto sotto eccitazione ottica pulsata a bassa temperatura. Quindi, mostreremo il primo laser a stato stazionario ottenuto a eccitazione continua. Questo risultato finale dimostra la fattibilità dell'approccio basato sulla deformazione del germanio e mette alla prova i modelli di guadagno e perdita, permettendo di ottenere informazioni fondamentali riguardo l'allineamento delle bande elettroniche e di osservare l'incremento della perdita ottica in funzione della deformazione e della temperatura. In conclusione, questa tesi riporta la realizzazione del laser basato sul germanio deformato e riflette la nostra comprensione dei principi fisici per lo sviluppo di laser basati su materiali del gruppo IV.

Contents

Abstract	i
Riassunto	iii
1 Introduction	1
1.1 From silicon electronics to silicon photonics	1
1.2 On Si light sources: from III-V integration to all-group-IV	4
1.3 Thesis outline	7
2 Strained germanium principles	9
2.1 Band edges vs strain	10
2.2 Strain amplification technology	12
2.3 Optical cavity	15
2.4 Strained Ge cavities fabrication	16
2.5 Strain determination and enhancement upon cooling	20
2.6 Summary	23
3 Strained germanium laser modeling	25
3.1 Full band structure of strained germanium	26
3.2 Electron and hole statistic	28
3.3 Gain and loss	31
3.3.1 Gain and $\Delta E_{\Gamma,L}$	33
3.3.2 Gain spectrum and transparency	35
3.3.3 n-doping	37
3.3.4 Parasitic losses	38
3.4 Optical resonator	40
3.4.1 Cavity modes and loss	40
3.4.2 Q factor of the cornercube cavity	42
3.4.3 Multimode cavity pattern	46
3.4.4 3D cavity modeling	49
3.4.5 Cavity scattering loss	50
3.4.6 Excitation wavelength dependence and absorption	51

3.5	Thermal load	54
3.6	Summary	56
4	Lasing upon optical pulsed excitation	59
4.1	Introduction	60
4.2	Experimental set up: CW, OPO	60
4.3	Photoluminescence measurement upon CW	62
4.4	Lasing upon pulsed excitation	64
4.4.1	Excitation energy dependence	66
4.4.2	Carrier concentration estimation	67
4.4.3	Quantum efficiency	70
4.4.4	Linewidth	72
4.4.5	Temperature dependence	73
4.5	Non-equilibrium carrier distribution	75
4.6	Intervalence band Raman lasing	79
4.7	Summary	81
5	Steady state lasing	83
5.1	Introduction	84
5.2	Samples and experimental set-up	85
5.3	Main lasing characteristics	90
5.4	Gain vs loss	94
5.5	Lasing analysis: from transparency to lasing	96
5.6	High strain: missing lasing	101
5.7	Temperature dependence	102
5.8	Intervalence band absorption	105
5.9	Energy difference $\Delta E_{\Gamma,L}$ vs strain	107
5.10	Discussion: energy difference $\Delta E_{\Gamma,L}$	113
5.11	Discussion: steady state lasing	115
5.12	N-doping	116
5.13	Laser linewidth analysis	120
5.13.1	Linewidth measurements	120
5.14	Summary	127
6	Summary and conclusions	129
A	Appendix	133
A.1	Absorption lines by air gases	134

A.2 CW beam spot at sample position	134
A.3 Confinement factor	136
A.4 Smoothing function to measure the PL background	137
A.5 Band gap determination	138
A.6 The Schawlow–Townes Linewidth	138
A.7 Population inversion factor	142
A.8 Linewidth technical noise sources	145
A.9 Fundamental linewidth deviations from S-T theory	147
Bibliography	149
Acknowledgements	169
Curriculum Vitae	171
List of Publications	173

Introduction

Contents

1.1 From silicon electronics to silicon photonics	1
1.2 On Si light sources: from III-V integration to all-group-IV	4
1.3 Thesis outline	7

1.1 From silicon electronics to silicon photonics

Not many technologies had such a profound impact on our everyday life as silicon (Si) technology. The unique combination of its physical properties, functionalities, and material availability led to a fast and progressively cheaper technological advancement that revolutionized the world surrounding us in few decades, transforming it from analogical to digital.

The invention of the first semiconductor transistor at the Bell Labs in 1948 [1] and the fast growth of semiconductor physics during the 1950s triggered the idea of integrating all electronic components into a single semiconductor crystal. During only one decade, the complementary metal-oxide-semiconductor (CMOS) technology solved the initial issues of integration, isolation, and connection. This made possible the modern integrated circuits (ICs), as proposed for the first time by Noyce [2], whose patent was issued in 1961. In this regard, it is worth remembering that the usually cited patent of Kilby [3], who won the Nobel prize in 2000, was filed before [2], but it lacked lithographically defined interconnections between the transistors, which are a fundamental integrated circuits feature. Kilby's patent was indeed issued only some years later, in 1964. Interestingly, germanium (Ge) was initially the forefront material in semiconductor research and industry. Compared to Si, germanium has advantages of technical nature, like the lower melting temperature and the ability to get high purity material, and physical nature, as its high carrier mobility. However, high-power

devices based on germanium showed at high temperatures poor performances. Eventually, silicon, which can better dissipate heat and whose oxide has higher quality, overtook Ge.

The fast improvement of the photolithography, which is the working horse of scalability, increased the electronic component's density exponentially. This growth led one of Intel's co-founders, Gordon Moore, to state his well-known prediction about the doubling of transistor density every two years [4]. The progress in the semiconductor industry indeed followed Moore's law. The microprocessor's power exponentially rose, and the cost per chip declined. These two elements undoubtedly played a massive role in shaping the world as we know it. Nowadays, every person can hold in its hand for a reasonably accessible price a processing power and a memory orders of magnitude larger than those possessed by the first computers.

The current state-of-the-art of lithography, already implemented in production, is 5 nm [5], as declared by TSMC, one of the major semiconductor company worldwide. By employing extreme ultra violet (EUV) based lithography, it is possible to integrate as many as 10^8 transistors per mm^2 . However, the constant shrink of the dimensions is an intrinsically limited process. At the nanometer scale, the classical transistor's reliability will be dominated by quantum effects. Besides, heating issues arise as well. As already occurring, the device's performances will saturate.

However, Moore's law is not meant to end. New ideas and novel approaches can study and exploit novel silicon properties to push further the edge of its functionalities. For example, silicon is rising as a novel quantum electronics platform. Indeed, silicon is an ideal host for quantum bits based on the electron spin, thanks to its low spin-orbit coupling. Moreover, the possibility to work with its pure isotope ^{28}Si , which ensures long coherence time, is advantageous. Quantum technologies based on silicon and group-IV are nowadays a growing research field [6–9]. The interested reader can refer to more specific reviews on the topic [10, 11].

Alternatively, silicon's transparency at wavelengths longer than $1.1 \mu\text{m}$ and its strong refractive index contrast with SiO_2 make it a suitable platform to guide light. This idea extended to include the generation, modulation, and detection of light and started to take hold in the mid-'80s [12]. This vision aims to give silicon new functionalities by developing silicon photonics (SiPh) integrated circuits based on the mature CMOS technology. Silicon photonics also has the potential to enhance performances in electronics [13], data- and telecommunications, sensing of chemical and biological compounds, neural networks [14], and quantum computation [15, 16]. Silicon photonics is rising as a concrete reality in the data communication market and it is a crucial technology for the coming future [17]. Data centers demand higher capacity and more efficient components to support the exponential increase of global data traffic. Optical transceivers (transmitter and receiver device) based

on SiPh technology, like those sold by Intel or Luxtera, meet the requirements of bandwidth and low power consumption (few pJ/bit). Their market share is predicted to increase in the future [18] substantially.

However, the rapidity at which SiPh is growing in the data communication market must not mislead about silicon's optical radiative properties. Silicon's electronic properties are excellent and its transparency in the infrared (IR) region of the spectrum is attractive. However, it is not ideal for generating and detecting light due to its indirect band gap configuration, neither for modulating it via electro-optic effect. In the last two decades, both research and industry put great efforts into solving the nodes of light generation, detection, and modulation. The integration on Si of already existing solutions, as offered by the III-V compounds, is engaging. However, it brings the burden of CMOS incompatibility, low integration density and high cost. Thus, the extension of silicon's functionalities, by exploiting the well-established and highly reliable CMOS technology, addresses many research efforts.

Traditionally, light is modulated by exploiting the linear electro-optic (Pockels) effect in non-centro-symmetric material, like lithium niobate. Thus, silicon-based optical modulators require new solutions. The most popular modulator's proposals rely on plasma dispersion [19] and thermo-optic effect [20]. The latter technology can be implemented in Mach Zehnder interferometer (MZI) modulators like in [14], which, however, can not be usefully integrated due to their slow speed, large size and high power consumption. Higher speed modulators are currently under study, like the plasmonic modulator [21]. Regarding the node of light detection, silicon's transparency beyond 1.1 μm oriented the research towards germanium. The Ge-on-Si growth is rather challenging due to the lattice mismatch of 4.2 % and the related defects. Nonetheless, Ge photodetectors are the most advanced CMOS-compatible solution, showing performances similar to the III-V compounds devices [22–24]. Ge photodetectors cover the traditional telecommunications wavelengths of 1.3 and 1.5 μm . However, the reduced absorption coefficient at wavelengths beyond 1.55 μm still represents an obstacle in C-band telecommunications.

The modulation and detection nodes are essentially solved, and their performance improvement is instead a technical matter. On the contrary, the generation of coherent light on Si in a CMOS-compatible way is still challenging. These difficulties are fundamental and derive from silicon's band structure: the minimum of the conduction band in the reciprocal \mathbf{k} space is not aligned to the maximum of the valence bands. Silicon, as well as germanium, is thus referred to as an indirect band gap semiconductor. Consequently, electrons excited in the upper states recombine with a hole in the valence band by emitting a photon only via inefficient second-order processes, involving zone-boundary phonons for momentum conservation. On the contrary, in direct band gap materials, like the III-V compounds, an

electron-hole pair can radiatively recombine without phonons' mediation.

In the next section, we discuss the different approaches proposed to overcome the silicon's intrinsic limitation to generate light. After describing the hybrid integration solutions, the fully CMOS compatible way is detailed, guiding the reader towards this thesis's topic.

1.2 On Si light sources: from III-V integration to all-group-IV

The integration of a mature technology like the III-V based lasers on silicon is the most straightforward approach to enable silicon photonics' full capabilities. However, the intrinsic incompatibilities between the III-V alloys and Si is a burden of both technical and economic nature.

Due to lattice, thermal expansion, and polarity mismatch, a III-V epitaxial layer grown directly on silicon presents high density of crystallographic defects, such as threading dislocation and anti-phase domains (APDs). The threading dislocations can not be avoided entirely, but their density can be minimized below the carrier diffusion length. The anti-phase boundaries (APBs) separating the anti-phase domains are highly conductive, act as shorts, and be considered the real device killers.

The heterogeneous integration can overcome these limitations. The III-V material is grown on a native substrate, bonded on a pre-patterned silicon substrate, and then lithographically processed. The so obtained devices show exceptional performances, as high as those on a native substrate. The heterogeneous integration is indeed one of the most exploited approaches, both in research [25–28] and semiconductor companies [29,30]. As a counterpart, this technology's high cost and the lack of a 200 mm diameter III-V wafer hinder mass production at low cost. From this perspective, the growth of a III-V epitaxial layer on silicon is more advantageous, despite the crystallographic defects mentioned above. A popular technique to reduce the defect's density foresees the silicon substrate's miscut of some degrees towards the [011] plane to induce a double atomic step, suppressing the APDs formation. Despite the impressive results obtained with the latter technique [31,32], off-cutting the silicon substrate is not a suitable option for the semiconductor industry.

The technology to grow defect-free material on an on-axis silicon substrate is the most rewarding path towards cheaper and larger scale III-V integration. Recently developed technologies use a v-grooved Si substrate [33] or anneal the Si layer at high temperature before the III-V deposition [34]. Both techniques confine the APDs in the first layer of the III-V deposition. Promising results are achieved with these techniques in quantum dots lasers [35,36] operating at telecom wavelength. The technology described in [34] is also applied to the Sb-based materials. Compared to the traditional InP and GaAs compounds,

Sb-based materials are more challenging due their larger lattice mismatch with Si (12 %) and show a smaller band gap in the mid-infrared (MIR). The successful demonstration of the first GaSb-based laser on Si operating at 2.3 μm [37] was followed by the realization of a quantum cascade laser (QCL) grown directly on Si [38, 39]. These achievements pave the way towards the integration on the same silicon chip of light sources operating from the visible to the MIR region, expanding the on-chip functionalities to gas spectroscopy, chemical detection and environmental gas monitoring.

The improvements mentioned above brought the III-V based light sources to work routinely on silicon in continuous operation, at room temperature and beyond. Nonetheless, the development of a laser source based on a group IV element remains a long-standing wish. An all-group-IV laser is the only practical way to fully exploit the potential of the CMOS ultra-large-scale-integration (ULSI) technologies and thus enable mass production at low cost.

Different strategies were developed to tackle group IV elements' intrinsic low radiative properties and increase the internal quantum efficiency. The proposals included low-dimensional silicon nanostructures [40–42] and porous silicon [43, 44]. Despite the claim of gain [41], lasing was not observed. Another strategy investigated doping with rare earth ions like Er^{3+} , whose atomic transition at telecom wavelength of 1540 nm allows light amplification [45]. Superlattice structures made of Si and Ge monolayers [46–48], following the concept of zone-folding [49], were alternative approaches, which did not result in any lasing demonstration. The idea is to modify an indirect band gap host material to a direct band gap one by superimposing an additional periodic electronic potential. Consequently, the first Brillouin zone (FBZ) size is expected to reduce and the electronic bands in the extended band diagram fold in the reciprocal space in a direct band gap fashion.

Lasing action based on stimulated Raman scattering was shown in silicon [50–52]. However, this achievement finds feasible applications only as very inefficient optical converter, as lasing requires an off-chip optical pump. A challenging and rewarding approach is realizing a Si-based QCL to exploit the intersubband transitions instead of the inefficient interband ones. Despite the QCL based on the III-V materials being a robust technology, researchers could demonstrate so far only electroluminescence in structures made of Si/SiGe [53, 54]. This device's p-type nature made it difficult to engineer the gain properly and the not yet mature epitaxy technology of group IV materials limited the number of necessary periods. Recent efforts converge toward the study of n-type Ge/SiGe QCL [55–58].

Germanium-based solutions show exciting progress. Indeed, lasing was shown in Ge defect-enhanced quantum dots (DEQDs) [59]. The usual low radiative efficiency of defect-free quantum dots (QDs) is overcome by self interstitial defects induced by Ge ions' implan-

tation [60]. Like the superlattice concept, a direct band gap was claimed by alternating Ge and SiGe atomic stacking with hexagonal crystal lattice [61]. Despite the encouraging results of the photoluminescence, the essential requirement of gain is not demonstrated yet.

Thus, the primary strategy in Ge-based solutions is to push the quasi-Fermi level up to the Γ valley, either by heavy n-doping or by coercing the Ge to become direct. Such an idea stems from the low energy difference between the germanium's Γ and L band edges, i.e., $\Delta E_{\Gamma,L} = E_{\Gamma} - E_{L}$, equal to about $\Delta E_{\Gamma,L} = 140$ meV at room temperature. The first attempt to demonstrate lasing in germanium exploited doping density of $N_d > 10^{19}$ cm⁻³ [62–64]. However, these results are not reliable enough for practical solution and are in strong contradiction with proof of principle experiment [65], showing that gain is not reached in the doping and low strain range there explored.

So far, the most promising approach aims to make germanium a direct band gap material, either by alloying it with tin (Sn) [66] or by loading it with tensile strain [67]. After many years of intense focus on the material growth research, unambiguous lasing at low temperature was shown for the first time in a GeSn Fabry-Perot cavity [68]. This result triggered the race towards a group-IV laser operating at room temperatures under continuous electrical injection. Research is currently following different strategies to improve the lasing performances in terms of operating temperature and threshold: increase the Sn content to induce a large negative energy difference between the Γ and L band energy minima [69–71], in combination with quantum confinement [72,73] or tensile strain [74,75]. The recent demonstration of continuous wave operation under optical pumping [75] and pulsed electrical injection [76] at low temperature show the GeSn approach's feasibility. However, to overcome the traditional lower material quality, compared to germanium, and the poor thermal conductivity typical of the alloys, the path toward a GeSn laser with all the desired characteristics will necessarily involve using low Sn content, combined with tensile strain. This approach is doubly challenging: Sn has low solubility, and its incorporation induces compressive rather than tensile strain.

The transition from indirect to direct band gap uniquely upon applying tensile strain is studied in germanium. Aside from the epitaxial approach, whose results are limited to a thin film of the order of 10 nm [77], higher values of tensile strain in bulk structure can be achieved with external SiN stressor layer [78–80], or by following the geometrically based concept of strain amplification [81]. The latter allows loading germanium with high strain values in uniaxial [82–87], biaxial [88,89] or polyaxial [90,91] configuration. Lasing in germanium was first achieved upon pulsed excitation at low temperature in microbridge structures loaded with a tensile strain of about 5.9% [92]. This result suggests that the cross-over from indirect to direct band gap occurs at a strain level much higher than the often

reported prediction of 4.4% [93], contradicting previous lasing claims in similar germanium platforms at low temperature [87, 89].

Despite the encouraging results and the group IV lasing platforms' progress, many fundamental physical quantities require further studies. For instance, understanding the germanium band structure dependence on the strain, which is one of the group IV approaches' cornerstones, is essential for the correct prediction of the lasing performances. Similarly, the role played by parasitic losses, like the intervalence band absorption, or by the carrier dynamic lacks full understanding. Thus, this thesis aims to gather in-depth insights into the group IV lasing physics fundamentals to tackle the challenges of developing the next generation of all-group-IV lasers.

1.3 Thesis outline

The goal of the thesis is to demonstrate and study in detail the lasing in strained germanium. The improvement of the processing quality enables the extension of the strain to values never explored before. The band structure dependence on the strain is unraveled by studying the gain at the lowest temperature. Among other observations, the lasing characteristics' temperature dependence witnesses the build-up of parasitic intervalence band absorption.

After the presentation given in chapter 1 about this work's motivations, chapter 2 describes the strained germanium's fundamentals. We describe the theoretical models predicting the crossing to the direct band gap configuration, highlighting the role played by the tight-binding framework, which correctly foresees the nonlinear redshift of the direct band gap transition when strain is larger than 1.5%. We then give a short description of the employed strain amplification technology necessary to achieve high strain routinely. By highlighting the work developed before this thesis, we describe the integration of the active material into the optical cavity. We report the improvements carried out during this project at the processing level. This, combined with the high strain thus achieved, reveals indeed to be fundamental to unlock lasing in steady state, as described in chapter 5.

Chapter 3 is devoted to the modeling of the strained germanium laser. After calculating the carrier distribution between the two conduction bands, we focus on the optical gain modeling. In particular, the model addresses the impact of $\Delta E_{\Gamma,L}$, i.e., the energy difference between the edges of the Γ and L valleys, on the material optical radiative properties. The calculations indicate that the emergence of the gain at low temperature is strictly related to $\Delta E_{\Gamma,L} \sim 0$ meV. The model reveals a large transparency region's build-up, whose formation explains previous Ge lasing claims, and it is a powerful tool to distinguish between transparency and gain. Moreover, the amount of gain achieved for a given excitation density

at low temperature is particularly sensitive to few meV change of $\Delta E_{\Gamma,L}$. As shown in the last chapter 5, gain serves as a perfect probe of the band structure. Calculations within the tight-binding framework of the parasitic loss induced by the intervalence absorption at high strain are presented. The second part of this chapter models the optical confinement in the corner cube resonator. In particular, the cavity modes' role as an experimental tool to access the gain and the loss is discussed, together with experimental examples.

The following chapter 4 presents the first lasing in strained germanium. Cavity samples strained from 5.4 up to 5.9 % show, upon pulsed excitation of 100 ps, all the features typical of lasing, such as threshold in emitted intensity, mode competition, i.e., the transition from multimode to single mode spectra, gain clamping, and high quantum efficiency. In addition to the clear emergence of gain upon pulsed excitation, the lack of lasing in continuous wave excitation gives us insights into the band structure. Having excluded possible issues related to high thermal loading or low carrier density in steady state excitation, we find that germanium is not direct yet at 5.9 % of strain. However, the Γ and L band minima are closed enough to allow within the 100 ps long excitation pulse a transient population inversion in Γ . The latter is achieved at low temperature thanks to the lack of phonons mediating the scattering from Γ to L.

Chapter 5 presents the latest achievement of the thesis work, the unraveling of steady state lasing in strained germanium upon continuous wave (CW) excitation when strained is increased above 6 %. Combined with high-quality optical cavity, drastically reducing the loss and the amount of gain needed to reach the threshold, steady state lasing upon continuous wave pumping at low temperature aligns the group-IV approach to the traditional III-V laser. It is a clear signature of the high quality of the material and the achieved direct band gap configuration. However, the gain analysis as a function of the strain reveals that the energy difference between the conduction band edges closes slower than predicted. This effect, combined with the increased overlap of the Γ -VB1 transition energy with the intervalence band absorption, hinders the observation of lasing action at the highest strain here achieved of 6.6 %. Moreover, the linewidth narrowing above threshold as a function of the emitted power is discussed. In the final part, we give a first gain analysis of photoluminescence measurements of lower strained samples with moderate n-type doping. The last chapter resumes the outcomes of the thesis work.

2

Strained germanium principles

Contents

2.1 Band edges vs strain	10
2.2 Strain amplification technology	12
2.3 Optical cavity	15
2.4 Strained Ge cavities fabrication	16
2.5 Strain determination and enhancement upon cooling	20
2.6 Summary	23

In this chapter, we discuss the building blocks of strained germanium. We first understand the evolution of the band edges under strain, highlighting the alignment of the Γ and L valleys. The strain amplification technology adopted to load germanium with high uniaxial stress is first shown, followed by a description of how the active material is integrated into a strain maintaining optical cavity. With the main fabrication steps, the improvement carried out at the processing level to enhance the optical cavity quality is reported. The method to determine the strain is then illustrated.

Parts of section 2.5 were published in a similar form in the supplementary information of F.T. Armand Pilon et al., Lasing in strained germanium microbridges, *Nature Communications*, **10(1)**, 2724 (2019) [[92](#)].

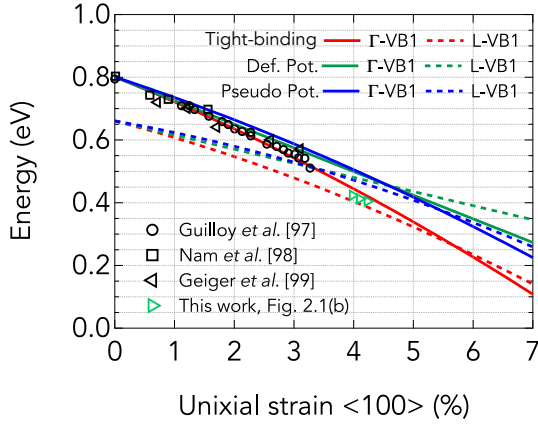
2.1 Band edges vs strain

The typical poor optical radiative properties of germanium stem from its indirect band gap nature, coercing the electron in the L valley to inefficient radiative recombination mediated by phonons for momentum conservation. The path toward an efficient light emitter based on germanium thus requires a direct band gap, in line with typical III-V lasers platforms: this novel configuration can be achieved by loading the material with tensile strain [67].

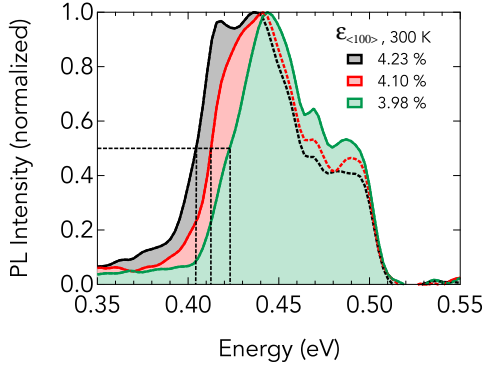
Prediction of the Ge band structure dependence on strain is thus of fundamental importance to evaluate the physical feasibility of such approach, as well as to develop a suitable strain technology. In Fig. 2.1(a) are reported the fundamental energy transitions as a function of strain along the equivalent set of crystallographic directions $\langle 100 \rangle$ for different models: green, blue and red colors refer to the deformation potential [84, 93], the pseudo potential [94, 95] and the tight-binding [92, 96] models, respectively. The solid and dashed lines indicate for all cases the interband transition between the bottom of the Γ valley and top of the valence band, i.e. Γ -VB1, and the indirect transition L-VB1, respectively. All the calculations here reported, as well the experimental data compared with, refer to a temperature of 300 K. These energy transitions, although do not represent the overall band structure, are in first analysis the fundamental ones, determining whether germanium can cross to the direct band gap configuration at a practical strain. The full band structure is give in section 3.1.

All models predict that the Γ valley decreases with a rate faster than the L valley, such that crossing to direct band gap is predicted at 300 K at 4.6 %, 5.4 % and 5.7 % of uniaxial strain according to the deformation potential, the pseudo potential, and the tight-binding models, respectively. While the deformation potential predicts a linear dependence of the band edges on strain, the pseudopotential and tight-binding models foresee a non linear dependence, which for the latter becomes dominant starting already from 2 % of strain. We note that at low temperature, by considering the temperature parametrization of the band gap [100], the crossing occurs at strain higher than the previous values. In particular, at 20 K the tight-binding prediction is 6 %.

To check the validity of these models, Fig.2.1(a) reports the experimental values available in the literature of the accessible direct Γ -VB1 transition as a function of the strain. For all the reported experiments the strain is measured via Raman spectroscopy at room temperature. The band gap is extracted either via fitting of the photoluminescence [98, 99] or by electroabsorption measurement [97]. At low strain below 1.5 % the scattered experimental points do not allow a precise comparison among the models. At higher strain, the measured direct band gap Γ -VB1 points are correctly followed by the tight-binding prediction. The validity of the tight-binding model is further confirmed up to more than 4 % by the work



- (a) Interband transition energies in Ge, for uniaxial strain along one of the equivalent crystallographic directions $\langle 100 \rangle$ at 300 K. The solid lines refer to the Γ -VB1 transition, while the dashed lines refer to the indirect transition L-VB1. The colors indicate the deformations potential, the pseudopotential, and the tight binding models, that are inferred from [84], [95] and [92], respectively. The experimental values are inferred from [97–99].



- (b) Low resolution photoluminescence measurement of highly strained germanium microbridges carried out at 300 K upon continuous wave excitation running at 590 meV.

Figure 2.1

of this thesis: the data points highlighted in green are extracted via photoluminescence measurements at room temperature, whose spectra are reported in Fig. 2.1(b).

The strain of the samples here investigated are 3.98, 4.10 and 4.23 %, as determined by Raman scattering. The latter measurement is carried out by Jeremie Chretien at CEA, IRIG-DEPHY, Grenoble (France). Photoluminescence measurements are carried out at room temperature in continuous wave excitation running at 590 meV. The band gap position is estimated as the energy corresponding to the half maximum spectral intensity of the photoluminescence background, as indicated in the figure. Further example of band gap extraction is given in section A.5. This approximation is adopted in order to avoid during the fitting procedure modulation in the emission due to multiple interference effects or absorption by air gases. Modulation between 450 and 490 meV is attributed to air gases absorption, as detailed in section A.1. High energy emission is suppressed by the long pass filter at 2440 nm (508 meV), employed to filter out possible excitation laser light reflected from the sample. Moreover, as the integrated intensity of the samples at room temperature is compatible with the thermal background, the low energy side of the photoluminescence of Fig. 2.1(b) is affected by the tail of the latter.

The overall general agreement between the experimental data and the tight-binding calculation about the Γ -VB1 transition justify its adoption as the model we reference to throughout this thesis. Moreover, the work of Guilloy et al. [97] shows that the tight-binding model well agrees with the measured splitting at Γ point between the VB1 and VB2 up to 3 % of strain. However, to our knowledge, no experimental works about the L-VB1 dependence on uniaxial strain along $\langle 100 \rangle$ are reported in literature. The position of the L valley respect to the top of the valence band is a quantity well known in relaxed and bulk Ge [101], but optically difficult to access to. Indeed when the Γ and L band minima are close, the direct recombination from Γ masks the inefficient phonon mediated photoluminescence from L. Thus the validity of the L-VB1 dependence on strain is still, in our opinion, an open and rather fundamental question to be answered to. Indeed, as analyzed in the next chapter, the energy difference between the Γ and L band edges, i.e., $\Delta E_{\Gamma,L} = E_{\Gamma} - E_L$, is the main parameter driving the optical enhancement of Ge. One of the goal of this thesis is to deliver this essential information by studying the lasing action in strained germanium.

2.2 Strain amplification technology

The traditional epitaxial method to introduce strain makes use of the difference in the lattice constants between the deposited layer and the substrate. In particular, to introduce tensile strain, Ge is grown on a substrate with larger lattice constant, such as InGaAs [77, 102, 103].

Beside the CMOS incompatibility, this approach is limited by the achievable thickness of the order of tens of nm, which is not compatible for optical applications in the near- and mid infrared region.

An alternative method compatible with the large scale semiconductor industry is the use of an external stressor layer, namely Si_3N_4 , which is indeed CMOS compatible and offers a very good control on the induced stress, by controlling its deposition parameters [104]. Following the relaxation of a compressively strained silicon nitride layer, biaxial strain below 1% are obtained in waveguide [78, 79, 105–107], micro pillar structures [108] and membrane [109]. Larger values are achieved in microdisks cavity [89, 107, 110–112], in combination with circular Bragg reflectors [80, 113].

According to the tight-binding model, germanium turns into a direct band gap material when loaded at low temperature with about 2% biaxial strain [92], which was reached only by the work of Millar et al. [111]. However, this work exhibits only photoluminescence emission. The adoption of silicon nitride as the stressor layer may lead to inhomogeneity in the strain, and thus gain, distribution. Additionally, the microdisk concept itself is prone to thermal management issues [112].

Alternatively, high level of strain can be achieved via external forces, like stretching nano membrane with gas pressure [114], or by mechanical bending with the tip of an atomic force microscopy [115, 116]. Although the latter are interesting in terms of material properties understanding [115], they do not represent a feasible large scale approach.

The technology adopted for this work relies on the concept of strain amplification. This approach was developed and demonstrated at Paul Scherrer Institut (PSI), Villigen (Switzerland) by Suess et al. [82] in Ge and by Minamisawa et al. [81] in Si. In the following its principles are introduced. For further detail the reader may refer to the reference [117].

The strain enhancement technology relies on the minimization of the elastic energy of a positively pre stressed layer which relax along geometrically defined directions, following its release from the sacrificial substrate. Having as a reference a germanium layer with a residual strain patterned as shown in Fig. 2.2, with B and b indicating the total length and width of the pads, which are connected together by a microbridge of length and width A and a , the following conservation condition holds:

$$(1 + \epsilon_0)B = \int_{-B/2}^{B/2} [1 + \epsilon_{<100>}(x)] dx \quad (2.1)$$

Equation 2.1 expresses the fact that once released from the substrate, the pads will relax by contracting as much as the microbridge will be stretched. In equation 2.1 ϵ_0 and $\epsilon_{<100>}$ refer to the residual biaxial pre strain of germanium and the variable strain along the

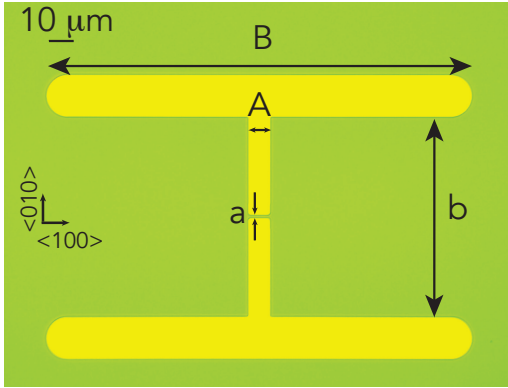


Figure 2.2: Optical microscope image taken after the definition of the chromium mask during the fabrication of a strained germanium microbridge, by exploiting the strain enhancement concept. Indicated with A and B the length of the microbridge and the pads, respectively, and with a and b the width of the microbridge and the pad, respectively. The geometry is aligned along the crystallographic direction $\langle 100 \rangle$.

direction of contraction x . Being at equilibrium requires that the sum over the forces is null, such that via Hooke's law the following relation holds true:

$$\epsilon^{pads} / \epsilon^{bridge} = a/b \quad (2.2)$$

By combining the equations 2.1 and 2.2, and taking into account an additional under etching of length L , we obtain the relation linking the geometry to the final strain of the microbridge via the enhancement factor EF:

$$EF = \frac{\epsilon_{\langle 100 \rangle}^{bridge}}{\epsilon_0} = \frac{2L + B}{B} \left[\frac{A}{B - A} + 1 \right] / \left[\frac{A}{B - A} + \frac{a}{b} \right] \quad (2.3)$$

The relation of equation 2.3 shows that the final strain of the suspended microbridge is determined solely by the (i) the built-in biaxial pre strain of the Ge layer ϵ_0 and (ii) the geometrical dimensions of the structure. The strength of this approach relies on its applicability to different scale, its compatibility with large scale integration and being independent of the material used. Moreover, with proper design, it is possible to obtain very high strain level, starting from low ϵ_0 value, such that the limit of this technology is represented uniquely by the ultimate strength of the material. The latter, for Ge, is 15 GPa, corresponding to a strain of about 14.6% [115, 118].

From a technologic point of view, the main node to be solved to access the strain enhancement method is developing a germanium layer with a biaxial residual strain ϵ_0 , on top of a sacrificial substrate. Highly strained germanium microbridges throughout this work are obtained by processing a germanium-on-Insulator (GeOI) platform, fabricated at CEA-LETI, Grenoble (France) [119]. Following the approach of thermal expansion mismatch between Ge and Si, the final stack consist of a high quality Ge layer of $1\ \mu\text{m}$ with a residual biaxial strain of about $\epsilon_0 = 0.16\%$ on top of $1\ \mu\text{m}$ sacrificial SiO_2 layer, processed on a 200 mm Si wafer. The strain amplification technology allows to reach uniaxial strain along $\langle 100 \rangle$ up to 4.9% at room temperature [120] and up to almost 6% at low temperature [92]. Its applicability is not restricted uniquely to the uniaxial strain, but also can serve to load germanium with biaxial strain in a cross-like fashion [85], or from multiple directions [90, 91, 121].

2.3 Optical cavity

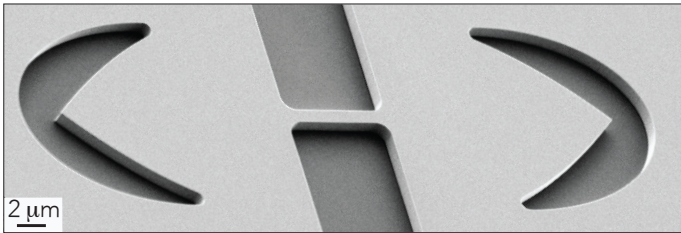


Figure 2.3: SEM image of microbridge embedded in strain maintaining cornercube cavity.

As much as the design of the gain medium, engineering the laser resonant cavity is of fundamental importance. The optical resonator sustain certain standing waves, i.e. modes, whose frequencies are determined by the cavity configuration and provides the positive feedback necessary for amplifying light and reaching lasing oscillation. Light can be confined by simple reflection between two planar mirrors, the so called Fabry-Perot resonator, via whispering gallery modes near the surface of microdisks, or with dielectric layers periodically stacked, such as the distributed Bragg reflectors, which are widely used in the vertical-cavity surface-emitting lasers (VCSELs). Alternatively, light confinement can be achieved in two dimensions in periodically engineered dielectric material, as in photonics crystals.

To achieve lasing, the active strained microbridge has to be embedded into a strain-maintaining optical cavity. The solution adopted throughout this work has the form of cornercube mirrors, whose concept was proposed by Christopher Bonzon at ETH in 2014 [122], and then further developed at PSI by Richard Geiger, Thomas Zabel and Esteban

Marin. As shown in Fig. 2.3, each of the two mirrors is formed by two parabola sections, whose foci are placed at the entrance of microbridge, guaranteeing that the light exiting the constriction is first collected and then refocused back into the microbridge.

On the contrary of similar solutions [87], which exploit concentric DBR reflectors, the parabolic design has the additional advantage that light hits the interface above the critical angle of total internal reflection, which for the Ge/air interface is as low as 14.5° , leading theoretically to a very high mirror reflectivity. As further detailed in 3.4, the cornercube solutions act as Fabry-Perot optical resonator and, on the contrary of DFB- of DBR-based concepts, is multimode, being the optimal solution in this early stage of demonstration of lasing in strained germanium. Indeed the emission peaks at different energies depending on the strain and on the temperature. Moreover, from a processing point of view, the cornercube can be defined during the same lithographical step as the rest of the geometry, guaranteeing good alignment with the active material, without additional fabrications steps.

The modeling of the eigenfrequencies which built up in the cornercube resonator and the concept of cavity modes as the experimental tool to access gain and loss information are extensively discussed in 3.4

2.4 Strained Ge cavities fabrication

The process flow for the fabrication of the suspended and strained microbridges embedded in the cornercube resonator was developed at PSI by Richard Geiger, Thomas Zabel and Esteban Marin [83, 123]. In this section it is then shortly described, focusing on the improvement developed during this thesis work for the hard Cr mask definition step, which lead to an increase of the final yield and to a substantial reduction of the cavity losses.

Fig. 2.4 resumes the processing flow. Starting from a germanium on Insulator (GeOI) substrate, which consist of a Ge layer biaxially pre-strained at 0.16 % over a $1\ \mu\text{m}$ SiO_2 layer, as previously described, the first step involves the deposition of 30 nm of Chromium (Cr) as the hard mask for the Ge definition via electron beam deposition. The design consist of two stressor pads, connected by a $8\ \mu\text{m}$ long and $1\ \mu\text{m}$ wide microbridge, and the optical cavity, formed by two parabolically shaped cornercube mirrors, focused in microbridge edges.

The gain material has a volume of $8\ \mu\text{m}^3$ and the cavity length, defined as the distance between the two cornercube tips, is set as $44\ \mu\text{m}$, if not stated otherwise. The geometry is defined via electron-beam lithography (eBEAM), using polymethylmethacrylat (PMMA) as the resist. The design is developed in a solution of MIBK and isopropanol, transferred to the hard Cr mask via dry metal etching and then finally transferred to germanium via inductively-coupled reactive-ion-etching. For the latter, a mixture of fluorine-based gases,

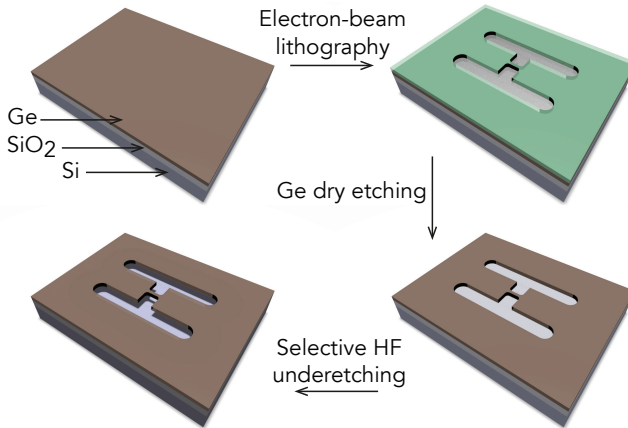


Figure 2.4: Main processing steps of the microbridge fabrication. The image is reproduced from [123].

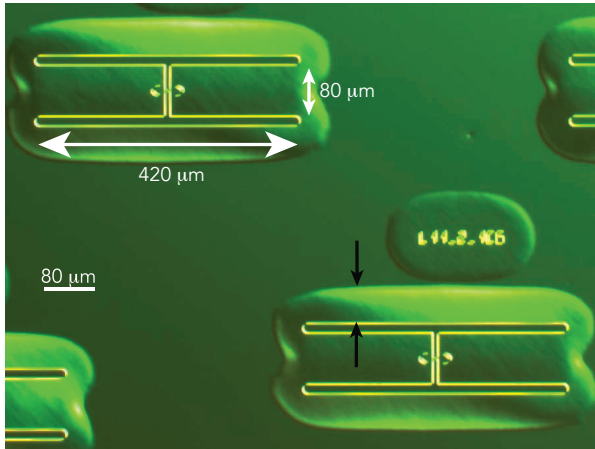


Figure 2.5: Image taken during a test run, after the completion of the SiO₂ under etching, in differential contrast mode. The black arrows highlight the underetched area. The white arrows represent the total length and width of the pads of 420 and 80 μm , respectively.

ICP (W)	RF (W)	Cl ₂	O ₂	Pressure (mTorr)	time (s)
350	5	50	8	10	90

Table 2.1: Cr mask etching recipe.

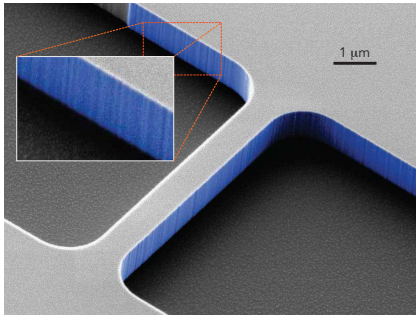
SF₆ and C₄F₈, and O₂ is employed, in proportion of 8:14:1, respectively, at base temperature of -10° .

The final steps involves the selective etching of the underlying silicon oxide by vapor HF, as shown in Fig. 2.5, in order to release the Ge structure and enabling the pads to elastically relax. The microbridge is then uniaxially stretched along the crystallographic direction $\langle 100 \rangle$, to an amount uniquely defined by the material and the geometry of the patterning.

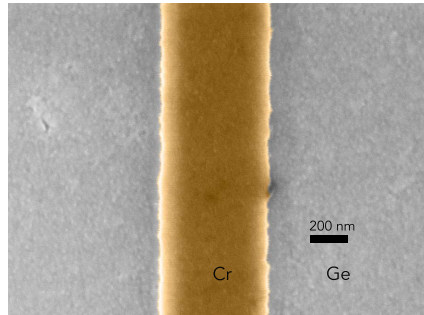
The microbridge sidewall roughness represent the main limit factor in terms of final yield [83] and optical losses. The typical vertical signatures of the microbridge sidewall, c.f. Fig. 2.6(a), indicate that such pattern is not caused by the Ge dry etching itself, but it is transferred to the Ge by the irregular definition of the hard Cr mask on top. Fig. 2.6(b) shows a reference SEM of the Cr mask defining the microbridge, where it is possible to notice indeed the irregular shape of the edges.

To improve this step, following the PMMA development, the sample undergoes to an oxygen/argon plasma step in RF, in order to better define the sidewall and get rid of possible footsteps, which stem from not proper development of the resist. The new developed recipe for the metal etching step is defined in table 2.1. The low pressure of 10 mTorr, together with the low ratio between O₂ and Cl₂ of 16 %, improves the Cr etching selectivity, as well the anisotropy of the process [124].

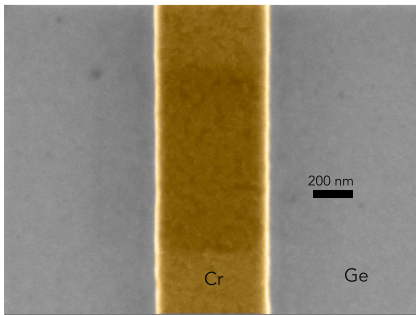
Fig. 2.6(c) shows the Cr hard mask defined with the recipe of table 2.1: compared to the previous results, the edges are highly defined, without footsteps and with low level of irregularities. With such higher quality hard mask, the sidewall of the microbridge are smooth and better defined, as shown in Fig. 2.6(d). This improvement lead not only to higher yield, but more importantly to a strong reduction of the cavity scattering losses, as discussed in section 3.4.6, which, combined to the high strain, enables lasing action under continuous wave excitation, as shown in the experiment of chapter 5.



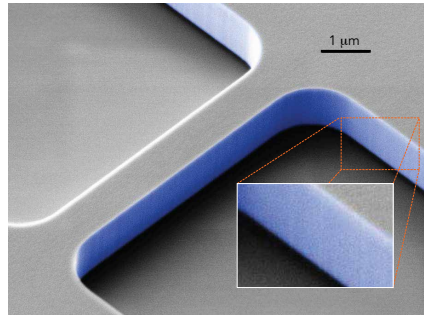
(a) Tilted SEM image of a microbridge processed with the reference recipe. The vertically oriented roughness indicate that the defects are transferred from the previous step, i.e. the Cr hard mask (b)



(b) Top view of the Cr hard mask defined with the reference recipe during a test run. The edge irregularities size are of the order of 10 nm



(c) Top SEM view of the Cr mask defined with the recipe of table 2.1 during a test run. Compared to (b) the edges are smooth and regular



(d) Tilted SEM image highlighting in false colour the sidewall. The improvement of the hard mask etching (c) leads to the sidewall smoothness.

Figure 2.6: Hard Cr mask definition improvement lead to an overall higher quality cavity sidewalls, increasing the yield and drastically reducing the optical scattering losses.

2.5 Strain determination and enhancement upon cooling

As shown in section 2.2 the microbridge geometry is defined by the bridge length (A) and width (a), the total pad length (B) and width (b), as well as the additional under etching of the pads (L), which is the only parameter related to the processing step. If not stated otherwise, throughout this work the typical microbridge structure dimensions are the following: 8, 1 and 80 μm for the microbridge length (A), width (a) and the pad width (b), respectively, while the strain is modulated by varying the pad length.

In tables 2.2 and 2.3 are reported the values of the pad length for a typical series of samples, without and with cavity, respectively. Each geometry is related to the enhancement factor EF of equation 2.3. An additional under etching length $L = 10 \mu\text{m}$ is considered for both tables. Reported in the fourth columns, the predicted strain values at room temperature, obtained from the calculated pre-strain value of $\epsilon_0 = 0.154\%$. The latter value is calculated from equation 2.5 and well compares to the measured $\epsilon_0 = 0.16\%$ via x-ray diffraction.

The modeled strain values agree with the experimental strain measurements, reported in the last column, carried out via Raman scattering for a subset of cavities. The Raman shift is related to the strain along the crystallographic direction $\langle 100 \rangle$ by the following non linear relationship, calibrated by means of micro X ray diffraction measurements [120]:

$$\epsilon_{\langle 100 \rangle} = -0.019\Delta\omega^2 + 0.68\Delta\omega \quad (2.4)$$

where $\Delta\omega$ is the Raman shift in units of cm^{-1} . We compare the experimental strain values of samples with the same microbridge structure with and without cavity. We observe a reduction of about 10% when the cavity is integrated, finding good agreement with finite element method (FEM) simulation. As shown in table 2.3, the strain reduction due to the cavity reduces the EF of the same factor.

The pre strain value is predicted as the difference between the germanium and silicon thermal expansion coefficient, i.e. $\epsilon_0 = \int_{T_0}^{T_1} \alpha_{Ge}(T) - \alpha_{Si}(T) dT$. The reduction of the experimental temperature further enhances ϵ_0 . Its increase can be parametrized via the following expression, which fits the Ge and Si thermal expansion coefficients, as obtained from [125] and [126], respectively:

$$\begin{aligned} \frac{\epsilon_0(T)}{100} = & -2.65466 \cdot 10^{-4} \exp[-0.00588 T_0] + 2.65466 \cdot 10^{-4} \exp[-0.00588 T] \\ & + 2.298 \cdot 10^{-6} (T_0 - T) + 1.5266 \cdot 10^{-9} (T_0^2 - T^2) \\ & - 1.16667 \cdot 10^{-13} (T_0^3 - T^3) \end{aligned} \quad (2.5)$$

This section 2.5 was published in a similar form in the supplementary information of [92].

Sample	Pad Length	EF	$\epsilon_{<100>} (%)$	$\epsilon_{<100>} (%)$	$\Delta\omega (cm^{-1})$	$\epsilon_{<100>} (%)$
	B (μm)	w/o cavity	@300 K	@20 K	w/o cavity	from eq.2.4
L1	186	20.15	3.10	5.04		
L2	212	21.99	3.38	5.50	6.07	3.38
L3	240	23.85	3.66	5.97		
L4	260	25.11	3.85	6.28	6.96	3.74
L5	280	26.32	4.05	6.60		
L6	300	27.47	4.22	6.87	-	-

Table 2.2: Geometrical dimensions of samples labelled L1 to L6 without cavity, with increasing total pad length. The predicted strain values at 300 and 20 K are reported, together with the experimental Raman measurement at room temperature, when available.

Sample	Pad Length	EF	$\epsilon_{<100>} (%)$	$\epsilon_{<100>} (%)$	$\Delta\omega (cm^{-1})$	$\epsilon_{<100>} (%)$
	B (μm)	with cavity	@300 K	@20 K	with cavity	from eq.2.4
L1	186	18.13	2.78	4.54		
L2	212	19.80	3.04	4.96	5.24	3.00
L3	240	21.46	3.30	5.37		
L4	260	22.60	3.47	5.66	5.90	3.30
L5	280	23.68	3.64	5.93		
L6	300	24.72	3.80	6.19	6.95	3.74

Table 2.3: Geometrical dimension and parameters of samples with cavity, together with the experimental Raman measurement at room temperature, when available.

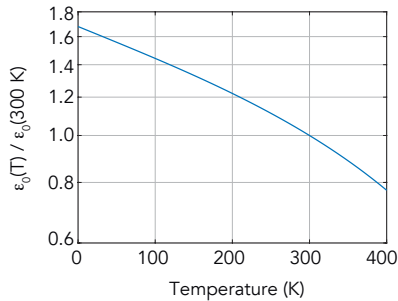


Figure 2.7: $\epsilon_0(T)$ dependence on temperature, normalized to $\epsilon_0(300 \text{ K})$, following equation 2.5. The vertical axis is in logarithmic scale.

where T and T_0 are in unit of Kelvin and T_0 refers to the temperature at which the Ge layer is relaxed. For the processing of the GeOI stack employed in this work, T_0 is found to be 701 K [83] and it corresponds to the temperature of the growth or the possible subsequent annealing temperature. Fig. 2.7 reports the enhancement of $\epsilon_0(T)$ upon cooling, normalized to $\epsilon_0(300 \text{ K})$ in logarithmic scale.

Fig. 2.8 shows the photoluminescence spectra from room temperature down to 20 K of a cavity with nominal dimensions equivalent to L6. The photoluminescence emission strongly red shifts, following the increase of the strain upon cooling. From the nominal L6 enhancement factor EF (c.f. table 2.3), we predict the strain per each temperature via Fig. 2.7. The black lines on top report the nominal Γ -VB1 positions. The latter are inferred from the tight-binding model, as described in 2.1, and by considering the Varshni shift with temperature [100].

The predictions systematically overestimate the band gap positions already from room temperature. This discrepancy is attributed to (i) inhomogeneity of the HF under etching rate and (ii) uncertainty within 100 nm in the definition of the microbridge dimensions during the processing. Raman measurements for this processing batch are not available. We thus assign at room temperature a band gap of 444 meV, as indicated in bottom of the figure, corresponding to 4 % of strain and EF=26. From this value, we indicate the expected band gap position per each temperature, finding a good agreement down to 100 K.

However, at 20 K the photoluminescence emission shows a deviation from the expected strain. We attribute this effect to a reduction at low temperature of the geometrical dimension effectively contributing to the strain enhancement. Further details of this effect are given in section 5.2.

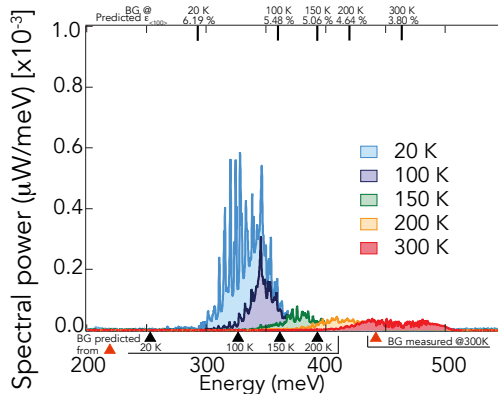


Figure 2.8: Temperature induced red shift of the photoluminescence emission of a sample with nominal dimensions of L6, embedded in a cornercube cavity. The emission peak at room temperature is affected by water molecules absorption (c.f. A.1). The black lines at the top indicate for each temperature the nominal band gap position predicted by the geometrical dimensions. The band gap positions inferred from the photoluminescence at room temperature are indicated in the bottom. The spectra are carried out upon continuous wave excitation of $E_{exc} = 590$ meV.

2.6 Summary

This chapter showed the fundamentals of the strained germanium. Prediction of the band structure dependence on uniaxial loading is of fundamental importance to evaluate the strain approach's feasibility. The tight-binding model foresees the crossing to direct band gap configuration at room (low) temperature at about 5.7% (6 %) of strain along the $\langle 100 \rangle$ crystallographic directions. Moreover, it correctly predicts the non linear red shift of the direct band gap transition Γ -VB1 at strain larger than 1.5 %, as experimentally found in literature and here confirmed for strain larger than 4 % by photoluminescence measurements at room temperature. However, to our knowledge, no experimental verification of the L-VB1 dependence on strain exists, and thus the crossing to direct band gap configuration is not yet backed up by any experiment. The gain emergence will provide in the next chapters further knowledge about the energy difference $\Delta E_{\Gamma,L}$ between the Γ and L band edges.

The technology adopted to reach high levels of strain routinely is based on the amplification of the residual strain. Starting from a germanium-on-insulator layer biaxially strained at $\epsilon_0 = 0.16\%$, microbridges strained up to more than 4% are obtained at room temperature. The active strained material is integrated into a strain-maintaining optical cavity.

The strained germanium microbridge's fabrication integrated into the cavity starts from a high-quality germanium-on-insulator layer, with a thickness of $1\ \mu\text{m}$. Processing-wise, the chromium hard mask's definition for the germanium dry etching is found to be the principal limit in terms of sidewall roughness. This step's improvement leads to almost roughness-free sidewalls, improving the yield and reducing the optical scattering losses, as shown in the next chapter.

As inferred from the geometry, the nominal strains at room temperature compare well with the Raman scattering measurements. The temperature reduction increases further the strain, following the residual pre strain ϵ_0 enhancement, and strongly red shifts the direct band gap Γ -VB1. However, at 20 K the photoluminescence onset deviates from the expected strain. This discrepancy may arise from mechanical deviations of the geometry effectively contributing to the strain. This effect's comprehension requires further studies, as Raman scattering at low temperature and 3D strain modeling. When strain deviation occurs at low temperatures, the strain is inferred from the photoluminescence. At 20 K we achieved 6% of strain, allowing access to the predicted region of crossing between indirect and direct band gap configuration.

3

Strained germanium laser modeling

Contents

3.1 Full band structure of strained germanium	26
3.2 Electron and hole statistic	28
3.3 Gain and loss	31
3.3.1 Gain and $\Delta E_{\Gamma,L}$	33
3.3.2 Gain spectrum and transparency	35
3.3.3 n-doping	37
3.3.4 Parasitic losses	38
3.4 Optical resonator	40
3.4.1 Cavity modes and loss	40
3.4.2 Q factor of the cornercube cavity	42
3.4.3 Multimode cavity pattern	46
3.4.4 3D cavity modeling	49
3.4.5 Cavity scattering loss	50
3.4.6 Excitation wavelength dependence and absorption	51
3.5 Thermal load	54
3.6 Summary	56

The previous chapter presented the principles of the strained germanium. Here, we aim to study the laser's building blocks based on it: the strained germanium's radiative properties and the cornercube cavity. We first expose the full band structure of Ge upon uniaxial strain along $\langle 100 \rangle$. After detailing the carriers statistic, the optical gain calculations as a function of the energy difference $\Delta E_{\Gamma,L}$ between the Γ and L minima are carried out and presented with the prediction of the intervalence band absorption, representing the main loss channel. In the second part, the cavity modes, which are the primary

experimental tool to access gain and loss information, are modeled within the cornercube cavity. Finally, we present a preliminary study of the thermal load in suspended Ge microbridge upon continuous wave excitation.

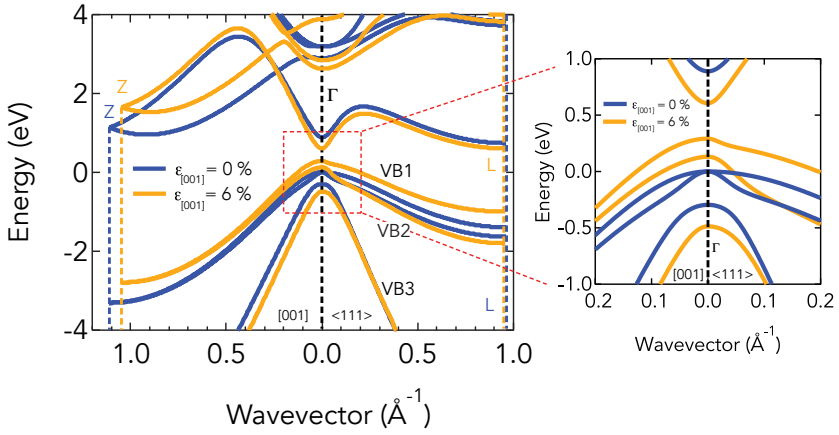
Parts of sections 3.1 and 3.4.4 were published in a similar form in the supplementary information of F.T. Armand Pilon et al., Lasing in strained germanium microbridges, *Nature Communications*, **10(1)**, 2724 (2019) [92].

3.1 Full band structure of strained germanium

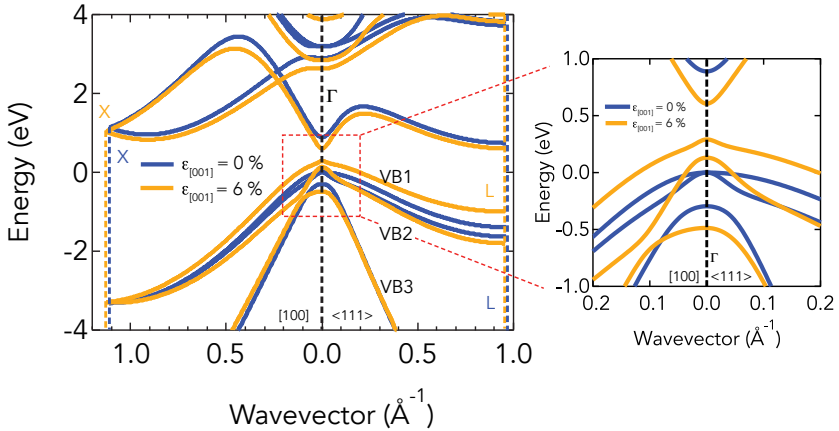
The tight-binding model of section 2.1 indicated the strain at which the cross-over to the direct band configuration occurs. The next sections of this chapter aim to investigate the impact on the optical gain of the energy difference between the Γ and L minima, i.e., $\Delta E_{\Gamma,L} = E_{\Gamma} - E_L$. However, a complete understanding of the lasing mechanism requires the comprehension of the loss and the dependence on the strain of the valence bands. Before the Ge optical gain calculations, this section reports about the evolution of the germanium full band structure upon uniaxial strain, carried out with the tight-binding model.

Fig. 3.1 shows the full band structure for relaxed (blue) and 6% strained germanium (orange). The band structure calculations are normalized to 20 K and the strain is applied along the direction [001]. At 6% of strain and at low temperature the energy difference $\Delta E_{\Gamma,L}$ is zero. At the same time, the degeneracy of the top two valence bands VB1 and VB2 is lifted up to a predicted value of $\Delta E_{VB1,VB2} = E_{VB1} - E_{VB2} = -0.160$ eV. Under steady population inversion, the direct interband transitions between the bottom of the Γ valley and the top of the valence bands are responsible for the optical gain. Concurrently, the direct intervalence band transitions, between VB1, VB2, and VB3 account for the major loss channel, i.e., the intervalence band absorption. The intervalence band absorption modeling as a function of hole density and temperature is of fundamental importance for predicting lasing and it is presented in section 3.3.4.

Moreover, from Fig. 3.1 we notice that the strain breaks the crystal symmetry, as shown by the difference when moving along the direction Z- Γ -L (c.f. Fig. 3.1(a)) and X- Γ -L (c.f. Fig. 3.1(b)). The latter is equivalent to Y- Γ -L. Upon strain the absolute distance from Γ to Z (a) and to X (b) decreases and increases, respectively, as reported by the shift of the dashed lines. In contrast, the symmetry of the band structure from Γ to L is conserved under uniaxial strain.



(a) Germanium band structure along the Z, Γ , L points. Due to strain the absolute position of Z decreases. Inset: enlarged view around the Γ point.



(b) Germanium band structure along the X, Γ , L points. Due to strain the absolute position of X increases, following the Poisson's relation. Inset: enlarged view around the Γ point.

Figure 3.1: Germanium's band structure calculated with the tight-binding model and normalized to 20 K upon 6% (orange) and 0% (blue) of strain along the [001] direction. For both (a) and (b) the dashed orange (blue) lines correspond to the symmetry points of the strain (unstrained) of the first Brillouin zone (FBZ). The calculations are performed by Yann-Michel Niquet at CEA-IRIG-DePhy, Grenoble (France).

3.2 Electron and hole statistic

The prediction of the strained germanium optical gain first requires modeling the carrier distribution between the conduction bands. In relaxed germanium, the carrier population in the Γ valley, which can efficiently recombine radiatively without phonon interaction, is negligible. Its density depends on the temperature and the electron-electron and electron-phonon processes from the L valley. However, at sufficiently high strain, the energy difference $\Delta E_{\Gamma,L}$ reduces enough such that a certain fraction of the total carriers density steadily populates the Γ valley. In a semiconductor the carrier statistics is described by the Fermi distribution function

$$f(E, T, \mu) = \frac{1}{\exp\left(\frac{E-\mu}{k_b T}\right) + 1} \quad (3.1)$$

where μ is the quasi-Fermi level, and by the three-dimensional density of states:

$$\rho^{3D}(E, E_0, m^*) = \frac{1}{2\pi} \frac{(2m^*)}{\hbar^3} \sqrt{E - E_0} \quad (3.2)$$

The integration over the energy of the product between equations 3.1 and 3.2, gives the total number of carriers. In particular, for the case of germanium, the total numbers of electrons in the conduction bands and holes in the valence bands are, respectively:

$$N_{tot}^{el} = \int_{\min(E_{\Gamma}, E_L)}^{\infty} \sum_{i=\Gamma, L} \rho_i^{3D}(E, E_i, m_i^*) f_c(E, T, \mu_c) dE \quad (3.3)$$

and

$$N_{tot}^h = \int_{E_{HH}}^{-\infty} \sum_{i=VB1, VB2, VB3} -\rho_i^{3D}(-E, -E_i, m_i^*) [1 - f_v(E, T, \mu_v)] dE \quad (3.4)$$

where μ_c and μ_v are the quasi-Fermi levels of electrons in thermal equilibrium at temperature T in the conduction and valence bands. Their distribution is described by Fermi distribution functions f_c and f_v , respectively. E_i is the band edge energy of the i^{th} band. Charge neutrality requires that $N_{tot}^{el} = N_{tot}^h = N_{tot}$.

The longitudinal and transverse masses are determined using the tight-binding model and are reported in table 3.1 for uniaxial strain of 0 and 6 % along [100]. The band edges positions relative to the top of the valence band VB1 normalized to 20 K are reported as well. For the Γ and the valence bands, m^l indicates the component longitudinal to the strain, i.e. along [001], while m^t indicates the components along [100] and [010]. For the L band, m^l and m^t mean the components along the [111] and [1-10] directions, respectively. While for relaxed germanium the masses at Γ are isotropic along $\langle 100 \rangle$, the strain, by breaking the crystal symmetry, leads to anisotropic effects.

	$\epsilon_{<100>} = 0 \%$			$\epsilon_{<100>} = 6 \%$		
	Band edge (eV), 20 K	m_i^l	m_i^t	Band edge (eV), 20 K	m_i^l	m_i^t
Γ	0.888	0.03799	0.03799	0.314	0.03329	0.01813
L	0.740	1.59430	0.08246	0.314	1.55567	0.09067
VB1	-	0.21116	0.21116	-	0.17987	0.02763
VB2	0	0.04722	0.04722	-0.160	0.12504	0.04192
VB3	-0.296	0.10000	0.10000	-0.777	0.03715	0.23103

Table 3.1: Longitudinal and transverse masses at 0 and at 6 % of tensile strain applied along [001] for the Γ and L bands and for the three valence bands VB1, VB2 and VB3. The band edges values are normalized to 20 K. The values here reported are calculated using the tight-binding model and carried out by Yann-Michel Niquet at CEA-IRIG-DePhy, Grenoble (France).

From table 3.1 we extract the density of states effective masses used in equations 3.3 and 3.4. For the Γ and L valleys, $m_\Gamma^* = (m_\Gamma^l m_\Gamma^t m_\Gamma^t)^{1/3}$ and $m_L^* = (d^2 m_L^l m_L^t m_L^t)^{1/3}$, where d is the L valley degeneracy equal to 4. At 6 % of strain the density of state effective masses are $m_\Gamma^* = 0.022$ and $m_L^* = 0.589$.

In the following, we discuss about the carrier distribution. In the previous section 2.1, we showed that the conduction band edges dependence on strain is still an open question and thus the main parameter considered here and afterward is not the uniaxial strain, but the energy difference $\Delta E_{\Gamma,L}$. If not stated otherwise, the energy difference between the Γ and L minima is modulated by keeping fixed the Γ band edge and by sweeping the L band position. As literature convention, a positive value of $\Delta E_{\Gamma,L}$ indicates an indirect band gap configuration, while negative values mean that Ge becomes direct.

The quasi-Fermi level μ_c of the conduction band is calculated self-consistently by inverting the equation 3.3 of the total electron density N_{tot}^{el} . The electron density in the Γ and L valleys are then calculated separately as:

$$N_{\Gamma,L}^{el} = \int_{E_\Gamma, E_L}^{\infty} \rho^{3D}(E, E_{\Gamma,L}, m_{\Gamma,L}^*) f(E, T, \mu_c) dE \quad (3.5)$$

Fig. 3.2(a) reports the contour plot of the electron density in the Γ valley, i.e., N_Γ , as a function of the energy difference $\Delta E_{\Gamma,L}$ between the Γ and L minima and the total carrier density N_{tot} at temperature of 50 K. While strained germanium is still an indirect band gap material, the electron population in Γ is almost negligible: when the $\Delta E_{\Gamma,L}$ is 20 meV, it is necessary to pump up to a total carrier density of $3 \cdot 10^{18} \text{ cm}^{-3}$ in order to populate Γ with a

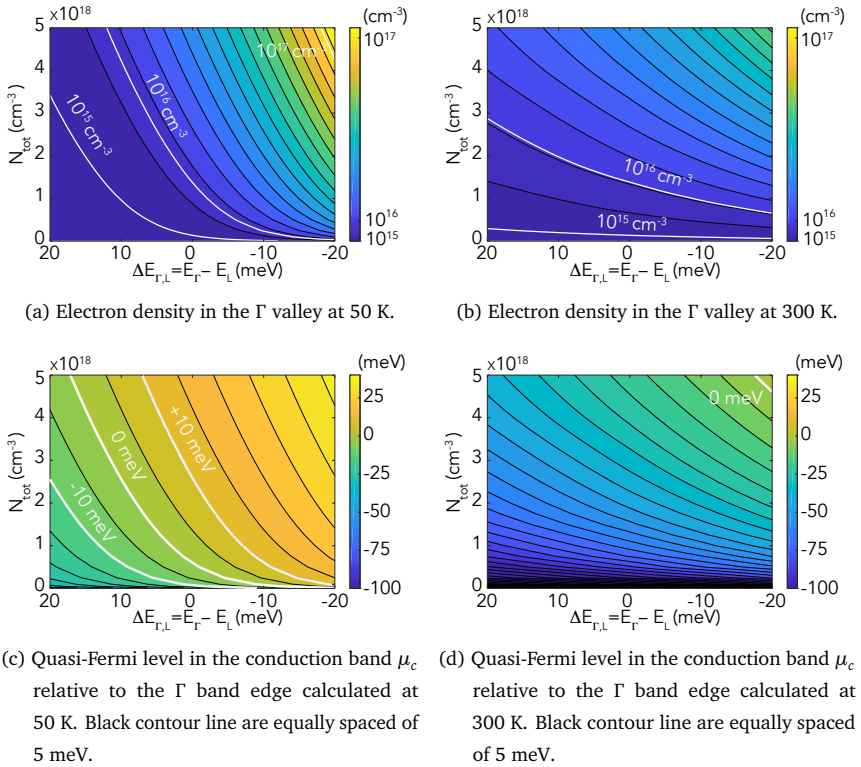


Figure 3.2: Electrons statistic as a function of the total carrier density and the energy difference $\Delta E_{\Gamma,L}$ between the Γ and L minima. The color scale is the same for figures (a) and (b) and for figures (c) and (d)

density of about 10^{15} cm^{-3} , corresponding to less than 1 carrier in the Γ valley over a total of 1000. The picture quickly changes by reducing energy difference $\Delta E_{\Gamma,L}$ between the Γ and L minima: the distribution of carriers in the Γ valley becomes more and more efficient such that when $\Delta E_{\Gamma,L} = -20 \text{ meV}$ is reached, it is possible to obtain a pumping efficiency in Γ of about 2%.

When the temperature is increased to 300 K, corresponding to additional energy of $k_b T = 26 \text{ meV}$, the electron distribution in the Γ valley loses efficiency, as can be seen in

Fig. 3.2(b). The broader Fermi distribution enhances the N_{Γ} population when germanium is still indirect. However, the percentage of total electron density in the Γ valley drastically drops for the direct configuration, compared to the low temperature case. As an indication, a carrier density of $N_{\Gamma} = 10^{17} \text{ cm}^{-3}$ upon total pumping of $3 \cdot 10^{18} \text{ cm}^{-3}$ can be reached only when $\Delta E_{\Gamma,L} = -50 \text{ meV}$.

The overall not optimal efficiency of the carrier pumping in the Γ valley stems from L valley's presence at the same energy level and the one order of magnitude difference in states density between the two conduction bands. Fig. 3.2(c) reports the quasi-Fermi level μ_c position relative to the Γ band edge, as a function of the energy difference $\Delta E_{\Gamma,L}$ and the total carrier density. When germanium is direct the μ_c grows rapidly and, once it reaches the L band edge, it keeps increasing, but with a rate one order of magnitude slower, following the larger L density of states. When Ge is indirect, the quasi-Fermi level struggles to reach the Γ band edge. Fig. 3.2(d) depicts the effect of the additional thermal energy at room temperature: the quasi-Fermi level μ_c is kept below the Γ band edge, even for direct band gap configuration.

The calculations reported in Fig. 3.2 make use of some approximations and are meant to give an overall qualitative picture. Nor electron-electron or electron-phonon processes are directly taken into account and thermal equilibrium is assumed, i.e. the carrier's distribution is characterized by the same temperature of the lattice. Moreover, the model here described treats the band dispersion as quadratic: such parabolic approximation is in general valid for the conduction bands, especially for L valley [127] and its validity is expected to depart, particularly for Γ valley, for large values of \mathbf{k} . However, for this work, the probed range of \mathbf{k} around the Γ point is usually small enough to guarantee the parabolic approximation's validity. The formalism and the approximation introduced here are adopted to calculate the optical gain in strained germanium in the next sections.

3.3 Gain and loss

This section is devoted to the calculation of the gain build-up in strained germanium, followed by the illustration of the parasitic losses.

The interband absorption coefficient spectrum is calculated as the ratio between the net photon number absorbed per second per unit of volume and the photon number incident per second per unit area. Using Fermi's golden rule we first calculate the probability of an electron interacting with an external radiation field with frequency ω and amplitude E_0 to make a transition from the initial state in the valence band $|\nu\rangle$ with energy E_i to the final state $|c\rangle$ with energy E_f :

$$P_{i \rightarrow f}(\hbar\omega) = \frac{2\pi}{\hbar} |H'_{vc}|^2 \delta(E_f - E_i - \hbar\omega) \quad (3.6)$$

where H'_{vc} is the matrix element of the perturbative hamiltonian between the initial and final states. In the first order perturbative approximation

$$H' = -\frac{qA_0}{2m_0} \hat{\mathbf{e}} \cdot \mathbf{p} \quad (3.7)$$

where A_0 and $\hat{\mathbf{e}}$ are the vector potential and the polarization of the electric field E_0 . The equation 3.6 implicitly states that the probability of stimulated absorption and emission are the same.

To calculate the net absorption rate we consider that under steady state external excitation the electron density in the conduction and valence bands are described separately by the two chemical potential $\mu_{c,v}$ and the Fermi distributions $f_{c,v}$, as described by equation 3.1. The net absorption rate is found by multiplying the equation 3.6 with the additional probability factor which expresses the net absorption:

$$f_v(E_i)[1 - f_c(E_f)] - f_c(E_f)[1 - f_v(E_i)] = f_v(E_i) - f_c(E_f) \quad (3.8)$$

The irradiance of the perturbative radiation field can be expressed as:

$$I = \frac{nc\epsilon_0\omega^2 A_0^2}{2} \quad (3.9)$$

and by combining equations 3.6, 3.8 and 3.9 and integrating over all possible combinations of states in the reciprocal space satisfying the conditions of energy and momentum conservations, the absorption is found as [127]:

$$\alpha_{IB}(\hbar\omega) = \frac{\pi e^2}{nc\epsilon_0 m_0^2 \omega} \int \frac{2 d^3k}{(2\pi)^3} |\hat{\mathbf{e}} \cdot \mathbf{p}_{vc}|^2 \delta(E_f - E_i - \hbar\omega) [f_v(E_i) - f_c(E_f)] \quad (3.10)$$

There is no distinction between the two transverse electric (TE) and transverse magnetic (TM) polarizations. The dipole matrix element is defined as $|\hat{\mathbf{e}} \cdot \mathbf{p}_{vc}|^2 = \frac{m_0}{2} E_t$, where E_t is the energy parameter. For the interband transitions between the Γ valley and the top two valence bands VB1 and VB2, the tight-binding model finds for 0 and 6 % of strain $E_t(\Gamma\text{-VB1})=13.6$ eV and $E_t(\Gamma\text{-VB2})=4.5$ eV, and $E_t(\Gamma\text{-VB1})=11.3$ eV and $E_t(\Gamma\text{-VB2})=10.6$ eV, respectively. The dipole matrix elements are independent of the TE and TM polarizations. The ratio between the Γ -VB1 and Γ -VB2 transitions changes at large strain likely due to the hybridization between the VB2 and VB3 bands. The calculation of the dipole matrix elements was performed by Yann-Michel Niquet at CEA-IRIG-DePhy, Grenoble (France).

In the following, we do not consider strain dependent variation of the dipole matrix element and the masses around 6 % of strain, i.e., $\Delta E_{\Gamma,L} = 0$ meV. Gain modeling is performed

only for the transition between the Γ valley and top valence band VB1. Transitions between Γ and VB2 are allowed only at high power and depend on the valence bands dispersion, whose effect is not described by our modeling's quadratic dispersion. According to the tight-binding model, the quasi-Fermi level μ_v is far from reaching the top of the VB2 within the excitation density of $5 \cdot 10^{18} \text{ cm}^{-3}$.

3.3.1 Gain and $\Delta E_{\Gamma,L}$

An estimation of the amount of gain required to reach the lasing threshold can be made by considering that the predicted quality factor of the cornercube resonator is about 2000 (c.f. 3.4.2). This figure corresponds, for a laser mode whose resonance frequency is about 80 THz, to total optical loss of about 37 cm^{-1} . Considering that strained germanium active volume represents only less than 20% of the total cavity, to compensate for such losses, the material has to deliver an amount of gain of about 200 cm^{-1} . This number represents a lower bound, as the optical simulation does not consider the unavoidable cavity scattering losses (see section 3.4.6). Thus, for a more straightforward comparison with the figures, we take a gain value of 250 cm^{-1} as reference.

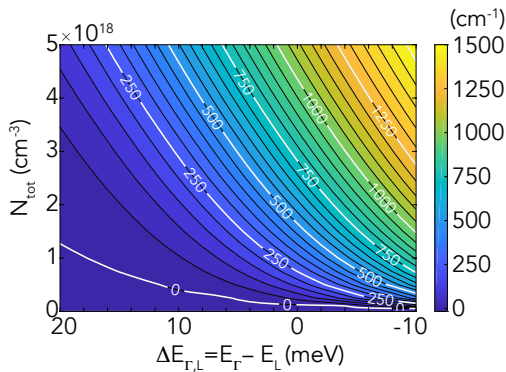
Fig. 3.3(a) shows the contour map of the peak gain as a function of the total injected carrier density and the energy difference $\Delta E_{\Gamma,L}$, at low temperature of 50 K. The interband absorption calculation is convoluted with a lorentzian function of width $\Gamma_{lor} = 4 \text{ meV}$, to consider the homogeneous state broadening due to electron-electron and electron-phonon interaction.

Assuming negligible losses up to $5 \cdot 10^{18} \text{ cm}^{-3}$, Fig. 3.3(a) shows that threshold condition can be reached only in proximity of the crossing between indirect to direct band gap configuration. Independently on the model used, an energy difference $\Delta E_{\Gamma,L}$ below 20 meV corresponds to uniaxial strain larger than 4 and 5%, as predicted by the deformation potential and the tight-binding models, respectively. When germanium turns direct, the number of carriers available in Γ increases, as understood from Fig. 3.2, such that threshold gain of 250 cm^{-1} can be reached well below a carrier density of $1 \cdot 10^{18} \text{ cm}^{-3}$. Evidentially, a marginally direct band gap configuration is a necessary prerequisite to achieving a considerable amount of gain. In contrast, a clear direct band gap strongly reduces the threshold, improving the overall efficiency.

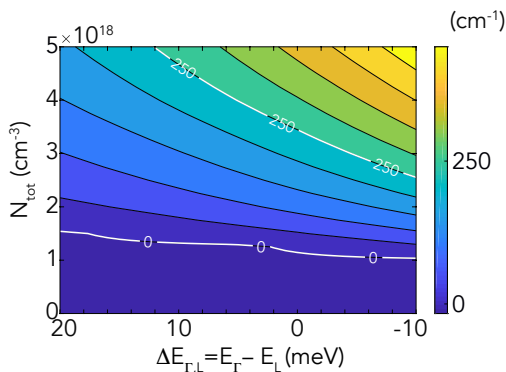
Moreover, Fig. 3.3(a) shows that gain at low temperature can be an excellent probe of the energy difference between the Γ and L minima, thanks to its sensitivity of the order of meV, especially approaching $\Delta E_{\Gamma,L} = 0 \text{ meV}$. Such a concept is extensively used in chapter 5 to understand the evolution of the energy difference $\Delta E_{\Gamma,L}$ at high strain.

Fig. 3.3(b) shows the calculations for $T=300 \text{ K}$. When germanium is direct the energy

difference between the Γ and L minima is $|\Delta E_{\Gamma,L}| < k_b T$, where k_b is the Boltzmann constant and the optical gain strongly reduces compared to low temperature. Considering possible parasitic loss enhancement at room temperature, as described in section 3.3.4, the threshold's achievement requires an energy difference $\Delta E_{\Gamma,L}$ more similar to the III-V platforms.



(a) Optical peak gain of strained Ge at 50 K



(b) Optical peak gain of strained Ge at 300 K

Figure 3.3: Contour plots of the peak gain as a function of the energy difference $\Delta E_{\Gamma,L}$ between the Γ and L minima and the total carrier density at (a) 50 K and (b) room temperature. The black lines indicate the increment of gain in steps of 50 cm^{-1} .

This section showed that the optical gain at low temperature could be obtained only in proximity of $\Delta E_{\Gamma,L} \sim 0 \text{ meV}$. We analyze how gain builds up for a specific energy difference

$\Delta E_{\Gamma,L}$ in section 3.3.2, and we explore how n-doping may enhance the gain in section 3.3.2. Losses are considered in section 3.3.4.

3.3.2 Gain spectrum and transparency

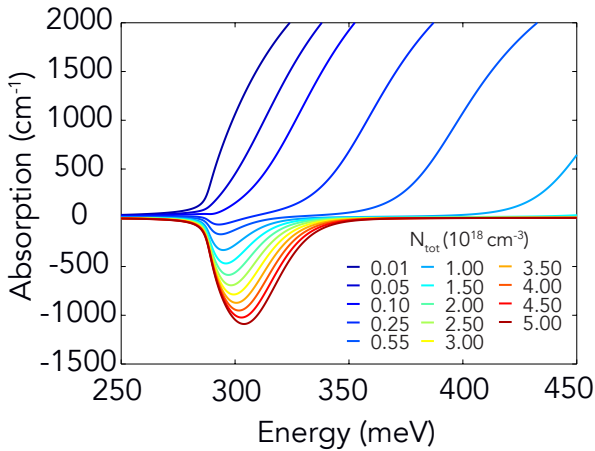
Fig. 3.4(a) shows how gain develops at low temperature as a function of the total carrier density for a specific energy difference $\Delta E_{\Gamma,L}$. Gain emergence is related to marginally direct band gap configuration. Thus, for the sake of generality, the $\Delta E_{\Gamma,L}$ is chosen to be equal to 0 meV. The Γ and L band edges are both placed at 288 meV higher than the top valence band VB1.

As soon as the total carrier density grows above $2.5 \cdot 10^{17} \text{ cm}^{-3}$, material gain, i.e., negative absorption, can be observed for transition energies just above the band gap. By increasing the carrier density up to $5 \cdot 10^{18} \text{ cm}^{-3}$, a gain bandwidth of about 30 meV forms, reaching a peak gain higher than 1000 cm^{-1} . Besides, a large transparency band where $\alpha_{IB} = 0$ develops at transition energies higher than the gain band. The transparency region forms as reported in the schematic representation of Fig. 3.4(b).

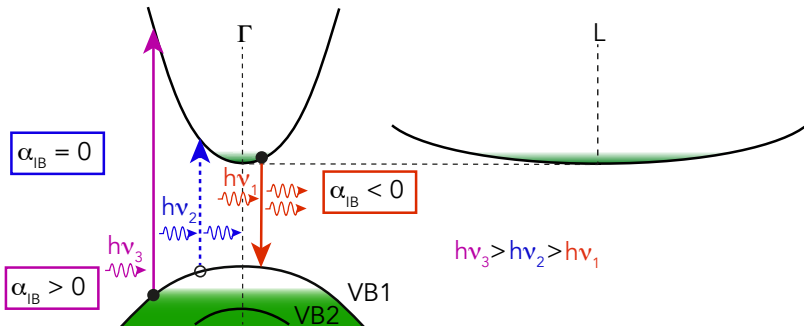
With only a relatively weak gain, this large transparency band is a direct consequence of the L valley's carrier filling and substantial holes population of the VB1 valence band. On the contrary of the typical picture of a III-V laser, L valley's presence clamps the quasi-Fermi levels μ_c (c.f. Fig. 3.2(c)), such that the peak gain slowly shifts towards higher energy. Photons with transition energy $h\nu_2$ larger than $h\nu_1$ are thus transparent in the material.

The transparency band's development and extension is determined in first order analysis by the ratio between the mass dispersion of the VB1 and VB2 and Γ at large \mathbf{k} . The picture of Fig. 3.4(a), as based on parabolic approximation, can not consider such effects quantitatively. However, the transparency band can qualitatively extend more than 100 meV above the band gap.

This analysis allows us to better understand previous lasing claims, like the experiment of Bao et al. [87], performed at strain value of $\epsilon_{<100>} = 1.6\%$. At this low strain level the expected energy difference $\Delta E_{\Gamma,L}$ is more than 100 meV. The absence of mode amplification clearly indicates the lack of gain and the observation of the linewidth narrowing can be understood as reduction of loss driven by transparency, which builds up during the valence band's hole filling. The work of Bao et al. [87] exemplifies the traditional difficulty in attributing the reduction of loss to transparency or gain. The above exposed modeling represents then a powerful tool to access the cavity loss and gain, and it represents the building block of the analysis of chapter 5.



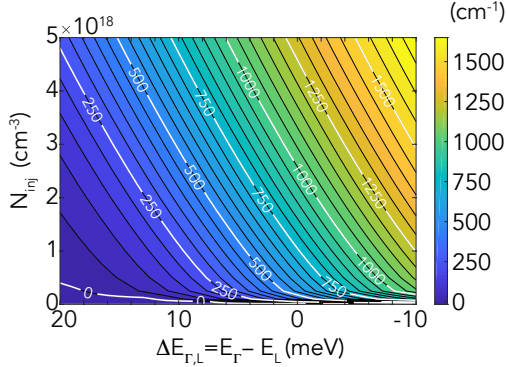
(a) Absorption spectra for different total carrier density, calculated at 50 K. The calculation is carried out for $\Delta E_{\Gamma,L} = 0$ meV, with the conduction band edges positioned at about 290 meV above the top of the VB1 band. A transparency region develops above the gain region.



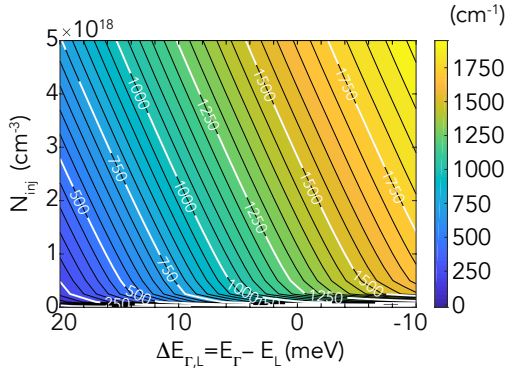
(b) Schematic representation of the electronic band structure of highly strained Ge. Bands are approximated as parabolic. Under steady population inversion, interband transition with increasing energy experience optical amplification, transparency, and absorption.

Figure 3.4: (a) Absorption spectra as a function of the carrier density, highlighting the development of the transparency region, whose formation is schematically reported in (b).

3.3.3 n-doping



(a) N-type doped germanium peak gain at 50 K, with $N_d = 1.8 \cdot 10^{18} \text{ cm}^{-3}$.



(b) N-type doped germanium peak gain at 50 K, with $N_d = 6.3 \cdot 10^{18} \text{ cm}^{-3}$.

Figure 3.5: Peak gain contour plots as a function of the energy difference $\Delta E_{\Gamma,L}$ between the Γ and L minima and the total carrier density for doped germanium with (a) $N_d = 1.8 \cdot 10^{18} \text{ cm}^{-3}$ and (b) $N_d = 6.3 \cdot 10^{18} \text{ cm}^{-3}$ at temperature of 50 K. The black lines show the increment of gain every 50 cm^{-1} .

Fig. 3.5(a) and Fig. 3.5(b) reports peak gain calculation for $N_d = 1.8 \cdot 10^{18} \text{ cm}^{-3}$ and

$N_d = 6.3 \cdot 10^{18} \text{ cm}^{-3}$, respectively, at 50 K. The role of n-type doping is to increase the electron concentration, avoiding further filling of the valence bands with holes and thus possible intervalence band absorption (c.f. section 3.3.4). Besides the overall enhancement of the gain compared to the undoped case, thanks to the more robust differential gain at low power, n-type doping helps in relaxing the requirement of low $\Delta E_{\Gamma,L}$, as long as it pushes the quasi-Fermi level toward the Γ valley.

With respect to the undoped case and using the reference gain of 250 cm^{-1} , doping concentration of $N_d = 1.8 \cdot 10^{18} \text{ cm}^{-3}$ slightly relax the requirement of small energy difference between the Γ and L minima. When doping density increases to $N_d = 6.3 \cdot 10^{18} \text{ cm}^{-3}$, gain of 250 cm^{-1} is obtained at the lowest carrier injection and when germanium is still strongly indirect. We remind that the figures here reported represent an ideal upper bound. Although not directly affecting the gain, we did not consider carrier-carrier scattering processes broadening the optical transition. Here, we kept for simplicity $\Gamma_{lor} = 4 \text{ meV}$, as for the undoped case. Moreover, we considered neither possible reduction of the carrier lifetime, i.e., injection efficiency, nor increased free carrier absorption. The experiment of chapter 5 will show that the effects mentioned above can not be neglected.

3.3.4 Parasitic losses

So far, we only discussed the gain induced by the population inversion and neglected any loss. In the following, the two main loss channels will be discussed: the free carrier absorption due to electrons and the intervalence band absorption.

The free carrier absorption due to electrons stems from the light absorption of electrons within the same conduction band, mediated by phonon scattering or impurities to satisfy energy and momentum conservation. Thus, we expect the free carrier absorption due to electrons to increase at low photon energies and to depend on the carrier density and the effective masses of the conduction bands, as the transition occurs within the same band. When $\Delta E_{\Gamma,L} \sim 0 \text{ meV}$, in steady state condition the majority of the electrons still populates the L valley (c.f. 3.2(a)) and thus we expect the free carrier absorption due to electrons to be in first approximation independent of the strain. In relaxed n-doped germanium with $N_d = 1.6 \cdot 10^{18} \text{ cm}^{-3}$ and at low temperature, the free carrier absorption due to electrons is found below 20 cm^{-1} for photon energy of about 250 meV [128].

However, the intervalence band absorption, represents the primary hurdle in highly strained germanium. This loss channel stems from the holes direct transitions between the three valence bands [129, 130]. Its magnitude in relaxed or slightly biaxially strained germanium is found to be stronger than the gain at room temperature [65, 131].

For increasing strain, the intervalence band absorption is expected to increase substantially

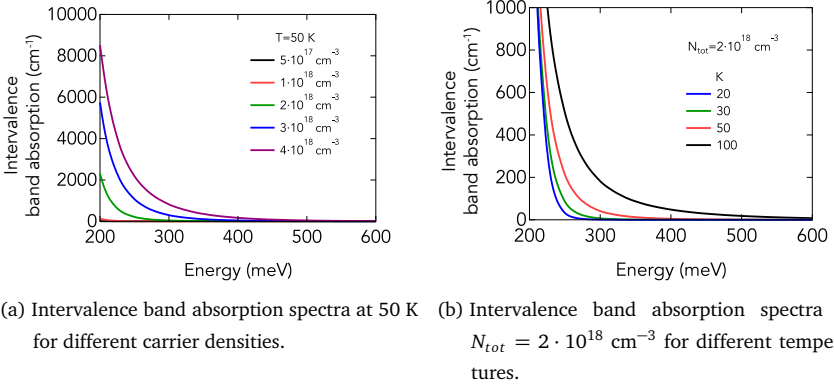


Figure 3.6: Intervalence band absorption spectra calculated with the tight-binding model at 6% of strain, corresponding to zero energy difference $\Delta E_{r,L}$. The calculations consider only light TE and TM polarized, propagating along the direction of the uniaxial strain. The calculations are carried out by Yann-Michel Niquet at CEA-IRIG-DePhy, Grenoble (France).

at low energy due to the splitting between the top two valence bands and the shrink of the direct band gap (c.f. Fig. 3.1). Fig. 3.6(a) and Fig. 3.6(b) report the intervalence band absorption spectra for different carrier density and temperature between 20 and 100 K, for the case of 6% of strain. The absorption is characterized by a strong non linear dependence on both the carrier density and the temperature. This follows from the growing holes' states filling in the reciprocal space. The strongest contribution to the intervalence band absorption comes from the transitions between the VB1 and the VB2.

We remind the qualitative nature of these calculations. Uncertainties may derive from the valence band's dispersion for large \mathbf{k} and the hole state lifetime. We give experimental insights about the intervalence band absorption at high strain and low temperature in chapter 5.

3.4 Optical resonator

Previous sections described the strained germanium's optical radiative properties. In the following, we study and model the resonator optics of the cornercube cavity. We first detail the cavity modes' concept and then model the cornercube resonator using the Finite Element Method (FEM) of COMSOL. The cornercube's concept was introduced in section 2.3. Finally, experimental results exemplify the idea of cavity modes as a practical way to access gain and loss information: such approach represents the cornerstone of the lasing experiments shown in Chapters 5

3.4.1 Cavity modes and loss

The easiest concept of optical resonator is represented by the Fabry-Perot etalon, which is constituted by two flat, parallel, and lossless mirrors separated by a certain distance d . In such configuration the light inside the cavity satisfying the boundary conditions for the electric field at the interface is a discrete set of standing waves with wavelength such that:

$$m \frac{\lambda_m}{2} = d \quad (3.11)$$

where m is a positive integer. Switching to the frequency regime, the m^{th} resonance mode can be expressed as

$$\nu_m = m \frac{c}{2d} \quad (3.12)$$

The spacing between two side modes is referred to as the free spectral range (FSR), which is inversely proportional to the length of the cavity:

$$\Delta\nu_{FSR} = \frac{c}{2d} \quad (3.13)$$

When the resonator is filled with a dispersive medium, the free spectral range reads as:

$$\Delta\nu_{FSR} = \frac{c}{2dn_g(\nu_m)} = \frac{c}{2d \left[n(\nu_m) + \nu_m \frac{\partial n}{\partial \nu} \right]} \quad (3.14)$$

where n_g is the group refractive index. In unit of energy the free spectral range is:

$$\Delta E_{FSR} = \frac{hc}{2dn_g(\nu_m)} \quad (3.15)$$

We can understand the build-up of discrete frequencies inside a cavity in the alternative way as light traveling back and forth and self-reproducing itself. By loosening the condition of lossless mirror and assuming a reflectance $R < 1$, the light can not anymore perfectly

reproduce due to loss-related phase shift and amplitude reduction. As a result, the spectrum of a real optical resonator is still composed of the resonant frequencies described by equation 3.14, but with a finite spectral width.

The relation between the linewidth and the optical loss can be understood as follows. The field amplitude of a monochromatic light oscillating with frequency ν_m , whose intensity decays with time not only due to mirror losses, but also to possible the material absorption, is expressed in a complex form as:

$$E(t) = \exp(i2\pi\nu_m t) \exp\left(-\frac{t}{2\tau}\right) + cc. \quad (3.16)$$

under the simple assumption that the electric field decays exponentially by a factor $1/\sqrt{e}$ after a time τ , corresponding to an intensity decaying by a factor $1/e$. Its spectral intensity, via Fourier transform, is proportional to a lorentzian whose spectral width is:

$$\Gamma_{FWHM} = \Delta\nu = \frac{1}{2\pi\tau} \quad (3.17)$$

The previous equation shows that the finite linewidth of a mode oscillating in the cavity with a certain resonance frequency is inversely proportional to the photon decaying time τ . It is then useful to introduce the concept of quality factor Q , which is a dimensionless parameter measuring the strength of the optical loss in a resonator. By definition the Q factor is the ratio between the energy stored in the resonator U and the energy loss per oscillation period $T = 1/\nu$:

$$Q = 2\pi \frac{U}{\frac{dU}{dt} T} = 2\pi \nu_m \frac{U}{\frac{dU}{dt}} \quad (3.18)$$

The Q factor of the m^{th} resonant cavity mode can be expressed in the following experimentally accessible expression:

$$Q = \frac{\nu_m}{\Delta\nu} = 2\pi \nu_m \tau = \omega_m \tau \quad (3.19)$$

It is straightforward to show that $Q = \omega_m/\Delta\omega = \lambda_m/\Delta\lambda$. In view of the next chapters experiments, we express the photon decaying time τ as loss with dimension of inverse space as $\alpha_{tot} = n_g/(c\tau)$, such that after a distance $1/\alpha_{tot}$, the mode intensity decays by a factor $1/e$. The linewidth read as $\Delta\nu = \frac{c}{2\pi n_g} \alpha_{tot}$. Throughout this work we express the linewidth in energy as follows:

$$\Delta E = \frac{hc}{2\pi n_g} \alpha_{tot} \quad (3.20)$$

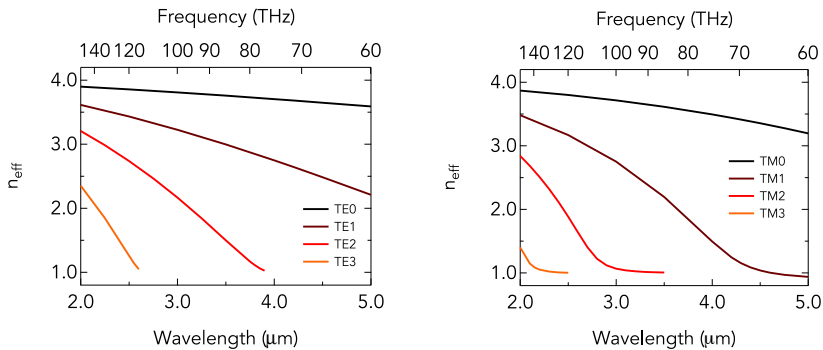
As a reference, by using $n_g = 4.5$ (c.f. section 3.4.3) a linewidth of $\Delta E = 0.1$ meV corresponds to a total loss $\alpha_{tot} = 22.8 \text{ cm}^{-1}$.

The dependence of the cavity modes linewidth on the amount of carrier injected in the system allows thus to study how the loss evolves with the input power. In a semiconductor material, transparency and then gain drive the reduction of the absorption, and thus of the linewidth. Section 3.3.2 gave the theoretical tool to distinguish between gain and transparency and the next one is devoted to the modeling of the loss of the empty cavity, i.e., a cavity filled with a transparent (loss free) material.

3.4.2 Q factor of the cornercube cavity

Contrary to other kinds of resonators, like distributed feedback (DFB) or the distributed Bragg reflectors (DFR), the cornercube cavity is multimode. We extract the cavity quality factor for different eigenmodes and for the two TE and TM polarizations. The calculation allows to understand the mirror losses and to interpret the multimode pattern observed in photoluminescence experiments.

We approximate the three-dimensional cornercube structure to a two-dimensional system. Light propagates only in the xz plane, such as the solutions do not depend on the out of plane and uniform y direction, like in a planar waveguide problem. The effective refractive index, which is defines as $n_{eff} = \beta/k_0$, where β is the propagation constant and $k_0 = 2\pi/\lambda$ is the vacuum phase change per unit of length, further reduces the dimensionality of the system.



(a) Effective refractive index for light TE polarized as a function of wavelength and frequency. (b) Effective refractive index for light TM polarized as a function of wavelength and frequency.

Figure 3.7: Effective refractive index calculated for a germanium slab waveguide of $1\ \mu\text{m}$, between infinite air layer, for TE (a) and TM (b) polarizations.

We approach the model by computing the n_{eff} for a $1\ \mu\text{m}$ germanium slab, with refractive index $n_{Ge} = 4$, between two infinite vacuum layers with $n_{air} = 1$. Fig. 3.7 reports the effective refractive index dispersion for the fundamental and higher order modes, for both the transverse electric (TE) and transverse magnetic (TM) polarizations. TE polarization indicate that the electric field is purely transversal to the propagation direction and is parallel to the uniform direction of the slab system. On the contrary, light TM polarized has a non vanishing component in the propagation direction. With the effective refractive index so calculated, the eigenfrequencies and their Q factor for the cornercube cavity are calculated by means of Finite Element Method (FEM) with COMSOL, as shown in Fig. 3.8.

The simulation is carried out by considering an empty cavity, i.e., no propagation losses,

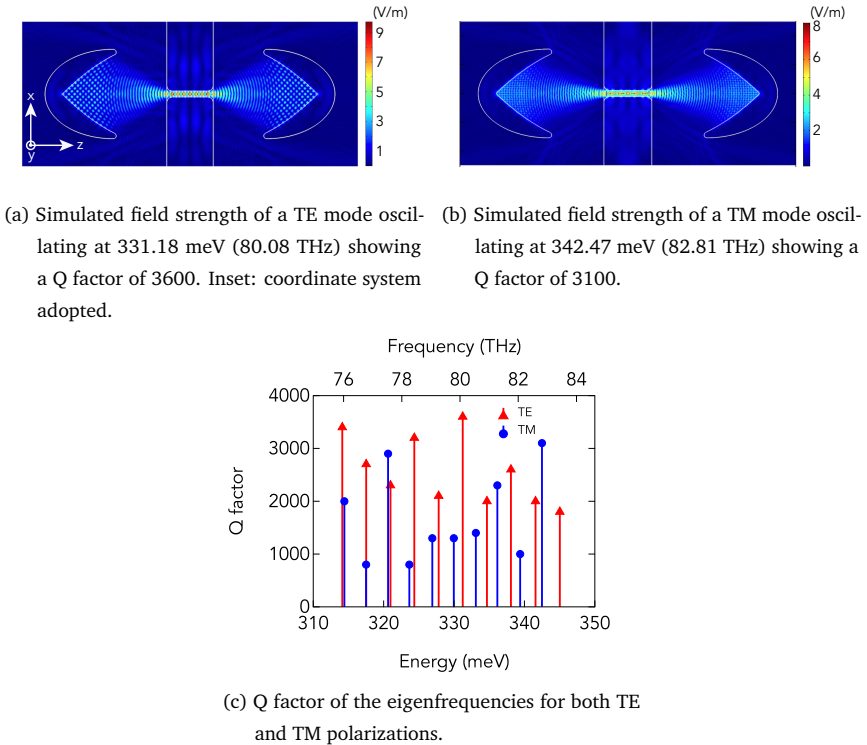


Figure 3.8: Extraction of the Q factor by means of Finite Element Modeling of the 2D cornercube cavity for both TE and TM polarizations.

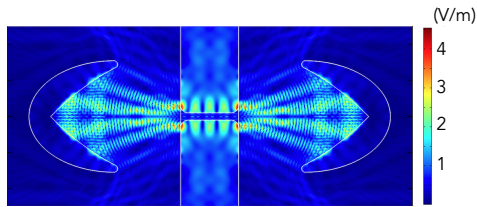


Figure 3.9: Formation of a parasitic cavity formed by the cornercube and the pad edge. The Q of the parasitic TM mode is 500.

and assuming that the TE and TM modes are independent. Following the previous definition and the adopted coordinate system, as reported in the inset of Fig. 3.8(a), TE electric field is along the y direction, while TM electric field lies entirely in the xz plane.

Fig. 3.8(a) and Fig. 3.8(b) report the optical field of a fundamental TE and TM mode, whose Q factors are $Q=3600$ and $Q=3100$, corresponding to mirror loss of about 21 and 24 cm^{-1} , respectively. Fig. 3.8(c) reports the Q factor as a function of the energy for the fundamental TE and TM orders. By exploring the energy range from 310 to 350 meV, we find that the Q factor varies from one mode to the other. This effect is more pronounced for the TM polarization, whose Q factor varies between 800 and more than 3600.

Possible source of radiation loss is the intersection point between the two parabola sections. This point does not satisfy the condition of total internal reflection. Back reflection of the light at the entrance junction of the bridge may also contribute to optical loss as well as parasitic cavities. The inefficiency of the coupling between the back reflection and the microbridge entrance may explain the previous effect. The imperfection in the mode matching seems validated by the formation of modes oscillating in a parasitic cavity formed by the cornercube and the pad edge, as shown in Fig. 3.9.

To verify this idea, the shape of the junction between the pad and the microbridge is changed in order to enhance the coupling efficiency. Instead of the typical rounded corner, an elliptical entrance is chosen, as shown in Fig. 3.10(a). In the following simulation we study how the radiative loss varies with the side vertex height. We choose the TM eigenfrequency oscillating at 339.4 meV of Fig. 3.8(c), which shows an anomalous high loss with the original rounded corner approach. Fig. 3.10(b) reports the variation of its Q factor as a function of the ellipse side vertex height.

The ellipse side vertex is varied between 0.2 and $1.4 \mu\text{m}$. The loss drastically reduces up to a factor 7 when the side vertex height is equal to $0.4 \mu\text{m}$, as depicted by the orange point.

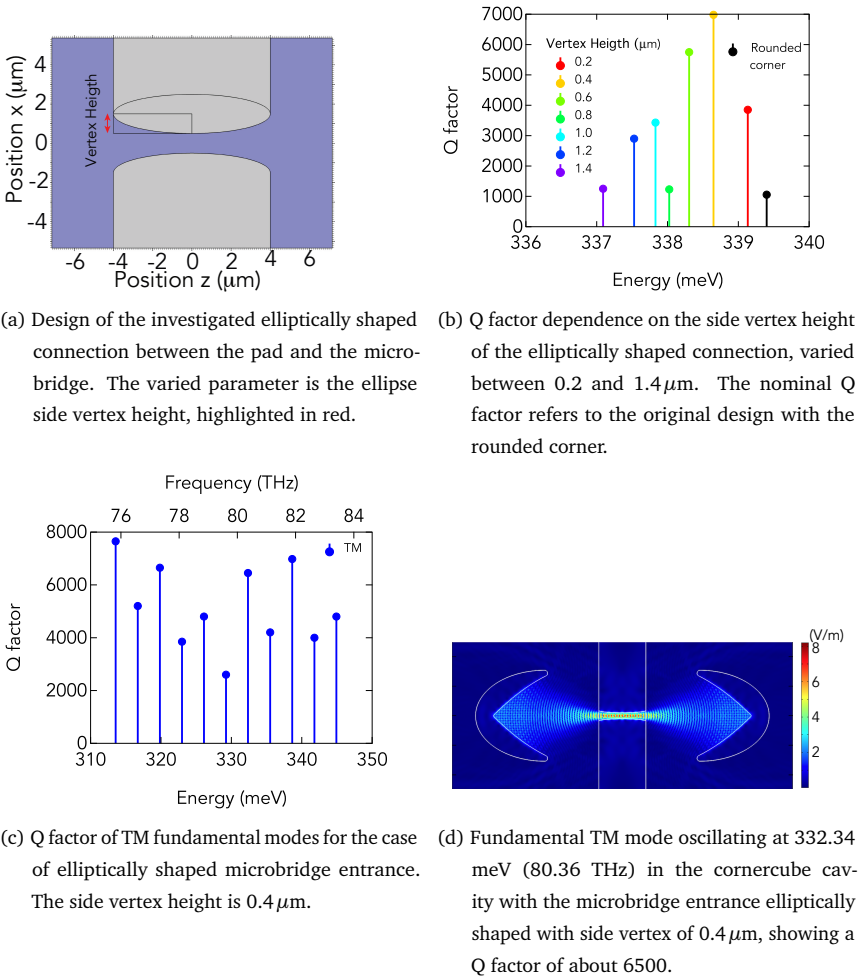


Figure 3.10: Impact on the optical confinement of the connection shape between the microbridge and the pad.

By further increasing the entrance width, the Q factor is decreasing again. This approach is limited by the degradation of the beam divergence while exiting the microbridge and by lateral interference effects.

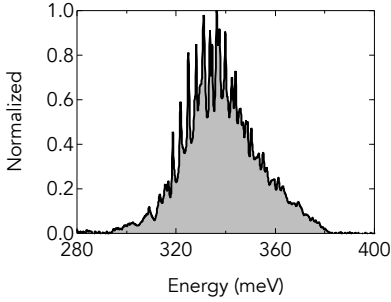
When the side vertex of the elliptical entrance is set at the optimal height of $0.4\ \mu\text{m}$, we observe from Fig. 3.10(c) that the Q factor of the TM fundamental is enhanced, with an average value of about 5000. Fig. 3.10(d) reports the field distribution of the eigenfrequency at 332.34 meV showing a Q factor of 6500. However, although less pronounced compared to the rounded corner case, the Q factor still fluctuates considerably. This effect may be less important for the TE polarization. Evidentially, the new shape of the connection improves the collection efficiency and reduces overall the radiation losses, but is not a wavelength-independent solution. Further studies may test the design proposed by Bao et al. [87], whose transition between the microbridge and the pad is smoother compared to the previously proposed design.

Although the elliptical entrance gives arguments in favor of further studies to optimize this concept, an enlargement of the microbridge connection to the pad reduces the strain distribution uniformity, and may limit the achievable strain. Moreover, the effective cavity filling factor would diminish too, likely compensating the gain in Q factor. The experiments are then based on the original rounded corner proposal, as proven to lead to high and uniform strain distribution and thus gain. Thus, active material embedded in the cornercube cavity has to deliver gain to compensate the loss corresponding to a Q factor of about 2000. This number represents naturally an upper bound, as the simulation do not take into account the unavoidable additional scattering and material losses. The former is estimated experimentally in section 3.4.6, while chapter 5 analyzes the latter's impact.

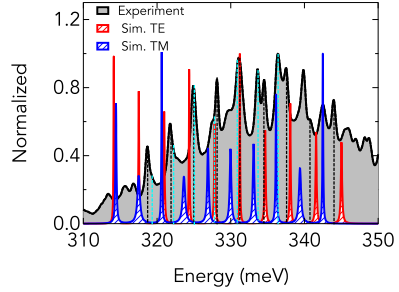
3.4.3 Multimode cavity pattern

We compare the mode pattern from the previous simulation, with the experimental results. Fig. 3.11(a) shows the photoluminescence of a strained germanium microbridge embedded in a cavity, cooled at 20 K, upon continuous wave excitation running at $E_{exc} = 590$ meV. The photoluminescence is strongly modulated by the cavity modes. Fig. 3.11(b) compares a portion of the spectrum to the simulation of the previously found fundamental TE and TM eigenfrequencies of Fig. 3.8(c), which are represented as lorentzians. The figure compares only the simulated mode pattern with the experiment, and not the Q factor.

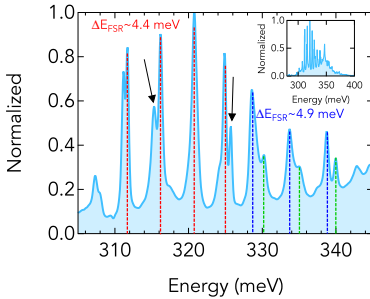
The simulation predicts that the cornercube cavity acts as a Fabry-Perot resonator. The eigenfrequencies of the fundamental order TE, in red, and TM, in blue, show a free spectral range of 3.42 meV and 3.11 meV. From the relation between the free spectral range and the cavity length of equation 3.15, we understand that the effective cavity length is $d = 44\ \mu\text{m}$,



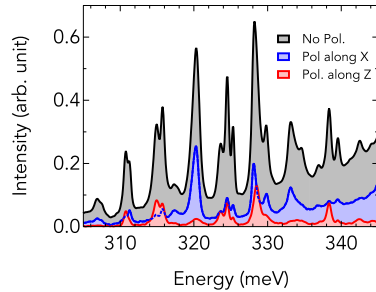
(a) Emission spectrum of a strained germanium microbridge embedded in a cornercube cavity. The cavity is cooled at 20 K and excited with 3.5 mW of power from a diode laser running in continuous wave at $E_{exc} = 590$ meV



(b) Enlarged view of the cavity emission of (a). The cavity modes indicated by the dashed black and light blue lines are equally spaced by 3.1 meV and 2.8 meV. Superimposed, the simulation of the cavity mode pattern. The fundamental order of TE and TM are shown in red and blue, respectively.



(c) Spectral emission of a short cornercube cavity with distance $d = 28 \mu\text{m}$ between the two cornercube tips. In inset the total photoluminescence view.



(d) In black, enlarged view of the PL of (c). In blue the emission through a linear polarizer aligned along x , in red along z , following the coordinate system of Fig. 3.8(a).

Figure 3.11: Experimental cavity mode pattern and comparison to the model.

which corresponds to the distance between the two tips of the cornercubes. The effective group indexes n_g used in the simulation for the TE and TM polarizations are 4.10 and 4.44, respectively, as inferred from Fig. 3.7, and approximated constant in the energy range studied. The larger TM value derives from the stronger dispersion, according to the simple slab waveguide picture.

The simulation qualitatively agrees with the experiment, but is far from correctly identifying all the experimental cavity modes. From the measurement, we recognize two sets of modes equally separated by each other. Starting from the mode at energy 344 meV, the modes indicated by the black dashed lines have a free spectral range of about 3.1 meV. From energy 336.4 meV, the modes indicated by the light blue dashed lines are equally separated by about 2.8 meV. Below 325 meV the light blue lines indicate the expected positions. In the following, we try to identify them either as TE or TM polarized.

From the effective cavity length of $44\ \mu\text{m}$, we infer for light with wavelength of about $4\ \mu\text{m}$ an effective group index of 4.5 and 5.0 for the modes with free spectral range of 3.1 meV (black lines) and 2.8 meV (light blue lines), respectively. The values are larger compared to the previous calculation, indicating a stronger dispersion due to the three-dimensional confinement of the microbridge. However, due to the symmetry in the transversal confinement, the effective group index in the microbridge is expected to be polarization-independent. The difference between 4.5 and 5.0 stems from the pads, where the out of plane TE polarization is less confined than TM, and more wavelength dependent. Thus we attribute the modes with free spectral range of 3.1 meV (black lines) and $n_g = 4.5$ to the TM polarization, while the modes with free spectral range of 2.8 meV (light blue lines) and $n_g = 5.0$ to the TE polarization.

We test the model on a shorter cavity. Fig. 3.11(c) shows the spectral emission of a cornercube resonator, whose distance between the two cornercubes tips is $28\ \mu\text{m}$ instead of $44\ \mu\text{m}$, as in the previous case. The expected free spectral range for TE polarization is $\Delta E_{FSR}(\text{TE}) = 4.4\ \text{meV}$, while for TM is $\Delta E_{FSR}(\text{TM}) = 4.9\ \text{meV}$. Indicated in red and blue, we identify two sets of modes whose free spectral range corresponds to the prediction. The modes indicated by the green lines are identified as first order TM modes with free spectral range of 5.1 meV. However, experimentally it is often the case that the recognition of the pattern is made difficult by the presence of modes which apparently do not belong to any order, like those ones indicated by the black arrow. We attribute them to parasitic modes (c.f. Fig. 3.9).

In Fig. 3.11(d) we filter the collected light through a linear polarizer at the exit of the microscope, to select the TE and TM polarizations. The polarizer is aligned in the direction normal or parallel to strain, thus along the x or z directions, following the notation used in

Fig. 3.8(a). We find that the photoluminescence background is suppressed along z . The x direction seems to select certain modes, like those ones at about 320 and 328 meV. However, the previous analysis attributed them to orthogonal polarization. A simple linear polarization seems not to be effective in selecting TE and TM modes. In particular, a calculation of the modes propagation from the mirror and the corresponding far field needs a proper three-dimensional calculator, as detailed in the next section.

3.4.4 3D cavity modeling

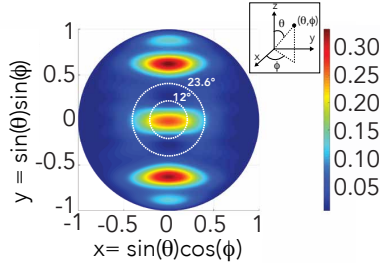


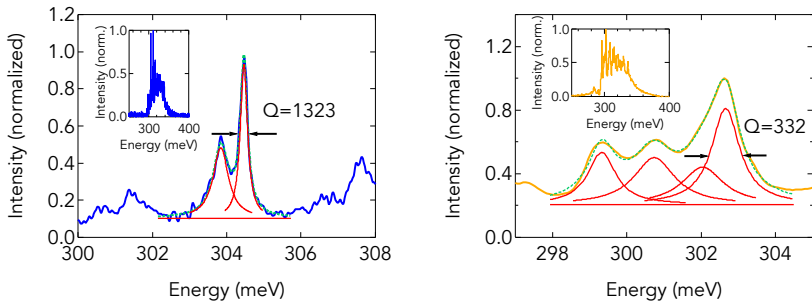
Figure 3.12: Polar projection of the far field intensity distribution of the light emitted from a cornercube resonator whose length is $d = 44 \mu\text{m}$. The main light emission's directions are: $(\theta, \phi) = (\pm 40^\circ, 90^\circ)$ and $(\theta, \phi) = (0^\circ, 0^\circ)$. The light is effectively collected by the microscope objective within the two dashed white circles at $\theta = 12^\circ$ and $\theta = 23.6^\circ$. We adopted the spherical coordinate reported in the inset. The calculation is performed by Vincent Reboud at CEA, LETI, Grenoble (France).

To estimate the lasing efficiency is important to calculate the light propagation in 3D. The following calculation is carried out with 3D Finite-difference Time-Domain (FDTD) method. We consider a cavity, whose cornercubes vertex is positioned $18 \mu\text{m}$ away from the microbridge's exit and whose distance between the two cornercube tips is $44 \mu\text{m}$. The simulation is performed assuming an empty cavity and no sidewall scattering losses. A fundamental TE mode at 354 meV is launched from the centre position of the microbridge. The power back reflected from a single corner cube is 90.6%, corresponding to a cavity loss per round trip of 18%. The cavity loss per unit of length is then $\alpha_m = \frac{1}{L} \ln(1/R^2) = 45 \text{ cm}^{-1}$. The corresponding quality factor is $Q \sim 1800$, which compares well to the finite element method calculation of section 3.4.2.

Fig. 3.12 shows the distribution of the far-field intensity for the cornercube cavity. 15% of the total radiated losses per round trip is scattered out of plane in the direction of the

optical microscope, which corresponds to 2.8% (0.15×0.18) of the total optical power. By integrating the upward optical loss within the solid angle covered by the microscope objective, whose numerical aperture (NA) is 0.4, the Cassegrain collection efficiency is calculated to be 9.1%. We considered in the calculation the shadow cone within $NA = 0.2$ of the microscope objective, c.f. Fig. 3.12.

3.4.5 Cavity scattering loss



- (a) In blue, the emission spectrum of a sample processed with the improved recipe, showing a sidewall quality as of Fig. 2.6(d). The mode at 304.5 meV is fitted by considering also the side mode. The results of the fitting are shown in red and in dashed green. The same procedure is applied to (b).
- (b) In orange, the emission spectrum of a reference sample, showing a sidewall quality as of Fig. 2.6(a). At similar condition of (a), the mode at 302.6 meV exhibits a Q factor 4 times lower.

Figure 3.13: Evaluation of the scattering losses reduction following the improvement of the optical cavity sidewalls. Two samples with different processing runs are compared at similar conditions.

In the following two sections, we reports experimental examples of how the Q factor gives access to gain and loss information. The quality factor previously found via finite element simulation represents the limit of the optical losses the light undergoes when the material is transparent. However, a real cavity in transparency condition exhibits a lower Q due to the unavoidable edge imperfections, leading to additional cavity scattering not considered in the simulations. As shown in this section, scattering losses are directly linked to the processing quality.

Section 2.4 described the processing step of the hard Cr mask definition. The thus obtained microbridge sidewalls were reported in Fig. 2.6(d) and Fig. 2.6(a), for the improved and the reference recipe, respectively. Here, we report the emission spectra of two samples: one processed with the new recipe (Fig. 3.13(a)) and the other one with the reference fabrication (Fig. 3.13(b)).

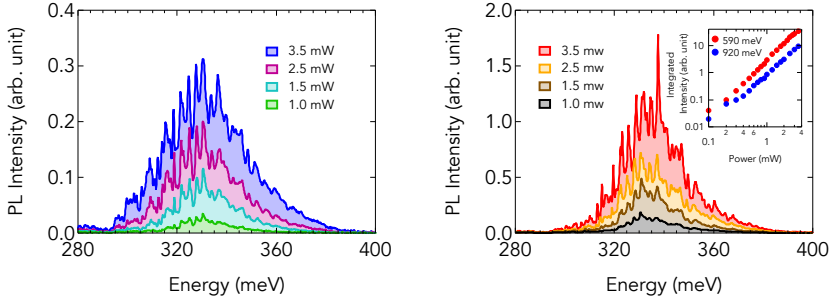
The two samples are cooled down at 20 K, excited with power density of about 9 kW/cm^2 upon continuous wave excitation with a diode laser running at 590 meV ($2.1 \mu\text{m}$) and show similar PL onset and thus strain, as can be seen from the insets. In particular, the novel processing leads to a Q factor of the mode at 304.5 meV equal to 1323, whilst in similar condition and excitation power the mode at 302.6 meV of the reference processing exhibits a Q factor of 332. By considering that both samples share the same optical cavity design and assuming that the material losses are the same, the novel processing leads to an improvement of the cavity quality by a factor of 4.

3.4.6 Excitation wavelength dependence and absorption

The excitation energy dependence of the photoluminescence allows to quantify via the cavity modes the optical absorption in the relaxed volume of the pads, induced by the higher energy excitation. Fig. 3.14 shows the photoluminescence of the same cavity cooled at 20 K, excited with continuous wave excitation of 920 meV ($1.34 \mu\text{m}$) and 590 meV ($2.10 \mu\text{m}$), as shown in Fig. 3.14(a) and Fig. 3.14(b), respectively. The here reported excitation power in mW are calibrated through a $10 \mu\text{m}$ diameter pinhole at the sample position.

In this preliminary experiment, both excitation lasers are focused with a beam size larger than the pinhole diameter. Both experiments show an increasing photoluminescence emissions by driving the power up to 3.5 mW, as well modulation by the cavity modes. The inset of Fig. 3.14(b) shows in logarithmic scale the signal integrated over the emission as a function of the input power for the two excitation wavelength. The signal upon higher excitation energy, reported in blue, is a factor 4 lower with respect the case upon 590 meV.

The considerable difference in PL efficiency stems from different sources. (i) Possible experimental uncertainties derive from the fact that the experiments are taken at different runs. In addition, some important factors determining the efficiency are difficult to access to. (ii) The mechanism an electron cools down in the bottom of the Γ valley is rather complicated and may depend on the excess energy the carrier is excited with. (iii) A fraction of the carriers that are generated in the pad with the shorter excitation may be collected into the bridge, which energetically forms a well. Rather than the comparison of the photoluminescence, which may bring a certain degree of uncertainty, in the following we analyze the excitation energy dependence of the Q factor.



(a) Power dependence spectra upon excitation energy of 920 meV ($1.34 \mu\text{m}$). (b) Power dependence spectra upon excitation energy of 590 meV ($2.10 \mu\text{m}$). Inset: comparison of the LL curves.

Figure 3.14: Photoluminescence spectra comparison of the same sample at 20 K, upon two different excitation energies.

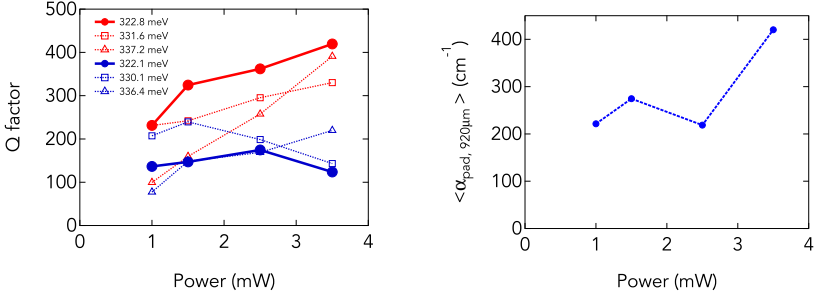
The Q factor extracted from the experiment of Fig. 3.14 are shown in Fig. 3.15(a): in red and in blue are reported the quality factors upon excitation energy of 590 meV and 920 meV, respectively, as a function of the excitation power. While the red Q values generally increase with the input power, indicating a reduction of the absorption, the Q factors obtained upon higher excitation energy are overall constant. Such difference stems from the fact that photons with energy of 920 meV are absorbed also in the unstrained germanium area of the pads [132], inducing optical losses. This effect is critical, as light travels for almost 80 % of its time outside the microbridge. On the contrary, the 590 meV excitation is closer to resonance condition and is absorbed uniquely by the strained germanium.

The following analysis is carried out for the mode at about 322 meV. We express the Q factor as follows:

$$Q_i(P) = \omega \frac{n_g}{c} \frac{1}{\alpha_{cavity} + \langle \alpha_{IB,i} [N_{\Gamma,i}(P)] \rangle + \langle \alpha_{pad,i}(P) \rangle} \quad (3.21)$$

where P is the excitation power and the index i refers to the excitation energy. The loss terms $\alpha_{IB,i}$ and $\alpha_{pad,i}$ are averaged over the entire cavity and we consider $\langle \alpha_{pad,i} \rangle = 0$ for $i = 590$ meV. Moreover, we assume for simplicity that $N_{\Gamma,i}(P)$, and thus $\langle \alpha_{IB,i} [N_{\Gamma,i}(P)] \rangle$, are independent of the excitation energy.

From equation 3.21 the general expression for the absorption in the pad reads as:



- (a) Q factor as a function of the input power for the two different excitation energies. In red and in blue the quality factor upon 590 meV and 920 meV, respectively. In solid lines the Q factor of the mode analyzed in the text.
- (b) Absorption in the pads averaged over the cavity length induced by the high energy excitation, as calculated from equation 3.23.

Figure 3.15: Comparison of the cavity mode quality factors between low and high excitation energy for the same sample at 20 K. The different power dependence in (a) is attributed to the additional loss in the pads induced by the excitation energy of 920 meV, which is estimated in (b).

$$\langle \alpha_{pad,i}(P) \rangle = \omega \frac{n_g}{c} \frac{1}{Q_i} - \alpha_{cavity} - \langle \alpha_{IB,i} [N_{\Gamma,i}(P)] \rangle \quad (3.22)$$

For the higher excitation energy we then obtain:

$$\langle \alpha_{pad,920meV}(P) \rangle = \omega \frac{n_g}{c} \left[\frac{1}{Q_{920meV}(P)} - \frac{1}{Q_{590meV}(P)} \right] \quad (3.23)$$

where $\omega = 2\pi \cdot 78$ THz and $n_g = 4.5$ (c.f. 3.4.3). Fig. 3.15(b) reports the evolution of the absorption attributed to the pads obtained from equation 3.23. The values are a lower bound, as averaged over the entire cavity. By considering that the excitation beam is estimated to illuminate about 30 % of the total unstrained pad area, the $\alpha_{pad,920meV}$ for the highest excitation power of $P=3.5$ mW is larger than 1500 cm^{-1} . Possible uncertainties may derive from the simple assumption that the carrier injection efficiency is independent of the wavelength. The α_{pad} calculated takes into account the free carrier absorption due to electrons in the L valley, and most importantly the intervalence band absorption. The latter, when germanium is relaxed, exhibits a strong resonance between the VB1 and VB3 bands at transition energy of about 300 meV, which corresponds to the energy range here investigated.

Overall, these results, together with previous experimental [133] and theoretical [95]

works, suggest the adoption of excitation energy transparent in the unstrained volume of the cavity, as carried out in the lasing experiment of chapters 4 and 5.

3.5 Thermal load

Thermal loading upon optical pumping may affect the lasing efficiency, in terms of carrier injection and thus gain. The ability to dissipate heating can limit a laser device from operating at higher temperature and/or under continuous wave operation [74].

The role of thermal loading and heat dissipation was discussed also in the context of strained germanium [87, 89]. Bao et al. proposed the stiction of the strained germanium nanowire to a SiO₂ layer to improve the heat conduction [87], while Elbaz et al. developed an aluminum metallic pedestal aimed to relieve the heating of the micro disk [89]. Both work proceeded from the assumption that the thermal load in a free standing microbridge is severe. However, the following modeling suggests that thermal load at low temperature is far from being critical.

To assess the thermal loading in germanium microbridges highly strained and suspended in air, we employ finite element method (FEM) modeling. The latter quantitatively solves the heat flow equation:

$$\rho c_p \nabla T - \nabla \cdot (k \nabla T) = Q_0 \quad (3.24)$$

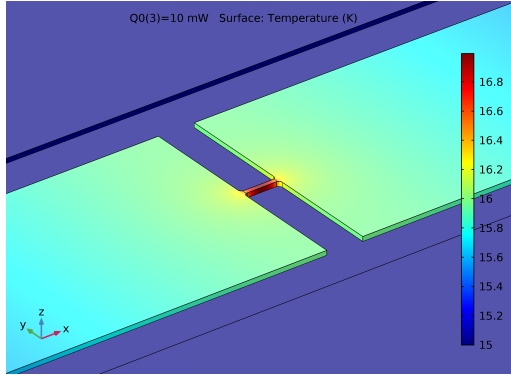
where ρ , c_p , and k are the density, the specific heat, and the thermal conductivity of the material, respectively. We infer the temperature dependent thermal conductivity of Ge and Si from the bulk values [134]. Q_0 is the volumetric heat source. Laser beam induced heating is modeled by placing on the top surface an inward heat source described as [135]:

$$Q_0 = P_0 Abs \frac{4 \ln 2}{\pi FWHM^2} \exp\left(-4 \ln 2 \frac{x^2 + y^2}{FWHM^2}\right) \quad (3.25)$$

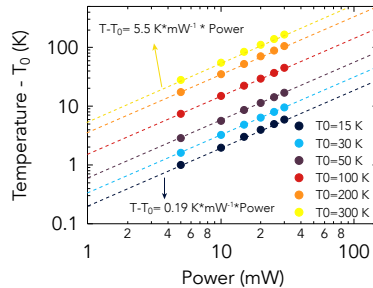
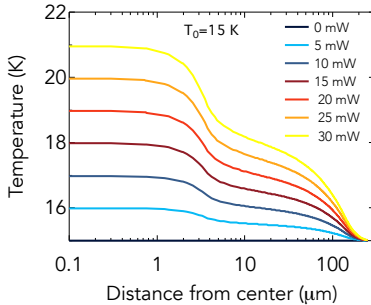
where P_0 refers to the total excitation power of the beam focused with a circular gaussian distribution, characterized by a $FWHM = 9 \mu\text{m}$. The beam is positioned in the centre of the constriction. Abs is the absorbance for a $1 \mu\text{m}$ thick germanium layer strained at 6% strain, considering multiple interference effects, as described in section 4.4.2. For excitation energy of $E_{exc} = 590 \text{ meV}$, $Abs = 0.4$. The relaxed pads are transparent at this energy.

Fig. 3.16(a) shows the 3D thermal load of a suspended Ge microbridge cooled at 15 K upon excitation power of 10 mW. The microbridge temperature increase of 2 K with respect to the base temperature.

The temperature profile along the microbridge centre position and crossing the whole pad length, as reported in Fig. 3.16(b), indicates that the temperature enhancement quickly falls



- (a) 3D finite element method (FEM) simulation of the steady state temperature of a strained germanium microbridge. Heating is induced by a continuous wave optical excitation focused in the centre of the constriction with a $FWHM$ of $9 \mu\text{m}$. The simulation is carried out for the case of $P_0 = 10 \text{ mW}$ and $T_0 = 15 \text{ K}$.



- (b) Temperature profile along the constriction for different excitation powers for the case of $T_0 = 15 \text{ K}$.
- (c) Relative temperature enhancement in the centre of the microbridge as a function of the excitation power for base temperatures ranging from 15 to 300 K. The dashed lines indicate the linear fits.

Figure 3.16: Thermal load Finite element method (FEM) simulation carried out with COMSOL Multiphysics software of a strained germanium microbridge, upon continuous wave optical excitation for different power and base temperatures.

off at about $4 \mu\text{m}$, corresponding to the connection of the pads. The temperature reaches the base temperature at the edge of the pad. By increasing the power up to 30 mW, the thermal load in the microbridge is still modest, of the order of 5 K.

Fig. 3.16(b) shows in double logarithmic scale the relative thermal enhancement as a function of the excitation power for different base temperatures, from $T_0 = 15 \text{ K}$ up to room temperature. The dashed lines indicate the linear fit and the extracted thermal enhancement at zero power is always null. By increasing the base temperature, the Ge thermal conductivity reduces from $1700 \text{ W m}^{-1} \text{ K}^{-1}$ at 15 K to about $60 \text{ W m}^{-1} \text{ K}^{-1}$ at room temperature. Correspondingly, the thermal enhancement at 300 K is 30 times stronger compared to low temperature.

However, this model does not consider finite size effects on the thermal conductivity at low temperature. Indeed the thermal conductivity of bulk Ge peaks at 15 K [134], which approximately corresponds to the temperature at which the mean free path of the phonon-phonon scattering is comparable to the surface scattering length. The peak of thermal conductivity in Ge nanowires with diameter of about $0.1 \mu\text{m}$ is predicted to reduce by two orders of magnitude [136], as well as in silicon [137]. However, even by considering a reduction by one order of magnitude, a thermal conductivity of about $170 \text{ W m}^{-1} \text{ K}^{-1}$, which is reached at temperature of $T_0 = 100 \text{ K}$, is enough to ensure a good heat flow. As shown in the last chapter, steady state lasing upon continuous wave excitation is reached at power lower than 10 mW. The thermal load of about 10 K (c.f. Fig. 3.16(c)) corresponds to an additional energy of less than 1 meV.

These preliminary results suggest that at low temperature free standing Ge microstructures do not require a specific heat flow engineering, like stiction to the substrate [87]. The latter requires an additional step in the processing and degrades the mode optical confinement factor and thus the threshold power. Further studies should address the effect of finite size of about $1 \mu\text{m}$ on the thermal conductivity at low temperature.

3.6 Summary

This chapter elucidates some fundamentals of the strained germanium radiative properties and the cornercube cavity. When loaded with 6% of uniaxial strain along $\langle 100 \rangle$ at low temperature, the tight-binding model foresees the energy difference $\Delta E_{\Gamma,L}$ between the Γ and L band edges going to zero.

Absorption calculations at low temperature as a function of the energy difference $\Delta E_{\Gamma,L}$ between the Γ and L minima shows that optical gain of about 250 cm^{-1} for a total carrier below $N_{tot} = 5 \cdot 10^{18} \text{ cm}^{-3}$ is reached only when $\Delta E_{\Gamma,L} \sim 0 \text{ meV}$. The optical gain for a given

total carrier density quickly increases when the energy difference $\Delta E_{\Gamma,L}$ approaches 0 meV, making it a useful tool to probe the alignment of the conduction bands. Due to the L valley's presence, which firmly clamps the quasi-Fermi level μ_c , and holes' occupation of the valence band states far out in momentum space, a transparency region accompanies the optical gain's formation at higher energy. The latter allows distinguishing between the linewidth reduction due to upcoming transparency or the gain build-up. Moderate n-doping up to $N_d = 6.3 \cdot 10^{18} \text{ cm}^{-3}$ seems to relax the requirement of small energy difference $\Delta E_{\Gamma,L}$ between the Γ and L minima and enhance the optical gain when germanium is indirect. However, our simplified model did not consider carrier lifetime reduction and lifetime broadening due to n-doping.

Parasitic loss in highly strained germanium stems from the transitions between the split top two valence bands VB1 and VB2. Theory predicts strong non linearity on both holes density and temperature of the intervalence band absorption.

Finite element method calculates the radiative losses of the cornercube cavity in the condition of an empty cavity. We obtain a typical Q factor of about 2000, equivalent to mirror losses of 37.6 cm^{-1} at 330 meV photon energy. The gradual enlargement of the microbridge entrance could reduce the losses up to a factor 7, but at the strain distribution uniformity expenses. The simulation shows that the cornercube cavity acts as a Fabry-Perot resonator, whose effective length is equal to the two cornercube tips' distance. We infer an effective group refractive index between 5 and 4.5 for the TE and TM polarizations. 3D mode propagation indicates that 1.35 % of the scattered light is collected by the objective microscope used in the following experiments.

From the experimental study of the Q factor, we understand that reducing the sidewall scattering reduces the cavity loss up to a factor of 4 the cavity loss. Finally, preliminary modeling of the excitation-induced heating on suspended germanium microbridges indicates that the thermal loading at low temperature is not critical for the carrier distribution.

4

Lasing upon optical pulsed excitation

Contents

4.1 Introduction	60
4.2 Experimental set up: CW, OPO	60
4.3 Photoluminescence measurement upon CW	62
4.4 Lasing upon pulsed excitation	64
4.4.1 Excitation energy dependence	66
4.4.2 Carrier concentration estimation	67
4.4.3 Quantum efficiency	70
4.4.4 Linewidth	72
4.4.5 Temperature dependence	73
4.5 Non-equilibrium carrier distribution	75
4.6 Intervalence band Raman lasing	79
4.7 Summary	81

The previous chapter considered the building blocks for the development of a strained germanium laser. Here, we give its first demonstration under optical pulsed excitation at low temperature. After a brief description of the experimental set-up, we describe the main lasing features of mode competition and high efficiency. Lasing upon pulsed excitation follows from a non-equilibrium distribution of the carriers between the Γ and the L minima. The energy difference between the Γ and L band edges seems not vanished yet in the investigated samples.

Parts of this chapter were published in a similar form as F.T. Armand Pilon et al., Lasing in strained germanium microbridges, *Nature Communications*, **10(1)**, 2724 (2019) [92].

4.1 Introduction

Chapters 2 and 3 presented the primary building blocks of the strained germanium laser. In the following, we give the first unambiguous demonstration of lasing action in strained germanium. We observe the lasing upon optical pulsed excitation in samples loaded with uniaxial strain ranging from 5.4 up to 5.9 % and up to a maximal temperature of 100 K. These findings provide a benchmark for previous lasing claims in strained germanium at lower strain [87, 89].

Here, we first report the main lasing characteristics, whose comparison to the typical photoluminescence emission serves as a reference for analyzing the steady state lasing of chapter 5. We observe mode competition and intensity threshold sustained by almost single mode emission. We characterize the lasing dependence on the excitation energy and temperature. The absorption as a function of the excitation energy is modeled, allowing to access the differential efficiency.

We develop a non-equilibrium model for the carrier distribution between the Γ and L valleys, which consistently describes the lasing dependence on the excitation energy and the temperature and the lack of lasing upon continuous wave excitation.

This chapter reports the main findings of the original publication [92]. In addition, we extend the carrier concentration analyzes by including multiple reflections in the slab, append a discussion about the build-up of a non-equilibrium carrier distribution between Γ and L, and give preliminary insights about the intervalence band Raman lasing.

4.2 Experimental set up: CW, OPO

Samples are mounted in a He flow cryostat using a clamping system to avoid glue solvent near the sample. They are optically excited using a continuous wave (CW) semiconductor diode laser from Brolis operating at 590 meV ($2.10 \mu\text{m}$). Its strongly diverging output is collimated via a combination of an aspherical and a cylindrical lens. A second excitation line is given by an optical parametric oscillator (OPO) from EKSPLA, enabling pulsed excitation with a repetition rate of 83 MHz and pulse length of 100 ps. The output energy can be tuned continuously between 551 meV ($2.25 \mu\text{m}$) and 370 meV ($3.35 \mu\text{m}$). The excitation energies employed in the experiment are absorbed uniquely by the strained microbridge, avoiding free carrier absorption in the pads (c.f. section 3.4.6).

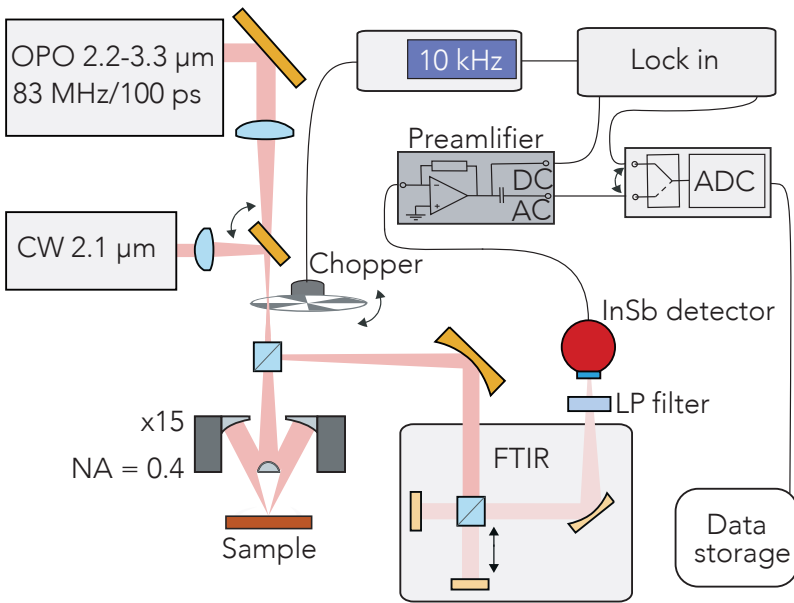


Figure 4.1: Schematic of the experimental set-up, reporting the main elements: optical-parametric-oscillator (OPO), continuous wave (CW) diode laser, Fourier transform infrared (FTIR) spectrometer, long pass (LP) filter and the InSb detector.

Both laser excitations as well as the collection of the emitted light occur via a reverse metal based Cassegrain microscope objective, with a $\times 15$ magnification and a numerical aperture (NA) of 0.4. The emission is collected in the direction normal to the sample surface, and then guided in free space through an FTIR spectrometer, that runs either in step-scan or fast-scan configuration, providing a non apodized spectral resolution of 0.062 meV. The emission is detected by a liquid nitrogen cooled InSb photodiode (PD) with an active area of $250\ \mu\text{m}$ diameter, equipped with a customized cold shield to reduce the field of view and thus the thermal background. Before being detected, the light passes through a long pass filter to filter out possible excitation light scattered from the sample.

The signal from the diode is amplified with a variable gain, usually set at $10^8\ \text{V/A}$, before being read-out by a lock-in amplifier, when the experiment is run in step-scan configuration, or directly recorded by an analogue to digital converter (ADC) when the measurement is carried out in fast scan. The sensitivity of the optical set-up inclusive the detector and

amplifier was calibrated against a thermal source of known temperature. The found efficiency is $\eta_{setup} = 0.04$, enabling to convert the emission intensity as the averaged power harvested within the NA of the microscope. This experiment exploits a large range of excitation energy. Thus, the excitation intensities, for both the pulsed and continuous wave excitation lines, are defined as the power calibrated through a $15\ \mu\text{m}$ pinhole¹ placed at the sample position. In particular, for the pulsed optical-parametric-oscillator excitation the reported power values are the time averaged ones.

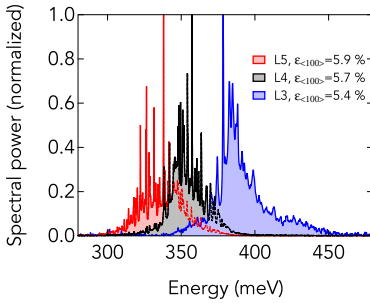
4.3 Photoluminescence measurement upon CW

For the experiment described in this chapter, we studied three differently strained Ge microbridges integrated in the cornercube resonator, whose distance between the cornercube tips is $44\ \mu\text{m}$. The samples are labelled L3, L4 and L5: the notation refer to the total pad length of 240, 260 and $280\ \mu\text{m}$, respectively, as reported in section 2.5. Their strain at room temperature, as obtained from geometrical consideration and validated by the Raman measurement, are about 3.30, 3.47 and 3.64%. Once cooled at 20 K, the strains are enhanced up to about 5.4, 5.7 and 5.9%. The corresponding energy transitions Γ -VB1 foreseen by the tight-binding model are 382, 348 and 325 meV, respectively, matching with the energy position of the normalized photoluminescence spectra of Fig. 4.2(a).

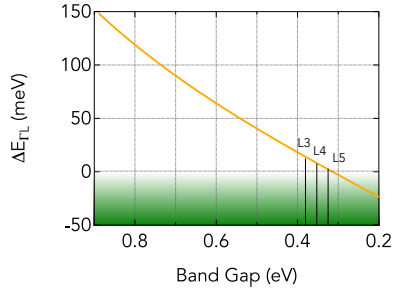
The measurements are carried out upon continuous wave excitation with power of 4 mW at 20 K. The photoluminescence red shift according to the direct band gap position for increasing strain and the emissions are modulated by the cavity modes. Fig. 4.2(b) describes the energy difference between the Γ and L band edges, i.e., $\Delta E_{\Gamma,L} = E_{\Gamma} - E_L$, of the samples as predicted by the tight-binding model: despite closely approaching the transition at $\Delta E_{\Gamma,L} = 0$ meV, as highlighted in green, the samples are still indirect, with an energy difference $\Delta E_{\Gamma,L}$ ranging from 15 to 2 meV.

The waterfall plot of Fig. 4.2(c) shows the power dependent spectra of the highest strained sample L5 upon continuous wave excitation at 20 K. The broad emission is modulated by the cavity modes already at low power. The emission increases quadratically with the power, as shown by the so called Light-in Light-out (LL) curve of Fig. 4.2(d), while the cavity modes become more prominent with respect to the background. Such feature, together with the narrowing of the linewidth, is a signature of reduction of loss, driven by the optical pumping. Analysis about gain and loss upon continuous wave excitation is given in chapter 5.

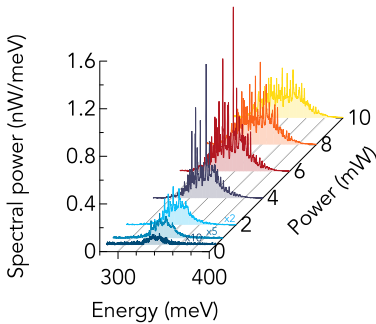
¹The diameter value of $15\ \mu\text{m}$, instead of the $10\ \mu\text{m}$ as reported in [92], comes from an a-posteriori inspection. However, this change is compensated by the improved analysis of the carrier concentration estimation of section 4.4.2, without affecting the original findings.



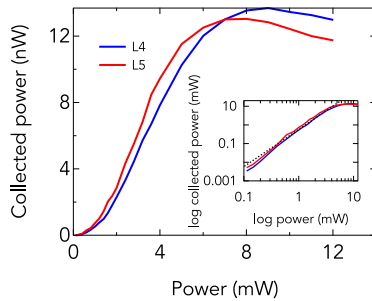
(a) Normalized PL spectra of samples L3, L4, and L5 at 20 K upon continuous wave excitation. The reported strains are obtained from the deterministic geometrical model of section 2.5 and agree well with the tight-binding relation between Γ -VB1 energy transition and strain.



(b) According to the tight-binding model, the samples studied in this experiment are approaching $\Delta E_{\Gamma,L} < 0$ meV, highlighted in green.



(c) Power dependence photoluminescence of sample L5 upon continuous wave excitation at 20 K



(d) LL curve of samples L5 and L4 upon continuous wave at 20 K. Inset: LL curve in logarithmic scale. The dashed line represents the quadratic increase.

Figure 4.2: Samples photoluminescence characterization upon continuous wave excitation at 20 K. The broad and uniformly enhanced photoluminescence emission, together with clear lack of intensity threshold, indicate that samples up to 5.9% of strain do not lase upon continuous wave excitation.

However, the cavity emission starts saturating at power of about $P = 6$ mW, together with the cavity modes collapse and the linewidth broadening. This effect is due to the upcoming intervalence band absorption. Overall, the multimode emission upon continuous wave increases uniformly with increasing power, indicating that the carriers recombination is still dominated by the spontaneous emission. The emission characteristics change drastically when the samples starts lasing, as we show in the following paragraph and later in chapter 5.

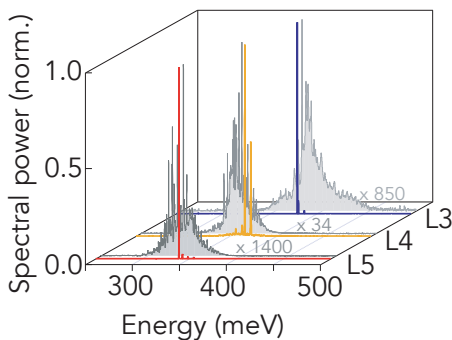
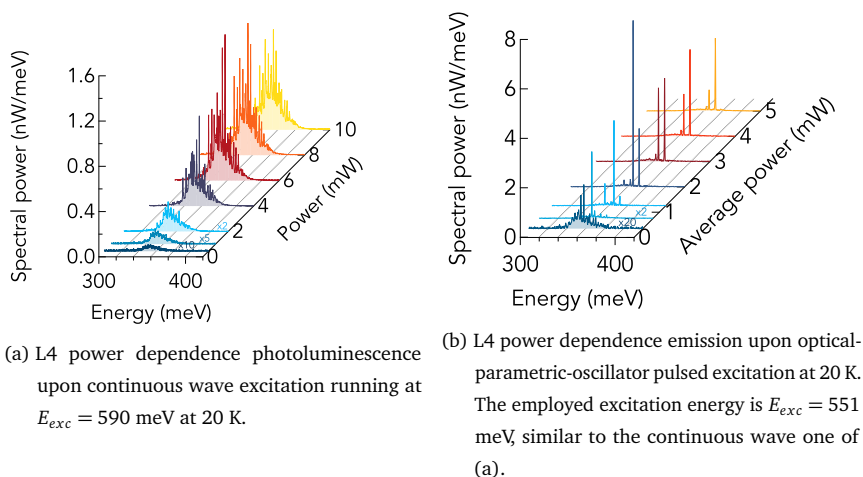
4.4 Lasing upon pulsed excitation

Fig. 4.3(a) shows the power dependence photoluminescence of the sample L4 upon continuous wave excitation at 20 K. Similarly to Fig. 4.2(c), the broad emission, as well the cavity modes, are uniformly enhanced with increasing power. In contrast, the same sample L4 upon optical-parametric-oscillator pulsed excitation with energy 551 meV shows the typical lasing features, which are remarkably different than the photoluminescence emission.

As reported in Fig. 4.3(b), the emission upon the optical-parametric-oscillator is broad and multimode, similarly to the case upon continuous wave, but only at the lowest power. When the power is increased above the threshold of 0.575 mW, the emission is dominated mainly by a single mode at 355 meV. The peak intensity of the lasing mode intensity increases further with the excitation power, raising above the background of about two orders of magnitude. While driving further the excitation, the main mode quenches and the lasing evolves toward a multimode configuration, where the emission is sustained by the higher energy modes due to the upcoming intervalence band absorption at low energy. The observed mode competition and the occurrence of a threshold are unmistakable fingerprints of lasing.

Fig. 4.3(c) shows in colors the normalized lasing spectra of samples L3, L4, and L5 obtained by means of the optical-parametric-oscillator at power of 2 mW. The excitation energies employed are $E_{exc} = 551$ and 428 meV, for L4 and L3, L5, respectively. The lasing spectrum of each samples is then compared to the corresponding photoluminescence emission upon continuous wave in grey color. The relative magnification of the photoluminescence spectrum with respect to the corresponding laser spectrum shows that lasing intensity can be many orders of magnitude stronger than the photoluminescence, as expected from a system operating in stimulated emission regime, where the majority of the input energy is transformed into output light.

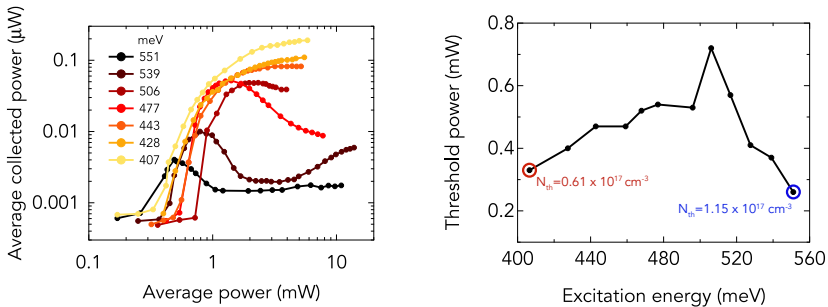
In the next sections we characterize the excitation energy and temperature dependence of the lasing action.



(c) Normalized spectra taken at 20 K of L3, L4 and L5. In grey colors the photoluminescence spectra taken at about 4 mW of excitation power upon continuous waves excitation. In blue, orange and red, the corresponding lasing spectra obtained when the excitation is switched to the pulsed regime at an average excitation power of 2 mW, with energy of E_{exc} of 551 and 428 meV, for L4 and L3, L5 samples, respectively.

Figure 4.3: Comparison between the photoluminescence and lasing spectra. Sample L4 strained at 5.7% shows (a) photoluminescence emission upon steady state excitation and (b) lasing action upon pulsed optical-parametric-oscillator excitation at the same temperature. (c) L3, L4, and L5 lasing spectra.

4.4.1 Excitation energy dependence



(a) Average collected power of L5 as a function of the average on-sample at 20 K. (b) L5 average power threshold as a function of the excitation energy.

Figure 4.4: Excitation energy dependence of L5.

Fig. 4.4(a) reports the time averaged and spectrally integrated emission intensity, the so-called light-in light-out (LL) curve, for a series of excitation energies ranging from 551 to 407 meV for the L5 bridge on a double logarithmic plot, showing, independent of the excitation wavelength, a strong non linear response of the collected intensity with respect to the pump power.

Compared to the inset of Fig. 4.2(d), where the collected power as a function of the continuous wave pump power follows a quadratic dependence, the curves of Fig. 4.4(a) show a sharp transition from the sub threshold to the lasing regime, whose intensity can be some orders of magnitude stronger. Beyond threshold, we indeed observe a strong increase in intensity, which rolls-over at an excitation strength that increases while decreasing the excitation energy from 551 meV to ~ 477 meV.

By further decreasing the excitation energy, and thus approaching the resonant excitation condition, the rolling over features is taken over by the emission intensity raising continuously up to the highest applied power, but sub linearly with the excitation power.

The dependence of the lasing threshold on the pump photon energy is shown in Fig. 4.4(b). Overall, the lowest threshold power of 0.26 mW is found for the highest pumping energy of $E_{exc} = 551$ meV. The threshold power then peaks at 0.72 mW at $E_{exc} = 506$ meV and then it decreases again down to 0.33 mW, for $E_{exc} = 407$ meV. The presence of the local maximum threshold pumping power at $E_{exc} = 506$ meV is attributed to a simultaneous occurrence of the intervalence band resonance between the VB1 and VB2 bands, i.e. when the energy difference between the absorbed and emitted photon, $E_{exc} - E_{out}$, is equal to

the energy difference between the two valence bands $E_{VB1} - E_{VB2}$. The threshold peak occurs when the Raman scattering competes with the inversion gain [138, 139]. We give the observation of stimulated Raman emission in section 4.6.

4.4.2 Carrier concentration estimation

The carrier concentration at threshold N_{th} is calculated from the integrated number of photons per pulse absorbed by the structure, taking into account the light fraction actually interacting with the microbridge and the absorbed fraction derived from Fresnel losses and multiple reflections.

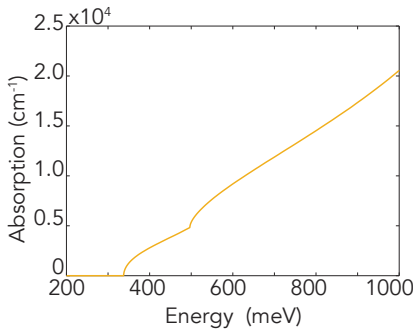
Fig. 4.5(a) shows the absorption spectrum of germanium loaded with about 6% of uniaxial strain along the crystallographic direction $\langle 100 \rangle$. The calculation is carried out by means of the tight-binding model, in order to take into account the non parabolic dispersion of the valence bands for large \mathbf{k} and considering only direct band gap transitions not mediated by phonons. The absorption edge strongly red shifts in the Mid Infrared (MIR) and it is composed by the Γ -VB1 and Γ -VB2 transitions, which are split in energy by 161 meV due to strain.

The reflectance, transmittance and absorbance of light incident on $1 \mu\text{m}$ thick germanium layer characterized by the absorption profile of Fig. 4.5(a) is calculated in Fig. 4.5(b). The calculations are carried out in the approximation of plane wave incident with an angle of 23.6° , as derived from the objective NA, on a absorbing germanium slab between semi-infinite air portions [140]. Such results may bring uncertainties due to finite size of the microbridge and the silicon surface $1 \mu\text{m}$ far from the germanium slab. The spectra are characterized by interferences occurring from multiple light reflections at the air-germanium interfaces.

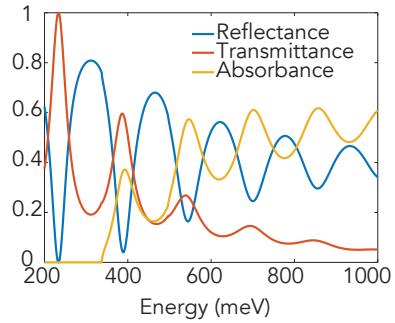
In particular, we can observe that for photon energy of 551 meV, corresponding to the highest excitation energy here employed, the absorbed light fraction locally peaks to about 0.58. For the excitation energy of $E_{exc} = 551 \text{ meV}$, the excited carrier density per average power, measured through the pinhole of $15 \mu\text{m}$ diameter at the sample position, is estimate as:

$$N(551 \text{ meV}) = \frac{O_{\Sigma} Abs}{E_{exc} q} \frac{1}{V} \frac{100 \text{ ps}}{DC} = 4.45 \cdot 10^{17} \text{ cm}^{-3} / \text{mW} \quad (4.1)$$

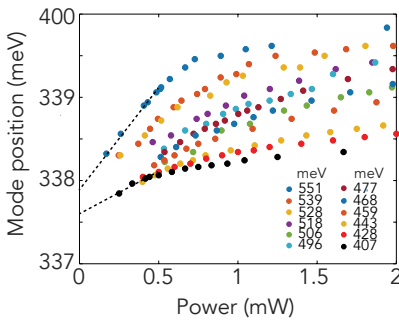
where O_{Σ} is the geometrical overlap of 0.045 of the $15 \mu\text{m}$ pinhole diameter with the $1 \mu\text{m}$ wide and $8 \mu\text{m}$ long microbridge. The absorbed light fraction, according to Fig. 4.5(b), is $Abs = 0.58$. q is the electric charge to convert the excitation energy $E_{exc} = 551 \text{ meV}$ in unit of Joule, and the volume of the microbridge is $V = 8 \cdot 10^{-12} \text{ cm}^{-3}$. 100 ps is the excitation pulse length, while DC is the duty cycle of the optical-parametric-oscillator pumping, equal



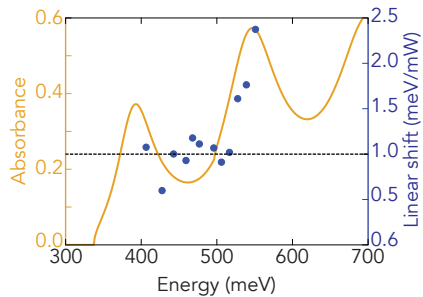
(a) Absorption of germanium strained at $\sim 6\%$ calculated by means of tight-binding model. The calculation is carried out by Yann-Michel Niquet at CEA-IRIG-DePhy, Grenoble (France).



(b) Light reflectance, transmittance and absorbance trough $1\mu\text{m}$ strained Ge layer, whose absorption is calculated in (a).



(c) Experimental shift of the main L5 lasing mode as a function of the average excitation power for different excitation energies.



(d) Linear slope dependence on the excitation energy in blue, extracted from (c), superimposed to the absorbance of (b).

Figure 4.5: Strain modifies germanium band gap and thus its absorption spectrum. Germanium uniaxially strained at 6% becomes transparent for photon energies below $\sim 310\text{meV}$. Considering multiple reflections, the absorbed light model is used to calibrate the carrier concentration.

to $8.3 \cdot 10^{-3}$. The light transmission through the cryostat CaF_2 window, whose value is close to unity and wavelength-independent in this region of the spectrum, is already taken into account in the initial power calibration. For the excitation energy of 551 meV the threshold power of 0.26 mW yields a threshold carrier density of $N_{th} = 1.15 \cdot 10^{17} \text{ cm}^{-3}$. In the following we describe the extraction of the threshold densities for lower excitation energy.

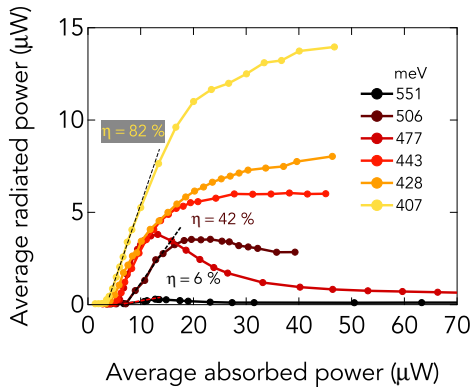
In Fig. 4.5(c), we study the position of the L5 main lasing mode as a function of the average excitation power, up to 2 mW, for excitation energies ranging from 551 to 407 meV. The mode blue shifts linearly, followed by a sub linear increase when the excitation is driven above ~ 0.5 mW. We notice that the mode unpumped position, i.e., the extrapolated mode position equivalent to zero excitation power, depends on the excitation energy, as shown in Fig. 4.5(c). We attribute this apparent difference of about 0.3 meV to the fast holes' filling of the upper VB1 band and the absorption reduction with power. This effect is stronger at higher excitation energy. However, for the analysis we report the mode shifts to a common unpumped position at 337.6 meV. Fig. 4.5(d) shows in blue the slope of the mode shift as a function of the excitation energy, as extracted from the linear fit at low power of Fig. 4.5(c). Superimposed, we report the absorbance of Fig. 4.5(b). Due to the carriers excitation, the mode position shifts according to the change of the refractive index $\Delta n_r \propto -N_c/E^2$ [141, 142], where N_c and E are the carrier density and the unpumped mode position, respectively. The refractive index dependence on the excitation energy is thus a convenient tool to extract the excited carrier density, by normalizing the mode shift slopes to the reference excitation energy of 551 meV. Furthermore, the mode shift slopes and the absorbance calculated with the approximated model of Fig. 4.5(b) find an overall good agreement, justifying the here adopted approach.

For each excitation energy lower than 551 meV, we then first determine from Fig. 4.5(d) the ratio of its slope value with respect to the reference one, namely 2.4 meV/mW. For convenience, for all energies below 518 meV we consider an average slope value of 1 meV/mW, as indicated by the dashed line. As an example, for the lowest excitation energy of 407 meV, the estimated carrier density per average power is:

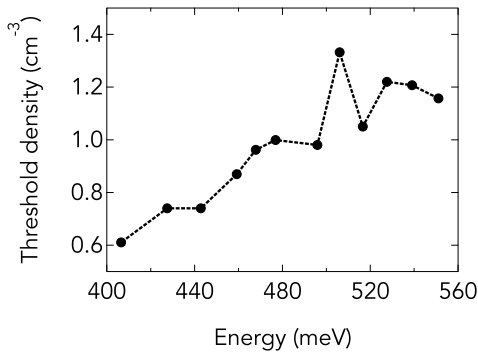
$$N(407 \text{ meV}) = 4.25 \cdot 10^{17} \text{ cm}^{-3}/\text{mW} \frac{1}{2.4} = 1.85 \cdot 10^{17} \text{ cm}^{-3}/\text{mW} \quad (4.2)$$

Equation 4.2 corresponds to a pumping efficiency of 18%, i.e., one excited carrier per about 5.5 photons impinging on the microbridge. The threshold carrier density for the lowest excitation energy of $E_{exc} = 407$ meV, whose power is 0.33 mW, is estimated as $0.61 \cdot 10^{17} \text{ cm}^{-3}$. This value is about of a factor 2 lower compared to $N_{th}(551 \text{ meV}) = 1.15 \cdot 10^{17} \text{ cm}^{-3}$, despite a larger excitation power.

4.4.3 Quantum efficiency



(a) L5 average radiated power as a function of the average absorbed power for different excitation energies. The differential efficiency increases when the system is excited more resonantly.



(b) Threshold density as a function of the excitation energy, inferred from the absorbed power of (a).

Figure 4.6: (a) enhancement of the differential power efficiency and (b) reduction of the threshold density when the excitation energy approaches the resonant condition.

Having developed in the previous section the analysis to study the amount of light absorbed as a function of the excitation energy, here we study the differential efficiency of the strained germanium laser, by invoking the calculation of the power radiated from the cavity of section 3.4.4.

Indeed, an ideal laser is expected to exhibit an internal differential efficiency approaching

unity, when all the energy given above threshold is converted into out-coupled light. Thus, any possible reduction from this ideal case is a convenient tool to study the losses of the lasing system. Fig. 4.6(a) converts the L5 samples average excitation and collected power of the Light-in Light-out curves of Fig. 4.4(a) to the average absorbed and radiated power, respectively.

The absorption is obtained from the conversion explained in the previous section, while for the radiated power we use the 3D calculations of section 3.4.4. The latter predicts that about 15% of the total optical losses are radiated upwards toward the optics. The 85% of out-coupled light, i.e., the light radiated in plane or downwards, is not collected by the microscope. By mapping the Cassegrain geometry of the collection optics to the computed cornercube cavity far-field, we find that 9.1% of the light emitted upwards out of plane is collected by the optics, yielding a collection efficiency of 1.35%.

Thus, at low temperature the sample L5 exhibits for the highest excitation energy of 551 meV a differential efficiency as low as 6%. The efficiency increases drastically for lower excitation energy approaching the resonant condition. Indeed, for the excitation energy of 407 meV the differential power efficiency is about 80%. By considering that the excitation energy is 407 meV, while the laser oscillates at 338 meV, the differential efficiency converts into a differential quantum efficiency close to unity. With quantum efficiency we intend the ratio between the number of photons radiated per second from the cavity and the number of photons absorbed per unit time.

Naturally, our estimation come with a large uncertainty, which derives in first instance from the calibration of the optical set-up, in particular from the conversion of the detector signal to collected power. Moreover, we systematically neglect any scattered light from potentially rough surfaces. We estimate the lower bound of the differential quantum efficiency to be about 50%. Such number represent a high figure for the differential quantum efficiency, especially when compared to the reported 1.5% efficiency of the first GeSn laser [68].

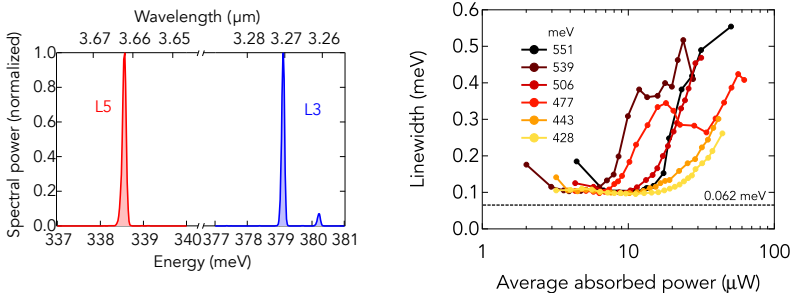
The efficiency enhancement is confirmed by the threshold reduction. Fig. 4.6(b) extracts from Fig. 4.6(a) the absorption corrected threshold values as a function of the excitation energy. By approaching the resonance condition, the threshold density decreases by a factor of 2, reaching values below 10^{17} cm^{-3} . The local peak at about $E_{exc} = 500 \text{ meV}$ is attributed to the competition with the Raman scattering (c.f. section 4.6). The reported findings allow to understand that (i) strained germanium is a favorable platform for efficient lasing and (ii) the parasitic losses, such as the intervalence band absorption, are low at carrier density of about 10^{17} cm^{-3} .

4.4.4 Linewidth

The narrowing of the spectral linewidth of the emitted spectrum during the transition from the sub-threshold to above threshold regime, followed by continuous narrowing with the emitted lasing power, is a feature typical of lasing. However, the theory describing the standard linewidth physics is developed for steady state lasing [143, 144], and not for transient pumping like in this experiment. The standard linewidth theory is applied in the next chapter 5 for the study of the strained germanium laser upon continuous wave pumping.

Fig. 4.7(a) reports a magnified view of almost single mode lasing spectra of L5 and L3. We infer a linewidth of 0.135 meV and 0.105 meV, respectively. In Fig. 4.7(b), we analyze the linewidth power dependence of the main L5 lasing mode for different excitation energies. Due to the low duty cycle of the pumping, and hence lack of signal, the spectra, which are carried out in fast scan mode, could not be measured with enough sensitivity below threshold, such that the reported linewidth generally refer to emission already in the lasing regime. As a reference, the linewidth at low power under continuous wave pumping is found to be typically broad about 0.5 meV, as shown in the next chapter.

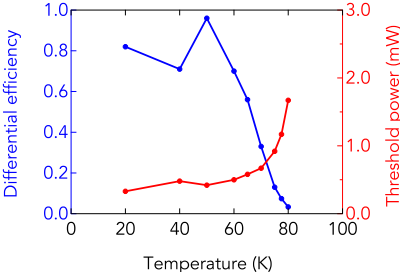
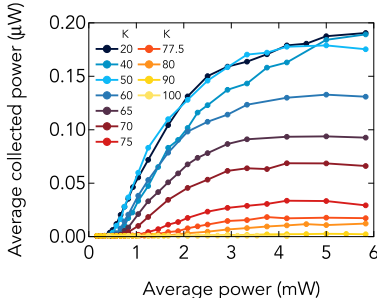
Independently on the excitation energy, the linewidth of the laser emission is largely independent of the emitted power and it narrows down to about 0.1 meV, until transient effect increases the linewidth at high power regime. We observe similar linewidth narrowing down to 0.1 meV in steady state lasing. This indicates that, despite the transient optical pumping, a pulse length of 100 ps is long enough to establish a close-to steady state condition. Section 5.13 of the next chapter addresses the nature of linewidth limit at about 0.1 meV.



(a) Magnified view of L5 and L3 lasing spectra at 20 K, excited at 428 meV energy with an average power of 2 mW. (b) L5 lasing mode linewidth for different excitation energies. The linewidth are apodized. The instrumental resolution is 0.062 meV.

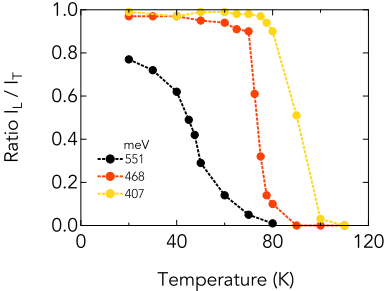
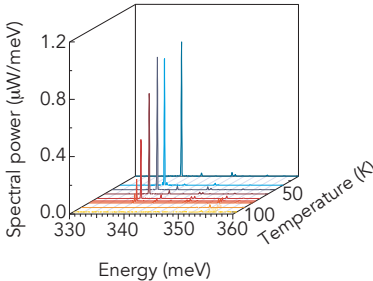
Figure 4.7

4.4.5 Temperature dependence



(a) Average power collected at the exit of the microscope from L5 sample as a function of the average excitation power for different temperatures. The excitation energy here employed is $E_{exc} = 407 \text{ meV}$.

(b) Differential efficiency and threshold power dependence on temperature of L5 sample upon $E_{exc} = 407 \text{ meV}$, extracted from (a).



(c) Lasing spectra between 20 and 100 K at 2.91 mW and $E_{exc} = 407 \text{ meV}$ of L5 sample.

(d) Ratio between all the lasing modes intensity I_L and total intensity I_T of L5 as a function of temperature, for three different excitation energies.

Figure 4.8: Temperature dependence of the strained germanium laser upon pulsed excitation.

This section is dedicated to investigate the temperature dependence of the lasing. Similarly to Fig. 4.4(a), Fig. 4.8(a) shows in linear scale the average power collected at the exit of the microscope as a function of the average power on the sample for different temperature,

carried out for the L5 sample, upon the excitation energy of $E_{exc} = 407$ meV. We notice the transition from the high efficiency regime at low temperature to the final quench of the lasing at high temperature.

Fig. 4.8(b) extracts from Fig. 4.8(a) the differential efficiency of the lasing as a function of the temperature superimposed to the temperature dependence of the threshold. We extract the differential efficiency with the previously described conversions of collected to radiated and on-sample to absorbed power. Up to about 60 K the differential efficiency stays constant at $\sim 80\%$, rapidly decreasing between 60 and 80 K to close to 0% values. In contrast, the threshold change with temperature is slower compared to the efficiency variation rate. We observe a similar effect in steady state lasing, as described in the next chapter, and we attribute it to the set-in of the intervalence band absorption at high power.

Fig. 4.8(c) depicts the rapid quench of L5 lasing between 60 and 80 K, by showing in a waterfall like plot the spectra taken at 2.91 mW excitation power and excitation energy of 407 meV up to 100 K. When the temperature approaches 80 K, the intensity of the main mode at 338 meV rapidly declines and at about 100 K lasing altogether stops. When $T > 80$ K only some modes keep lasing at high energy, while the lower energy mode seems to suffer from upcoming parasitic intervalence band absorption. The build-up of the intervalence band absorption starting from low energy is observed as well as in steady state lasing in chapter 5.

To quantitatively assess the lasing quenching, Fig. 4.8(d) shows the ratio between the intensity of all the lasing modes, indicated as I_L , and the total total intensity I_T , which comprises of all the modes intensity as well the background. This figure approaches 1 when the device operates in stimulated emission regime and almost all the power is radiated via the lasing modes and 0 when the system emission is dominated by the spontaneous emission background. The analysis is carried out for different excitation energies at the onset of the intensity roll-over or the sub-linear regime.

At the lowest excitation energy of 407 meV and low temperature, nearly all the emission goes into the lasing modes, as $I_L/I_T = 0.99$. Above 80 K, the relative intensity of the lasing modes quickly decreases to 0. The quenching of lasing is remarkably abrupt, similarly to the temperature dependence of the first GeSn laser, which turns off at 90 K [68]. Here, however, the temperature at which lasing is quenched depends on the excess energy of the excitation and the strain applied: for excitation at 407, 468 and 551 meV, the temperature at which $I_L/I_T < 0.5$, which we refer to T_{max} , decreases from 90 to 70 and 40 K, respectively. For the lower-strained sample L3, lasing turns off at 65 K upon excitation of 468 meV, as shown in Fig. 4.9. Such temperature limit of the strained germanium laser is not a characteristic typical of group IV lasing, as maximal operational temperatures close to 200 K [70] and approaching room temperature [73, 74] have been shown in GeSn platforms.

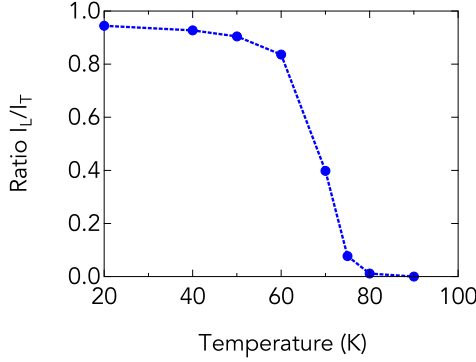


Figure 4.9: Ratio between all the lasing modes intensity I_L and total intensity I_T of L3 as a function of temperature, upon $E_{exc} = 468$ meV.

As shown in the next section, the remarkable sensitivity to excitation excess energy and the fast drop of I_L/I_T points towards a non-equilibrium distribution between the population of the electrons in Γ and L.

4.5 Non-equilibrium carrier distribution

Fig. 4.10 shows the energy resolved phonon-mediated carrier transfer time from Γ to L. The calculations are carried out using an atomistic approach, as outlined in [96, 145]. The transfer time is computed as the scattering time from an initial state in the Γ valley to a final state outside the Γ valley, which is approximated as the L valley and it is carried out as a function of the energy relative to the bottom of the Γ valley.

Two different configurations are analyzed: a generic $\Delta E_{\Gamma,L} = 0$ meV, corresponding to about 6% of strain, according to the tight-binding model (c.f. 3.1), and relaxed Ge with $\Delta E_{\Gamma,L} = 140$ meV. For the latter case, studied at a temperature of 50 K, and reported in grey color, the transfer time is about 200 fs, and largely independent of both the electron energy and the temperature, being in very good agreement with previous experiments [146].

For the tensile strained case with $\Delta E_{\Gamma,L} = 0$ meV, the calculation is carried out at 20, 50 and 100 K, as reported in blue, green and red colors, respectively. For large energy relative to the bottom of the Γ valley the electron transfer time to the L valley approaches that for relaxed germanium, independently of the temperature. However, electrons near the bottom of the Γ band with kinetic energy beneath $\hbar\omega_{LA} \sim 28$ meV, which corresponds to the energy

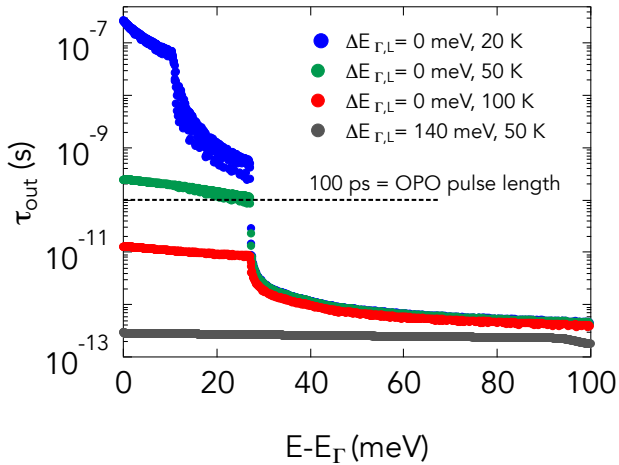


Figure 4.10: Tight-Binding calculation of the phonon-assisted scattering time from Γ to L as a function of energy relative to E_{Γ} . Blue, green and red colour refers to temperature of 20, 50 and 100 K when the energy difference $\Delta E_{\Gamma,L}$ is zero. Grey colour refers to $\Delta E_{\Gamma,L} = 140$ meV at 50 K. The calculations are carried out by Yann-Michel Niquet at CEA-IRIG-DePhy, Grenoble (France).

of the longitudinal-acoustic (LA) zone-boundary phonon [147], are essentially blocked.

At 20 K the scattering time quickly increases up to 10^{-7} s, thanks to the additional lack of transverse-acoustic (TA) phonon-assisted scattering channel, whose energy is about $\hbar\omega_{TA} \sim 10$ meV. At 50 and to 100 K, the availability of the thermally created phonons degrades the electron blocking effect: the scattering time reduces down to about 10^{-10} and then 10^{-11} , respectively.

Despite the phonon-mediated calculations gives only a simplified picture of the carrier dynamic, as neither the scattering between electrons, nor the backscattering from the L valley are included in the study, it allows to qualitatively understand the observed lasing characteristics, its temperature dependence, as well as the lack of lasing upon continuous wave.

The build-up of a non-equilibrium population inversion in the Γ valley at low temperature, and thus lasing, occurs as long as the energy difference $\Delta E_{\Gamma,L}$ is sufficiently lower than the phonon energy $\hbar\omega_{LA} = 28$ meV and the number of phonons available for absorption is sufficiently low.

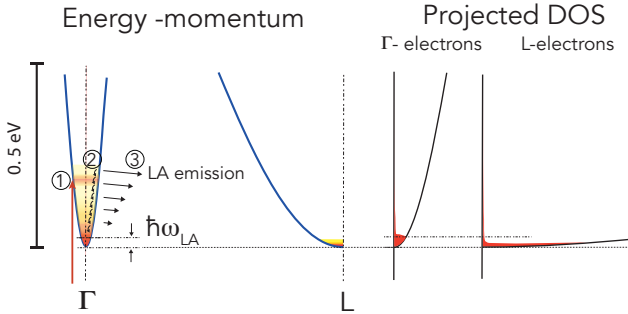


Figure 4.11: Schematic of the carrier distribution between the Γ and L valleys within the pulse length of 100 ps.

The distinct drop in efficiency of lasing at temperature at about 80 K, found for the most resonant excitation energy of 407 meV, thus follows from the scattering time becoming shorter than the excitation pulse of 100 ps between 50 and 100 K. When the excess energy is increased or the strain is lowered, the reduction of the maximal operational temperature for increasing excitation energy is associated to the growth of the carrier population in the L valley, at the expense of the population in Γ and thus gain.

This mechanism is also responsible for the threshold density increase for increasing excitation energy at the constant temperature of 20 K. Furthermore, the absence of the intensity roll-over for low excess energy is attributed to a situation where the quasi-Fermi level of the Γ valley stays below the energy level $E_L + \hbar\omega_{LA}$, where E_L is the L valley band edge.

The non equilibrium model gives a proper understanding also for the lack of lasing upon continuous wave excitation. Traditionally, the achievement of lasing under pulsed excitation is easier to demonstrate due to (i) lack of thermal load issues and (ii) higher carrier density. However, (i) and (ii) do not hold for the here employed continuous wave excitation. As previously found in section 3.5, at low temperature the heat induced by the continuous wave excitation in suspended and strained germanium microbridge is not critical for the carrier population in Γ , such that (i) can be disregarded. Moreover, the low threshold densities of about 10^{17} cm^{-3} upon pulsed excitation can be easily exceeded by more than one order of magnitude in continuous wave operation, allowing to neglect also (ii).

Thus, lasing in steady state excitation is missing due to a fundamental band structure

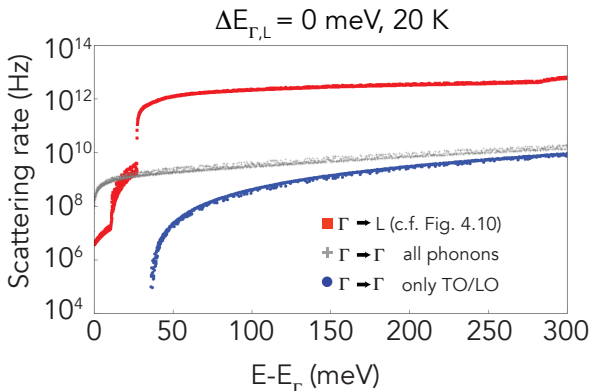


Figure 4.12: Phonon mediated relaxation rate as a function of the energy relative to E_{Γ} for the case of $\Delta E_{\Gamma,L} = 0$ meV at 20 K. In red, the valley scattering to L rate (c.f. Fig. 4.10), in grey and blue the intraband cooling rate mediated by acoustic and optical phonons and only by optical phonon, respectively. The calculations are performed by Yann-Michel Niquet at CEA-IRIG-DePhy, Grenoble (France).

reason: at the maximum strain probed in this experiment of 5.9%, the energy difference $\Delta E_{\Gamma,L}$ seems sufficiently close to zero to exploit at low temperature the phonon blocking effect ($\Delta E_{\Gamma,L} < 28$ meV), but it is not yet small enough to allow a sufficient steady distribution of carrier in Γ to overcome the losses. This understanding will receive further support in the following chapter, where we will discuss lasing upon continuous wave pumping. However, before we go further, we point out that we have not yet a quantitative understanding of our observation. We address the following to motivate further investigations.

To support the discussion, we visualize the non-equilibrium carrier distribution in momentum space: following the schematics of Fig. 4.11, a steady state is achieved where electrons are optical excited at certain energy above the bottom of the Γ valley (1). The electrons undergo intraband cooling (2) or, by the emission of a zone-boundary phonon, they scatter to the L valley (3). The momentum conservation requires the emission of a phonon. At the lowest temperature, phonon absorption is excluded. Once the carriers reach the energy below $\hbar\omega_{LA}$ the scattering to L is blocked.

These are the carriers available for the stimulated recombination and thus lasing. Quantitatively, we ask ourselves which fraction of the electrons reach this point in Γ below $\hbar\omega_{LA}$ and which fraction is lost to L. Experimentally, the answer is based on the gain requirement to overcome the cavity losses. From a microscopic point of view, the considerations shown

in Fig. 4.12 is of relevance.

The fraction of electrons reaching the bottom of the Γ valley depends on the competition between the processes (2) and (3) of Fig. 4.11. Fig.4.12 reports preliminary calculations of the phonon mediated intraband cooling rate in the Γ valley, compared to rate of the valley scattering to L. We obtain that above the energy $\hbar\omega_{LA}$, the valley scattering via emission of an LA phonon is more than 2 orders of magnitude faster than the cooling within Γ . Moreover, from Fig.4.12 we understand that most of the intraband scattering processes are mediated by zone-centre acoustic phonons, whose emission releases less energy than the generation of optical phonons. Thus, to dissipate energy electrons may have to scatter first to L via emission of zone-boundary LA phonons. However, the gain build-up would require the electrons to back scatter to Γ from L, which, due to the low Γ state density, is unlikely.

We think that the observation of high differential efficiency, suggesting that from threshold most of the electrons populate the bottom of the Γ valley, is then a remarkable result asking for further theoretical understanding. Evidentially, the phonon-mediated processes can not picture the complexity of the carrier dynamic and future studies may require to include other mechanisms like carrier-carrier scattering and the ultrafast time scale below 100 fs. In a system where a significant carrier fraction populates already the bottom of the Γ valley, while the 100 ps long pumping still occurs with moderate excess energy, Coulomb interactions may help an efficient carrier cooling, before phonon-mediated valley scattering occurs.

4.6 Intervalence band Raman lasing

This section gives a preliminary description of the intervalence band Raman lasing, whose build-up competes with the population inversion gain.

The top inset of Fig.4.13 reports an enlarged view of the band structure near the Γ point normalized to 20 K, upon 6% of uniaxial strain along [001], as extracted from Fig. 3.1. The splitting between the top two valence bands allows the photons to resonantly participate to an intervalence band Raman scattering. The photon with energy E_{exc} excites an electron of the VB2 band in the conduction band. The photo-excited electron makes then a vertical transition to an empty VB1 state, emitting a photon with energy E_{out} . As a result of this momentum and energy conserving process, a VB1 hole is scattered into the VB2 band.

Under stimulated emission condition, we observe intervalence band Raman lasing when (i) the resonant condition $E_{exc} \sim E_{out} + (E_{VB1} - E_{VB2})$ is satisfied and (ii) E_{out} corresponds to the energy of a cavity mode. Fig. 4.13 shows the power dependent spectra of L5 at 20 K upon excitation energies of 551, 539, 527 and 516 meV. We report the spectra as a function of the average absorbed power. Per each excitation energy, the spectra are normalized to the

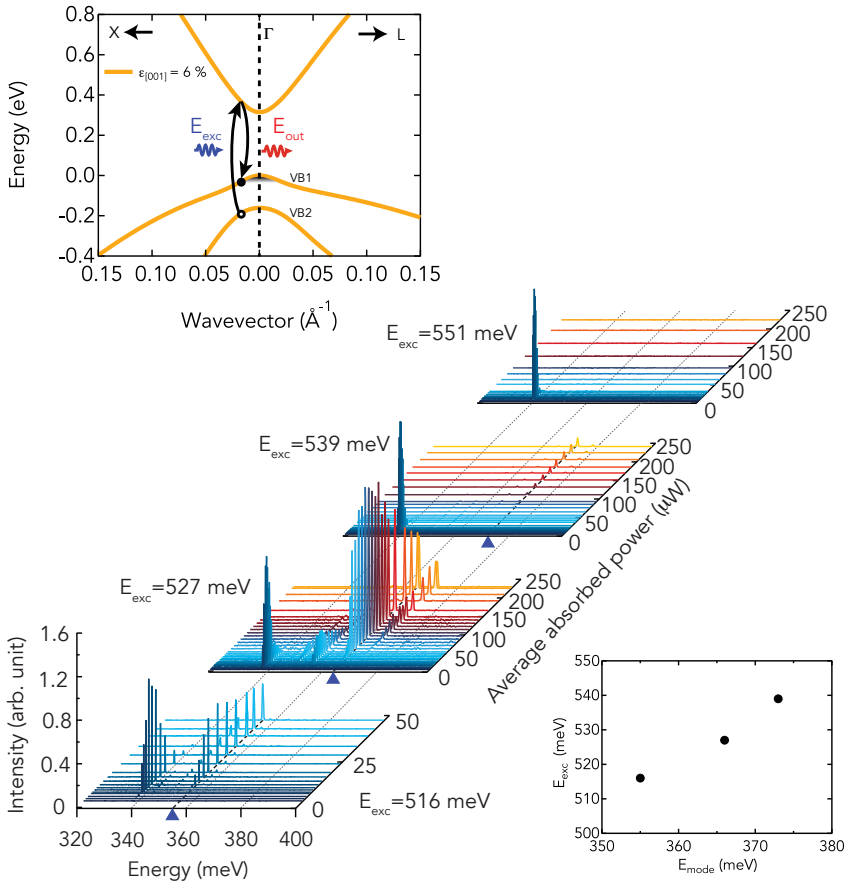


Figure 4.13: L5 power dependent spectra at 20 K for different excitation energies E_{exc} ranging from 551 to 516 meV. Upper inset: germanium band structure upon uniaxial strain of 6 % along [001], normalized to 20 K, with the vertical resonant transitions. In the final state a hole is scattered in the VB2 band. Lower inset: excitation energy as a function of the energy of the most Raman amplified mode.

maximum intensity of the inversion lasing mode at about 339 meV. At the highest excitation energy of 551 meV, we observe only inversion lasing at 339 meV of energy, which quickly quenches. By decreasing the excitation energy down to 516 meV, the spectra at high power are dominated by Raman lasing at high energy.

Stimulated Raman scattering occurs at energy shifting with the excitation energy. The maximum Raman amplification occurs at about 373, 366, and 355 meV, as indicated by the triangles in Fig. 4.13 and reported in the lower inset, upon excitation energy of 539, 527 and 516 meV, respectively. For the excitation energies of 527 and 516 meV, we can infer a splitting of the top two valence bands of about $E_{VB1} - E_{VB2} = 161$ meV, in accordance with the tight-binding model's prediction (c.f. table 3.1). For the excitation energy of 539 meV the splitting is $E_{VB1} - E_{VB2} = 166$ meV. We find that the Raman lasing threshold reduces by decreasing the excitation energy, due to the faster holes' filling of the VB1 band. At the highest excitation energy Raman threshold is not reached within the excitation power range.

4.7 Summary

This chapter reported the first demonstration of lasing action in strained germanium. We observed lasing upon optical pulsed excitation of 100 ps and up to temperature of 100 K in samples strained from 5.4 % up to 5.9 %. The lasing observation allows understanding the typical lasing fingerprints of mode competition and threshold in intensity. The transition from a broad and multimode spectrum to an emission dominated by a single cavity mode is in striking contrast with the typical uniform amplification of the photoluminescence. These findings offer a solid background to benchmark previous lasing claims.

We characterize the lasing dependence on the excitation energy. We first estimate the absorbed power as a function of the excitation energy by modeling the absorbance through 1 μm thick germanium layer and by studying the shift of the lasing mode, which brings the refractive index dependence on the excited carrier density. We find that the absorption of the lowest excitation energy $E_{exc} = 407$ meV is lower by a factor of 3 compared to the highest excitation energy of $E_{exc} = 551$ meV.

The conversion from on-sample to absorbed power and the 3D model of the out-coupling radiation give access to the differential power efficiency as a function of the excitation energy. For $E_{exc} = 551$ meV we find a differential efficiency of 6 %, which increase up to about 80 % when we approach the resonant condition at $E_{exc} = 407$ meV. We find that the highest efficiency corresponds to the lowest threshold density of $N_{th}(407 \text{ meV}) = 0.61 \cdot 10^{17} \text{ cm}^{-3}$, which is lower by a factor of about 2 than $N_{th}(551 \text{ meV}) = 1.15 \cdot 10^{17} \text{ cm}^{-3}$. The excitation energy dependence of the threshold density reveals that inversion gain competes with

stimulated intervalence band Raman emission. Its observation for excitation energies of about $E_{exc} = 500$ meV at 5.9 % of strain, allows inferring a splitting of the top two valence bands of about $E_{VB1} - E_{VB2} \sim -162$ meV, in accordance to the tight-binding model.

We characterize the linewidth and the temperature dependence. The former shows a narrowing down to about 1 meV, before transient effects occur at high power. A similar value observed in the next chapter allows inferring that within 100 ps pulse length a near to steady state condition is reached. Lasing at 5.9 % of strain operates up to about 100 K upon $E_{exc} = 407$ meV, showing a fast decline of the maximum intensity starting from 80 K. The onset of the maximum intensity reduction is excitation energy dependent. Upon $E_{exc} = 551$ meV lasing starts decreasing at about 40 K.

Lasing upon pulsed excitation is discussed in terms of a non-equilibrium distribution of the conduction bands' carriers. Tight-binding based calculations reveal that at low temperature and for $\Delta E_{\Gamma,L} = 0$ meV the carrier scattering time from Γ to L increases up to ns when the carrier energy is lower than $\hbar\omega_{LA} = 28$ meV. The latter corresponds to the energy of the zone-boundary longitudinal acoustic phonon. However, the build-up of high efficient lasing indicates, for future carrier dynamic studies, the necessity to include mechanisms like the carrier-carrier processes, in addition to the electron-phonon scattering.

The phonon blocking mechanism allows to understand the dependence on excitation energy of the threshold and the emission characteristics at 20 K, and the rapid decrease of the lasing with temperature. Such effect may be relevant not only for strained germanium but also for any marginally direct system, such as GeSn. Time-resolved measurement by exciting the laser via a pump and probe-like excitation scheme may unravel the carriers dynamic.

5

Steady state lasing

Contents

5.1 Introduction	84
5.2 Samples and experimental set-up	85
5.3 Main lasing characteristics	90
5.4 Gain vs loss	94
5.5 Lasing analysis: from transparency to lasing	96
5.6 High strain: missing lasing	101
5.7 Temperature dependence	102
5.8 Intervalence band absorption	105
5.9 Energy difference $\Delta E_{\Gamma,L}$ vs strain	107
5.10 Discussion: energy difference $\Delta E_{\Gamma,L}$	113
5.11 Discussion: steady state lasing	115
5.12 N-doping	116
5.13 Laser linewidth analysis	120
5.13.1 Linewidth measurements	120
5.14 Summary	127

In the following chapter, we present the steady state lasing upon continuous wave pumping. Lasing action is unlocked by the increased strain and the reduced cavity losses, and it is observed only in a narrow strain region between 6.1 and 6.2% and at low temperature. Via experimental extraction of the cavity losses, we gather direct access to the band structure energy difference between the Γ and L band edges, i.e., $\Delta E_{\Gamma,L}$. Temperature measurements reveal the interplay with upcoming parasitic intervalence band absorption. The latter, together with an energy difference $\Delta E_{\Gamma,L}$ reducing slower than predicted by the tight-binding model, allows to describe the lasing action in steady state

condition consistently and to understand the lack of threshold in the highest strained samples.

5.1 Introduction

The experiment described in chapter 4 allowed us to demonstrate the typical lasing fingerprints in strained germanium, but left partially unsolved the question about the cross over from indirect to direct band gap. In the following chapter, we present steady state lasing in strained germanium cavities. The latter represents a unique way to gather essential information about the energy difference between the Γ and L band edges, i.e., $\Delta E_{\Gamma,L} = E_{\Gamma} - E_L$, and its evolution at higher strain. Besides being the first demonstration of lasing action upon continuous wave pumping in strained germanium, this result demonstrates the power of the strain approach and aligns with a similar demonstration in GeSn. [75].

The strain amplification technology and the processing improvement, as outlined in section 2.4, enable us to extend the strain limit of 5.9% of chapter 4. Here, we employ samples whose strain span from about 5.8 up to 6.6%. First, we describe in detail the steady state lasing in samples with a strain of about 6.1 and 6.2% and give the main lasing characteristics, as previously understood from the pulsed excitation experiment. We then compare the experimental laser threshold to the gain model introduced in section 3.3 and determine the energy difference $\Delta E_{\Gamma,L}$.

However, cavities with strain larger than 6.2% and processed together with the previous lasing samples show only photoluminescence, whereas our model predicts lasing at low threshold. Further investigation of the temperature dependence of the lasing reveals the interplay of upcoming intervalence band absorption. By accounting for such additional parasitic loss, we develop a qualitative gain and loss model which consistently describes (i) the lack of lasing at low strain, (ii) the limited power and temperature range of the lasing sample, and (iii) the missing threshold in the higher strain cavities. However, the latter implies that the dependence on the strain of energy difference between Γ and L is smaller than predicted by the tight-binding model, introduced in section 2.1.

Furthermore, we give a first study of the effect of n-doping and strain on germanium's radiative properties. In the final part of the chapter, we discuss the linewidth above threshold. The analysis aims to explain the disagreement between the observed marginal linewidth narrowing and the prediction from the standard theory.

Sample	Pad Length B (μm)	EF	$\epsilon_{<100>}$ (%), 300 K	$\epsilon_{<100>}$ (%), 15 K	BG (meV), 15 K
L5	280	22.89	3.52	5.77	340.9
L6	300	23.95	3.68	6.04	309.9
L7	320	24.96	3.83	6.30	279.7

Table 5.1: Batch A samples, theoretical values. Geometrical dimensions and expected strain values at room and low temperature, together with the band gap energy at low temperature as inferred from the tight-binding model.

Sample	$\Delta\omega$ (cm^{-1})	$\epsilon_{<100>}$ (%), 300 K, eq.2.4	BG _{meas.} (meV), 15 K	$\epsilon_{<100>}$ (%), 15 K
L5	6.69	3.69	335	5.82
L6	6.94	3.80	320	5.95
L7	7.29	3.94	304	6.09

Table 5.2: Batch A samples, experimental results. Strain values measured via Raman scattering, together with the band gap energy extracted from the PL at low temperature and the deduced strain value. The uncertainties in the band gap and strain determination are estimated as ± 3 meV and ± 0.025 %, respectively.

5.2 Samples and experimental set-up

In the following experiment, we study a new set of strained germanium cavities, processed in two different batches, which we refer to as *A* and *B*. Similarly to chapter 4, the microbridges are $8\ \mu\text{m}$ long and $1\ \mu\text{m}$ wide and integrated in a cornercube optical cavity $44\ \mu\text{m}$ long. The pad width is $80\ \mu\text{m}$, while the pad length varies for increasing strain as described in tables 5.1 and 5.3 for the processing batches *A* and *B*, respectively. During the processing of batches *A* and *B* samples, we noticed a progressive reduction with the pad length of the HF vapor efficiency in under etching the extreme ends of the pads. In the calculation of the enhancement factor EF in tables 5.1 and 5.3 an over etching length L between 5 and $0\ \mu\text{m}$ is considered, respectively. Theoretical strain values at room and low temperature are defined following the geometrical consideration of section 2.5.

The experimental strain, measured via Raman scattering, ranges from 3.69% up to 4.23%, as reported in tables 5.2 and 5.4. The Raman measurements are carried out by Jeremie Chretien and Nicolas Pauc at CEA, IRIG-DEPHY, Grenoble (France). We observe a generally good agreement between the model and the measurements at room temperature. Possible discrepancies are attributed to (i) inhomogeneity of the HF under etching rate and

Sample	Pad Length B (μm)	EF	$\epsilon_{<100>}$ (%), 300 K	$\epsilon_{<100>}$ (%), 15 K	BG (meV), 15 K
L9	360	26.13	4.02	6.59	245.4
L10	380	27.04	4.15	6.82	217.9
L11	400	27.91	4.29	7.04	191.2

Table 5.3: Batch *B* samples, theoretical values. Geometrical dimensions and expected strain values at room and low temperature, together with the band gap energy at low temperature as inferred from the tight-binding model.

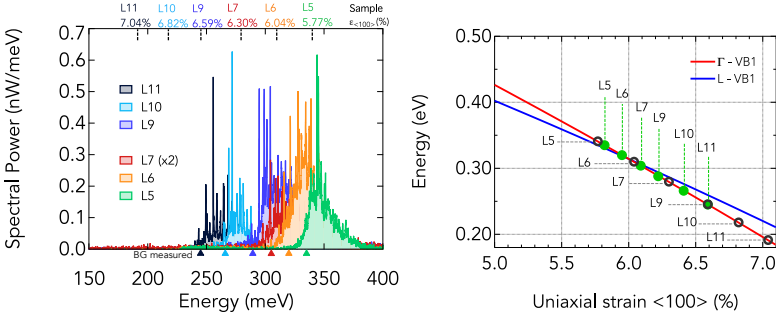
Sample	$\Delta\omega$ (cm^{-1})	$\epsilon_{<100>}$ (%), 300 K, eq.2.4	BG _{meas.} (meV), 15 K	$\epsilon_{<100>}$ (%), 15 K
L9	7.37	3.98	288*	6.22
L10	7.65	4.10	266	6.41
L11	8.02	4.23	245	6.59

Table 5.4: Batch *B* samples, experimental results. Strain values measured via Raman scattering, together with the band gap energy extracted from the PL at low temperature and the deduced strain value. The uncertainties in the band gap and strain determination are estimated as ± 3 meV and ± 0.025 %, respectively. (*) For L9, we assign a band gap of 288 meV due to absorption at low energy (c.f. Fig. 5.1(a)).

(ii) uncertainty within 100 nm in the definition of the microbridge dimensions during the processing.

Room temperature photoluminescence (PL) measurements at low resolution of batch *B* L9, L10, and L11 samples were shown in Fig. 2.1(b) in green, red and black colors, respectively. The measurements reveal good agreement between the measured strain and the band gap Γ -VB1 position predicted by the tight-binding model. The low temperature ($T=15$ K) photoluminescence spectra of samples from L5 to L11 are reported in Fig. 5.1(a). The photoluminescence of L7 is enhanced by a factor of 2. The discrepancy in intensity with the other samples is due to a not-optimized detector alignment. For each sample, the dashed line from the top indicates the nominal band gap position, calculated via the tight-binding model using the strain prediction based on the thermal expansion coefficient dependence on the temperature (c.f. Fig. 2.7). The strain and band gap predictions are reported in the last two columns of tables 5.1 and 5.3.

We also investigate in detail the lasing properties of an L9 cavity belonging to batch *B* and whose photoluminescence onset is alike that of sample L7 of batch *A*. This sample will



(a) Samples L5 to L11 photoluminescence at 15 K upon continuous wave excitation of about 6 mW. (b) Tight-binding Γ and L band edges dependence on strain, normalized to low temperature.

Figure 5.1: The photoluminescence of batch A and B samples cooled at 15 K exhibit a strong red shift of the direct band gap. The dashed line on the top of (a) indicate for each sample the nominal band gap position predicted by the geometrical dimensions and the tight-binding model, reported in the last column of tables 5.1 and 5.3, and in (b) by the black open circles. The band gaps, as inferred from the PL, are indicated in the bottom of (a), allowing the extraction of the strain via the tight-binding model in (b), as indicated by the green points.

be denoted as $L9^*$. The results of $L9^*$ and $L9$ allow a straightforward comparison between performances of differently strained samples, which are processed on the same batch and measured together.

The photoluminescence onsets observed at low temperature show a progressive deviation from the strain modeling for samples with increasing strain. While L5 emission follows the prediction, the discrepancy increases for samples L6 to L11. The agreement observed between the experiment and the model for the sample L5, which belongs to the same processing batch of L6 and L7, indicates that the thermal strain model of $\epsilon_0(T)$ is correct down to the lowest temperature. Other samples than those shown in Fig. 5.1(a) belonging to the same processing batches report the same deviations. This effect is highly deterministic, as the samples always exhibit the same onset after many cooling cycles. The effect is also highly reproducible. Fig. 5.2 reports the photoluminescence of a cavity sample with the same geometrical dimensions of L11, fabricated before this thesis work by Thomas Zabel and Esteban Marin at Paul Scherrer Institut, Villigen (Switzerland). Its photoluminescence at 20 K shows the same onset as the L11 sample of Fig. 5.1(a).

We hypothesize that, from a certain geometrical dimension, the strain enhancement

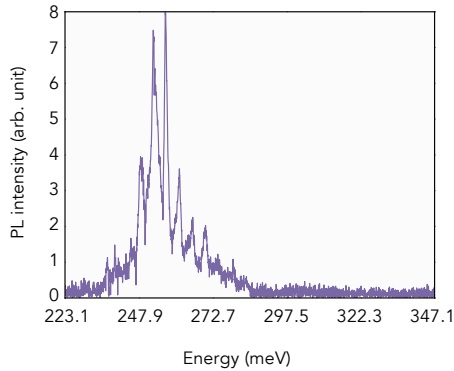


Figure 5.2: Photoluminescence of a strained germanium sample integrated into the cornercube cavity cooled at 20 K and excited upon continuous wave excitation of 60 mW running at 920 meV. The sample was processed in 2016 and has the same geometrical dimension of L11 of batch B (c.f. table 5.3) and exhibits the same energy onset of L11 (c.f. Fig. 5.1(a)). The processing and the measurement of the sample were carried out by Thomas Zabel and Esteban Marin at Paul Scherrer Institut, Villigen (Switzerland).

is not anymore purely planar, as assumed in the 2D analytical model of equation 2.3, but becomes three-dimensional. We report Fig. 5.3, which shows the SEM image of a 400 nm thin strained germanium microbridge to support this idea. The structure was supposed to land on the silicon layer underneath via a fast etching of the sacrificial SiO_2 layer. However, only the pads' lateral edges and corners landed, while the optical cavity is suspended. Fig. 5.3 shows that the forces may not be directed only in the plane, but also out of the plane, leading to deviations of the 2D analytical model and reducing the effective geometrical dimensions and thus the strain. This mechanical deviation seems to be enhanced by the presence of the cornercubes. To better address this mechanical deformation, strain mapping of both the microbridge and the pads at low temperature via Raman scattering should be carried out, as well 3D strain FEM modeling.

Thus, in contrast to the previous chapter, in this experiment the strain at low temperature is derived from the position of the band gap, i.e., the onset of the photoluminescence. The thus obtained experimental band gap values are indicated at the bottom of Fig. 5.1(a). Fig. 5.1(b) reports the transition energies Γ -VB1 and L-VB1, inferred from Fig. 2.1(a), and normalized to 15 K via Varshni shift [100]. The extracted band gap positions and the strain deduced from Fig. 5.1(b) are resumed in the last two columns of tables 5.2 and 5.4. The strain span from about 5.82 to 6.59%.

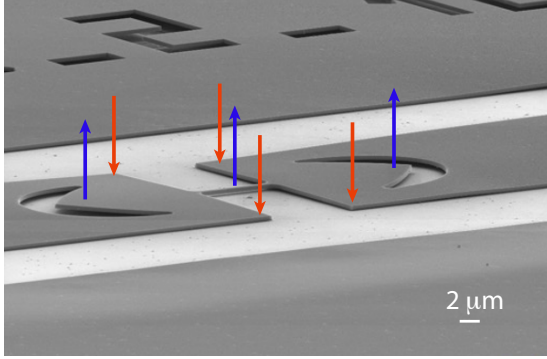


Figure 5.3: SEM image of a 400 nm thin strained germanium microbridge integrated into the corner-cube cavity. The sample does not belong to the experiment of this chapter. The red and blue arrows indicate the landed and suspended area, respectively. The image is taken in collaboration with Nicolas Pauc at CEA, IRIG-DEPHY, Grenoble (France)

The band gap position is estimated as the energy corresponding to the half maximum spectral intensity of the smooth PL background. We adopt this approximation to avoid in the fitting modeling hurdles due to multiple interference effects or air gases absorption, as between 286 and 295 meV, due to CO_2 , or between 440 and 490 meV, due to water vapor. An example of the band gap energy extraction is given in the appendix A.5. This method comes with an uncertainty of ± 3 meV, which translates into a strain error estimated as $\pm 0.025\%$. As indicated in Fig. 5.1(b), the tight-binding model foresees that samples L7 to L11 are direct: the next sections' experiments aim to verify this predictions.

In this experiment the cavities are studied employing uniquely the excitation line of the continuous wave diode laser running at 590 meV. The set up was described in Fig. 4.1. The excitation beam is focused at the sample position in a spot whose intensity varies radially following a gaussian profile with a *FWHM* of about $8.7\ \mu\text{m}$. Throughout this chapter, the reported excitation power is defined as the total power measured through the cryostat CaF_2 window at the sample position. The power density is approximated as uniformly distributed within an effective diameter and area of about $d_{TH} = 10.5\ \mu\text{m}$ and $\Sigma_{TH} = 85.8\ \mu\text{m}^2$, respectively. This approximation is referred to as top-hat approximation [148] and it is described in A.2.

The carrier density excited in the strained germanium per unit of excitation power is

then estimated as:

$$N = \frac{O_{\Sigma} Abs \tau}{E_{ph} q V} = 2.47 \cdot 10^{17} \frac{\text{cm}^{-3}}{\text{mW}} \quad (5.1)$$

where the overlapping factor between the microbridge surface and the excited area is $O_{\Sigma} = 9.3 \cdot 10^{-2}$. $Abs = 0.4$ is the absorbance for the excitation energy of $E_{ph} = 590$ meV, as calculated from the model of Fig. 4.5(b), taking into account multiple interference effects. The carrier lifetime used is $\tau = 5$ ns, as obtained from pump and probe measurement in relaxed germanium [142], while the volume of the microbridge is $V = 8 \cdot 10^{-12} \text{ cm}^{-3}$. The transition area between the strained microbridge and the relaxed pad is not included in the previous estimation.

In the following, the expression steady state lasing upon continuous wave excitation is used. Indeed, the continuous wave excitation term can be adopted whenever the time scale of the external excitation is larger than time scale of the probed system, e.g., carrier lifetime and thermal loading. Thus, in this experiment, the continuous wave excitation allows reaching a steady state condition, in contrast to chapter 4 experiment, where the external source's time scale was shorter than the carrier lifetime and, notably, the valley scattering time.

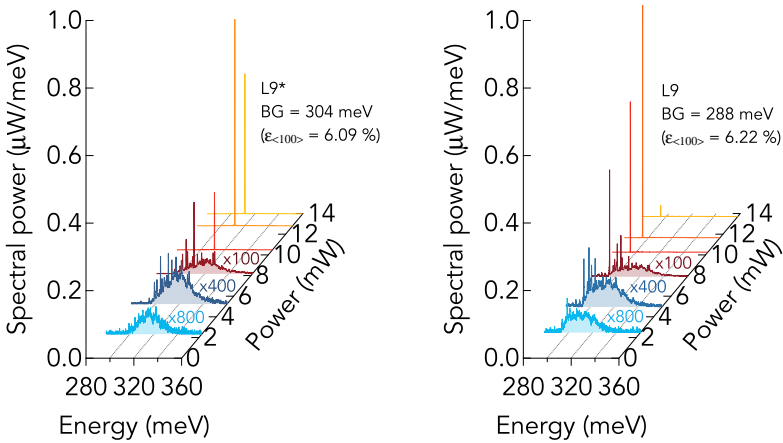
5.3 Main lasing characteristics

Figures 5.4(a) and 5.4(b) report the power dependent spectra of the lasing samples L9*, i.e., the sample with the geometry of L9 but with the same characteristic as L7, and L9, respectively. The samples are excited up to 14 mW upon continuous wave excitation, showing the typical fingerprints of lasing action, namely (i) the transition from a multimode to a single or few modes spectrum, together with (ii) strong increase in the emitted intensity, as learnt from the previous chapter. Both L9* and L9 spectral emissions at low power exhibit a broad photoluminescence background strongly modulated by Fabry-Perot cavity modes. The latter are amplified by increasing the excitation power and their intensity increases respect to the background. Once the excitation power is raised above threshold, the L9* and L9 spectral emissions are dominated by a single mode at 311 and 295 meV, respectively, whose peak intensity grows up to about three orders of magnitude above the PL background, as shown by the spectra in logarithmic scale of Fig. 5.5(a) and 5.5(b).

This abrupt spectral transition is accompanied by a steep increase in the emitted power, as reported in Fig. 5.6, which shows in linear scale the spectrally integrated emission intensity as a function of the excitation power. The clear threshold in the total intensity marks the transition from spontaneous recombination to stimulated emission regime. From the linear increase above threshold we extract the threshold powers, which decreases with the strain.

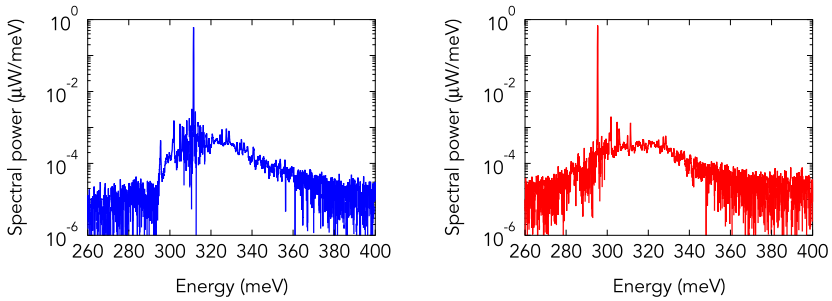
For the L9* and L9 samples threshold powers are $P_{th}(L9^*) = 9.3$ mW and $P_{th}(L9) = 8.1$ mW, respectively, which, by following equation 5.1, correspond to an estimated carrier density of $N_{th}(L9^*) = 2.3 \cdot 10^{18}$ cm⁻³ and $N_{th}(L9) = 2.0 \cdot 10^{18}$ cm⁻³. For both samples, the linear increase in the emitted intensity is then followed by a strong roll over, whose onset takes place at an excitation power which decreases with the strain.

We now want to better comprehend the mode competition supporting the transition from the sub threshold and multimode regime to the lasing regime, whose emission is sustained by a single mode. Fig. 5.7(a) shows an enlarged view of the sub threshold spectra of the lasing sample L7 belonging to the batch A measured at 15 K. The spectra are offset in the vertical direction for visualization purposes. At the lowest power the modes below 310 meV,



- (a) L9* power dependence upon continuous wave excitation at 15 K. Lasing oscillates at energy of 311 meV.
- (b) L9 power dependence upon continuous wave excitation at 15 K. Lasing oscillates at energy of 295 meV. The low energy emission is affected by CO₂ absorption in air.

Figure 5.4: Steady state lasing upon continuous wave excitation at 15 K, highlighting the transition from the broad multimode photoluminescence to single mode emission when the power exceeds the threshold.



(a) L9* spectral emission in logarithmic scale at excitation power of $P = 12.85$ mW at 15 K. (b) L9 spectral emission in logarithmic scale at excitation power of $P = 11.65$ mW at 15 K.

Figure 5.5: Spectral emission at 15 K in logarithmic scale of steady state Ge lasers upon excitation power at which the emitted intensity peaks.

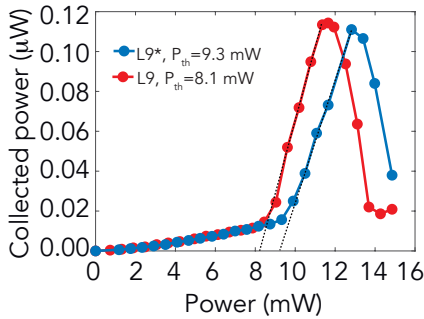
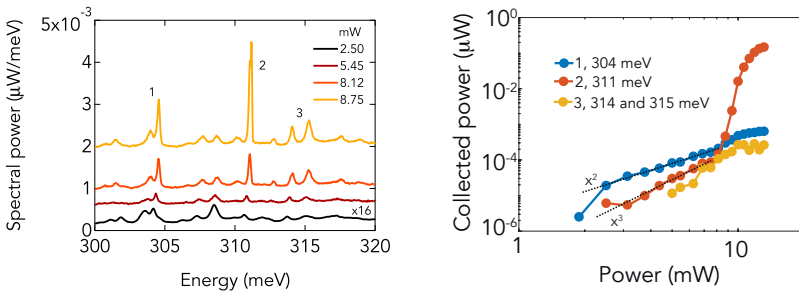


Figure 5.6: Total emitted power collected at the exit of the microscope as a function of the excitation power of the L9* and L9 lasing samples at 15 K. The dashed lines fit the linear emission above threshold in order to extract the threshold powers.

among which the reference mode labeled as 1, are the most pronounced with respect to the background, while the modes 2 and 3 at about 311 meV and 314.5 meV, respectively, are barely observable. The mode 3 accounts for the two modes at 314 and 315 meV. While the excitation power is increased, the intensity of mode 2 increases at a rate faster than the surrounding modes, such that at the excitation power of 8.12 meV is the most amplified one. Once the power is increased beyond threshold mode 2 finally prevails over all the others, by entering into the stimulated emission regime, as previously observed.

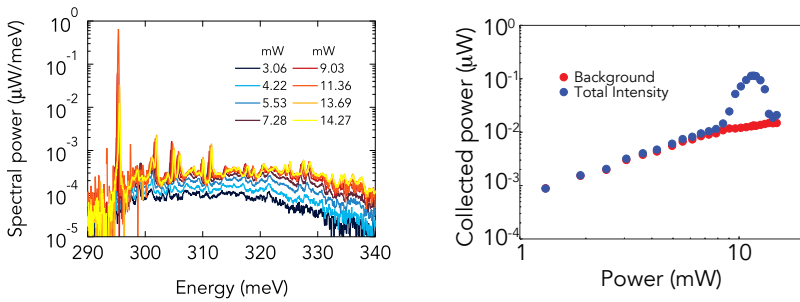
These observations can be quantitatively measured as reported in Fig. 5.7(b). The latter shows the intensity of the individual mode of Fig. 5.7(a) as a function of the excitation power. These quantities are calculated by spectrally integrating the individual cavity mode and subtracting the background, which is extracted via a smoothing function as described in A.4. The onset at which the mode emerges with respect to the background shifts toward higher power with the energy of the cavity mode. Whilst the lowest energy mode at 304 meV grows with a quadratic dependence, the lasing mode at 311 meV increases during the sub threshold regime with a faster rate, proportional to the cube until it reaches threshold condition. While the lasing mode strong amplification at threshold is a clear signature of gain, the non uniform amplification between the cavity modes far below threshold is attributed to a difference in optical losses: while modes with low Q factor, and thus more lossy, can be more easily observed in sub threshold regime, mode with higher Q, like the lasing mode of this experiment, can be detected only upon strong light amplification regime.

Once the lasing oscillation is established, it is possible to observe from Fig. 5.7(b) that



(a) Enlarged view of the spectral emission below threshold of the sample L7 of batch A. The spectra are offset in the vertical axis (b) L7 mode intensity indicated in (a) reported as a function of the excitation power at 15 K.

Figure 5.7: Gain amplifies non uniformly the cavity modes, leading to the typical lasing fingerprint of mode competition.



(a) L9 spectra in logarithmic scale measured out at 15 K. Above threshold the PL background is clamped. (b) Total spectrally integrated intensity in blue, compared to the background intensity in red of the L9 emission at 15 K

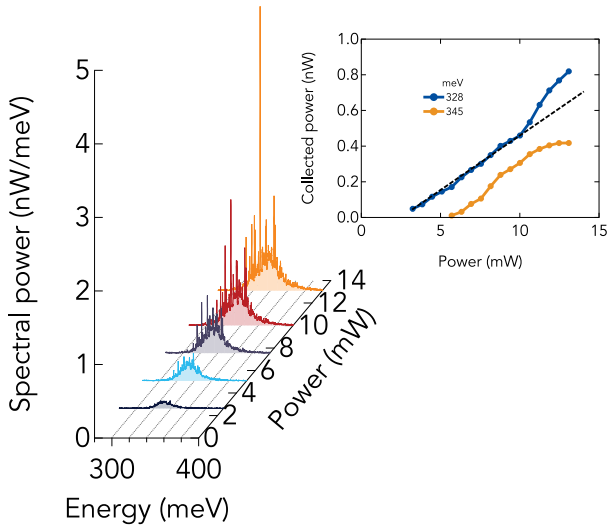
Figure 5.8: Under lasing condition gain and carrier density are clamped, leading to the background pinning.

the intensity of the non lasing cavity mode saturates. This effect is related to gain clamping. Fig. 5.8(a) shows power dependent spectra of the L9 lasing sample in logarithmic scale, highlighting the growth of the background below threshold and the following saturation when lasing oscillation is established. Fig. 5.8(b) extracts by means of the smoothing function described in A.4 the intensity of the background. Below threshold the total integrated intensity and the background overlap until the lasing condition is reached at $P_{th}(L9) = 8.1$ mW: while the total intensity abruptly grows as sustained by the lasing mode, above threshold the photoluminescence background overall pins to a total integrated intensity of about 15 nW.

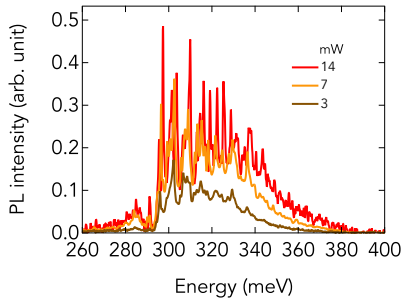
It is possible to observe that, although the background does not follow the same dependence as below threshold, it follows a slightly increasing rate, indicating upcoming material losses. The background pinning follows from the fact that in a laser cavity the gain has to be clamped to its threshold value g_{th} . If $g(P > P_{th}) > g_{th}$ light would be amplified without bound, breaking the energy conservation law. As the gain is in first approximation linearly dependent on the carrier density, gain clamping implies that carrier density above threshold is pinned to its threshold value N_{th} , determining the observed saturation of the PL background.

5.4 Gain vs loss

Fig. 5.9(a) reports the power dependent spectra of samples L6 carried out at 15 K. Sample L6 exhibits a band gap energy of 320 meV, corresponding to a deduced strain of about



(a) High quality L6 cavity power dependence upon continuous wave excitation at 15 K. Inset: L6 mode intensity as a function of the excitation power.



(b) Photoluminescence of an L9 sample fabricated with the old processing excited upon continuous wave excitation at 20 K.

Figure 5.9: Gain and sufficiently low loss determine the condition for lasing threshold. Lasing is not observed in both (a) and (b) cavities.

$\epsilon_{<100>} = 5.95\%$, lower than sample L7. The cavity modes modulate the broad photoluminescence from low power and, overall, the spectra are mostly independent of the excitation power, while the emitted power lacks a clear threshold. Interestingly, as reported in the upper inset of Fig. 5.9(a), the cavity mode's intensity at 328 meV experiences a small change in the growth rate at about excitation power of 10 mW. In contrast, the surrounding modes saturate, highlighting traces of gain and mode competition. This transition can be visually seen in the spectra taken at highest power of Fig. 5.9(a), where the mode at 328 meV seems to be at the edge of prevailing over the background and the surrounding modes.

However, high strain and gain are not sufficient conditions for lasing. Indeed the samples investigated in this experiment are processed following the improved hard mask recipe of section 2.4, allowing to substantially reduce the cavity losses up to a factor of 4, as previously shown in section 3.4.6.

Fig. 5.9(b) shows the power dependence of a sample fabricated with the reference processing, which exhibits a strain similar to the lasing L9 cavity. Up to the highest excitation, the spectra show the typical photoluminescence signatures (c.f. Fig. 4.3). The cavity modes are uniformly amplified and no lasing is observed. Evidentially, the amount of gain compensating the cavity loss of the high quality cavity (c.f. Fig. 5.4(b)) is not enough to overcome the larger losses derived from the reference processing.

Thus, the lasing threshold is a combination between a sufficiently high gain and a low optical loss: next section 5.5 gives a quantitative answer to both.

5.5 Lasing analysis: from transparency to lasing

In the following, we show that the linewidth analysis of a system operating in steady state condition and reaching lasing threshold represents a unique tool to probe the energy difference between the Γ and L minima, i.e., $\Delta E_{\Gamma,L} = E_{\Gamma} - E_L$. We exemplify the method by making use of the linewidth data obtained from the lasing sample L9.

Our analysis develops as follows: (i) we identify the modes running in transparency condition, which allow to extract the cavity loss, (ii) we identify the modes experiencing gain and (iii) we compare the observed gain build-up with the gain model developed in section 3.3.1, to estimate the energy difference $\Delta E_{\Gamma,L}$.

In Fig. 5.10 we show in the upper panel the L9 spectrum taken at excitation power of $P = 6.12$ mW. The lower panel reports the evolution with the total carrier density of the absorption calculated by means of the model of section 3.3. Absorption calculations are carried out for the case of $\Delta E_{\Gamma,L} = 0$ meV, with the the Γ and L band edges both positioned at 288 meV. Indeed for this case the calculation predicts that the peak gain position coincides

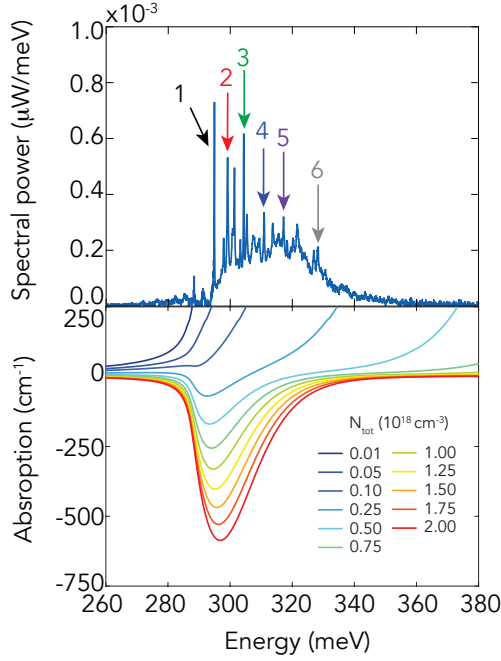


Figure 5.10: Comparison between L9 spectral emission at 15 K upon excitation power of $P = 6.12 \text{ mW}$ (upper panel) and the spectral absorption as a function of the total carrier density (lower panel) in order to identify the cavity modes in proximity of the transparency window. The modes labelled from 1 to 6 are analyzed in Fig. 5.11.

with the lasing mode at about 295 meV. Moreover, the calculations are performed for electron temperature of 50 K and considering a Lorentzian broadening of $\Gamma_{\text{lor}} = 4 \text{ meV}$. Many body effects, such as carrier-carrier scattering, which may reduce the gain, are not considered in our model.

Goal of the comparison between the emission and the gain spectra of Fig. 5.10 is to identify the cavity modes belonging to the transparency region, as previously treated in section 3.3.2. These modes experiences by definition zero optical absorption $\alpha_{IB} \sim 0$ and thus their linewidth is a direct measurement of the cavity loss. Among all the modes, we choose those with characteristics of being easily resolvable during the power dependence.

The chosen modes for the analysis are labelled from 1 to 6 in the upper panel of Fig. 5.10. We identify the modes 5 and in particular 6 as those whose Q factor can approximate

the cavity loss. Although, according to the model, transparency starts actually at 350 meV, modes 5 and 6 at 317 and 327 meV respectively, are expected to be weakly amplified by gain and largely independent of the power, due to the small differential gain at high energy.

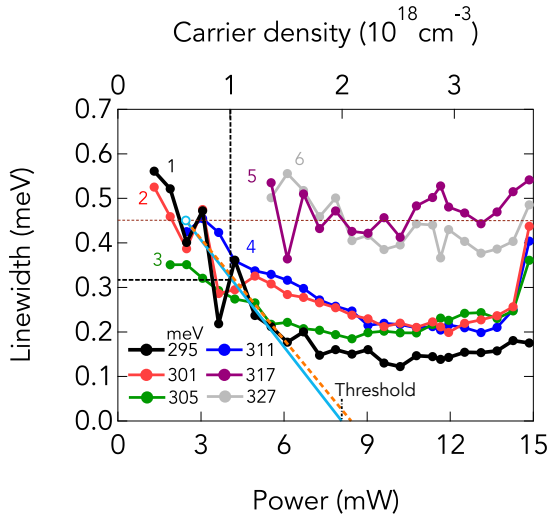


Figure 5.11: L9 linewidth at 15 K as a function of the excitation power of the modes labelled in Fig. 5.10. The horizontal dashed line at 0.45 meV indicate the transparency level. The differential gain is extracted from the linear regression between the transparency point and the lasing threshold and it is shown in light blue. It well agrees with the orange dashed line starting as well from transparency and obtained from the model as explained in section 5.9.

In Fig. 5.11 we report the linewidth evolution with respect to the input power of the modes labelled in Fig. 5.10. The reported linewidth are apodized. We identify three different regimes.

(i) We first observe that the linewidth of both modes 5 and 6 is indeed largely independent of the input power as expected for modes at the high energy tail of the gain spectrum (c.f. Fig. 5.10). Their linewidth values scatter around 0.45 meV, which translates to cavity loss of about 102.6 cm^{-1} , as calculated from the equation $\Delta E = hc\alpha_c / (2\pi n_g)$, following the transparency definition and equation 3.20.

(ii) The linewidth of the modes 1 to 4 narrows as driven by gain from below to above transparency. Compatibly with the assumption that lasing occurs at the gain peak, the lasing mode narrows the most.

(iii) Near and above threshold the linewidth narrowing saturates. The non lasing mode from 2 to 4 saturate at 0.20 meV. This behavior can be well understood from the Fermi level pinning under the lasing.

(iv) The lasing mode linewidth saturate as well at 0.15 meV. This unexpected behavior is treated a part in section 5.13.

In the following we address the energy difference $\Delta E_{\Gamma,L}$ between the Γ and L minima of L9. Threshold is achieved when the gain is high enough to compensate all the losses, comprising of the cavity and material contributions, such that the electric field can replicate exactly itself after one round trip:

$$\exp(\Gamma_{xy} g_{th} L_b) \exp(-\alpha_c L_c) \exp(-\Gamma_{xy} \alpha_{loss} L_b) = 1 \quad (5.2)$$

$\Gamma_{xy} = 0.94$ is the transversal confinement factor, as shown in A.3, g_{th} indicate the material gain at threshold, $L_b = 8 \mu\text{m}$ is the active material length, i.e., the microbridge, $\alpha_c = 102.6 \text{ cm}^{-1}$ is the cavity loss term, previously found from the transparency modes. The latter comprehends of both scattering and mirror losses, averaged over the entire cavity length $L_c = 44 \mu\text{m}$. α_{loss} represents possible material related optical losses, such the intervalence band absorption and the free carrier absorption due to electrons, which we approximate as exclusively related to the active material. From the previous equation, assuming that $\alpha_{loss} = 0$, we understand that the active material delivers at threshold a gain of at least:

$$g_{th} = \frac{1}{\Gamma_{xy}} \left[\alpha_c \frac{L_c}{L_b} \right] = 600 \text{ cm}^{-1} \quad (5.3)$$

The gain required to reach lasing threshold is considerable. This is due to the low filling factor of the active material, which is less than 20%. Threshold of the lasing mode 1 at $P_{th}(L9) = 8.1 \text{ mW}$ evidentially corresponds to the power at which gain compensate the cavity losses of 102.6 cm^{-1} , assuming no additional parasitic losses. The differential gain of the lasing mode 1, defined as the linear regression between the transparency point and the lasing threshold (c.f. blue line in Fig. 5.11) is $dg/dN = 4.32 \cdot 10^{-16} \text{ cm}^2$.

In Fig. 5.12 we report the material gain calculated at carrier density corresponding to the estimated L9 threshold density, $N_{th}(L9) = 2 \cdot 10^{18} \text{ cm}^{-3}$, for different energy difference $\Delta E_{\Gamma,L}$. For this calculation we keep the remaining band parameters, such as the effective electrons and holes masses, constant at their values for the case of Γ band edge at 288 meV, corresponding to strain of about 6.22 %. Evidentially, gain is an efficient probe of the energy difference $\Delta E_{\Gamma,L}$ between the Γ and L minima. When the $\Delta E_{\Gamma,L}$ changes of only 15 meV the gain increases from about 100 to almost 900 cm^{-1} . In order to reach a material gain of 600 cm^{-1} , which is highlighted by the black dashed line, the energy difference between the Γ and L band edges of L9 has to be at least about $\Delta E_{\Gamma,L} = 0 \text{ meV}$.

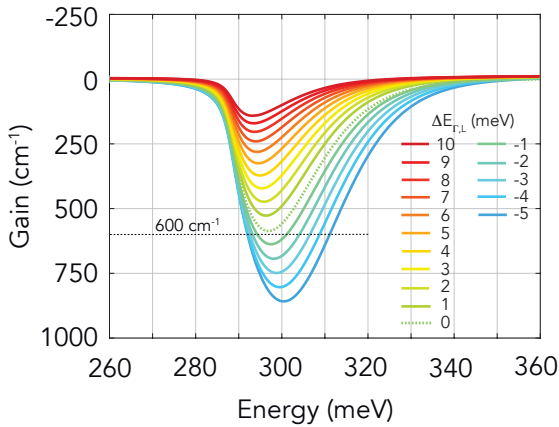


Figure 5.12: Gain spectra calculated at $N_{tot} = 2 \cdot 10^{18} \text{ cm}^{-3}$ as a function of the energy difference $\Delta E_{\Gamma,L}$

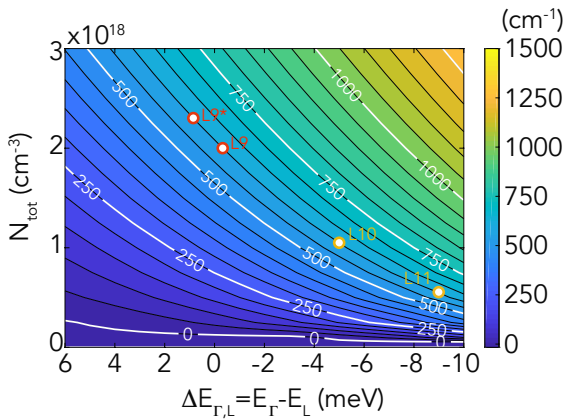
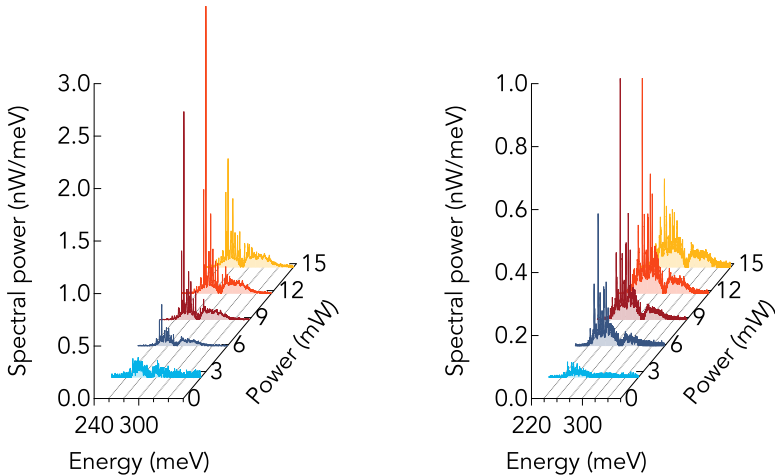


Figure 5.13: Peak gain color map as a function of the total carrier density and the energy difference $\Delta E_{\Gamma,L}$ around the crossing to direct band gap configuration. Reported in red, the threshold of the lasing samples L9* and L9, in yellow the anticipated threshold of higher strain samples L10 and L11. The threshold values do not consider the material losses.

This is a lower bound since neither the free carrier absorption due to electrons nor the intervalence band absorption are considered yet (c.f. section 5.8). Similarly, from the threshold $N_{th}(L9^*) = 2.3 \cdot 10^{18} \text{ cm}^{-3}$ found for L9* (6.09 %), we find an energy difference $\Delta E_{\Gamma,L}$ of about 1 meV.

Compared to the tight-binding model, the here found $\Delta E_{\Gamma,L}$ values seem to suggest that the strain needed to transform Ge from indirect to a direct band gap system may be about 3 % higher than the tight-binding model foresees. These results show that the energy difference $\Delta E_{\Gamma,L}$ drives the gain. By increasing the strain, lasing is expected to occur at considerable lower threshold power than L9* and L9 samples, as anticipated by the gain model of Fig. 5.13. In the next section the gain model is benchmarked by measuring the higher strain samples L10 and L11.

5.6 High strain: missing lasing



(a) L10 power dependence upon continuous wave excitation at 15 K. (b) L11 power dependence upon continuous wave excitation at 15 K.

Figure 5.14: Power dependent spectra of non lasing samples L10 and L11. The photoluminescence is overall uniformly amplified.

In this section we study the samples L10 and L11, whose band gap positions are 266 and 245 meV, respectively, corresponding to strain of about 6.41 and 6.59% ($\pm 0.025\%$). Fig. 5.14 shows the power dependent spectra of L10 and L11 cavities excited up to 15 mW at 15 K. Such results resemble the non lasing spectra of sample L6 of Fig. 5.9(a) and do not show threshold in the total intensity. The broad photoluminescence modulated by the cavity modes is overall uniformly excited from low to higher power, where intensity saturation occurs.

Unique trace of gain emergence seems to be represented by the L10 mode oscillating at 270 meV: from the excitation power of 6 mW, this mode's intensity increases prominently with respect to the background and the surrounding modes. However, its growth is not followed by lasing action, as the mode's intensity respect to the background soon rolls over. The emission of manifold modes in L11 comes without any traces of mode competition. We remind the reader that the samples from L9* to L11 are processed on the same GeOI and measured together. Consequently, the lack of lasing in the high strain samples is of fundamental reason rather than technical.

The lack of lasing in L10 and L11 samples is rather a surprising result. Indeed, according to the tight-binding model, samples L10 and L11 are expected to come with an energy difference $\Delta E_{\Gamma,L}$ between -5 and -9 meV, respectively, by considering the above mention discrepancy between the energy difference $\Delta E_{\Gamma,L}$ and the theory of about 3 %. Energy difference $\Delta E_{\Gamma,L}$ of -5 and -9 meV correspond to threshold value as low as $4 \cdot 10^{17} \text{ cm}^{-3}$ (c.f. Fig. 5.13).

The previous measurements on L10 and L11 indicate an upcoming discrepancy between the gain model and the predicted $\Delta E_{\Gamma,L}$. In the next section, we analyze the effect of temperature on (i) the lasing sample L9 and (ii) the non lasing L10 and L11.

5.7 Temperature dependence

The temperature dependence analysis is organized as follows: we first present the L9 light-in light-out curves up to 35 K, followed by the L9, L10 and L11 linewidth comparison between 15 and 30 K.

In Fig. 5.15 we show the light-in light-out curves of the lasing sample L9 as a function of the temperature in linear scale. The curves represent the power of the emitted light collected by the microscope objective as a function of the excitation power. The temperature is increased in step of 5 K (0.4 meV) up to 35 K. By raising the temperature the lasing efficiency degrades rapidly until at the highest temperature the lasing is suppressed. The onset at which the collected power rolls over is constant up to 25 K, then it rapidly shifts

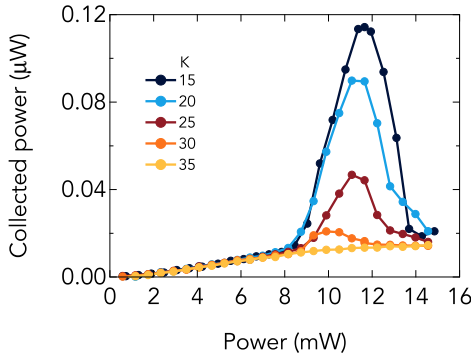


Figure 5.15: Power collected from the sample L9 at the exit of the microscope as a function of the excitation power for different temperatures, up to 35 K.

to lower power together with the lasing dousing. During the transition from the high to low efficiency regime the threshold power stays constant. Similar observation was made upon pulsed excitation (c.f. section 4.4.5), where the lasing efficiency drops faster than the threshold increases.

Fig. 5.16 shows the apodized cavity mode linewidth of L9, L10 and L11 at 15 K (c.f. (a), (c) and (e)) and 30 K (c.f. (b), (d) and (f)). The here analyzed modes of L9 were previously indicated in Fig. 5.10. Here, Fig. 5.17(a) and 5.17(b) show the chosen linewidth of L10 and L11, respectively. At 15 K, the linewidth of the low energy mode of L10 and L11 samples narrow when the excitation power is increased, indicating gain build-up. The modes at 271 (L10) and 256 meV (L11) are the most amplified ones, as seen from Fig. 5.17, and they narrow down to 0.18 and 0.17 meV, before saturation and broadening takes place. The linewidth value of 0.15 meV as obtained in L9 at threshold is thus not reached. The high energy modes of L10 are constant with respect to the excitation power and pinned to the transparency value of about $\Delta E = 0.45$ meV, compatibly with the previous observations made for L9. For L11 the only analyzable high energy cavity mode shows also the typical pinning between 0.4 and 0.5 meV. The presence of CO₂ absorption obstructs the analysis of modes with higher energy in the transparent region of the gain spectrum.

Despite fluctuations of the linewidth values, in particular at low power due to the reduced signal to noise ratio, from Fig. 5.16 it is possible to observe the following: at the lowest temperature of 15 K the cavity modes at low energy first exhibit gain before smoothly broaden. We interpret the transition from narrowing to broadening as the moment the differential loss takes over the differential gain. The power at which the linewidth broadening starts decreases

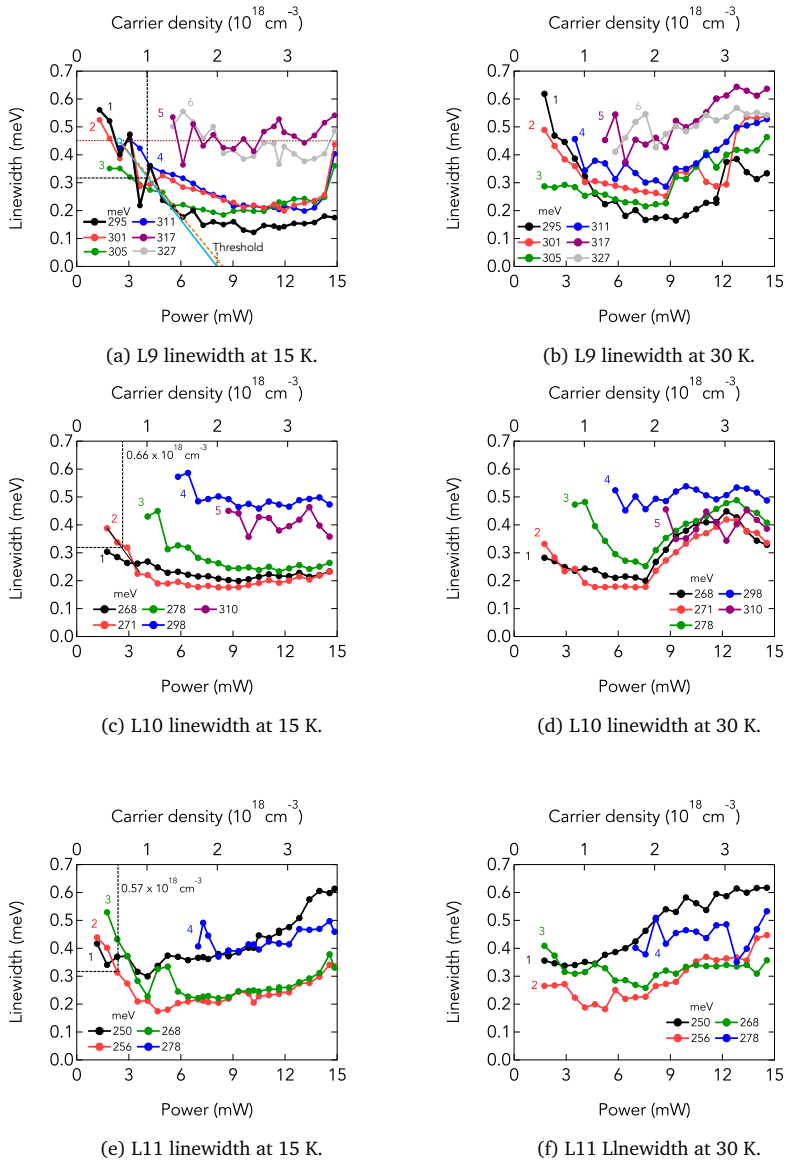
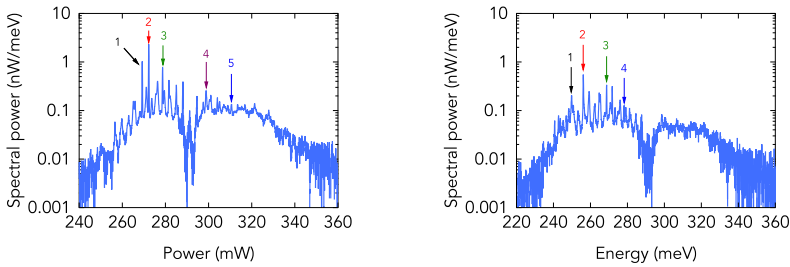


Figure 5.16: Linewidth as a function of power and temperature. The black dashed line in (a), (c), and (e) indicate the carrier density at which the linewidth reaches the value of 0.317 meV, as explained in section 5.9.



(a) L10 spectrum 15 K upon 12.32 mW of power. (b) L11 spectrum 15 K upon 12.32 mW of power.

Figure 5.17: L10 and L11 spectra at 15 K in logarithmic scale. For each sample the cavity modes analyzed in Fig. 5.16 are indicated. Note that both PL spectra are affected by the CO_2 absorption at about 290 meV.

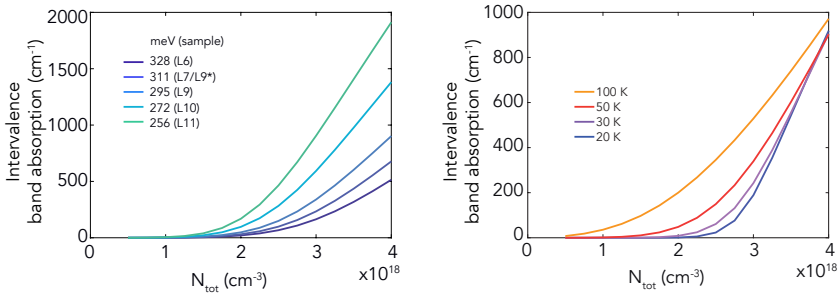
when reducing the cavity mode energy. For L9, L10 and L11 samples the broadening onset takes place at about 12, 9 and 4.5 meV, respectively.

At 30 K for a certain transition energy and excitation power the linewidth broadening accelerates. For L9 and L10 samples the broadening onset reduces to the excitation power of 9 and 7.5 mW, respectively. For L11, due to the linewidth fluctuations of the cavity modes oscillating at 250 and 256 meV, the observation of a clear onset is more difficult to assess, but it can be located between 3 and 6 mW, similarly as at 15 K. For the highest strained sample L11 the effect of the temperature increase is less evident than in L9 and L10.

5.8 Intervalence band absorption

So far, in our analysis we did not consider parasitic material loss. In the following, we neglect the role of the free carrier absorption due to electrons (c.f. 3.3.4), which is measured to be negligible at low temperature thanks to the lack of phonons [128], and we investigate the role of the intervalence band absorption. Fig. 5.18(a) reports the intervalence band absorption at 50 K as a function of the total excited carrier density for different photon energies. The data are extracted from the model of section 3.3.4. The chosen transition energies correspond to the energy of the most amplified cavity mode of the samples L6 to L11.

We observe that the absorption depends strongly on the total carrier density, following the hole filling of states with larger \mathbf{k} . Its intensity increases when approaching the transition VB1-VB2. Fig. 5.18(b) the intervalence band absorption spectra for the transition energy



- (a) Intervalence band absorption at 50 K as a function of the total carrier density for different photon energies, corresponding to the main resonant peak of the sample investigated in this chapter.
- (b) Intervalence band absorption at the energy of 295 meV as a function of the total carrier density for temperatures from 20 to 100 K.

Figure 5.18: Energy and temperature dependence of the intervalence band absorption, extracted from the calculation of section 3.3.4.

of 295 meV (L9) for temperature varying between 20 and 100 K. While at low power and low temperature the absorption is negligible, the temperature opens non linearly the holes transition channel at low carrier density.

As explained in the following, the non linear power and temperature dependence enables to give a qualitative description of our observations, namely:

(i) The intervalence band absorption is responsible for the L9* and L9 lasing roll over at 15 K. The roll-over onset shifts from 13 to 11.5 mW excitation because the intervalence band absorption onset shifts to lower density at lower energy. L9 lasing dousing takes place at about 14 mW, corresponding to a carrier density of about $3.5 \cdot 10^{18} \text{ cm}^{-3}$. At this carrier density and for the L9 energy difference $\Delta E_{T,L}$ of about 0 meV we estimate from Fig. 5.13 a gain of 800 cm^{-1} , sufficient to sustain an additional loss of about 200 cm^{-1} . However, the predicted value of the intervalence band absorption at this carrier density is 634 cm^{-1} , as extracted from Fig. 5.18(a), and lasing is thus not possible. Analogously, for L9* the expected material gain at dousing is about 750 cm^{-1} (c.f. Fig. 3.3(a)), while the intervalence band absorption's model foresees an absorption raising above 460 cm^{-1} .

(ii) The emergence of parasitic absorption for temperature increasing above 35 K makes that the modal gain stays below the necessary 600 cm^{-1} , at all injection intensities.

(iii) However, while it is plausible that the intervalence band absorption overtakes the gain at high carrier density and higher temperature, we understand that at low temperature

and largely independent of the transition energy, the parasitic absorption is negligible for carrier density below 10^{18} cm^{-3} . Thus, even by taking into account possible discrepancies in absolute values, which may derive from the modeling uncertainties, the intervalence band absorption can not account for the lack of lasing in the samples L10 and L11, whose threshold was predicted to be lower than $4 \cdot 10^{17} \text{ cm}^{-3}$ (c.f. Fig. 5.13). The discrepancy will be solved in the next section.

5.9 Energy difference $\Delta E_{\Gamma,L}$ vs strain

In this section we probe the energy difference $\Delta E_{\Gamma,L}$ as a function of the strain, by comparing the experimental linewidth to the gain model. We evoke the linewidth to deduce the differential gain, which is obtained with the usual relation $\Delta E = hc\alpha_{tot}/(2\pi n_g)$ and by including the material filling factor. The analysis includes both lasing samples (L9* and L9), whose $\Delta E_{\Gamma,L}$ was already estimated, and the non lasing cavities (L5, L6, L10 and L11).

The principle of the analysis follows from Fig. 5.19. It shows the peak gain calculated as a function of the total carrier density for different $\Delta E_{\Gamma,L}$ values, with resolution of 1 meV. The lasing sample L9 is represented via its excitation density at threshold $N_{th}(L9) = 2 \cdot 10^{18} \text{ cm}^{-3}$. We now estimate the gain at threshold considering also the intervalence band absorption. From the previous section, we infer for the L9 lasing energy an additional parasitic loss of about 50 cm^{-1} . The label (1) in Fig. 5.19 is on the peak gain curve corresponding to $\Delta E_{\Gamma,L} = -1 \text{ meV}$ and indicates a material gain of 640 cm^{-1} . The latter best approximates the gain required to overcome the total optical losses of $(600 + 50) \text{ cm}^{-1}$.

From (1), by following the green line, the solid black circle marks the L9 gain at half the threshold carrier density. Because at this excitation density we can safely neglect the loss due to the intervalence band absorption, we exploit this point to map the non lasing samples $\Delta E_{\Gamma,L}$: we either use a linear extrapolation from the transparency to the $1 \cdot 10^{18} \text{ cm}^{-3}$ point (2) or we map the excitation density at the corresponding linewidth (3). The linear extrapolation of the gain is very accurate for samples with energy differences $\Delta E_{\Gamma,L}$ larger than 1 meV, c.f. the measurement labeled as (2) on the fictive samples with $\Delta E_{\Gamma,L} = 5 \text{ meV}$. The so obtained linear extrapolation for the sample L9 is shown in orange in Fig. 5.11 and it corresponds to $dg/dN = 4.15 \cdot 10^{-16} \text{ cm}^2$. This value well agrees with $dg/dN = 4.32 \cdot 10^{-16} \text{ cm}^2$, as extracted from the linear interpolation from transparency to threshold (c.f. light blue line in Fig. 5.11). The mapping to a specific excitation density value is more accurate for samples with negative $\Delta E_{\Gamma,L}$, as exemplified by (3), plotted on the gain curve of a fictitious sample with $\Delta E_{\Gamma,L} = -4 \text{ meV}$.

We access the differential gain of samples L5 to L9* via the linewidth reduction of the

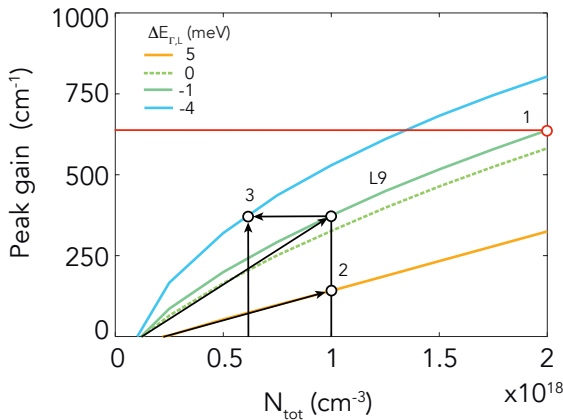


Figure 5.19: Peak gain as a function of the total carrier density for certain energy difference $\Delta E_{F,L}$. It illustrates the analysis method, as reported in the main text.

most amplified cavity mode, which we assume to be in correspondence of the peak gain. As said, the analysis assumes that at low temperature the intervalence band absorption is negligible at high energy, i.e., for the low strained samples, and anyway at low power. Fig. 5.20 reports the analysis of the apodized linewidth of samples L5, L6 and L9* at 15 K.

In Fig. 5.20, as previously for Fig. 5.11, we linearly fit the linewidth narrowing of the cavity mode experiencing the strongest reduction. The fit is carried out from the transparency level, which corresponds to 0.45 meV for all samples, confirming the uniformity of the overall processing and the validity of the analysis of section 5.5.

Sample	$d(FWHM)/dP$ (meV/mW)	dg/dN (10^{-16} cm ²)
L5	-0.038 ± 0.009	2.04 ± 0.45
L6	-0.055 ± 0.012	2.96 ± 0.61
L9*	-0.070 ± 0.010	3.78 ± 0.51
L9	-0.080 ± 0.014	4.32 ± 0.71

Table 5.5: Differential linewidth and differential material gain of samples L5, L6 and L9*, as inferred from Fig. 5.20, and L9, as inferred from Fig. 5.11.

Table 5.5 reports in the second column the linear coefficient of the linear fitting of the samples from L5 to L9, expressed in unit of meV/mW. The measured linewidth is related

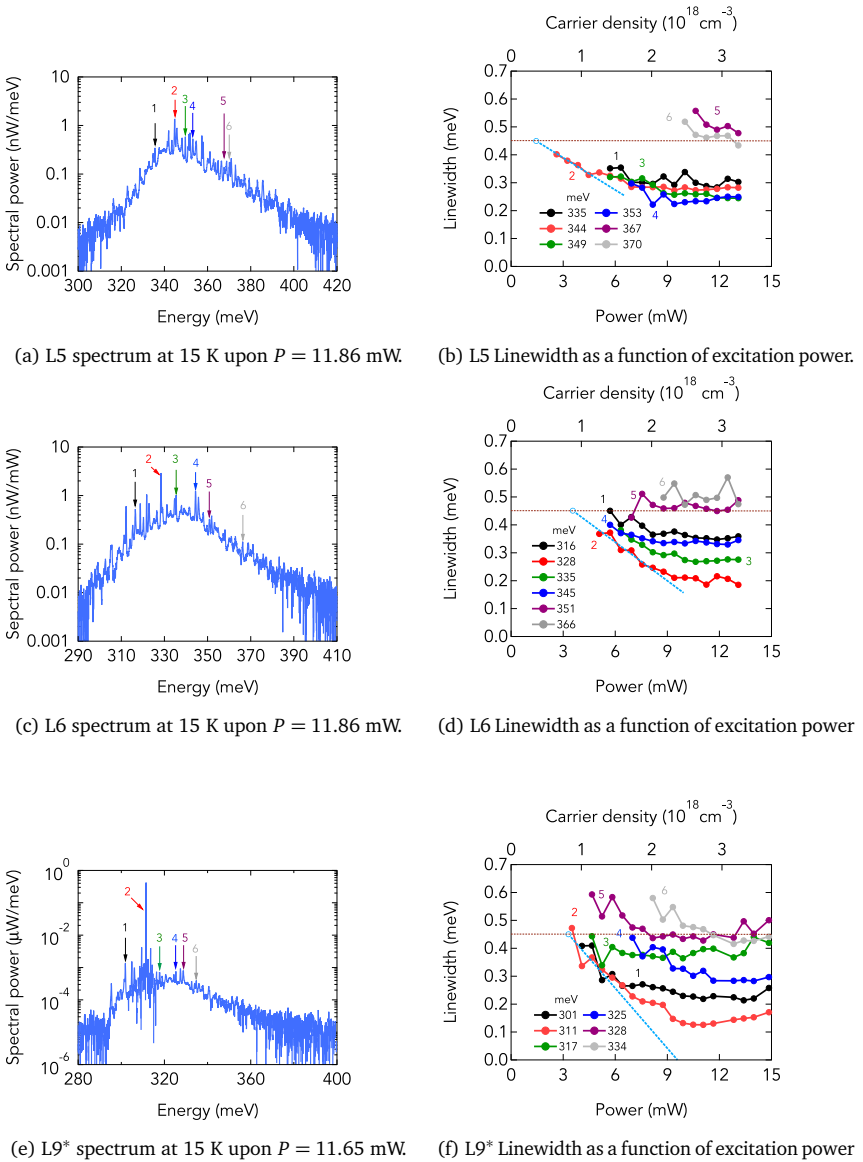


Figure 5.20: L5, L6 and L9* linewidth as a function of power. The linear fit represents the differential gain.

to the loss averaged over the entire cavity length via $\Delta E = hc\alpha_{tot}/(2\pi n_g)$. By taking into account the material filling factor as well as the power to carrier density conversion of equation 5.1, the differential linewidth is translated into the differential of the material gain in the third column, showing a progressive increase from L5 to L9.

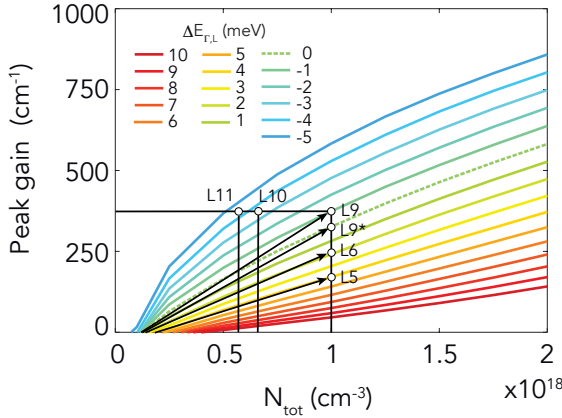


Figure 5.21: Peak gain as a function of the total carrier density for energy difference $\Delta E_{\Gamma,L}$ spanning from 10 meV to -5 meV.

Fig. 5.21 shows the peak gain as a function of the total carrier density for energy difference $\Delta E_{\Gamma,L}$ spanning from 10 to -5 meV. The peak gain dependence on the carrier density is quite linear when $\Delta E_{\Gamma,L} > 0$ meV. Thus, the $\Delta E_{\Gamma,L}$ of the samples with strain lower than L9 is extracted by evaluating the differential gain at total carrier concentration of $N_{tot} = 1 \cdot 10^{18} \text{ cm}^{-3}$ from transparency, as shown in Fig. 5.21. For the two higher strain samples L10 and L11, the energy difference $\Delta E_{\Gamma,L}$ is estimated from the carrier density at which the linewidth reaches the L9 linewidth value at $N_{tot} = 1 \cdot 10^{18} \text{ cm}^{-3}$, as pointed in Fig. 5.16. At $N_{tot} = 1 \cdot 10^{18} \text{ cm}^{-3}$ L9 exhibits a linewidth of $\Delta E = 0.317 \text{ meV}$, which is reached by L10 and L11 at $N_{tot} = 0.66 \cdot 10^{18} \text{ cm}^{-3}$ and $N_{tot} = 0.57 \cdot 10^{18} \text{ cm}^{-3}$, respectively.

The $\Delta E_{\Gamma,L}$ values so extracted are resumed in table 5.6. Fig. 5.22 resumes the gain as a function of the total carrier density of L6, L9 and L11 samples, superimposed to the loss, composed by the cavity loss and intervalence band absorption at 50 K. L6, as well L5, does not reach threshold due to the low amount of gain delivered. The $\Delta E_{\Gamma,L}$ of L9 is low enough to reach threshold at about $2 \cdot 10^{18} \text{ cm}^{-3}$. The non linear increase of the intervalence band absorption causes the lasing dousing at about $2.5 \cdot 10^{18} \text{ cm}^{-3}$, compatibly to the previous observations. In Fig. 5.22 the gain curve of L11 is approximated to $\Delta E_{\Gamma,L} = -3$ meV.

Sample	$\Delta E_{\Gamma,L}$ (meV)
L5	4
L6	2
L9*	0
L9	-1
L10	-3.5
L11	-4.5

Table 5.6: Energy difference $\Delta E_{\Gamma,L}$ between Γ and L for samples L5 to L11 inferred from Fig. 5.21, whose strain span from 5.82 to 6.59 %

Accordingly to the model, L11 reaches the lasing threshold at about $1.2 \cdot 10^{18} \text{ cm}^{-3}$, just before the strong parasitic loss onset. The model fails at describing the observed lack of lasing in L10 and L11 samples. However, discrepancies in the intervalence band absorption's calculation are possible due to uncertainties of the valence band dispersion at large \mathbf{k} and the holes' states lifetime.

We now compare the $\Delta E_{\Gamma,L}$ values as a function of strain of table 5.6 with the prediction of the tight-binding model, as reported in Fig. 5.23. Although the overall agreement about the position at which the crossing to the direct band gap configuration occurs, evidentially the experimental $\Delta E_{\Gamma,L}$ dependence is slower than the prediction at high strain. Moreover, the abrupt deviation of the experimental values may question the overall tight-binding prediction. Due to the lack of similar available works at low strain, we fit the experimental points at high strain and the widely accepted $\Delta E_{\Gamma,L}$ value at zero strain with a quadratic function. The fitting result is reported in Fig. 5.23 and it reads as follows:

$$\Delta E_{\Gamma,L,exp}(\text{eV}) = (0.148 \pm 0.409) - (3.70 \pm 0.06)\epsilon_{<100>} + (20.95 \pm 1.03)\epsilon_{<100>}^2 \quad (5.4)$$

The fitting function disagrees with the tight-binding modeling, both at low and high strain. Fig. 2.1(a) showed that the tight-binding model well describes the non linear dependence of the Γ -VB1 energy transition at large strain, such that the validity of the experimental $\Delta E_{\Gamma,L}$ of equation 5.4 is ascribed to a L band edge diverse from the nominal prediction. However, different modeling than the tight-binding one, like the linear deformation potential theory (DPT), finds a good agreement with the fitting function for moderate strain up to 3.0 %.

Deformation potential theory calculates the electronic band structure under perturbation of the hamiltonian upon strain and thus its validity is mainly restricted to small deformations

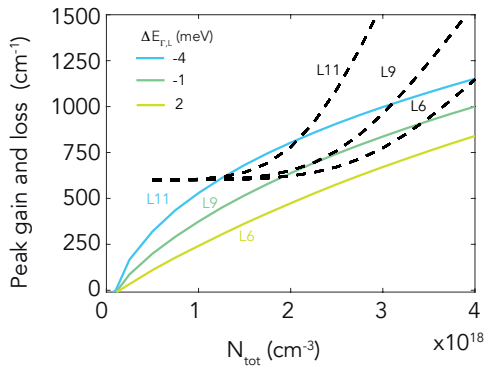


Figure 5.22: In color, peak gain as a function of the total carrier density up to $4 \cdot 10^{18} \text{ cm}^{-3}$ for the energy difference $\Delta E_{\Gamma,L}$ of L6, L9 and L11. In black dashed line the loss, composed by the cavity loss and the parasitic intervalence band absorption. The latter is extracted from Fig. 5.18(a) for temperature of 50 K.

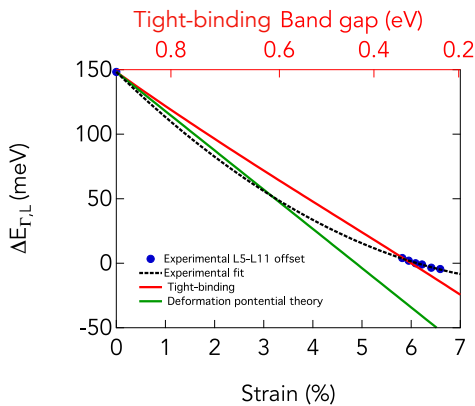


Figure 5.23: Energy difference $\Delta E_{\Gamma,L}$ as a function of uniaxial strain at 20 K. In red and green the prediction from the tight binding and deformation potential theory, while in blue dots the experimental points extracted from Fig. 5.21. The black dashed line fits quadratically the experimental points with the known value for relaxed Ge. The upper axis converts via the tight-binding model the strain in the Γ -VB1 transition energy.

up to 1% of strain. On the contrary, the tight-binding formalism takes into account possible anharmonic effects and it is designed to observe how the crystal lattice modifies at high strain. The observation that the deformation potential theory prediction for the L valley at low strain is not included within the tight-binding framework represents a point to be further investigated. In the next section the deviation between the experimental results and the theoretical prediction is discussed.

5.10 Discussion: energy difference $\Delta E_{\Gamma,L}$

In the following the discussion about the deviation of the experimental energy difference $\Delta E_{\Gamma,L}$ from the tight-binding prediction is about (i) possible uncertainties of the tight-binding model at high strain, (ii) material related carrier lifetime reduction and (iii) strain enhancement induced deviations.

(i) The position of the atoms in the unit cell upon strain represents the basic input for the tight-binding framework and thus it is computed via the semi-empirical Keating's valence force field [149]. The latter models the forces between nearest neighbors when an atom is displaced from its original set of coordinates and then calculates the new relative positions of the atoms composing the crystal. By considering the interatomic interaction upon strain deformation, the tight-binding framework reproduces on average the overall band structure.

The previously observed discrepancy may then originate from possible high order anharmonic effects at high strain that are not foreseen in the current Keating's model, which indeed was never tested for uniaxial strain larger than 6% like in this experiment. Similarly, variation of the Poisson's ratio at high strain may be responsible of non linearities. Experimental verification in strained germanium microbridges showed that the Poisson's ratio is constant, but up to uniaxial loading of only 3.5% [150], thus requiring further experimental verification at higher strain.

(ii) Material related parameter like the charge carrier lifetime needs to be considered as well. Auger non radiative recombination is indeed expected to become increasingly important at high strain due to the reduction of the band gap energy and of the effective masses [151–153]. The Auger coefficient was experimentally determined as $\gamma = 5.0 \cdot 10^{-31} \text{ cm}^{-6} \text{ s}^{-1}$ [123, 154] at room temperature for relaxed germanium and it is expected to be dominated by indirect transitions at high strain as well.

Fig. 5.24 compares the light-in light-out curves of the samples from L5 to L11. At high power the L10 and L11 photoluminescence suffer of intensity saturation, which may be an indication of additional non radiative recombination. However, in L5 and L6 cavities the PL saturation occurs at the same power, thus excluding band gap energy dependent Auger

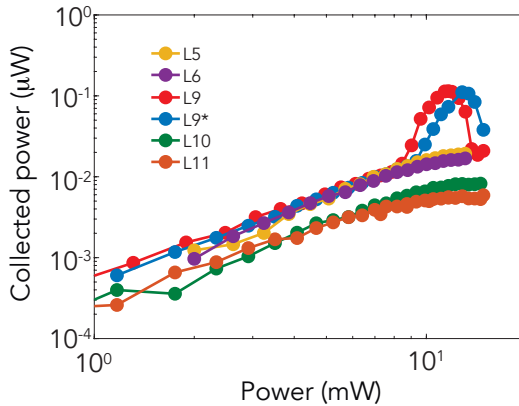


Figure 5.24: Collected power as a function of the excitation for the lasing samples L9* and L9 and the non lasing samples L5, L6, L10 and L11 at 15 K

recombination. We attribute the saturation of the photoluminescence to the hole filling of the top valence band.

In Fig. 5.24 no substantial increase of the photoluminescence is observed from strain higher than L5, although the reduction of $\Delta E_{\Gamma,L}$. Moreover, L10 and L11 photoluminescence reduces of by a factor 3 with respect to L9. An increasing deterioration of the material due to strain and the related reduction of the carrier lifetime may explain the gain deviation respect to the tight-binding prediction.

(iii) Shear strain can affect the L valley and thus the $\Delta E_{\Gamma,L}$. Lithographical misalignment of the microbridge respect to the crystal orientation may introduce shear strain in the samples. An upper bound of the latter is estimated as 1° . Anyhow, the fact that samples from L9* to L11 belong to the same processing batch makes the lithographical step unlikely to explain the experimental observations. However, the parallel occurrence of the reduced strain and the slower reduction of the energy difference between the Γ and L minima may indicate that the two effects are related. The out of plane bending of the beam, whom example we showed in Fig. 5.3, can alter the strain and may introduce shear strain. This effect seems deterministically bound to the geometry of the cavity and the pads. Further studies with modified cavity geometries may help to understand this effect. Moreover, the microbridges strain could be directly determined by low temperature Raman measurement.

5.11 Discussion: steady state lasing

In light of the findings of this chapter, we want to discuss the meaning of steady state lasing upon continuous wave excitation. On the same line of the first findings in III-V alloys [155], steady state lasing at low temperature is evidentially found whenever conditions of (i) gain and (ii) good optical cavity and (iii) good material are found together. The main hurdles to unlock lasing upon continuous wave pumping in strained germanium were (i) reducing the energy difference $\Delta E_{\Gamma,L}$ and (ii) the integration of the active material in a sufficiently good optical cavity.

(i) is usually reported in literature to takes place at 4.7% at low temperature. The crossing to the direct band gap configuration was claimed to occur between 4 and 4.5% and at 1.67% for the uniaxial [154] and biaxial loading [89], respectively. However, in the former case the analysis is based on temperature dependent photoluminescence intensity, which evidentially is subjected to larger uncertainties compared to a study based on the gain emergence. In [89] the measured biaxial strain is only related to the model.

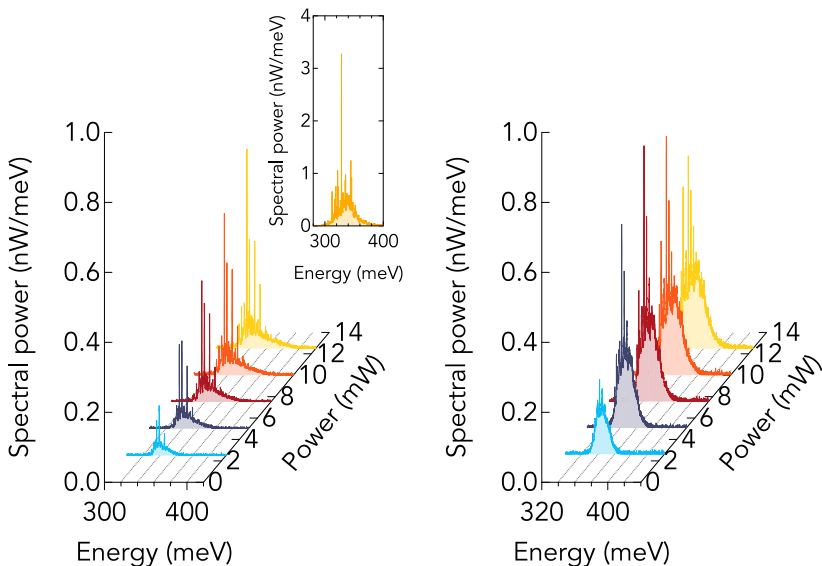
While (ii) was improved via optimization of the processing, (iii) is related to the high quality of the GeOI layer, as measured by the long carrier lifetime of 5 ns [142, 154]. On the contrary, the traditional ability of GeSn platforms to reach negative energy difference between the Γ and L band edges by tuning the Sn content is compensated by crystalline degradation. Indeed, the recent demonstration of GeSn lasing upon continuous wave excitation at low temperature [75] is understood as the results of the material quality improvement. In the following we give a comparison between the strained germanium laser results and [75].

The GeSn micro disk results [75] aligns well with the results of this chapter, showing all the typical fingerprints of gain emergence, like mode competition and threshold in intensity. The reported threshold value of 1.1 kW/cm^2 is about one order of magnitude lower then L9 threshold of $P_{th}(L9) = 8.1 \text{ mW}$, i.e., 9.35 kW/cm^2 . This difference stems from the reported energy difference between the Γ and L band edges of -70 meV, which, as previously understood, strained germanium is far from reaching. However, by assuming no strain induced degradation of the carrier lifetime, the gain modeling of Fig. 5.13 foresees a threshold as low as 1.1 kW/cm^2 already at $\Delta E_{\Gamma,L} = -10 \text{ meV}$.

Despite the energy difference between the Γ and L band edges is -70 meV, the highest operational temperature of about 45 K in [75] is similar to the previously shown limit of 30 K in strained germanium. As the lasing oscillates at about 500 meV, the maximal temperature seems to be limited by the heating, due to the material and the cavity. Finally, [75] shows a continuous narrowing of the lasing linewidth above threshold, in accordance with the standard linewidth theory upon steady state condition [143, 144]. Detailed comparison of the linewidth is given in section 5.13.

5.12 N-doping

The model of section 3.3.3 predicts that doping concentration of about $5 \cdot 10^{18} \text{ cm}^{-3}$ will enhance the gain to 600 cm^{-1} already for energy difference between Γ and L of about $\Delta E_{\Gamma,L} = 20 \text{ meV}$. Here, we present a first investigation of the photoluminescence response of strained germanium cavities processed from in-situ phosphorus doped GeOI. The samples are fabricated at CEA-LETI, Grenoble (France). The investigated doping levels are $N_d = 1.8 \cdot 10^{18} \text{ cm}^{-3}$ and $N_d = 6.3 \cdot 10^{18} \text{ cm}^{-3}$, as measured by secondary ion mass spectroscopy (SIMS) measurement at CEA-LETI.



- (a) Power dependence upon continuous wave excitation at 15 K of strained germanium cavity with $N_d = 1.8 \cdot 10^{18} \text{ cm}^{-3}$. In inset, spectrum of the undoped L6 sample at 15 K, excited in continuous wave excitation with $P = 12.48 \text{ mW}$.
- (b) Power dependence upon continuous wave excitation at 15 K of strained germanium cavity with $N_d = 6.3 \cdot 10^{18} \text{ cm}^{-3}$.

Figure 5.25: Comparison of the photoluminescence response of two cavities differently strained and n-doped. The inset of (a) compare the results with the undoped L6 sample.

Fig. 5.25(a) and 5.25(b) show power dependent photoluminescence spectra at 20 K of strained germanium cavities doped with $N_d = 1.8 \cdot 10^{18} \text{ cm}^{-3}$ and $N_d = 6.3 \cdot 10^{18} \text{ cm}^{-3}$, respectively, upon steady state excitation of 590 meV. The samples are labeled as low doped (LD) and high doped (HD). Both cavities are processed with the microbridge geometry of $8 \mu\text{m} \times 1 \mu\text{m}$ and pads width and length of 80 and $320 \mu\text{m}$, respectively. This is the same geometry as the former undoped L7 sample.

From the previous experiment with the undoped material, we expect the photoluminescence onset at about 300 meV. However, the observed emission onsets are considerably higher, i.e., 325 meV and 350 meV for the low and high doped samples, respectively. The samples compare more to the undoped samples of L5 and L6. This discrepancy is not fully understood yet and the investigation lacks of samples' Raman measurement at room temperature. The most straightforward explanation is a reduced pre-strain. However, Raman measurements at room temperature of the residual biaxial pre-strain ϵ_0 of the n-doped GeOI layer showed within the experimental resolution the expected shift. Doping may be responsible of a marginal modification of the Raman frequency. Further calibration of the residual strain should be addressed via high resolution X-ray diffraction.

Fig. 5.25(a) exhibits a broad photoluminescence background modulated already at low power by the cavity modes. The latter's robust amplification for power values below $P < 5 \text{ mW}$ is in contrast with the photoluminescence observed in the undoped L6 sample, as reported in Fig. 5.9(a), whose photoluminescence starts at about 300 meV. To qualitatively compare the doped and undoped sample, we consider the ratio between the mode intensities and the spontaneous emission background. We observe a ratio equal to 1 for excitation power between 8 and 10 mW in the undoped L6 samples (c.f. Fig. 5.9(a)), and already between 2 and 5 mW for the doped samples.

Despite the initially fast mode enhancement, the modes stay uniformly amplified up to the maximum excitation power. In contrast, the inset of Fig. 5.25(a) shows the trace of mode competition in the undoped L6 sample. Here, no lasing threshold is observed. Instead, as can be seen from the LL curve of Fig. 5.26, the PL efficiency decreases starting from the excitation power of $P = 3.75 \text{ mW}$. Gain signatures can be quantified in Fig. 5.27(a), reporting the linewidth as a function of the excitation power.

At the lowest accessible power, we measure the linewidth as narrow as about 0.30 meV, below the expected transparency value of $\Delta E = 0.45 \text{ meV}$. The most amplified cavity mode at 336 meV narrows down to below 0.2 meV. Saturation of the linewidth narrowing occurs from power of about $P = 3.0 \text{ mW}$. The larger linewidth of the mode at 339 meV, which narrows similarly to cavity mode at 336 meV, is likely due to the presence of an additional non resolvable side mode.

We analyze the differential gain using the same procedure as above and the same conversion factor that relates the excitation power to the carrier density of equation 5.1. For the low doped sample we obtain a differential gain is $dg/dN = 5.12 \cdot 10^{-16} \text{ cm}^2$, which is 1.7 and 2.5 times larger than the differential gain measured for the undoped L6 and L5 samples.

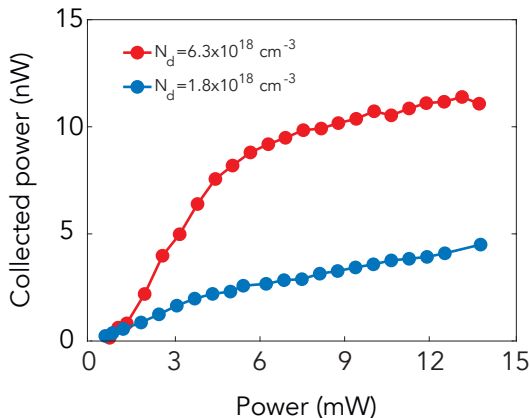
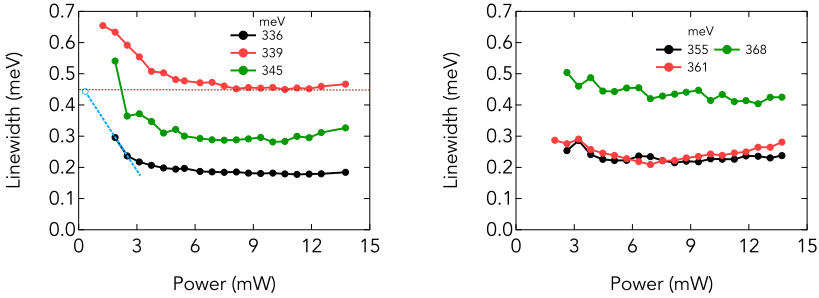


Figure 5.26: Collected power as a function of the continuous wave excitation for the doped cavities $N_d = 1.8 \cdot 10^{18} \text{ cm}^{-3}$ and $N_d = 6.3 \cdot 10^{18} \text{ cm}^{-3}$, in blue and red, respectively.

This value is consistent with our model for the low doped case and an energy difference $\Delta E_{\Gamma,L}$ as L5. Uncertainties may derive from an underestimation of the state lifetime broadening, which we left for simplicity to the previously used value of $\Gamma_{lor} = 4 \text{ meV}$, and from the excitation power conversion to carrier density.

Interestingly, we find that for the HD cavity of Fig. 5.25(b) the photoluminescence efficiency substantially increases compared to the LD sample. This can be understood from an increased quasi-Fermi level μ_c , as previously foreseen by the carrier statistic modeling (c.f. Fig. 3.2(c)). We also measure at the lowest power a linewidth already below 0.3 meV. However, the excitation increase is not followed by the linewidth narrowing, indicating that saturation of the gain build-up occurs earlier than the LD case and that this is related to the amount of doping. Considering that the linewidth develops from the transparency level of $\Delta E = 0.45 \text{ meV}$, this suggest that the differential gain at low power is even stronger compared to the LD case. Both doped sample seem far from reaching the lasing threshold.

Overall, this first and yet incomplete experiment indicates a high optical quality of the in-situ n-doped GeOI and a good photoluminescence efficiency at low temperature. However, at this point we can already conclude that the concept of n-doping to achieve lasing is not as



- (a) Linewidth as a function of continuous wave excitation at 15 K of strained germanium cavity with $N_d = 1.8 \cdot 10^{18} \text{ cm}^{-3}$. The linear fit represents the differential gain, as shown for the undoped samples' analysis.
- (b) Linewidth as a function of continuous wave excitation at 15 K of strained germanium cavity with $N_d = 6.3 \cdot 10^{18} \text{ cm}^{-3}$.

Figure 5.27: Comparison of the linewidth dependence on the excitation power of the two differently n-doped cavities.

straightforward as initially predicted [62,63]. The linewidth analysis shows that transparency is reached rapidly and that the differential gain seems to increase with doping. However, the gain development is restricted to low power. In contrast to the undoped case, the linewidth narrowing quickly saturates and the cavity modes are uniformly amplified at high power, without clear trace of mode competition. Evidentially, despite the low temperature, the gain does not build up sufficiently to reach the threshold.

The lack of gain may be related to the reduction of the carrier lifetime, limiting the steady state excess carrier density, as previously observed [156]. The latter seems to be correlated to the doping density, thus requiring more attention for the approaches aiming to doping concentration higher than 10^{19} cm^{-3} [86, 95, 157]. The HD sample experiment shows an overall deterioration of the doping effect on gain, which further questions the high doping approach. Future experiments should address the reduction of state and carrier lifetimes, doping effects on the strain and possible reduction of the photoluminescence onset due to an impurity induced band tail.

However, the promising results of the sample doped with $N_d = 1.8 \cdot 10^{18} \text{ cm}^{-3}$ indicates, for future studies, to focus on moderate doping in the range of $N_d = 1 \cdot 10^{18} \text{ cm}^{-3}$. A threshold at low power in the strain range of about 6% could be obtained. Such a system may safely operate the laser away from intervalence band absorption and increase the operational temperature.

5.13 Laser linewidth analysis

The linewidth is one of the most important laser properties as it measures the light coherence and the spectral purity of the device. Traditional single frequency semiconductor diode lasers exhibit a linewidth typically ranging from 100 MHz down to 1 MHz, which can be further reduced by many orders of magnitude by employing an external cavity [158–160], while fiber lasers integrated in fiber Bragg reflectors show linewidth of the order of 1 kHz [161].

To describe the evolution of a single mode laser linewidth above threshold we refer to the work of C. Henry [144], which nowadays represents the standard theory of reference. However, a similar formulation was first developed by A. Schawlow and C. Townes [143] in 1958, hence the name. Following [144], the linewidth dependence on the output power per round trip P_{out} is the following:

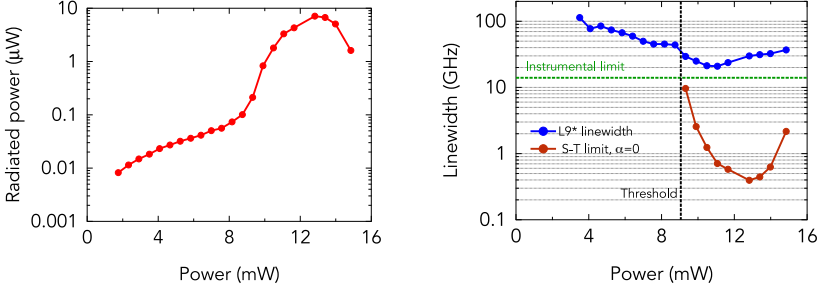
$$\Delta\nu = \frac{v_g^2 h\nu g n_{pi} \alpha_c}{4\pi P_{out}} (1 + \alpha^2) \quad (5.5)$$

where v_g is the group velocity, $h\nu$ is the photon energy, g indicates the gain, expressed as $g = \alpha_c + \alpha_{loss}$, where α_c and α_{loss} are the cavity and material loss, respectively. n_{pi} indicates the population inversion factor, which is described in A.7. The latter quantity is originally referred to as the spontaneous emission factor n_{sp} . However, in order to not create confusion with the parameter β , also commonly referred to as spontaneous emission factor in laser physics, we choose the convention of n_{pi} instead. α (c.f. section A.6), known as the Henry's factor, accounts for the coupling between the intensity and the phase noise. We address the reader to section A.6 for a more detailed exposition of the Schawlow-Townes linewidth theory.

The main feature of the Schawlow-Townes (S-T) equation 5.5 is the linear dependence on the inverse of the output power per round trip P_{out} : above threshold, gain clamping fixes the amount of carrier density to N_{th} , thus stabilizing the spontaneous emission events, and any increment of the input power is converted into a higher lasing field intensity I , reducing the random drift of the phase. We note that equation 5.5 predicts an infinitely narrow linewidth for infinitely high output power.

5.13.1 Linewidth measurements

The power radiated from the L9* lasing mode increases of about two orders of magnitude above threshold, as reported in Fig. 5.28(a) and the Schawlow-Townes theory predicts thus a strong narrowing of the linewidth. Fig.5.28(b) compares in logarithmic scale the experimental observation to the quantum limit's prediction for the ideal case of $\alpha=0$. The L9*



- (a) At threshold power of 9.30 mW the radiated power increases of about two order of magnitude. The power radiated from the lasing field is calculated following the calibration described in section 3.4.4.
- (b) Schawlow-Townes quantum limit with $\alpha = 0$ in red, calculated via equation 5.5, compared to the non apodized experimental linewidth in blue in function of the excitation power. The instrumental resolution of 15 GHz is highlighted in green.

Figure 5.28: (a) Power radiated from the L9* lasing field oscillating at 311 meV at 15 K as a function of the excitation power. (b) Comparison between the experimental non apodized linewidth of the L9* lasing mode oscillating at 311 meV and the theoretical quantum limit based on the radiated power of (a).

linewidth is more than one order of magnitude larger than the ideal case, before broadening occurs. In this analysis the experimental linewidth is non apodized and it is reported in unit of GHz to align to the literature. The calculation of the quantum limit is based on the power radiated from the lasing mode of Fig.5.28(a) and by considering the increasing parasitic loss with excitation power, as previously discussed. In particular, the following values are used: $\nu_g^2 = 4.41 \cdot 10^{19} \text{ cm}^2/\text{s}^2$, the energy of the photon is $h\nu = 0.311 \text{ eV}$, the gain at threshold is $g = (102 + 11) \text{ cm}^{-1}$, while $n_{pi} = 1$, as described in A.7.

Fig. 5.29 reports in linear scale the linewidth above threshold up to the broadening onset as a function of the reciprocal radiated power per round trip of Fig. 5.28(a). The linewidth narrows linearly, but it is strongly limited by a power-independent contribution. Indeed the value extrapolated for $P_{out}^{-1} = 0$ is not zero, as predicted by the standard equation 5.5, but has a finite value $\Delta\nu_0$ of about 21 GHz, such that the linewidth can be described as:

$$\Delta\nu = \Delta\nu_{S-T}(P_{out}^{-1}) + \Delta\nu_0 \quad (5.6)$$

where $\Delta\nu_{S-T}$ refers the power dependent Schawlow-Townes contribution. By subtracting the power-independent term $\Delta\nu_0$, the slope of the linewidth narrowing nicely matches the

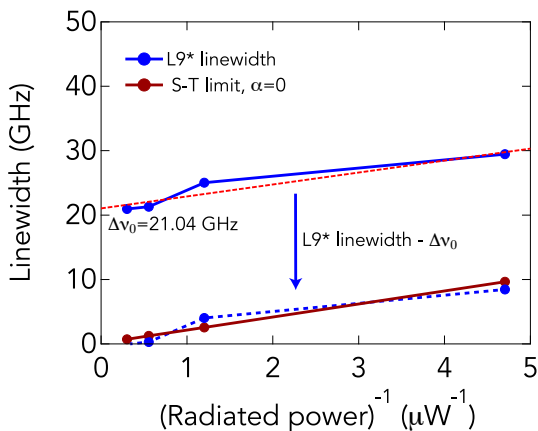


Figure 5.29: L9* linewidth measured at 15 K as a function of the reciprocal radiated power above threshold before broadening onset, compared to the ideal quantum limit with $\alpha=0$. The red dashed line is the linear function fitting the experimental narrowing, while the blue dashed line indicates the experimental results after the subtraction of the power-independent term $\Delta\nu_0$.

Schawlow-Townes prediction for the case of $\alpha=0$. This indicates that the energy at which the laser operates corresponds to the peak of the differential gain (c.f. section A.6). As detailed in A.7, the L valley acts as a clamper of the quasi-Fermi level μ_c , allowing the peak of the gain spectrum to be approximately in correspondence with the differential gain peak. This feature does not usually hold for traditional III-V systems, where the peaks of the gain spectrum and the differential gain are shifted apart [162, 163].

In the following, we address the mechanism leading to the access linewidth term. While different experiments validated the standard Schawlow-Townes theory [164–166], it was often observed that the linewidth of semiconductor lasers is limited by a power-independent contribution $\Delta\nu_0$ [167–173], further justifying equation 5.6. The origin of the power-independent contribution is still debated and it is often attributed to noise which adds on top of the quantum one, like $1/f$ noise [174, 175] or occupation fluctuation noise [176]. However, in the previously cited cases the linewidth saturates at values $\Delta\nu_0$ in the range of 1–10 MHz, orders of magnitude lower than our observation. Further details about these fundamental deviations are given in A.9. In section A.8 we address, and neglect, other possible power-independent sources, like the thermal noise and the evanescent light mode

coupling to the substrate.

To understand the possible origin of the large power-independent term $\Delta\nu_0$ of Fig. 5.29 we recall that the strained germanium laser actually deviates from the basic assumption of the standard linewidth theory [144], i.e., gain clamping. The latter fixes the carriers in Γ , suppressing the injection-recombination shot noise. However, when the strained germanium laser operates in steady state condition, most carriers still populate the L valley (c.f. Fig. 3.2(a)) and are not clamped. The noise due to the carrier density fluctuation in L may lead to a variation of the refractive index and to an additional broadening of the linewidth. This effect was identified first in wavelength-tunable laser diodes [177, 178]. In such devices, the excess linewidth is expressed as follows [178]:

$$\Delta\nu_0 = \frac{q I_t}{\pi} \left(\frac{\Delta\omega_e \tau}{q} \right)^2 \quad (5.7)$$

and it is estimated to be tens of MHz. I_t expresses the tuning current, $\Delta\omega_e$ is the change per carrier of the lasing angular frequency, while τ is the electron lifetime. We apply equation 5.7 to the strained germanium laser case, by expressing I_t as $q P_{abs}/E_{ph}$, where P_{abs} is the amount of power absorbed by the microbridge and E_{ph} is the excitation energy of 0.59 eV:

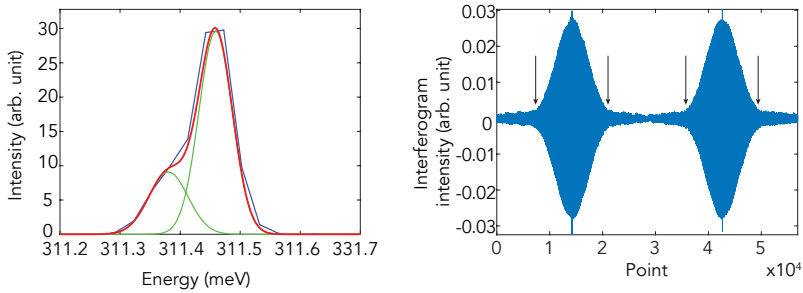
$$\Delta\nu_0 = \frac{P_{abs}}{E_{ph}} \frac{1}{\pi} (\Delta\omega_e \tau)^2 \quad (5.8)$$

By recalling equation 5.1, at the excitation power at threshold of 9.3 mW the power fraction absorbed is $P_{abs} = 9.3 \text{ mW} \cdot \mathcal{O}_\Sigma \cdot Abs = 0.37 \text{ mW}$. As the change of angular frequency is related to the change of refractive index via the relation $\Delta\omega/\omega = \Delta n/n$, we can express the change per carrier as:

$$\Delta\omega_e = \frac{\omega}{n_g} \frac{\Delta n_g}{N V} = \frac{\omega}{n_g} \frac{q^2 \mu_0 \hbar^2 c^2}{2 n_g (\hbar\omega)^2 m_0 \mu_{plasma}} \frac{1}{V} = 2.55 \cdot 10^5 \frac{\text{rad}}{\text{s}} \quad (5.9)$$

where N is the carrier density, μ_0 is the vacuum permeability, n_g is the unperturbed material group refractive index of 4.5, $\hbar\omega$ is the photon energy of 0.311 eV, the volume of the microbridge V is $8 \cdot 10^{-12} \text{ cm}^3$, and μ_{plasma} is the plasma mass. For germanium $\mu_{plasma} = 0.08 m_0$, derived from the effective mass of conductivity of the conduction and valence bands. The right hand side of equation 5.9 is obtained from the free carriers plasma contribution to the change of the real part of the refractive index [141]. Finally, we use a carrier lifetime of 5 ns, as inferred from pump and probe measurements in relaxed GeOI platform at room temperature [142]. At low temperature, such lifetime value may represent a lower bound.

By inserting equation 5.9 into equation 5.8 and converting the excitation energy in unit of Joule, we find a preliminary linewidth broadening due to the carrier fluctuation noise of about $\Delta\nu_0 = 2.0 \text{ GHz}$. Although one order of magnitude lower than our observation, the previous



- (a) In blue the non apodized L9* lasing spectrum upon $P = 11.07$ mW at 15 K. The fitting function in red is composed of a sum of two Voigt functions. (b) Interferogram of the L9* lasing emission upon $P = 12.82$ mW at 15 K.

Figure 5.30: (a) The non apodized spectrum allows to better resolve the lasing emission of the L9* cavity, identifying two modes. (b) The presence of two modes can be understood from the non uniform decaying of the interferogram envelope.

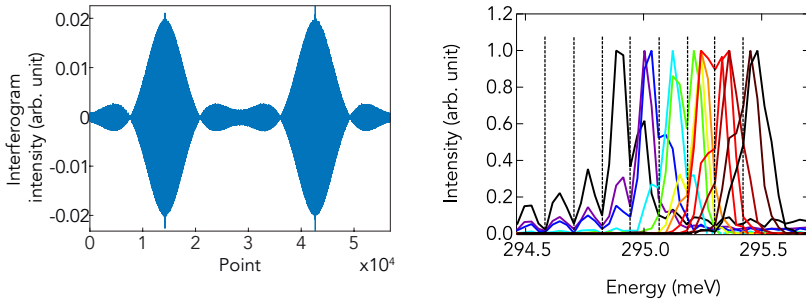
analysis indicates how the peculiar band alignment of the strained germanium severely affects the physics of the laser. The discrepancy with our observation may be attributed to the deviation from the single mode assumption of the standard Schawlow-Townes theory.

In the following, we show that L9* strained germanium laser is not an ideal single mode laser, but it is actually composed by two cavity modes separated by about 0.08 meV. Fig.5.30(a) shows the L9* non apodized lasing spectrum upon excitation power of $P = 11.07$ mW at 15 K, which allows to resolve the two modes composing the lasing emission. The fitting function suggests the presence of two modes separated by about 0.08 meV: the main one positioned at 311.45 meV and the side one less amplified at 311.38 meV.

The presence of two modes is supported by the interferogram, as shown in Fig. 5.30(b). The non uniform decaying as a function of the retardation of the interferometer arms with respect to each other suggests that the envelope function is determined by the beating of two frequencies of different intensity. By supposing that the retardation at which the envelope changes its decaying slope, as indicated by the arrows, corresponds to the first beating, we can extract the separation of the two frequencies from the following relation:

$$\cos(2\pi \nu_{1-2} \delta) = 0 \quad (5.10)$$

where $\nu_{1-2} = (\nu_1 - \nu_2)/2$ is the beating frequency. The retardation is $\delta = 0.57$ cm. The latter



(a) L9 interferogram upon $P = 10.78$ mW at 15 K. (b) Non apodized L9 lasing spectra at 15 K.

Figure 5.31: (a) the interferogram of L9 lasing emission reveals the presence of beating modes, (b) which are due equally spaced CO_2 absorption lines, as indicated by the black dashed lines.

is extracted considering that the instrument resolution is 0.5 cm^{-1} (0.062 meV) and the maximum delay is 1.207 cm [179]. From equation 5.10 we understand that the separation between the two frequencies is equal to $\nu_1 - \nu_2 = 0.87 \text{ cm}^{-1}$. The latter corresponds to $\nu_1 - \nu_2 = 0.10 \text{ meV}$, and well agrees with Fig. 5.30(a). The beating node at retardation of $\delta = 0.57 \text{ cm}$ is expected to be followed by a local maximum at $\delta = 1.14 \text{ cm}$, which, however, can not be resolved due to the finite modes linewidth, far from being instrumental limited.

For non ideal single mode or multimode lasers the power-independent contribution to the linewidth can reach values well above the GHz, strongly limiting the laser linewidth narrowing above threshold. Such deviation from the standard theory stems from the fact that the Schawlow-Townes model is developed by considering an ideal single lasing mode: it was qualitatively shown [180] that by considering two lasing modes, the linewidth of the first mode is limited by the intensity of the second one and by non linear coupling parameters. Such qualitative observations finds further support in studies analyzing the role played by mode partition noise and non linear gain in broadening the laser linewidth [181–183]. Mode partition noise is highly enhanced when the side mode intensity increases, taking over the main emitting mode. This competition phenomenon is here observed in L9* lasing and corresponds to the linewidth broadening onset starting at 11.65 mW , which does not correspond to the total intensity roll over at 12.82 mW .

Question raises whether the presence of the side lasing mode is an arbitrary condition

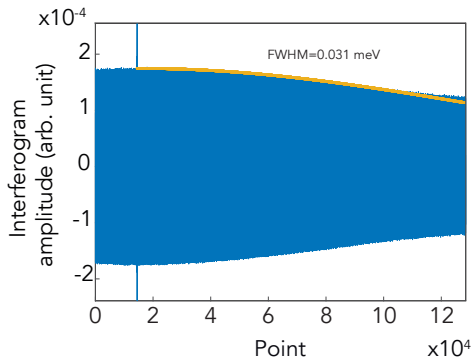


Figure 5.32: Interferogram of the GeSn microdisk continuous wave laser [75]. The yellow line represents the gaussian fit used to extract the non apodized linewidth. The analysis and the reproduction of the data are authorized by Moustafa El Khurdi of the Center for Nanoscience and Nanotechnology, Université Paris Sud (France).

affecting only L9*, due to the multimode character of strained germanium laser, or a fundamental phenomenon related to the material or the cavity itself. In the following the linewidth of L9 laser is then discussed. Fig. 5.31(a) shows the interferogram upon $P = 10.78$ mW at 15 K of L9 emission. Similarly to what previously observed for L9*, the interferogram envelope is not uniformly decaying, but rather it is strongly modulated by the beating of two frequencies with the same intensity.

However, the modes leading to such interferogram are artifact due to CO₂ absorption line, as we can observe from Fig. 5.31(b), where the non apodized L9 lasing spectra as a function of power are shown normalized. The absorption lines are equally spaced by 0.12 meV and affect the spectra up to an energy of 295.5 meV, altering the precision of the laser linewidth measurement above threshold. Notably, a possible narrowing of the linewidth down to the previously calculated intrinsic limit of 2.0 GHz, i.e., 0.008 meV, should not be hindered by the absorption lines, whose separation of 0.12 meV is more than order of magnitude larger. However, the lack of the L9 linewidth narrowing does not represent alone a conclusive proof in favor of a linewidth limitation intrinsic to the cavity. Further lasing experiments should be then carried out at different energies.

We now want to compare the results of similar lasing platform. Fig.5.32 shows the high resolution interferogram of the continuous wave GeSn laser upon excitation of $P = 2.09$ mW [75]: the linewidth results to be instrumental limited and if any beating phenomenon was present, the separation between the main and the possible side mode would be $\nu_1 - \nu_2 < 0.025$

meV. The latter value is extracted from the instrumental resolution of 0.031 meV. From the interferogram's envelope we can extract via gaussian fitting a non apodized linewidth of $\Delta\nu = 0.031$ meV (7.5 GHz), i.e., about 3 times smaller than the L9* linewidth. The latter value shows that material similar to strained germanium but in a microdisk cavity exhibits linewidth narrowing upon steady state excitation. This may suggest that the L9* linewidth may be limited, on top of the L valley's carriers noise, by the multimode nature of the cavity. While the cornercube cavity requires the non negligible amount of 600 cm^{-1} to operate, the optical loss, and thus the threshold gain, may be orders of magnitude lower in a microdisk cavity.

5.14 Summary

This chapter presented the first steady state lasing in strained germanium upon continuous wave excitation. The steady state lasing achievement demonstrates the straining approach's feasibility and, supported by the gain and loss models, represents a unique tool to understand fundamental physics underlying the strained germanium platform.

Explicit lasing action in samples strained at about 6.1 and 6.2 % is observed via threshold in intensity, sustained by single cavity mode increasing orders of magnitude above the background, mode competition, and gain clamping. Threshold power reduces with the strain down to 8.1 mW ,i.e., $2 \cdot 10^{18} \text{ cm}^{-3}$. We find that lasing is confined at low temperature, up to 30 K. The emergence of gain is a balance between gain and low loss, as understood from lack of lasing action in (i) high quality samples strained lower than 6.1 % and (ii) in lossy cavity strained at 6.2%.

The energy difference $\Delta E_{\Gamma,L}$ between the Γ and L valleys is investigated first in the lasing sample. By identifying the modes running in transparency condition, we extract the cavity loss. We found a value averaged over the cavity length of about 102.6 cm^{-1} . This figure derives from the improvement of the fabrication. We estimate a threshold gain of 600 cm^{-1} , which follows from the low filling factor of the active material. From the comparison with the gain model, we find that samples uniaxially strained at about 6.1 and 6.2 % have $\Delta E_{\Gamma,L}$ of 0 and -1 meV, respectively. Thus, the energy difference $\Delta E_{\Gamma,L}$ between the Γ and L band edges can be considered vanished between 6.1 and 6.2 % of strain.

However, cavities with strain larger than 6.2% and processed together with the previous lasing samples do not show any lasing action. Temperature dependent measurements indicate the resonant overlap with the upcoming intervalence band absorption, which hinders the threshold at low energy. Moreover, the non linearity on carrier density and temperature of the parasitic loss explains the roll over in lasing intensity at low temperature and lasing

efficiency's reduction with the temperature.

Moreover, by extending the linewidth analysis to the non lasing samples, we find that gain delivered at low power is lower than expected. The low amount of gain reveals that the energy difference between Γ and L reduces slower than predicted by the tight-binding model. At 6.6 % we observed a $\Delta E_{\Gamma,L} = -4.5$ meV, while the tight-binding model foresees an energy difference of -14 meV. The discrepancy is discussed in terms of non linear effects at high strain, not foreseen within the tight-binding framework, material degradation due to high strain affecting the carrier lifetime, and geometrical deformation modifying the L valley's position. The latter may be also responsible for the observed reduction of strain at low temperature and should be addressed with low temperature Raman investigations. However, independently from the origin of the energy difference $\Delta E_{\Gamma,L}$ deviation at high strain, steady state lasing with a low threshold and higher operational temperature could be achieved in a low loss cavity, like distributed feedback (DFB) cavity. This solution brings the additional advantage of a high filling factor.

The effect of moderate n-doping and high strain at low temperature was investigated. Cavity samples doped with $N_d = 1.8 \cdot 10^{18} \text{ cm}^{-3}$ and $N_d = 6.3 \cdot 10^{18} \text{ cm}^{-3}$ show only photoluminescence upon continuous wave excitation. Despite a differential gain at low power stronger by a factor of 2, the gain build-up quickly saturates. The n-doping approach is not as straightforward as initially predicted, and further studies need to address doping related effects on the carrier lifetime. Finally, we discussed the lasing mode's linewidth above threshold. The linewidth narrowing is limited by a power-independent contribution of 21 GHz (0.09 meV), in contrast to the prediction of the standard Schawlow-Townes theory. We found that the linewidth is fundamentally limited by the noise of the refractive index induced by the unclamped carriers populating the L valley.

6

Summary and conclusions

This doctoral work aimed at demonstrating the feasibility of the tensile strain approach to achieve lasing in germanium. The demonstration of lasing granted access to the study of gain and loss, addressing not yet explored fundamental physical quantities, such as the conduction bands' alignment and the intervalence band absorption. This work indicated also the hurdles to tackle for future generations of Ge-based light sources. These findings will help the ongoing development towards an efficient all-group-IV laser operating at room temperature.

The tight-binding model predicts germanium's cross-over to a direct band gap to occur at low temperature at about 6 % of strain uniaxially loaded along one of the equivalent directions $\langle 100 \rangle$. The prediction of the direct transition Γ -VB1 dependence on strain is well supported by the experiments up to about 4 %. However, the L-VB1 transition, equally fundamental for the germanium's optical radiative properties, was not backed up by any experiments.

To induce routinely such high strain, we adopted the strain amplification technology developed at PSI before this thesis. The so fabricated Ge microbridges integrated into an optical cavity formed by two cornercube mirrors access the required strain range at low temperature. The processing was improved, yielding a reduced cavity sidewall roughness. This improvement proved essential to achieving the lasing in steady state condition.

We developed a gain and loss analysis based on the cavity modes' quality factor. Absorption calculations at low temperature as a function of the energy difference between the Γ and L band edges, i.e., $\Delta E_{\Gamma,L} = E_{\Gamma} - E_L$, show that gain is very sensitive to $\Delta E_{\Gamma,L}$. Optical gain is thus an efficient tool to probe the conduction bands' alignment. Central to our analysis is the accurate determination of transparency, i.e., zero material loss. We showed that this condition is obtained for modes running at higher energies than the gain band. The build-up of transparency, as we showed, is a typical feature of marginally direct group-IV semiconductors and it offers an elegant method to experimentally separate the transparency

and the gain contributions to the light absorption.

We indicated that n-doping might relax the requirement of $\Delta E_{\Gamma,L} \sim 0$ meV to achieve optical gain. However, our simple model did not consider carrier lifetime reduction nor lifetime broadening effects. The results shown in the experimental section of the thesis reveals that n-doping improves the gain only marginally and that the effects mentioned above cannot be neglected.

Finite element method modeling revealed mirror losses for the cornercube resonator equivalent to a Q factor of about 2000. Experimentally, Q factors close to 1500 are achieved. However, this value is restricted to cavities fabricated with the improved fabrication recipe and when the excitation laser energy is lower than the absorption edge of relaxed germanium.

Lasing is demonstrated upon optical pulsed excitation of 100 ps in cavities with strain from 5.4 up to 5.9 %, and up to a maximal temperature of 100 K. We showed the typical lasing fingerprints, consisting of mode competition and intensity threshold, benchmarked against the photoluminescence features. Our study of the excitation energy dependence reveals a remarkably high differential efficiency close to unity when approaching the resonant condition. We developed a non-equilibrium model to explain the lasing under pulsed excitation and the lack of lasing upon continuous wave excitation in similar conditions. This non-equilibrium is based on the lack of phonons that can be absorbed at low temperatures.

Cavities with strain above 6 % and reduced optical loss, unlock steady state lasing upon continuous wave excitation. This achievement shows that strain, and thus $\Delta E_{\Gamma,L}$, is the driving parameter for optical gain. We observed steady state lasing in cavities strained between 6.1 and 6.2 % and up to 30 K. The corresponding energy differences $\Delta E_{\Gamma,L}$, based on the threshold and our gain model, are $\Delta E_{\Gamma,L} = 0$ and $\Delta E_{\Gamma,L} = -1$ meV, respectively. Remarkably, samples strained up to about 6.6 % do not show lasing, due to the increasing overlap with the parasitic intervalence band absorption, as inferred by temperature dependent measurement. The differential gain analysis allows the understanding of the evolution of the Γ and L bands' alignment with the strain. We found that the energy difference $\Delta E_{\Gamma,L}$ closes slower than predicted by the tight-binding model.

In conclusion, this thesis showed that it is possible to get germanium to lase when the uniaxial tensile strain is high enough to approach $\Delta E_{\Gamma,L} = 0$ meV. Lasing in strained germanium is a powerful platform to access fundamental physical quantities and offers a reliable benchmark for the group-IV field. We proved that germanium turns into a direct band gap material at strain of about 6 % and unveiled the gain and loss build-up dependence on the uniaxial strain.

Open questions, like the carrier dynamic and the phonon blocking mechanism that enables lasing with high differential efficiency, require further comprehension. Moreover,

the discrepancy between the model and our experiment concerning the reduction of the energy difference between the Γ and L band edges requires further investigations of both theoretical and experimental nature. Not yet understood is the progressive strain deviation for very high strain. Mechanical deformations could reduce the strain and introduce shear strain, impacting the energy difference $\Delta E_{\Gamma,L}$ at low temperature.

The experimental methods presented in this thesis can be efficiently implemented to quantify the n-doping's impact on the lasing and further develop other platforms, such as the biaxially strained Ge and the GeSn, also combined with tensile strain.

A

Appendix

Contents

A.1 Absorption lines by air gases	134
A.2 CW beam spot at sample position	134
A.3 Confinement factor	136
A.4 Smoothing function to measure the PL background	137
A.5 Band gap determination	138
A.6 The Schawlow–Townes Linewidth	138
A.7 Population inversion factor	142
A.8 Linewidth technical noise sources	145
A.9 Fundamental linewidth deviations from S-T theory	147

A.1 Absorption lines by air gases

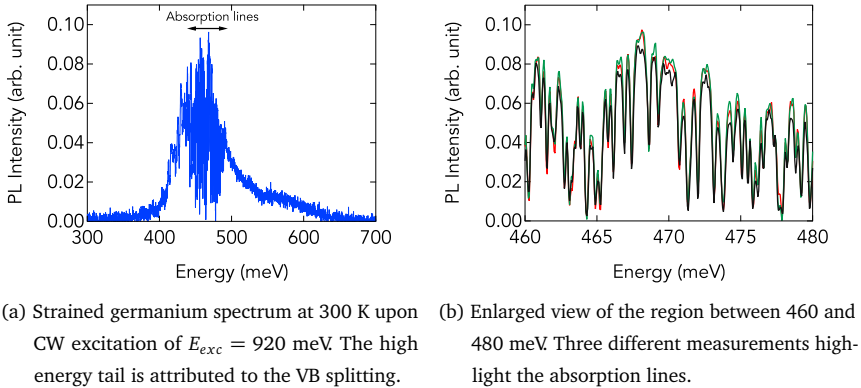


Figure A.1

Fig. A.1(a) reports the photoluminescence emission at room temperature of a strained germanium cavity. The measurement is carried out upon CW excitation running at 920 meV ($1.342 \mu\text{m}$) with resolution of 0.12 meV. The emission in the region between 440 and 490 meV is enlarged in Fig. A.1(b), where 3 different measurements exhibit the same modulation, which is attributed to air gases absorption lines in the infrared [184].

A.2 CW beam spot at sample position

The excitation power of the chapter 5 experiment is calibrated by measuring the beam spot size at the sample position. The employed continuous wave diode laser running at 590 meV is collimated by means of an aspherical and cylindrical lenses, and focused with a x15 Cassegrain microscope objective. The spot size is then determined by measuring the excitation intensity in function of the position of a covering razor blade which is scanned through at the sample position in step of $1 \mu\text{m}$, as shown in Fig. A.2(a) and A.2(b) along the x and y directions, respectively. From their first derivative, the intensity beam profile is obtained, along both horizontal and vertical directions, c.f. Fig. A.2(c) and A.2(d), whose $FWHM$ extracted from a gaussian fit are $8.77 \mu\text{m}$ and $8.65 \mu\text{m}$ in the horizontal and vertical directions, respectively. The excitation spot is then considered rather symmetric with a radial $FWHM$ of $8.7 \mu\text{m}$. The intensity profile of the gaussian beam can be then described as:

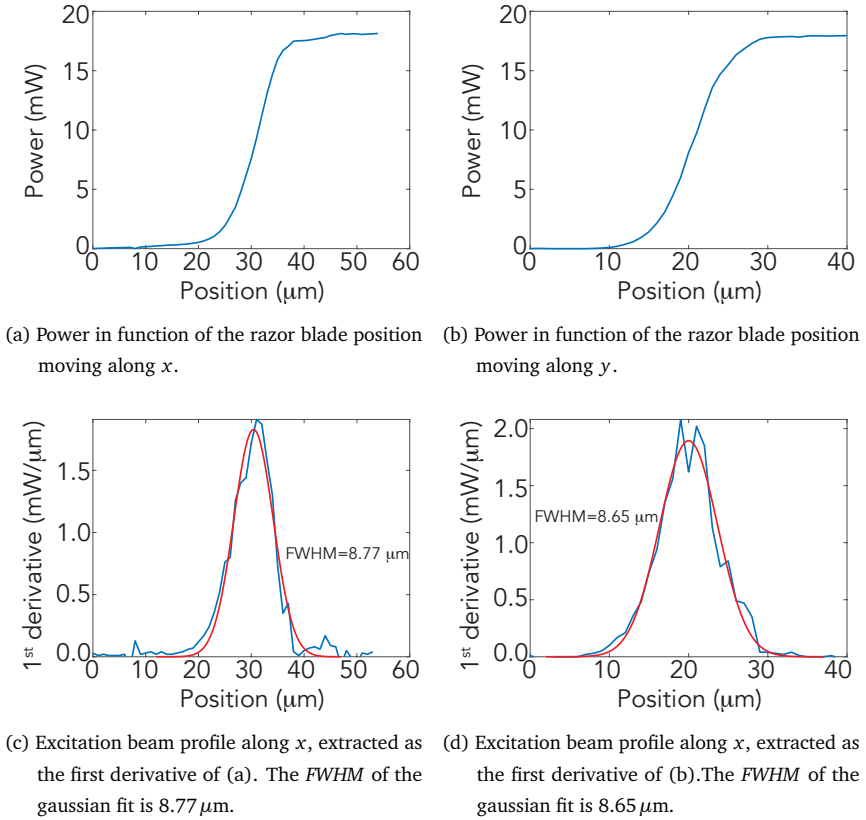


Figure A.2: Measurement of the CW excitation beam spot at the sample position.

$$I(r) = \frac{2P}{\pi w^2} e^{-2r^2/w^2} \quad (\text{A.1})$$

where P is the total power and w is the beam waist, corresponding to distance at which the intensity drops of a factor $1/e^2$. The beam waist is related to the measured $FWHM$ as $w = FWHM / \sqrt{2 \ln 2}$. Following the so called top-hat approximation [148], the gaussian spot is converted for convenience into a uniform cylindrical beam with the same peak intensity and the total power of the gaussian beam, with an effective diameter of $d_{TH} = \sqrt{2}w$ and area of $A_{TH} = \pi w^2/2$. In the experiment of chapter 5 the total measured excitation power at the sample position is then considered uniformly distributed within a spot of $d_{TH} = 10.45 \mu\text{m}$.

A.3 Confinement factor

The transverse confinement factor Γ_{xy} is the fraction of energy mode contained in the transverse section of the microbridge. It is defined as follows:

$$\Gamma_{xy} = \frac{\int_{-\frac{W}{2}}^{\frac{W}{2}} \int_{-\frac{T}{2}}^{\frac{T}{2}} |E_0(x,y)|^2 dx dy}{\int_x \int_y |E_0(x,y)|^2 dx dy} \quad (\text{A.2})$$

where W and T are the width and the thickness of the microbridge, respectively. From the simulation of figure A.3, the transverse confinement factor of the fundamental TE mode oscillating with a wavelength of $4 \mu\text{m}$ is $\Gamma_{xy}=0.94$, which, due to symmetry of the gain medium, is the same for light TM polarized. This close to unity number derives from the transversal dimensions of the gain medium of $1 \mu\text{m} \times 1 \mu\text{m}$ suspended in air, which allows to embody the entire fundamental mode and has evident advantages in terms of required material gain. To have a comparison with similar solutions proposed for the realisation of strained Ge laser Bao et al. [87] calculated a confinement factor of 0.45 for light propagating with wavelength of $\lambda=1530 \text{ nm}$ in a nanowire with transversal dimensions of $700 \text{ nm} \times 200 \text{ nm}$ over SiO_2 layer, which increases the required material gain already of factor 2.

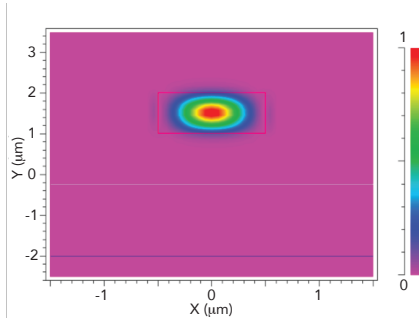


Figure A.3: Simulated spatial distribution of the Poynting vector magnitude of the fundamental TE mode with a wavelength of $4\ \mu\text{m}$ confined in a microbridge with thickness and width both equal to $1\ \mu\text{m}$. The simulations was carried by Vincent Reboud at CEA Grenoble, by means of 3D finite element method of the RSOFT Suite.

A.4 Smoothing function to measure the PL background

Fig. A.4 reports the spectral emission in logarithmic scale of sample L9 upon steady state excitation power of $9.61\ \text{mW}$. The red lines is a smoothing function which allows to approximate the background and thus evaluate its intensity with respect to the total intensity, which comprehends the background as well the amplified cavity modes.

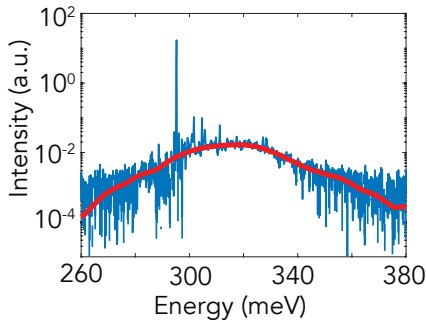


Figure A.4: L9 lasing spectrum taken carried out upon CW excitation at $15\ \text{K}$ in logarithmic scale. The background is approximated via a smoothing function, reported in red.

A.5 Band gap determination

Fig. A.5 illustrates how the band gap is determined. Via the smoothing function of section A.4, we approximate the maximum intensity of the background. The band gap corresponds to the half maximum intensity. For the L10 sample at 15 K reported in figure, the band gap is extracted at 266 meV.

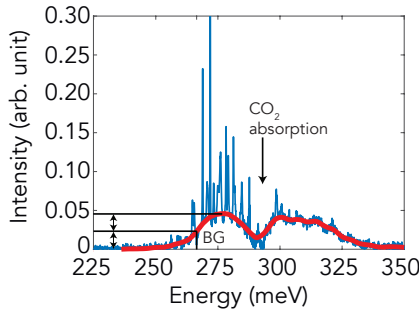


Figure A.5: L10 emission spectrum upon CW excitation of $P=6.4$ mW at 15 K. The red function represents the smoothing function, described in section A.4

A.6 The Schawlow–Townes Linewidth

Considering a complex electric field $E(t)$, the degree of temporal coherence is characterized via the normalized autocorrelation function $g(t)$, defined as [185]:

$$g(t) = \frac{G(t)}{G(0)} = \frac{\langle E^*(0)E(t) \rangle}{\langle E^*(0)E(0) \rangle} \quad (\text{A.3})$$

where $G(t)$ represents the autocorrelation function at time t . The absolute value of $g(t)$ measures the degree of correlation between the electric field at a certain time $t = 0$ and at a delayed time t and it varies between $0 \leq |g(t)| \leq 1$. For an ideal monochromatic light with $E(t) = E_0 \exp(i\omega_0 t)$ the degree of coherence obtained from equation A.3, is $|g(t)| = |\exp(i\omega_0 t)| = 1$, indicating that the field $E(0)$ and $E(t)$ are completely correlated for all time t . However, as it will be discussed, the degree of coherence of real laser devices is ultimately limited by the quantum noise and $|g(t)|^2$ decays to 0 for sufficiently large time t . The function describing the decaying of $g(t)$ determines then the laser coherence time as follows:

$$\tau_c = \int_{-\infty}^{\infty} |g(t)|^2 dt \quad (\text{A.4})$$

It is possible to access experimentally the laser coherence time τ_c via the linewidth of the power spectral density of the emitted light $S_E(\nu)$, simply referred to spectrum, via the Wiener-Khinchin theorem:

$$S_E(\nu) = \int_{-\infty}^{\infty} \langle E^*(0)E(t) \rangle \exp(-i2\pi\nu t) dt \quad (\text{A.5})$$

When the temporal coherence is limited by random noise, the autocorrelation function $\langle E^*(0)E(t) \rangle$ decays exponentially as $I \exp(i\omega_0 t) \exp\left(-\frac{t}{\tau_c}\right)$, where ω_0 is the laser oscillation angular frequency, and its Fourier transformed $S_E(\nu)$ is a lorentzian whose spectral width is

$$\Delta\nu = \frac{1}{\pi\tau_c} \quad (\text{A.6})$$

The narrower the spectral emission of a laser, the larger its coherence time and thus the coherence length $l_c = c\tau_c$. As a reference, a linewidth of $\Delta\nu = 1$ MHz corresponds to $\tau_c = 3.2 \cdot 10^{-7}$ s and $l_c = 95$ m. Highly coherent light sources find numerous applications as sensors, like fiber-based optical sensors, high resolution spectroscopy, light detection and ranging (LIDAR), gas detection, but also in coherent optical communication, metrology and in different scientific applications, like gravity-wave detector and laser cooling. In the next sections the theory of the quantum limit of the laser linewidth is first exposed and then compared to the experimental linewidth of strained germanium laser, previously described.

The linewidth of a laser is not infinitely narrow, but ultimately limited by the intrinsic quantum noise in the lasing field produced by the spontaneous emission events, leading to the decay of the coherence and thus to a finitely broad emission. In the following, we follow the description of [144]. The electric field of the laser can be described as the real part of the complex field

$$\vec{E}(\vec{r}, t) = E(t)\hat{n} \exp[i\vec{k} \cdot \vec{r}] = \sqrt{I(t)} \exp[i\phi(t)] \hat{n} \exp[i\vec{k} \cdot \vec{r}] \quad (\text{A.7})$$

where $\phi(t) = \phi_0 + \omega_0 t$ is the total phase, \vec{k} and ω are the laser wavevector and angular frequency, respectively and \hat{n} is the unitary polarization vector. The field amplitude $E(t)$ is represented in the complex space in Fig. A.6(a): an event of spontaneous emission photons in the laser field, represented by the small arrow, causes an instantaneous phase change $\Delta\phi'$ and alters the field intensity I by ΔI . As the spontaneous emission is an incoherent event, its phase θ is random, and the new vector field could be anywhere within the depicted circle. However, a laser operating under the assumption of gain clamping restores the intensity to its steady state value I via damped relaxation oscillations, in striking contrast to an incoherent light source, as depicted in Fig. A.6(b).

Such restoring force leads to a delayed phase change $\Delta\phi''$, in addition to the instantaneous $\Delta\phi'$, determining a further line broadening. The gain relaxation oscillations, whose

amplitude is proportional to a variation in the imaginary part of the refractive index $\Delta n''$, are indeed accompanied by a change in the carrier density, which ultimately alter the real part of the refractive index by $\Delta n'$ and thus the laser field phase. In particular, the ratio between the change of n' and n'' is referred to as Henry factor α [144] and is defined as:

$$\alpha = \frac{\Delta n'}{\Delta n''} = \frac{\frac{dn'}{dN} \Delta N}{\frac{dn''}{dN} \Delta N} = \frac{\left[\frac{dn'_{plasma}}{dN} + \frac{dn'_{KK}}{dN} \right]}{-\frac{\lambda}{4\pi} a} \quad (\text{A.8})$$

The real part n' has contribution from the free carrier n'_{plasma} and from the Kramers Kronig inversion n'_{KK} of the imaginary part [162]. Both are linear with respect to the carrier density N . In the second equality, a is the differential gain, following the relation $n'' = -g \frac{\lambda}{4\pi}$ [186], where g is the optical gain. Although in certain lasing platforms, like QCLs, it is predicted to be negligible [187], the α factor can not be neglected in traditional III-V interband semiconductor lasers where it ranges between 2 and 6 [188].

To better highlight the role of equation A.8, can be useful to express $\Delta n' = \Delta \phi'' \frac{\lambda}{2\pi}$ and $\Delta n'' = -\Delta g \frac{\lambda}{4\pi}$ [186], leading to the following expression, equivalent to A.8:

$$\alpha = -2 \frac{\Delta \phi''}{\Delta g} \quad (\text{A.9})$$

which couples the gain variation, following the intensity restoring force, to the additional phase noise.

Defining the total phase change as $\Delta \phi = \Delta \phi' + \Delta \phi''$, the spectral power density of the laser field and its spectral width can be extracted via the Fourier transformation of the autocorrelation function, following the Wiener-Khinchin theorem of equation A.5. The autocorrelation function $G(t)$ is:

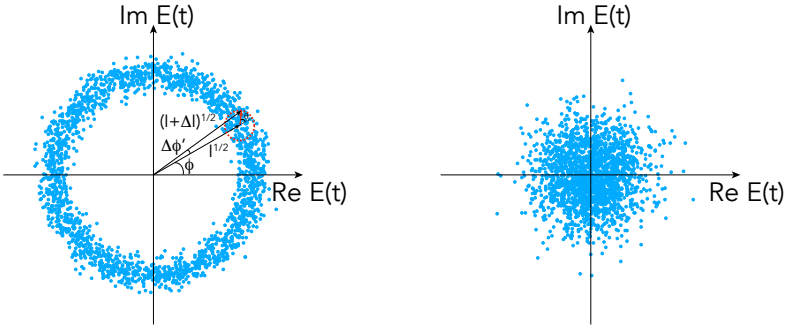
$$\langle E^*(0)E(t) \rangle = I(0) \exp[i\omega_0 t] \langle \exp i[\phi(t) - \phi(0)] \rangle \quad (\text{A.10})$$

Following the fact that the phase change are introduced by random and independent spontaneous emission events, $\Delta \phi = \phi(t) - \phi(0)$ can be considered to be distributed with a Gaussian probability density distribution, characterized by the variance $\langle \Delta \phi^2 \rangle$. It can thus be shown [189, 190] that:

$$\langle \exp i[\phi(t) - \phi(0)] \rangle = \exp \left[-\frac{\langle \Delta \phi^2 \rangle}{2} \right] \quad (\text{A.11})$$

For a white frequency noise, the variance of the phase change $\langle \Delta \phi^2 \rangle$ increases with time delay t , expressing the Brownian motion of the phase change and it can computed as:

$$\langle \Delta \phi^2 \rangle = \frac{R}{2I} (1 + \alpha^2) t \quad (\text{A.12})$$



- (a) Electric field variation over time of a coherent light source. Due to random distribution of spontaneous emission phase θ the modified electric field can be anywhere within the red dashed line.
- (b) Field vector change in time for an incoherent light source, with intensity and phase randomly distributed.

Figure A.6: Change of the electric field due to spontaneous emission events representation in the complex space. (a) A single spontaneous emission event causes an instantaneous changes in both the field phase ϕ and magnitude \sqrt{I} , which become $\phi + \Delta\phi'$ and $\sqrt{I + \Delta I}$, respectively. Discontinuous and random spontaneous emission photons over a certain period of time walk the laser field in the complex space, as depicted by the blue dots. (b) An incoherent light source is characterized by a random distribution over time of the light field, as no restoring force keeps the intensity at the same magnitude.

where R is the spontaneous emission rate. Inserting previous expression into equation A.10 it is possible to observe that the autocorrelation function decays exponentially as

$$\langle E^*(0)E(t) \rangle = I(0) \exp[i\omega_0 t] \exp\left[-\frac{R}{4I}(1 + \alpha^2)t\right] \quad (\text{A.13})$$

with a coherence time $\tau_c = \frac{4I}{R(1 + \alpha^2)}$. The Fourier transformation leads to a lorentzian power spectral density $S_E(\nu)$, whose spectral width, from the relation expressed in the equation A.6, is:

$$\Delta\nu = \frac{1}{\pi\tau_c} = \frac{R}{4\pi I}(1 + \alpha^2) \quad (\text{A.14})$$

The laser field intensity, which expresses the number of photons in the lasing mode, can be expressed in function of the output power per round trip P_{out} with the following relation:

$$I = \frac{P_{out}}{h\nu \nu_g \alpha_c} \quad (\text{A.15})$$

where $h\nu$ is the photon energy, v_g is the group velocity and α_c expresses the cavity loss. The spontaneous emission rate R is equal to $R = v_g g n_{pi}$ [191], where g indicates the gain is expressed as $g = \alpha_c + \alpha_{loss}$, with α_{loss} for the material loss, and n_{pi} is the population inversion factor. The final expression of the linewidth reads as:

$$\Delta\nu = \frac{v_g^2 h\nu g n_{pi} \alpha_c}{4\pi P_{out}} (1 + \alpha^2) \quad (\text{A.16})$$

A.7 Population inversion factor

The population inversion factor n_{pi} expresses the probability of the emitted light to be reabsorbed by the gain material and thus it can contribute to broaden the linewidth. For semiconductor lasers it usually varies between 1 and 2 [188]. It is defined as follows:

$$n_{pi}(h\nu, N_{tot}, T) = \frac{f_c(1-f_v)}{f_c - f_v} = \frac{1}{1 - \exp\left[\frac{h\nu - \Delta E_F}{k_B T}\right]} \quad (\text{A.17})$$

where f_c and f_v are the electron distribution in the conduction and valence bands, respectively, assuming that are characterized by the quasi-Fermi levels μ_c and μ_v , whose energy separation is $\Delta E_F = \mu_c - \mu_v$. The formulation of equation A.17 is the semiconductor equivalent of the ratio $\frac{N_2}{N_2 - N_1}$ for a two levels atomic system, where N_2 is the number of state pairs that can interact with a photon of energy $h\nu$, in which the upper energy state level is occupied and the lower energy one is empty. Similarly, N_1 represent the number of state pairs in which the lower energy state is full and upper one empty. When $N_2 > N_1$ inversion of population is established and $\frac{N_2}{N_2 - N_1} > 0$.

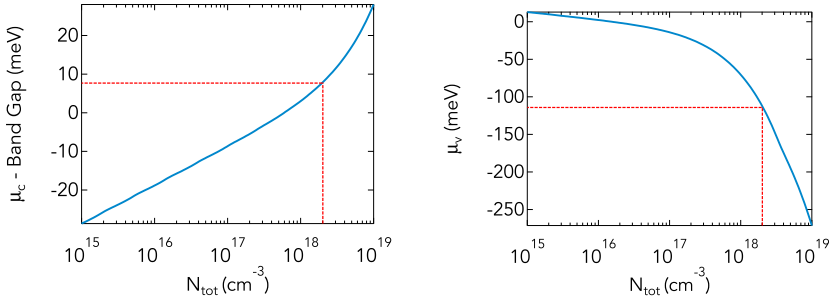
Analogously, in a semiconductor for transition energy $h\nu$ larger than the band gap energy E_{BG} inversion of population and thus net optical gain is achieved when $n_{pi} > 0$, i.e. when $E_{BG} < h\nu < \Delta E_F$, corresponding to the Bernard-Duraffourg condition [192]. By increasing the excited carrier density, the separation energy between the two quasi-Fermi levels increases and $n_{pi} \rightarrow 1$. It should be noted that the value of n_{pi} depends on the relative energy difference between the transition energy $h\nu$ and quasi-Fermi levels separation ΔE_F .

In the following, we provide calculation of n_{pi} for strained germanium. For sake of generality, we assume $\Delta E_{\Gamma,L} = 0$ meV. The model exposed in chapter 3.3 is adopted.

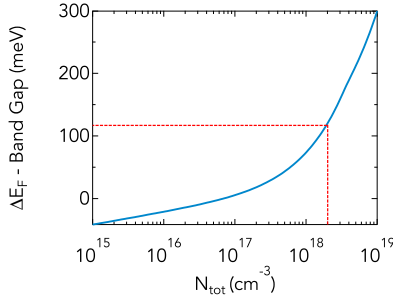
Fig.A.7(a) shows the quasi-Fermi level of the conduction band μ_c relative to the band gap as a function of the total excited carrier density at $T = 50$ K. As already observed in section 3.2, the presence of the L valley determines a slow increase of μ_c . At threshold density of about $2 \cdot 10^{18} \text{ cm}^{-3}$, as highlighted by the dashed line, μ_c is less then 10 meV above the band gap. On the contrary, the quasi-Fermi level of the valence bands increases of more than

100 meV. It should be noted that while strained germanium conduction bands dispersion can be well approximated as quadratic [127], the valence bands dispersion diverges from parabolic approximation at large wave vector. However, the tight-binding model gives at about $2 \cdot 10^{18} \text{ cm}^{-3}$ a quasi-Fermi level for the valence band $\mu_v = -75 \text{ meV}$, validating at qualitative level the parabolic approximation here used.

Fig.A.7(c) shows the evolution of the quasi-Fermi levels separation relative to the band gap and highlights that transparency is reached at density above 10^{17} cm^{-3} . The large quasi-

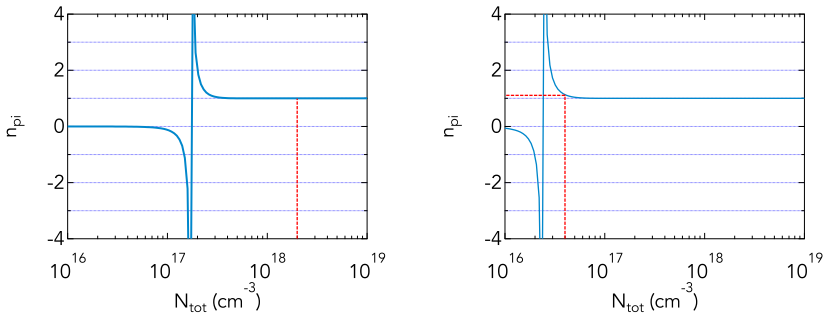


(a) μ_c relative to the band gap as a function of total carrier density. (b) μ_v relative as a function of total carrier density.



(c) Difference between the quasi-Fermi levels separation and the band gap energy as a function of the total carrier density.

Figure A.7: Evolution as a function of the total carrier density of (a) the quasi-Fermi level of the conduction band μ_c over the band gap, (b) the quasi-Fermi level of the valence band μ_v and (c) the relative difference between the quasi-Fermi level separation ΔE_F and the band gap E_{BG} . Calculations are carried out for $\Delta E_{\Gamma,L} = 0 \text{ meV}$ with $T = 50 \text{ K}$



- (a) n_{pi} evolution as a function of N_{tot} when $\Delta E_{\Gamma,L}$ 0 meV. The red-dashed line indicates the threshold density corresponding to 600 cm^{-3} of gain.
- (b) For truly direct band gap system transparency is quickly followed by threshold, highlighted by red-dashed line. For $h\nu$ 15 meV above the band gap $n_{pi} = 1.2$.

Figure A.8: Population inversion factor for transition energy 15 meV above the band gap as a function of the total carrier density N_{tot} for (a) aligned conduction bands and (b) hypothetical truly direct band gap strained germanium system with $\Delta E_{\Gamma,L} = -300 \text{ meV}$.

Fermi levels separation ΔE_F of more than 100 meV at threshold ensures that for transitions energies $h\nu$ within the gain bandwidth the population inversion factor n_{pi} is perfectly 1, as shown in Fig.A.8(a).

In an hypothetical truly direct strained germanium system with $\Delta E_{\Gamma,L} = -300 \text{ meV}$, which resemble more closely the traditional III-V lasers, the μ_c increases with a rate comparable to μ_v . Fig.A.8(b) reports then the population inversion factor for the transition energy of 15 meV above the band gap in this novel electronic configuration. At threshold the population inversion factor is $n_{pi} = 1.2$.

Although an n_{pi} factor between 1 and 2 can easily represent a second order effect in terms of linewidth broadening with respect to the α factor, Fig.A.8 shows the importance of a strong electron depletion of the valence bands in order to achieve a high population inversion factor. This feature, typical of marginally direct group IV systems directly links to the transparency formation in the gain spectra described in Sec. 3.3.2, whose role was previously shown in 5.5.

A.8 Linewidth technical noise sources

The ultimate linewidth a laser can reach has a strong dependence on the type of the device. Especially regarding solid state lasers consisting of discrete elements in addition to the gain medium, like an external cavity and/or optical intracavity elements, the Schawlow-Townes limit is difficult to reach. The employment of an external cavity is aimed to reduce the typical MHz diode laser linewidth to the kHz and below range, but such concept has the disadvantage of being easily subjected to different noise sources of technical character, like mechanical vibrations, thermal fluctuation or pump power fluctuations. Many efforts are addressed in this field in order to minimize such classical noise sources [193–196].

The linewidth of monolithic laser sources operating at low temperature, like the case of strained germanium, is not expected to be limited by mechanical or thermal noise. However, their power-independent nature is compatible with the experimental observation and in the following the role of classical noise sources is thus estimated.

Within a cavity of length L the frequency of the mode m built up as

$$\nu n_{eff} L = \frac{m c}{2} \quad (\text{A.18})$$

Differentiating the equation A.18, a general relationship between the frequency deviation and the uncertainties of the effective refractive index n_{eff} and the cavity length is established as

$$\Delta \nu = -\nu \left[\frac{\Delta n_{eff}}{n_{eff}} + \frac{\Delta L}{L} \right] \quad (\text{A.19})$$

A possible source of uncertainty in the optical path is the beam vibration. Indeed, the suspended strained microbridge is expected to mechanically oscillate due to the thermal noise of the environment, where molecules hit randomly and independently from each other the structure. Each collision transfers a certain amount of energy to the suspended microbridge, which starts to oscillate at the fundamental resonant frequency [197]:

$$\nu_r = \frac{1}{2} \sqrt{\frac{\sigma}{\rho L^2}} = 67 \text{ MHz} \quad (\text{A.20})$$

where the stress of the microbridge at 6 % of strain is $\sigma = E \cdot \epsilon_{100} = 102 \text{ GPa} \cdot 0.06 = 6.12 \text{ GPa}$, $\rho = 5.3 \cdot 10^3 \text{ kg/m}^3$ is Ge mass density and $L = 8 \mu\text{m}$ is the length of the suspended microbridge. Assuming that the system is in thermal equilibrium with the environment, it is possible to relate via the equipartition theorem the variance of the microbridge displacement to the equilibrium energy as follows [198]:

$$\frac{1}{2} k \langle z^2 \rangle = \frac{1}{2} m \langle v_z^2 \rangle = \frac{1}{2} k_b T \quad (\text{A.21})$$

where k is the elastic constant and z is the displacement from the equilibrium position. It follows that the root mean square of the microbridge displacement at temperature as low as 20 K is:

$$\sqrt{\langle z^2 \rangle} = \sqrt{\frac{k_b T}{k}} = 0.5 \text{ pm} \quad (\text{A.22})$$

The spring constant is evaluated as $k = m \cdot (2\pi \nu_r)^2$, where m is the mass of the suspended beam, and is about 10^3 N/m .

The beam oscillation leads to an increase of the actual length of the microbridge of an amount equal $\Delta L = \int_0^L z^2(x) dx$, where $z(x)$ is the displacement in function of the longitudinal position. Due to the quadratic behaviour in the integral of $z(x)$, ΔL can be neglected from equation A.19 as a second order effect. The effective refractive index has as well a dependence on the distance between the suspended microbridge and the oxide substrate. However, a displacement of sub pm over a distance of $1 \mu\text{m}$ between the Ge membrane and the SiO_2 leads to an effective refractive index variation of about $\Delta n_{eff} = \frac{\partial n}{\partial z} \sqrt{\langle z^2 \rangle} = -10^{-7}$. The uncertainty of the laser frequency due to the change of the optical path can be estimated as

$$\Delta \nu = -\nu \left[\frac{\Delta n_{eff}}{n_{eff}} \right] = 71 \text{ THz} \frac{10^{-7}}{4} = 1.8 \text{ MHz} \quad (\text{A.23})$$

which represent a value about 4 orders of magnitude lower with respect to the experimental power independent linewidth limit of about 21 GHz (c.f. Fig. 5.29). The thermal noise induced change of the optical path can be thus excluded as a power independent limit of the strained germanium linewidth.

It can be nevertheless of interest to remind that the evanescent coupling of the light into dielectric layer underneath is exploited in novel class of nano-mechanical based systems [199] which measured the suspended beam displacement upon optical forces of the order of nm. As the strained germanium lasing experiment is carried out in continuous wave optical excitation, such effect can be neglected. Moreover, it should also be noted that equation A.23 do not represent the spectral width of the laser field, but only the root mean square deviation of the cavity resonant frequency, and thus should be used as a qualitative picture. Indeed, a proper calculation of the linewidth would require the knowledge of how the temporal coherence of the lasing electric field decays due to the thermal noise induced phase change.

Analogously, the thermal noise can influence the effective refractive index via its thermo-optic coefficient as $\Delta n_{eff} = \frac{\partial n}{\partial T} \Delta T$. At 20 K for frequency of about 70 THz the thermo-optic coefficient is $\frac{\partial n}{\partial T} = 5.5 \cdot 10^{-5} \text{ K}^{-1}$ [200], while the deviation of the temperature is estimated as $\Delta T = \frac{k_b T}{C_p \rho V} = 6.4 \cdot 10^{-10} \text{ K}$, leading to a negligible change of the effective refractive index of $\Delta n_{eff} = 10^{-15}$.

A.9 Fundamental linewidth deviations from S-T theory

While for non ideal single mode and multimode character lasers the nature of the power independent term $\Delta \nu_0$ is qualitatively understood, for purely single mode lasers the origin of the power-independent contribution to the linewidth is still debated. Some explanations were proposed:

- $1/f$ noise [174, 175]
- occupation fluctuation noise [176]

After the first experimental observation of the residual linewidth [167], $1/f$ frequency noise was pointed out as a possible cause of the power-independent linewidth in single mode lasers. The frequency noise power spectral density (PSD) S_ν of a semiconductor laser usually exhibits for frequency below 100 kHz a $1/f$ component largely power-independent, such that it can be described as

$$S_\nu(\nu) = \frac{K}{\nu} + C \quad (\text{A.24})$$

where K is the strength of the $1/f$ component, measured in Hz^2 , and C describes the white frequency noise of the spontaneous emission inversely proportional to the laser output power, in unit of Hz^2/Hz . Depending on the magnitude of K , the $1/f$ noise can become the dominant noise source once the spontaneous emission white frequency noise decreases at high output power [201], limiting the laser linewidth to a finite value.

By neglecting the random spontaneous emission noise and considering only the $1/f$ component, the one side of S_ν reads as $S_\nu(\nu) = K/\nu$. It can be then shown [190] that the spectrum of the laser field emission subjected to such noise has a gaussian profile, with a spectral width

$$\Delta \nu = \sqrt{\frac{2K \ln 2 \ln \frac{5}{\nu_m \tau_c}}{\pi^3}} \quad (\text{A.25})$$

proportional to \sqrt{K} , with a dependence on the measurement lower frequency limit ν_m .

It is useful to remind that the $1/f$ frequency noise usually leads to a residual linewidth of about some MHz [173, 175], about 4 orders of magnitude lower than the observation in strained germanium. The $1/f$ noise origin is still not clear [190]. Although still debated, it is suggested that the $1/f$ frequency noise component is related to non-radiative recombination carrier noise [174, 202, 203], which is pointed out also as the source of the $1/f$ component in intensity noise PSD measurement [204]. Such observations in laser physics are supported by different studies in semiconductor based devices, like diode, transistors and resistors which show an intrinsic $1/f$ noise in the conductivity [205].

An alternative reason for the power-independent $\Delta\nu_0$ residual linewidth, but still linked to the concept of carrier induced noise, is the fluctuation of the conduction and valence bands state occupancy, as proposed in [176]. In the standard theory developed by Henry the contribution to the linewidth of the carrier density change is already taken into account and it is strictly linked to the α factor and the concept of gain clamping. An additional noise rises from the state occupancy fluctuations, which are driven by the carrier-carrier intra valley scattering. A power independent contribution to the linewidth of few MHz is predicted.

Bibliography

- [1] J. Bardeen and W. H. Brattain. Transistor, a semiconductor triode. *Proceedings of the IEEE* **86(1)**, 29–30 (1998).
- [2] R. Noyce. Semiconductor device-and-lead structure, US Patent 2981877 (1961).
- [3] J. S. Kilby. Miniaturized electronic circuits, US Patent 3138743 (1964).
- [4] G. E. Moore. Cramming more components onto integrated circuits. *Electronics* **38(8)**, 114 (1965).
- [5] G. Yeap, X. Chen, B. R. Yang, C. P. Lin, F. C. Yang, Y. K. Leung, D. W. Lin, C. P. Chen, K. F. Yu, D. H. Chen, C. Y. Chang, S. S. Lin, H. K. Chen, P. Hung, C. S. Hou, Y. K. Cheng, J. Chang, L. Yuan, C. K. Lin, C. C. Chen, Y. C. Yeo, M. H. Tsai, Y. M. Chen, H. T. Lin, C. O. Chui, K. B. Huang, W. Chang, H. J. Lin, K. W. Chen, R. Chen, S. H. Sun, Q. Fu, H. T. Yang, H. L. Shang, H. T. Chiang, C. C. Yeh, T. L. Lee, C. H. Wang, S. L. Shue, C. W. Wu, R. Lu, W. R. Lin, J. Wu, F. Lai, P. W. Wang, Y. H. Wu, B. Z. Tien, Y. C. Huang, L. C. Lu, J. He, Y. Ku, J. Lin, M. Cao, T. S. Chang, S. M. Jang, H. C. Lin, Y. C. Peng, J. Y. Sheu and M. Wang. 5nm CMOS Production Technology Platform featuring full-fledged EUV, and High Mobility Channel FinFETs with densest $0.021\mu\text{m}^2$ SRAM cells for Mobile SoC and High Performance Computing Applications. *Technical Digest - International Electron Devices Meeting, IEDM 2019-December*, 879–882 (2019).
- [6] J. J. Pla, K. Y. Tan, J. P. Dehollain, W. H. Lim, J. J. Morton, D. N. Jamieson, A. S. Dzurak and A. Morello. A single-atom electron spin qubit in silicon. *Nature* **489(7417)**, 541–544 (2012).
- [7] M. Veldhorst, C. H. Yang, J. C. Hwang, W. Huang, J. P. Dehollain, J. T. Muhonen, S. Simmons, A. Laucht, F. E. Hudson, K. M. Itoh, A. Morello and A. S. Dzurak. A two-qubit logic gate in silicon. *Nature* **526(7573)**, 410–414 (2015).
- [8] M. Veldhorst, H. G. Eenink, C. H. Yang and A. S. Dzurak. Silicon CMOS architecture for a spin-based quantum computer. *Nature Communications* **8(1)** (2017).
- [9] N. W. Hendrickx, D. P. Franke, A. Sammak, G. Scappucci and M. Veldhorst. Fast two-qubit logic with holes in germanium. *Nature* **577(January)** (2019).

- [10] F. A. Zwanenburg, A. S. Dzurak, A. Morello, M. Y. Simmons, L. C. Hollenberg, G. Klimeck, S. Rogge, S. N. Coppersmith and M. A. Eriksson. Silicon quantum electronics. *Reviews of Modern Physics* **85**(3), 961–1019 (2013).
- [11] G. Scappucci, C. Kloeffel, F. A. Zwanenburg, D. Loss, M. Myronov, J.-J. Zhang, S. D. Franceschi, G. Katsaros and M. Veldhorst. The germanium quantum information route (2020).
- [12] R. A. Soref and J. P. Lorenzo. Single-Crystal Silicon: A New Material For 1-3 And 1-6 Fim Integrated-Optical Components. *Electronics Letters* **21**(21), 953–954 (1985).
- [13] A. H. Atabaki, S. Moazeni, F. Pavanello, H. Gevorgyan, J. Notaros, L. Alloatti, M. T. Wade, C. Sun, S. A. Kruger, H. Meng, K. A. Qubaisi, I. Wang, B. Zhang, A. Khilo, C. V. Baiocco, M. A. Popović, V. M. Stojanović and R. J. Ram. Integrating photonics with silicon nanoelectronics for the next generation of systems on a chip (Nature, (2018), 556, 7701, (349-354), 10.1038/s41586-018-0028-z). *Nature* **560**(7716), E4 (2018).
- [14] Y. Shen, N. C. Harris, S. Skirlo, M. Prabhu, T. Baehr-Jones, M. Hochberg, X. Sun, S. Zhao, H. Larochelle, D. Englund and M. Soljačić. Deep learning with coherent nanophotonic circuits Supplementary Material. *Nature Photonics* **11**(7), 441–446 (2017).
- [15] X. Qiang, X. Zhou, J. Wang, C. M. Wilkes, T. Loke, S. O’Gara, L. Kling, G. D. Marshall, R. Santagati, T. C. Ralph, J. B. Wang, J. L. O’Brien, M. G. Thompson and J. C. Matthews. Large-scale silicon quantum photonics implementing arbitrary two-qubit processing. *Nature Photonics* **12**(9), 534–539 (2018).
- [16] J. Wang, J. Wang, S. Paesani, Y. Ding, R. Santagati, P. Skrzypczyk, A. Salavrakos, J. Tura, R. Augusiak, L. Man, D. Bacco, D. Bonneau, J. W. Silverstone, Q. Gong, A. Acín, K. Rottwitt, L. K. Oxenløwe, J. L. O. Brien, A. Laing and M. G. Thompson. Multidimensional quantum entanglement with large - scale integrated optics. *Science* **360**(April), 285–291 (2018).
- [17] T. Liljeberg. Silicon photonics and the future of optical connectivity in the data center. *6th IEEE Photonics Society Optical Interconnects Conference, OI 2017* 1–2 (2017).
- [18] A. M. Urbas, Z. Jacob, L. Dal, D. Thomson, A. Zilkie, J. E. Bowers and T. Komljenovic. Roadmap on silicon photonics. *Journal of Optics* **18**(7), 1–20 (2017).

- [19] D. J. Thomson, F. Y. Gardes, Y. Hu, G. Mashanovich, M. Fournier, P. Grosse, J.-M. Fedeli and G. T. Reed. High contrast 40Gbit/s optical modulation in silicon. *Optics Express* **19(12)**, 11507 (2011).
- [20] N. C. Harris, Y. Ma, J. Mower, T. Baehr-Jones, D. Englund, M. Hochberg and C. Galland. Efficient, compact and low loss thermo-optic phase shifter in silicon. *Optics Express* **22(9)**, 10487 (2014).
- [21] C. Haffner, W. Heni, Y. Fedoryshyn, J. Niegemann, A. Melikyan, D. L. Elder, B. Baeuerle, Y. Salamin, A. Josten, U. Koch, C. Hoessbacher, F. Ducry, L. Juchli, A. Emboras, D. Hillerkuss, M. Kohl, L. R. Dalton, C. Hafner and J. Leuthold. All-plasmonic Mach-Zehnder modulator enabling optical high-speed communication at the microscale. *Nature Photonics* **9(8)**, 525–528 (2015).
- [22] T. Yin, R. Cohen, M. M. Morse, G. Sarid, Y. Chetrit, D. Rubin and M. J. Paniccia. 31 GHz Ge n-i-p waveguide photodetectors on Silicon-on-Insulator substrate. *Optics Express* **15(21)**, 13965 (2007).
- [23] C. T. DeRose, D. C. Trotter, W. A. Zortman, A. L. Starbuck, M. Fisher, M. R. Watts and P. S. Davids. Ultra compact 45 GHz CMOS compatible Germanium waveguide photodiode with low dark current. *Optics Express* **19(25)**, 24897 (2011).
- [24] L. Vivien, A. Polzer, D. Marris-Morini, J. Osmond, J. M. Hartmann, P. Crozat, E. Cassan, C. Kopp, H. Zimmermann and J. M. Fédéli. Zero-bias 40Gbit/s germanium waveguide photodetector on silicon. *Optics Express* **20(2)**, 1096 (2012).
- [25] A. W. Fang, H. Park, O. Cohen, R. Jones, M. J. Paniccia and J. E. Bowers. Electrically pumped hybrid AlGaInAs-silicon evanescent laser. *Optics Express* **14(20)**, 9203 (2006).
- [26] J. Van Campenhout, P. Rojo-Romeo, P. Regreny, C. Seassal, D. Van Thourhout, L. Di Cioccio, J. M. Fedeli and R. Baets. Optimization of electrically pumped microdisk lasers integrated with a nanophotonic SOI waveguide circuit. *Optics InfoBase Conference Papers* **15(11)**, 6744–6749 (2007).
- [27] X. Sun, A. Zadok, M. J. Shearn, K. A. Diest, A. Ghaffari, H. A. Atwater, A. Scherer and A. Yariv. Electrically pumped hybrid evanescent Si / InGaAsP lasers **34(9)**, 1345–1347 (2009).
- [28] G. Crosnier, D. Sanchez, S. Bouchoule, P. Monnier, G. Beaudoin, I. Sagnes, R. Raj and F. Raineri. Hybrid indium phosphide-on-silicon nanolaser diode. *Nature Photonics* **11(5)**, 297–300 (2017).

- [29] D. Liang, X. Huang, G. Kurczveil, M. Fiorentino and R. G. Beausoleil. Integrated finely tunable microring laser on silicon. *Nature Photonics* **10(11)**, 719–722 (2016).
- [30] B. R. Koch, E. J. Norberg, B. Kim, J. Hutchinson, J. H. Shin, G. Fish and A. Fang. Integrated silicon photonic laser sources for telecom and datacom. *Optical Fiber Communication Conference, OFC 2013* 3–5 (2013).
- [31] S. Chen, W. Li, J. Wu, Q. Jiang, M. Tang, S. Shutts, S. N. Elliott, A. Sobiesierski, A. J. Seeds, I. Ross, P. M. Smowton and H. Liu. Electrically pumped continuous-wave III-V quantum dot lasers on silicon. *Nature Photonics* **10(5)**, 307–311 (2016).
- [32] A. Castellano, L. Cerutti, J. B. Rodriguez, G. Narcy, A. Garreau, F. Lelarge and E. Tournié. Room-temperature continuous-wave operation in the telecom wavelength range of GaSb-based lasers monolithically grown on Si. *APL Photonics* **2(6)** (2017).
- [33] M. Paladugu, C. Merckling, R. Loo, O. Richard, H. Bender, J. Dekoster, W. Vandervorst, M. Caymax and M. Heyns. Site selective integration of III-V materials on Si for nanoscale logic and photonic devices. *Crystal Growth and Design* **12(10)**, 4696–4702 (2012).
- [34] R. Alcotte, M. Martin, J. Moeyaert, R. Cipro, S. David, F. Bassani, F. Ducroquet, Y. Bogumilowicz, E. Sanchez, Z. Ye, X. Y. Bao, J. B. Pin and T. Baron. Epitaxial growth of antiphase boundary free GaAs layer on 300 mm Si(001) substrate by metalorganic chemical vapour deposition with high mobility **046101(001)** (2017).
- [35] Y. Wan, J. C. Norman, Y. Tong, M. J. Kennedy, W. He, J. Selvidge, C. Shang, M. Dumont, A. Malik, H. K. Tsang, A. C. Gossard and J. E. Bowers. 1.3 μm Quantum Dot-Distributed Feedback Lasers Directly Grown on (001) Si. *Laser and Photonics Reviews* **2000037(001)**, 1–9 (2020).
- [36] L. M. M. I. T. Chen Siming, J. W. U. Iang, M. Ickael, M. Artin, T. H. B. Aron, A. L. S. Eeds and H. U. L. Iu. InAs / GaAs quantum dot lasers monolithically grown on on-axis Si (001) substrates. *Optics Express* **25(5)**, 11381–11386 (2017).
- [37] M. Rio Calvo, L. Monge Bartolomé, M. Bahriz, G. Boissier, L. Cerutti, J.-B. Rodriguez and E. Tournié. Mid-infrared laser diodes epitaxially grown on on-axis (001) silicon. *Optica* **7(4)**, 263 (2020).
- [38] H. Nguyen-Van, A. N. Baranov, Z. Loghmari, L. Cerutti, J. B. Rodriguez, J. Tournet, G. Narcy, G. Boissier, G. Patriarche, M. Bahriz, E. Tournié and R. Teissier. Quantum cascade lasers grown on silicon. *Scientific Reports* **8(1)**, 1–8 (2018).

- [39] Z. Loghmari, J. B. Rodriguez, A. N. Baranov, M. Rio-Calvo, L. Cerutti, A. Meguekam, M. Bahriz, R. Teissier and E. Tournié. InAs-based quantum cascade lasers grown on on-axis (001) silicon substrate. *APL Photonics* **5(4)**, 1–5 (2020).
- [40] W. L. Wilson, P. F. Szajowski and L. E. Brus. Quantum confinement in size-selected, surface-oxidized silicon nanocrystals. *Science* **262(5137)**, 1242–1244 (1993).
- [41] L. Pavesi, L. Dal Negro, C. Mazzoleni, G. Franzò and F. Priolo. Optical gain in Silicon nanocrystals. *Nature* **408**, 440–444 (2000).
- [42] K. Kůsová, P. Hapala, J. Valenta, P. Jelínek, O. Cibulka, L. Ondič and I. Pelant. Direct Bandgap Silicon: Tensile-Strained Silicon Nanocrystals. *Advanced Materials Interfaces* **1(2)**, 1–9 (2014).
- [43] A. G. Cullis and L. Canham. Visible-light emission due to quantum size effects in porous crystalline silicon. *Nature* **353**, 335–338 (1991).
- [44] U. Gösele and V. Lehmann. Light-emitting porous silicon. *Materials Chemistry & Physics* **40(4)**, 253–259 (1995).
- [45] B. Zheng, J. Michel, F. Y. G. Ren, L. C. Kimerling, D. C. Jacobson and J. M. Poate. Room-temperature sharp line electroluminescence at $\lambda=1.54\ \mu\text{m}$ from an erbium-doped, silicon light-emitting diode. *Applied Physics Letter* **64(2842)** (1994).
- [46] C. Zeller and G. Abstreiter. Electric subbands in Si/SiGe strained layer superlattices. *Zeitschrift für Physik B Condensed Matter* **64(2)**, 137–143 (1986).
- [47] H. Presting, H. Kibbel, M. Jaros, R. M. Turton, U. Menczgar, G. Abstreiter and H. G. Grimmeiss. Ultrathin SimGen strained layer superlattices - A step towards Si optoelectronics. *Semiconductor Science and Technology* **7(9)**, 1127–1148 (1992).
- [48] M. D’Avezac, J. W. Luo, T. Chanier and A. Zunger. Genetic-algorithm discovery of a direct-gap and optically allowed superstructure from indirect-gap Si and Ge semiconductors. *Physical Review Letters* **108(2)**, 1–5 (2012).
- [49] U. Gnutzmann and K. Clausecker. Theory of direct optical transitions in an optical indirect semiconductor with a superlattice structure. *Applied Physics* **3(1)**, 9–14 (1974).
- [50] H. Rong, R. Jones, A. Liu, O. Cohen, D. Hak, A. W. Fang and M. J. Paniccia. A continuous-wave Raman Silicon laser. *Nature* **433(7027)**, 717–719 (2005).

- [51] H. Rong, Y.-H. Kuo, S. Xu, A. Liu, R. Jones, M. Paniccia, O. Cohen and O. Raday. Monolithic integrated Raman silicon laser. *Optics Express* **14(15)**, 6705 (2006).
- [52] H. Rong, S. Xu, Y. H. Kuo, V. Sih, O. Cohen, O. Raday and M. Paniccia. Low-threshold continuous-wave Raman silicon laser. *Nature Photonics* **1(4)**, 232–237 (2007).
- [53] G. Dehlinger, L. Diehl, U. Gennser, H. Sigg, J. Faist, K. Ensslin, D. Grützmacher and E. Müller. Intersubband electroluminescence from silicon-based quantum cascade structures. *Science* **290(5500)**, 2277–2280 (2000).
- [54] S. A. Lynch, R. Bates, D. J. Paul, D. J. Norris, A. G. Cullis, Z. Ikonik, R. W. Kelsall, P. Harrison, D. D. Arnone and C. R. Pidgeon. Intersubband electroluminescence from Si/SiGe cascade emitters at terahertz frequencies. *Applied Physics Letters* **81(9)**, 1543–1545 (2002).
- [55] Y. Busby, M. De Seta, G. Capellini, F. Evangelisti, M. Ortolani, M. Virgilio, G. Grosso, G. Pizzi, P. Calvani, S. Lupi, M. Nardone, G. Nicotra and C. Spinella. Near- and far-infrared absorption and electronic structure of Ge-SiGe multiple quantum wells. *Physical Review B - Condensed Matter and Materials Physics* **82(20)**, 7–11 (2010).
- [56] T. Grange, D. Stark, G. Scalari, J. Faist, L. Persichetti, L. Di Gaspare, M. De Seta, M. Ortolani, D. J. Paul, G. Capellini, S. Birner and M. Virgilio. Room temperature operation of n -type Ge/SiGe terahertz quantum cascade lasers predicted by non-equilibrium Green's functions. *Applied Physics Letters* **114(11)** (2019).
- [57] K. Gallacher, M. Ortolani, K. Rew, C. Ciano, L. Baldassarre, M. Virgilio, G. Scalari, J. Faist, L. Di Gaspare, M. De Seta, G. Capellini, T. Grange, S. Birner and D. J. Paul. Design and simulation of losses in Ge/SiGe terahertz quantum cascade laser waveguides. *Optics Express* **28(4)**, 4786 (2020).
- [58] D. Stark, M. Mirza, L. Persichetti, M. Montanari, S. Markmann, M. Beck, T. Grange, S. Birner, M. Virgilio, C. Ciano, M. Ortolani, C. Corley, G. Capellini, L. Di Gaspare, M. De Seta, D. J. Paul, J. Faist and G. Scalari. THz intersubband electroluminescence from n-type Ge/SiGe quantum cascade structures. *ArXiv:2101.05518v1* (2021).
- [59] M. Grydlik, F. Hackl, H. Groiss, M. Glaser, A. Halilovic, T. Fromherz, W. Jantsch, F. Schäffler and M. Brehm. Lasing from Glassy Ge Quantum Dots in Crystalline Si. *ACS Photonics* **3(2)**, 298–303 (2016).

- [60] M. Grydlik, M. T. Lusk, F. Hackl, A. Polimeni, T. Fromherz, W. Jantsch, F. Schäffler and M. Brehm. Laser Level Scheme of Self-Interstitials in Epitaxial Ge Dots Encapsulated in Si. *Nano Letters* **16(11)**, 6802–6807 (2016).
- [61] E. M. Fadaly, A. Dijkstra, J. R. Suckert, D. Ziss, M. A. van Tilburg, C. Mao, Y. Ren, V. T. van Lange, K. Korzun, S. Kölling, M. A. Verheijen, D. Busse, C. Rödl, J. Furthmüller, F. Bechstedt, J. Stangl, J. J. Finley, S. Botti, J. E. Haverkort and E. P. Bakkers. Direct-bandgap emission from hexagonal Ge and SiGe alloys. *Nature* **580(7802)**, 205–209 (2020).
- [62] J. Liu, X. Sun, R. Camacho-Aguilera, L. C. Kimerling and J. Michel. Ge-on-Si laser operating at room temperature. *Optics Letters* **35(5)**, 679 (2010).
- [63] R. E. Camacho-Aguilera, Y. Cai, N. Patel, J. T. Bessette, M. Romagnoli, L. C. Kimerling and J. Michel. An electrically pumped germanium laser. *Optics Express* **20(10)**, 11316 (2012).
- [64] R. Koerner, M. Oehme, M. Gollhofer, M. Schmid, K. Kostecky, S. Bechler, D. Widmann, E. Kasper and J. Schulze. Electrically pumped lasing from Ge Fabry-Perot resonators on Si. *Optics Express* **23(11)**, 14815 (2015).
- [65] L. Carroll, P. Friedli, S. Neuenschwander, H. Sigg, S. Cecchi, F. Isa, D. Chrastina, G. Isella, Y. Fedoryshyn and J. Faist. Direct-gap gain and optical absorption in germanium correlated to the density of photoexcited carriers, doping, and strain. *Physical Review Letters* **109(5)**, 1–5 (2012).
- [66] C. H. Goodman. Direct-Gap Group Iv Semiconductors Based on Tin. *IEEE Proceedings I: Solid State and Electron Devices* **129(5)**, 189–192 (1982).
- [67] P. Vogl, M. M. Rieger, J. A. Majewski and G. Abstreiter. How to convert group-iv semiconductors into light emitters. *Physica Scripta* **1993(T49B)**, 476–482 (1993).
- [68] S. Wirths, R. Geiger, N. Von Den Driesch, G. Mussler, T. Stoica, S. Mantl, Z. Ikonik, M. Luysberg, S. Chiussi, J. M. Hartmann, H. Sigg, J. Faist, D. Buca and D. Grützmacher. Lasing in direct-bandgap GeSn alloy grown on Si. *Nature Photonics* **9(2)**, 88–92 (2015).
- [69] D. Stange, S. Wirths, R. Geiger, C. Schulte-Braucks, B. Marzban, N. V. D. Driesch, G. Mussler, T. Zabel, T. Stoica, J. M. Hartmann, S. Mantl, Z. Ikonik, D. Grützmacher, H. Sigg, J. Witzens and D. Buca. Optically Pumped GeSn Microdisk Lasers on Si. *ACS Photonics* **3(7)**, 1279–1285 (2016).

- [70] V. Reboud, A. Gassenq, N. Pauc, J. Aubin, L. Milord, Q. M. Thai, M. Bertrand, K. Guilloy, D. Rouchon, J. Rothman, T. Zabel, F. Armand Pilon, H. Sigg, A. Chelnokov, J. M. Hartmann and V. Calvo. Optically pumped GeSn micro-disks with 16% Sn lasing at $3.1 \mu\text{m}$ up to 180 K. *Applied Physics Letters* **111**(9) (2017).
- [71] W. Dou, Y. Zhou, J. Margetis, S. A. Ghetmiri, S. Al-Kabi, W. Du, J. Liu, G. Sun, R. A. Soref, J. Tolle, B. Li, M. Mortazavi and S.-Q. Yu. Optically pumped lasing at $3 \mu\text{m}$ from compositionally graded GeSn with tin up to 22.3%. *Optics Letters* **43**(19), 4558 (2018).
- [72] D. Stange, N. von den Driesch, T. Zabel, F. Armand-Pilon, D. Rainko, B. Marzban, P. Zaumseil, J.-M. Hartmann, Z. Ikonic, G. Capellini, S. Mantl, H. Sigg, J. Witzens, D. Grützmacher and D. Buca. GeSn/SiGeSn Heterostructure and Multi Quantum Well Lasers. *ACS Photonics* acsphotronics.8b01116 (2018).
- [73] Q. M. Thai, N. Pauc, J. Aubin, M. Bertrand, J. Chrétien, V. Delaye, A. Chelnokov, J.-M. Hartmann, V. Reboud and V. Calvo. GeSn heterostructure micro-disk laser operating at 230 K. *Optics Express* **26**(25), 32500 (2018).
- [74] J. Chrétien, N. Pauc, F. Armand Pilon, M. Bertrand, Q.-M. Thai, L. Casiez, N. Bernier, H. Dansas, P. Gergaud, E. Delamadeleine, R. Khazaka, H. Sigg, J. Faist, A. Chelnokov, V. Reboud, J.-M. Hartmann and V. Calvo. GeSn lasers covering a wide wavelength range thanks to uniaxial tensile strain. *ACS Photonics* acsphotronics.9b00712 (2019).
- [75] A. Elbaz, D. Buca, N. von den Driesch, K. Pantzas, G. Patriarche, N. Zerounian, E. Herth, X. Checoury, S. Sauvage, I. Sagnes, A. Foti, R. Ossikovski, J. M. Hartmann, F. Boeuf, Z. Ikonic, P. Boucaud, D. Grützmacher and M. El Kurdi. Ultra-low-threshold continuous-wave and pulsed lasing in tensile-strained GeSn alloys. *Nature Photonics* (**Pgi** 9) (2020).
- [76] Y. Zhou, Y. Miao, S. Ojo, H. Tran, G. Abernathy, J. M. Grant, S. Amoah, G. Salamo, W. Du, J. Liu, J. Margetis, J. Tolle, Y.-h. Zhang, G. Sun, R. A. Soref, B. Li and S.-Q. Yu. Electrically injected GeSn lasers on Si operating up to 100 K. *Optica* **7**(8), 924 (2020).
- [77] Y. Bai, K. E. Lee, C. Cheng, M. L. Lee and E. A. Fitzgerald. Growth of highly tensile-strained Ge on relaxed $\text{In}_x\text{Ga}_{1-x}\text{As}$ by metal-organic chemical vapor deposition. *Journal of Applied Physics* **104**(8) (2008).
- [78] G. Capellini, G. Kozłowski, Y. Yamamoto, M. Lisker, C. Wenger, G. Niu, P. Zaumseil, B. Tillack, A. Ghrib, M. De Kersauson, M. El Kurdi, P. Boucaud and T. Schroeder.

- Strain analysis in SiN/Ge microstructures obtained via Si-complementary metal oxide semiconductor compatible approach. *Journal of Applied Physics* **113(1)** (2013).
- [79] G. Capellini, C. Reich, S. Guha, Y. Yamamoto, M. Lisker, M. Virgilio, A. Ghrib, M. El Kurdi, P. Boucaud, B. Tillack and T. Schroeder. Tensile Ge microstructures for lasing fabricated by means of a silicon complementary metal-oxide-semiconductor process. *Optics Express* **22(1)**, 399 (2014).
- [80] M. El Kurdi, M. Prost, A. Ghrib, A. Elbaz, S. Sauvage, X. Checoury, G. Beaudoin, I. Sagnes, G. Picardi, R. Ossikovski, F. Boeuf and P. Boucaud. Tensile-strained germanium microdisks with circular Bragg reflectors. *Applied Physics Letters* **108(9)** (2016).
- [81] R. A. Minamisawa, M. J. Süess, R. Spolenak, J. Faist, C. David, J. Gobrecht, K. K. Bourdelle and H. Sigg. Top-down fabricated silicon nanowires under tensile elastic strain up to 4.5%. *Nature Communications* **3(May)** (2012).
- [82] R. Süess, M. J. and Geiger, R. Minamisawa, G. Schiefler, J. Frigerio, D. Chrastina, G. Isella, R. Spolenak, J. Faist and H. Sigg. Analysis of enhanced light emission from highly strained germanium microbridges. *Nature Photonics* **7(June)**, 466–472 (2013).
- [83] T. Zabel, R. Geiger, E. Marin, E. Müller, A. Diaz, C. Bonzon, M. J. Süess, R. Spolenak, J. Faist and H. Sigg. Top-down method to introduce ultra-high elastic strain. *Journal of Materials Research* **32(4)**, 726–736 (2017).
- [84] D. S. Sukhdeo, D. Nam, J.-H. Kang, M. L. Brongersma and K. C. Saraswat. Direct bandgap germanium-on-silicon inferred from 5.7% 100> uniaxial tensile strain [Invited]. *Photonics Research* **2(3)**, A8 (2014).
- [85] A. Gassenq, K. Guilloy, G. Osvaldo Dias, N. Pauc, D. Rouchon, J. M. Hartmann, J. Widiez, S. Tardif, F. Rieutord, J. Escalante, I. Duchemin, Y. M. Niquet, R. Geiger, T. Zabel, H. Sigg, J. Faist, A. Chelnokov, V. Reboud and V. Calvo. 1.9% Bi-Axial Tensile Strain in Thick Germanium Suspended Membranes Fabricated in Optical Germanium-on-Insulator Substrates for Laser Applications. *Applied Physics Letters* **107(19)**, 2–6 (2015).
- [86] J. Petykiewicz, D. Nam, D. S. Sukhdeo, S. Gupta, S. Buckley, A. Y. Piggott, J. Vučković and K. C. Saraswat. Direct Bandgap Light Emission from Strained Germanium Nanowires Coupled with High-Q Nanophotonic Cavities. *Nano Letters* **16(4)**, 2168–2173 (2016).

- [87] S. Bao, D. Kim, C. Onwukaeme, S. Gupta, K. Saraswat, K. H. Lee, Y. Kim, D. Min, Y. Jung, H. Qiu, H. Wang, E. A. Fitzgerald, C. S. Tan and D. Nam. Low-threshold optically pumped lasing in highly strained germanium nanowires. *Nature Communications* **8**(1), 1–7 (2017).
- [88] K. Gallacher, R. Millar, A. Bashir, I. MacLaren, D. J. Paul, G. Isella, J. Frigerio and A. Ballabio. Analysis of Ge micro-cavities with in-plane tensile strains above 2 %. *Optics Express* **24**(5), 4365 (2016).
- [89] A. Elbaz, M. El Kurdi, A. Aassime, S. Sauvage, X. Checoury, I. Sagnes, C. Baudot, F. Boeuf and P. Boucaud. Germanium microlasers on metallic pedestals. *APL Photonics* **3**(10) (2018).
- [90] D. Burt, A. Al-Attili, Z. Li, F. Gardès, M. Sotto, N. Higashitarumizu, Y. Ishikawa, K. Oda, O. M. Querin, S. Saito and R. Kelsall. Enhanced light emission from improved homogeneity in biaxially suspended Germanium membranes from curvature optimization. *Optics Express* **25**(19), 22911 (2017).
- [91] D. Burt, J. Gonzales, A. Al-Attili, H. Rutt, A. Z Khokar, K. Oda, F. Gardes and S. Saito. Comparison of uniaxial and polyaxial suspended germanium bridges in terms of mechanical stress and thermal management towards a CMOS compatible light source. *Optics Express* **27**(26), 37846 (2019).
- [92] F. T. Armand Pilon, A. Lyasota, Y.-M. Niquet, V. Reboud, V. Calvo, N. Pauc, J. Widiez, C. Bonzon, J. M. Hartmann, A. Chelnokov, J. Faist and H. Sigg. Lasing in strained germanium microbridges. *Nature Communications* **10**(1), 2724 (2019).
- [93] C. Van de Walle. Band lineups and deformation potentials in the model-solid theory. *Physical Review B* **39**(2) (1989).
- [94] J. R. Chelikowsky and M. L. Cohen. Nonlocal pseudopotential calculations for the electronic structure of eleven diamond and zinc-blende semiconductors. *Physical Review B* **14**(2), 556–582 (1976).
- [95] S. Gupta, D. Nam, J. Vuckovic and K. Saraswat. Room temperature lasing unraveled by a strong resonance between gain and parasitic absorption in uniaxially strained germanium. *Physical Review B* **97**(15), 155127 (2018).
- [96] Y. M. Niquet, D. Rideau, C. Tavernier, H. Jaouen and X. Blase. Onsite matrix elements of the tight-binding Hamiltonian of a strained crystal: Application to silicon, germanium,

- and their alloys. *Physical Review B - Condensed Matter and Materials Physics* **79(24)** (2009).
- [97] K. Guilloy, N. Pauc, A. Gassenq, Y. M. Niquet, J. M. Escalante, I. Duchemin, S. Tardif, G. Osvaldo Dias, D. Rouchon, J. Widiez, J. M. Hartmann, R. Geiger, T. Zabel, H. Sigg, J. Faist, A. Chelnokov, V. Reboud and V. Calvo. Germanium under High Tensile Stress: Nonlinear Dependence of Direct Band Gap vs Strain. *ACS Photonics* **3(10)**, 1907–1911 (2016).
- [98] D. Nam, D. S. Sukhdeo, S. Gupta, J. H. Kang, M. L. Brongersma and K. C. Saraswat. Study of Carrier Statistics in Uniaxially Strained Ge for a Low-Threshold Ge Laser. *IEEE Journal on Selected Topics in Quantum Electronics* **20(4)** (2014).
- [99] R. Geiger, T. Zabel and H. Sigg. Group IV direct band gap photonics: Methods, Challenges and Opportunities. *Frontiers in Materials* **2(52)** (2015).
- [100] Y. P. Varshni. Temperature Dependence of the Energy Gap in Semiconductors. *Physica* **34**, 149–154 (1967).
- [101] G. G. Macfarlane, T. P. McLean, J. E. Quarrington and V. Roberts. Fine structure in the absorption-edge spectrum of Si. *Physical Review* **111(5)**, 1245–1254 (1958).
- [102] Y. Huo, H. Lin, R. Chen, M. Makarova, Y. Rong, M. Li, T. I. Kamins, J. Vuckovic and J. S. Harris. Strong enhancement of direct transition photoluminescence with highly tensile-strained Ge grown by molecular beam epitaxy. *Applied Physics Letters* **98(1)**, 1–4 (2011).
- [103] R. Jakomin, M. De Kersauson, M. El Kurdi, L. Largeau, O. Mauguin, G. Beaudoin, S. Sauvage, R. Ossikovski, G. Ndong, M. Chaigneau, I. Sagnes and P. Boucaud. High quality tensile-strained n-doped germanium thin films grown on InGaAs buffer layers by metal-organic chemical vapor deposition. *Applied Physics Letters* **98(9)**, 2009–2012 (2011).
- [104] W. A. P. Claassen, W. G. J. N. Valkenburg, M. F. C. Willemsen and W. M. v. d. Wijgert. Influence of Deposition Temperature, Gas Pressure, Gas Phase Composition, and RF Frequency on Composition and Mechanical Stress of Plasma Silicon Nitride Layers. *Journal of The Electrochemical Society* **132(4)**, 893–898 (1985).
- [105] M. de Kersauson, M. E. Kurdi, S. David, X. Checoury, G. Fishman, S. Sauvage, R. Jakomin, G. Beaudoin, I. Sagnes and P. Boucaud. Optical gain in single tensile-strained germanium photonic wire. *Optics Express* **19(19)**, 17925 (2011).

- [106] A. Ghrib, M. De Kersauson, M. El Kurdi, R. Jakomin, G. Beaudoin, S. Sauvage, G. Fishman, G. Ndong, M. Chaigneau, R. Ossikovski, I. Sagnes and P. Boucaud. Control of tensile strain in germanium waveguides through silicon nitride layers. *Applied Physics Letters* **100(20)**, 1–5 (2012).
- [107] K. Tani, K. Oda and T. Ido. Analysis of stress distribution for strain engineering with external stressors for enhanced light emission in germanium. *Optics Express* **28(25)**, 38267–38279 (2020).
- [108] R. Millar, K. Gallacher, A. Samarelli, J. Frigerio, D. Chrastina, G. Isella, T. Dieing and D. Paul. Extending the emission wavelength of Ge nanopillars to 225 μm using silicon nitride stressors. *Optics Express* **23(14)**, 18193 (2015).
- [109] D. Nam, D. Sukhdeo, S. L. Cheng, A. Roy, K. Chih-Yao Huang, M. Brongersma, Y. Nishi and K. Saraswat. Electroluminescence from strained germanium membranes and implications for an efficient Si-compatible laser. *Applied Physics Letters* **100(13)**, 1–5 (2012).
- [110] A. Ghrib, M. El Kurdi, M. Prost, S. Sauvage, X. Checoury, G. Beaudoin, M. Chaigneau, R. Ossikovski, I. Sagnes and P. Boucaud. All-Around SiN Stressor for High and Homogeneous Tensile Strain in Germanium Microdisk Cavities. *Advanced Optical Materials* **3(3)**, 353–358 (2015).
- [111] R. Millar, K. Gallacher, A. Bashir, I. MacLaren, D. J. Paul, G. Isella, J. Frigerio and A. Ballabio. Analysis of Ge micro-cavities with in-plane tensile strains above 2 %. *Optics Express* **24(5)**, 4365 (2016).
- [112] M. El Kurdi, M. Prost, A. Ghrib, S. Sauvage, X. Checoury, G. Beaudoin, I. Sagnes, G. Picardi, R. Ossikovski and P. Boucaud. Direct Band Gap Germanium Microdisks Obtained with Silicon Nitride Stressor Layers. *ACS Photonics* **3(3)**, 443–448 (2016).
- [113] A. Elbaz, M. El Kurdi, M. Prost, A. Ghrib, S. Sauvage, X. Checoury, F. Aniel, N. Zerounian, G. Picardi, R. Ossikovski, G. Beaudoin, I. Sagnes, F. Boeuf and P. Boucaud. Direct Band Gap Germanium. *ECS Transactions* **75(8)**, 177–184 (2016).
- [114] J. R. Sánchez-Pérez, C. Boztug, F. Chen, F. F. Sudradjat, D. M. Paskiewicz, R. B. Jacobson, M. G. Lagally and R. Paiella. Direct-bandgap light-emitting germanium in tensilely strained nanomembranes. *Proceedings of the National Academy of Sciences of the United States of America* **108(47)**, 18893–18898 (2011).

-
- [115] L. T. Ngo, D. Alméjija, J. E. Sader, B. Daly, N. Petkov, J. D. Holmes, D. Erts and J. J. Boland. Ultimate-strength germanium nanowires. *Nano Letters* **6(12)**, 2964–2968 (2006).
- [116] P. H. Lim, S. Park, Y. Ishikawa and K. Wada. Enhanced direct bandgap emission in germanium by micromechanical strain engineering. *Optics Express* **17(18)**, 16358 (2009).
- [117] M. Süess. Highly strained Si and Ge micro- and nanobridges for micro- and optoelectronic applications. Ph.D. thesis (2014).
- [118] A. L. Ruoff. On the ultimate yield strength of solids. *Journal of Applied Physics* **49(1)**, 197–200 (1978).
- [119] V. Reboud, J. Widiez, J. M. Hartmann, G. Osvaldo Dias, D. Fowler, A. Chelnokov, A. Gassenq, K. Guilloy, N. Pauc, V. Calvo, R. Geiger, T. Zabel, J. Faist and H. Sigg. Structural and optical properties of 200 nm germanium-on-insulator (GeOI) substrates for silicon photonics applications **9367(i)**, 936714 (2015).
- [120] A. Gassenq, S. Tardif, K. Guilloy, G. Osvaldo Dias, N. Pauc, I. Duchemin, D. Rouchon, J. M. Hartmann, J. Widiez, J. Escalante, Y. M. Niquet, R. Geiger, T. Zabel, H. Sigg, J. Faist, A. Chelnokov, F. Rieutord, V. Reboud and V. Calvo. Accurate strain measurements in highly strained Ge microbridges. *Applied Physics Letters* **108(24)** (2016).
- [121] D. S. Sukhdeo, D. Nam, J.-H. Kang, M. L. Brongersma and K. C. Saraswat. Bandgap-customizable germanium using lithographically determined biaxial tensile strain for silicon-compatible optoelectronics. *Optics Express* **23(13)**, 16740 (2015).
- [122] C. Bonzon. Phase and mode control of structured semiconductor lasers. Ph.D. thesis (2014).
- [123] R. Geiger. Direct Band Gap Germanium for Si-compatible Lasing. Ph.D. thesis (2016).
- [124] C. Constantine, D. J. Johnson, R. J. Westerman, T. P. Coleman and T. B. Faure. Plasma etching of Cr photomasks: parametric comparisons of plasma sources and process conditions. In N. Aizaki (Editor), *Photomask and X-Ray Mask Technology IV*, volume 3096, 11 – 18. International Society for Optics and Photonics (1997).
- [125] H. P. Singh. Determination of thermal expansion of germanium, rhodium and iridium by X-rays. *Acta Crystallographica Section A* **24(4)**, 469–471 (1968).

- [126] Y. Okada and Y. Tokumaru. Precise determination of lattice parameter and thermal expansion coefficient of silicon between 300 and 1500 K. *Journal of Applied Physics* **56(2)**, 314–320 (1984).
- [127] M. Virgilio, C. L. Manganelli, G. Grosso, G. Pizzi and G. Capellini. Radiative recombination and optical gain spectra in biaxially strained n-type germanium. *Physical Review B - Condensed Matter and Materials Physics* **87(23)**, 1–11 (2013).
- [128] H. Y. Fan, W. Spitzer and R. Collins. Infrared Absorption in n-type Germanium. *Physical Review* **101(2)** (1956).
- [129] A. R. Adams, M. Asada, Y. Suematsu and S. Arai. The temperature dependence of the efficiency and threshold current of InGaAsP lasers related to intervalence band absorption. *Japanese Journal of Applied Physics* **19(10)**, L621–L624 (1980).
- [130] G. N. Childs, S. Brand and R. A. Abram. Intervalence band absorption in semiconductor laser materials. *Semiconductor Science and Technology* **1(2)**, 116–120 (1986).
- [131] S. A. Srinivasan, C. Porret, M. Pantouvaki, Y. Shimura, P. Geiregat, R. Loo, J. Van Campenhout and D. Van Thourhout. Carrier scattering induced linewidth broadening in in situ P-doped Ge layers on Si. *Applied Physics Letters* **113(16)** (2018).
- [132] M. Levinshtein, S. Rumyantsev and M. Shur. *Handbook Series on Semiconductor Parameters, Vol. 1*, volume 1 (1996).
- [133] W. Kaiser, R. J. Collins and H. Y. Fan. Infrared absorption in p-type germanium. *Physical Review* **91(6)**, 1380–1381 (1953).
- [134] C. Glassbrenner and G. Slack. Thermal Conductivity of Silicon and Germanium from 3 K to the Melting Point. *Physical Review A* **134(4A)** (1964).
- [135] S. T. Yang, M. J. Matthews, S. Elhadj, D. Cooke, G. M. Guss, V. G. Draggoo and P. J. Wegner. Comparing the use of mid-infrared versus far-infrared lasers for mitigating damage growth on fused silica (2010).
- [136] N. Mingo, L. Yang, D. Li and A. Majumdar. Predicting the Thermal Conductivity of Si and Ge Nanowires. *Nano Letters* **3(12)**, 1713–1716 (2003).
- [137] D. Li, Y. Wu, P. Kim, L. Shi, P. Yang and A. Majumdar. Thermal conductivity of individual silicon nanowires. *Applied Physics Letters* **83(14)**, 2934–2936 (2003).

-
- [138] K. Tanaka, H. Ohtake and T. Suemoto. Resonant inter-valence-band Raman scattering of photoexcited holes in germanium. *Physical Review B* **50(15)**, 10694–10701 (1994).
- [139] E. Nazvanova, T. Suemoto, S. Maruyama and Y. Takano. Inter-valence-band electronic Raman scattering due to photoexcited holes in Ge(1-x)Si(x). *Physical Review B - Condensed Matter and Materials Physics* **62(3)**, 1873–1877 (2000).
- [140] M. Born and E. Wolf. *Principles of Optics - Electromagnetic Theory of propagation, Interference and Diffraction of Light*. Pergamon Press, London, first edition (1959).
- [141] F. K. Reinhart. Direct determination of the free-carrier injection density, the free-carrier absorption, and the recombination factors in double heterostructure diodes by optical phase measurements. Part III. *Journal of Applied Physics* **97(12)** (2005).
- [142] R. Geiger, J. Frigerio, M. J. Süess, R. A. Minamisawa, D. Chrastina, G. Isella, R. Spole-nak, J. Faist and H. Sigg. Excess carrier lifetimes in Ge layers on Si. *Applied Physics Letter* **062106** (2014).
- [143] A. L. Schawlow and C. H. Townes. Infrared and optical masers. *Physical Review* **112(6)**, 1940–1949 (1958).
- [144] C. H. Henry. Theory of the Linewidth of Semiconductor Lasers. *IEEE Journal of Quantum Electronics* **18(2)**, 259–264 (1982).
- [145] W. Zhang, C. Delerue, Y. M. Niquet, G. Allan and E. Wang. Atomistic modeling of electron-phonon coupling and transport properties in n -type [110] silicon nanowires. *Physical Review B - Condensed Matter and Materials Physics* **82(11)**, 2–8 (2010).
- [146] G. Mak and W. W. Rühle. Femtosecond carrier dynamics in Ge measured by a luminescence up-conversion technique and near-band-edge infrared excitation. *Physical Review B* **52(16)**, 584–587 (1995).
- [147] G. Nilsson and G. Nelin. Phonon dispersion relations in Ge at 80 K. *Physical Review B* **3(2)**, 364–369 (1971).
- [148] Anthony E. Siegman. *Lasers* (1986).
- [149] P. N. Keating. Effect of invariance requirements on the elastic strain energy of crystals with application to the diamond structure. *Physical Review* **145(2)**, 637–645 (1966).
- [150] S. Tardif, A. Gassenq, K. Guillo, N. Pauc, G. Osvaldo Dias, J. M. Hartmann, J. Widiez, T. Zabel, E. Marin, H. Sigg, J. Faist, A. Chelnokov, V. Reboud, V. Calvo, J. S. Micha,

- O. Robach and F. Rieutord. Lattice strain and tilt mapping in stressed Ge microstructures using X-ray Laue micro-diffraction and rainbow filtering. *Journal of Applied Crystallography* **49(5)**, 1402–1411 (2016).
- [151] A. Beattie and P. Landsberg. Auger Effects in Semiconductors. *Proc. Roy. Soc. A.* **301(1413)**, 355–361 (1967).
- [152] L. Huldt. Band-To-Band Auger Recombination in indirect gap Semiconductors. *Physica Status Solidi (a)* **173(8)** (1971).
- [153] G. P. Agrawal and N. K. Dutta. *Semiconductor Lasers*. ISBN 9788578110796 (1993).
- [154] R. Geiger, T. Zabel, E. Marin, A. Gassenq, J. M. Hartmann, J. Widiez, J. Escalante, K. Guilloy, N. Pauc, D. Rouchon, G. O. Diaz, S. Tardif, F. Rieutord, I. Duchemin, Y. M. Niquet, V. Reboud, V. Calvo, A. Chelnokov, J. Faist and H. Sigg. Uniaxially stressed germanium with fundamental direct band gap. *ArXiv* **1** (2015).
- [155] W. Howard, F. F. Fang, F. H. Dill and M. I. Nathan. CW Operation of a GaAs Injection Laser. *IBM journal (January)*, 14–15 (1963).
- [156] M. R. Barget, M. Virgilio, G. Capellini, Y. Yamamoto and T. Schroeder. The impact of donors on recombination mechanisms in heavily doped Ge/Si layers. *Journal of Applied Physics* **121(24)** (2017).
- [157] B. Dutt, D. S. Sukhdeo, D. Nam, B. M. Vulovic, Z. Yuan and K. C. Saraswat. Roadmap to an efficient germanium-on-silicon laser: Strain vs. n-type doping. *IEEE Photonics Journal* **4(5)**, 2002–2009 (2012).
- [158] K. C. Harvey and C. J. Myatt. External-cavity diode laser using a grazing-incidence diffraction grating. *Optics Letters* **16(12)**, 910 (1991).
- [159] A. Garnache, A. Ouvrard and D. Romanini. Single-Frequency operation of External-Cavity VCSELs: Non-linear multimode temporal dynamics and quantum limit. *Optics Express* **15(15)**, 9403 (2007).
- [160] H. Stoehr, F. Mensing, J. Helmcke and U. Sterr. Diode laser with 1 Hz linewidth. *Optics Letters* **31(6)**, 736 (2006).
- [161] C. Spiegelberg, J. Geng, Y. Hu, Y. Kaneda, S. Jiang and N. Peyghambarian. Low-Noise Narrow-Linewidth Fiber Laser at 1550 nm. *Journal of Lightwave Technology* **22(1)**, 57–62 (2004).

- [162] C. H. Henry, R. A. Logan and K. A. Bertness. Spectral dependence of the change in refractive index due to carrier injection in GaAs lasers. *Journal of Applied Physics* **52(7)**, 4457–4461 (1981).
- [163] J. T. Olesberg, M. E. Flatté and T. F. Boggess. Comparison of linewidth enhancement factors in midinfrared active region materials. *Journal of Applied Physics* **87(10)**, 7164–7168 (2000).
- [164] T. Lee, C. A. Burrus, K. Y. Liou, N. Olsson, R. Logan and D. Wilt. Measured spectral linewidth of single-frequency 1.3 and 1.5 μm injection lasers. *Electronics Letters* **20(24)**, 1011–1012 (1984).
- [165] K. Kikuchi, T. Okoshi and R. Arata. Measurement of linewidth and FM-noise spectrum of 1.52 μm InGaAsP lasers. *Electronics Letters* **20(13)**, 535–536 (1984).
- [166] K. Y. Liou, N. K. Dutta and C. A. Burrus. Linewidth-narrowed distributed feedback injection lasers with long cavity length and detuned Bragg wavelength. *Applied Physics Letters* **50(9)**, 489–491 (1987).
- [167] D. Welford and A. Mooradian. Observation of linewidth broadening in (GaAl)As diode lasers due to electron number fluctuations. *Applied Physics Letters* **40(7)**, 560–562 (1982).
- [168] W. Elsässer, E. O. Göbel and J. Kuhl. Coherence Properties of Gain- and Index-Guided Semiconductor Lasers. *IEEE Journal of Quantum Electronics* **19(6)**, 46 (1983).
- [169] J. Harrison and A. Mooradian. Spectral characteristics of (GaAl)As diode lasers at 1.7 μm . *Applied Physics Letters* **45(4)**, 318–320 (1984).
- [170] W. Elsässer and E. O. Göbel. Spectral linewidth of gain- and index-guided InGaAsP semiconductor lasers. *Applied Physics Letters* **45(4)**, 353–355 (1984).
- [171] K. Kojima, S. Noda, S. Tai, K. Kyuma and T. Nakayama. Measurement of spectral linewidth of AlGaAs/GaAs distributed feedback lasers. *Electronics Letters* **22(8)**, 425–427 (1986).
- [172] D. W. Rush, G. L. Burdge and P. T. Ho. The linewidth of a Mode-Locked Semiconductor Laser Caused By Spontaneous Emission: Experimental Comparison To Single-Mode Operation. *IEEE Journal of Quantum Electronics* **QE-22(11)**, 2088–2091 (1986).
- [173] K. Kobayashi and I. Mito. Progress in narrow-linewidth tunable laser sources. In *Optical Fiber Communication*, WC1 (1987).

- [174] M. J. O'Mahony and I. D. Henning. Semiconductor laser linewidth broadening due to $1/f$ carrier noise. *Electronics Letters* **19(23)**, 1000–1001 (1983).
- [175] K. Kikuchi and T. Okoshi. Dependence of semiconductor laser linewidth on measurement time: evidence of predominance of $1/f$ noise. *Electronics Letters* **21(22)**, 13–14 (1985).
- [176] K. Vahala and A. Yariv. Occupation fluctuation noise: A fundamental source of linewidth broadening in semiconductor lasers. *Applied Physics Letters* **43(2)**, 140–142 (1983).
- [177] M. C. Amann and R. Schimpe. Excess linewidth broadening in wavelength-tunable laser diodes. *Electronics Letters* **26(5)**, 279–280 (1990).
- [178] M. C. Amann. The Effect of Spatial Correlation on the Linewidth Broadening in Tunable Laser Diodes. *IEEE Journal of Quantum Electronics* **29(6)**, 1799–1804 (1993).
- [179] S. Albert, K. K. Albert and M. Quack. *Handbook of High-resolution Spectroscopy*, volume 2. ISBN 9780470066539 (2011).
- [180] W. Elsässer and E. O. Göbel. Multimode Effects in the Spectral Linewidth of Semiconductor Lasers. *IEEE Journal of Quantum Electronics* **21(6)**, 687–692 (1985).
- [181] U. Krüger and K. Petermann. The Semiconductor Laser Linewidth Due to the Presence of Side Modes. *IEEE Journal of Quantum Electronics* **24(12)**, 2355–2358 (1988).
- [182] S. E. Miller. The Effect of Side Modes on Linewidth and Intensity Fluctuations in Semiconductor Lasers. *IEEE Journal of Quantum Electronics* **24(5)**, 750–757 (1988).
- [183] G. R. Gray and G. P. Agrawal. Effect of Cross Saturation on Frequency Fluctuations in a Nearly Single-Mode Semiconductor Laser. *IEEE Photonics Technology Letters* **3(3)**, 204–206 (1991).
- [184] W. Benedict and E. Plyler. Absorption spectra of water vapor and carbon dioxide in the region of 2.7 microns. *Journal of Research of the National Bureau of Standards* **46(3)**, 246 (1951).
- [185] B. Saleh and M. Teich. *Fundamentals of photonics*. Wiley-Interscience, second edition (2007).
- [186] P. Y. Yu and M. Cardona. *Fundamentals of Semiconductor - Physics and Materials Properties*. Fourth edition. ISBN 3642294995 (2010).

-
- [187] J. Faist, F. Capasso, D. Sivco and A. Hutchinson. Quantum cascade laser. *Science* **264**, 553–556 (1994).
- [188] L. Coldren, S. Corzine and M. Mazanovic. *Diode laser and photonic integrated circuits*. ISBN 9789896540821.
- [189] M. Lax. Classical noise. V Noise in self-sustained oscillators. *Physical Review* **160(2)**, 290–307 (1967).
- [190] K. Petermann. *Laser Diode Modulation and Noise*. ISBN 9780792312048 (1988).
- [191] C. H. Henry, R. A. Logan and F. R. Merritt. Measurement of gain and absorption spectra in AlGaAs buried heterostructure lasers. *Journal of Applied Physics* **51(6)**, 3042–3050 (1980).
- [192] M. G. Bernard and G. Duraffourg. Laser Conditions in Semiconductors. *Physica Status Solidi (B)* **1(7)**, 699–703 (1961).
- [193] W. Liang, V. S. Ilchenko, D. Eliyahu, A. A. Savchenkov, A. B. Matsko, D. Seidel and L. Maleki. Ultralow noise miniature external cavity semiconductor laser. *Nature Communications* **6** (2015).
- [194] A. B. Matsko, A. A. Savchenkov, N. Yu and L. Maleki. Whispering-gallery-mode resonators as frequency references. I. Fundamental limitations. *Journal of the Optical Society of America B* **24(6)**, 1324–1335 (2007).
- [195] K. Numata, A. Kemery and J. Camp. Thermal-noise limit in the frequency stabilization of lasers with rigid cavities. *Physical Review Letters* **93(25)**, 1–4 (2004).
- [196] D. R. Hjelme, A. R. Mickelson and R. G. Beausoleil. Semiconductor Laser Stabilization By External Optical Feedback. *IEEE Journal of Quantum Electronics* **27(3)**, 352–372 (1991).
- [197] A. Suhel, B. D. Hauer, T. S. Biswas, K. S. Beach and J. P. Davis. Dissipation mechanisms in thermomechanically driven silicon nitride nanostrings. *Applied Physics Letters* **100(17)** (2012).
- [198] M. Poot and H. S. van der Zant. Mechanical systems in the quantum regime. *Physics Reports* **511(5)**, 273–335 (2012).
- [199] M. Li, W. H. Pernice, C. Xiong, T. Baehr-Jones, M. Hochberg and H. X. Tang. Harnessing optical forces in integrated photonic circuits. *Nature* **456(7221)**, 480–484 (2008).

- [200] B. J. Frey, D. B. Leviton and T. J. Madison. Temperature-dependent refractive index of silicon and germanium. *Proc. SPIE, Optomechanical Technologies for Astronomy* (2006).
- [201] M. Ohtsu and S. Kotajima. Derivation of the Spectral Width of a 0.8 μ m AlGaAs Laser Considering 1/f Noise. *Japanese Journal of Applied Physics* **23(6R)**, 760–764 (1984).
- [202] A. Dandridge and H. Taylor. Correlation of Low-Frequency Intensity and Frequency Fluctuations in GaAlAs Lasers. *IEEE Transactions on Microwave Theory and Techniques* **30(10)** (1982).
- [203] M. Fukuda, T. Hirono, T. Kurosaki and F. Kano. 1/f Noise Behavior in Semiconductor Laser Degradation. *IEEE Photonics Technology Letters* **5(10)**, 1165–1167 (1993).
- [204] G. Tenchio. Low-Frequency intensity fluctuations of C.W. D.H. GaAlAs-Diode lasers. *Electronics Letters* **12(21)**, 2–3 (1976).
- [205] F. Hooge. 1 / f Noise Sources. *IEEE Transaction on Electron Devices* **41(11)**, 1926–1935 (1994).

Acknowledgements

First of all, I wish to thank my supervisors, Dr. Hans Sigg and Prof. Jérôme Faist. Their passion for science has been an example to me throughout these years, and their vision could adjust the course of my efforts every time it was needed. I am especially indebted to Dr. Hans Sigg for his daily guidance and constant push for improvement. I certainly profited a lot as a scientist from our frequent discussions and his capacity to ask the correct question.

I would like to thank Prof. Jim Harris from Stanford University and Dr. Alexei Tchelnokov from CEA Grenoble for being co-examiners of this thesis and reading this manuscript.

I am grateful to Dr. Thomas Zabel, who accompanied me during the first steps of this thesis, introducing me to the strained germanium project. Although we never worked together, I am also thankful to Dr. Richard Geiger, Dr. Martin Süess and Esteban Marin: their work laid the foundations of this thesis. I want to thank Dr. Alexey Lyasota, with whom I observe the first spectra of the pulsed strained germanium laser.

My gratitude goes to Dr. Simon Gerber and Dr. Guy Matmon, and all the members of the Quantum Technology group: I could always count on them during these years. I am particularly grateful to Stefan Stutz for his precious and constant help in the laboratory, his cheering up during the many downs of this thesis and his many stories across Switzerland and Italy. Thanks to the QT cycling group for the rides to PSI and not only, with many more to come.

I am thankful to the former and current heads of LMN, Prof. Jens Gobrecht and Dr. Yasin Ekinci. Thanks to the LMN technical staff, in particular to Dario Marty, Christopher Wild, Konrad Vogelsang, Eugen Deckart, Anja Weber and Thomas Neiger. I thank Dr. Vitaly Guzenko for his e-beam and Sentech's support and for letting his door always open and Dr. Konstantinis Jefimovs for his precious hints about the dry etching process. I am very grateful to the LMN PhD students, in particular Nicolò, Judith, Pooja and Adrian, for sharing the ups and downs of this journey. Thanks to Dr. Dimitrios Kazazis and Dario Marty for the many laughs at LMN.

I want to thank also Dr. Daniel Treyer, Dr. Luka Debenjak and Mario Jurcevic for their

technical support at SLS.

I would like to thank the team from CEA, Grenoble, for the great collaboration on the strained Ge and GeSn lasers projects, namely Dr. Alexei Tchelnokov, Dr. Vincent Reboud, Dr. Vincent Calvo, Dr. Mathieu Bertrand and Dr. Jean-Michel Hartmann. I am particularly grateful to Dr. Yann-Michel Niquet for his support about the tight-binding model and Dr. Nicolas Pauc and Dr. Jeremie Chretien for the many days spent measuring at the optical lab at PSI. Similarly, I would like to thank Dr. Dan Buca and Dr. Daniela Stange from the Forschungszentrum Jülich.

Completing a Ph.D. with a minimum level of inner balance certainly requires good friends outside the lab. I want to thank my long-time friends from Milano for their support and for making me always laugh whenever I come back. I am particularly grateful to the new friends that I found here in Zürich during these years, Paolo, Valeria, Andrea and Francesca: thanks for getting me out of my self-dig tunnels and for pushing me toward the goal until the end. I am also thankful to the new/old friends Francesca and Luca for fun together and their sincere friendship.

I would like to thank my parents, without whom I would not be the person I am.

Last but not least, I want to express my deep gratitude to the love of my life, Maria Giulia. You always supported and encouraged me from the beginning until the end, and there is no doubt that you share a non-negligible amount of this thesis. But more importantly, I would like to thank you for our life together, making me realize every day how fortunate I am.

Curriculum Vitae

Personal Details

Name	Francesco Taro Armand Pilon
Date of Birth	21 July 1988
Place of Birth	Torino (Italy)
Nationality	Italian

Work Experience

10/2016 – 02/2021 Graduate student researcher,
Laboratory for Micro- and Nanotechnology, PSI, Villigen.
Quantum Optoelectronics Group, ETH Zürich.

Demonstration of lasing in strained germanium and investigation of the group-IV lasing physics.

- Micro fabrication of highly strained Ge microstructures.
- Lasing characterization via infrared spectroscopy and modeling.
- User support at the spectroscopy laboratory for investigations of group-IV lasing platforms.

Supervisors: Prof. Dr. Jérôme Faist and Dr. Hans Sigg.

03/2015 – 09/2016 Device engineer,
STMICROelectronics, Agrate Brianza (Italy).

- Analysis of the electrical parameters of power devices for automotive applications.
- Process integration.

02/2014 – 02/2015 Research intern,
STMICROelectronics, Agrate Brianza (Italy).

- Master thesis in collaboration with *Università degli Studi di Milano*

Supervisor: Prof. Dr. Valentino Liberali and Dr. Emanuele Brenna.

Education

March 2021

Doctor of Sciences,
ETH Zürich, Zürich, Switzerland.
Thesis title: *Strained Germanium Laser*

February 2015

Master of Science in Physics,
Università degli Studi di Milano, Milan, Italy.
Thesis title: *Analysis of silicon dopants deactivation phenomena induced by hydrogen diffused from a silicon nitride layer deposited with the LPCVD technique.*

February 2012

Bachelor of Science in Physics,
Università degli Studi di Milano, Milan, Italy.
Thesis title: *Study of the effects of nanostructures surfaces on PC12 cells differentiation process.*

List of Publications

Peer-reviewed journal publications

As primary author

1. **F.T. Armand Pilon**, A.Lyasota, Y.-M. Niquet, V. Reboud, V. Calvo, N. Pauc, J. Widiez, C.Bonzon, J.M. Hartmann, A. Chelnokov, J. Faist and H. Sigg. Lasing in strained germanium microbridges. *Nature Communications* **10(1)**, 2724, (2019).

As contributing author

1. J. Chretien, N. Pauc, **F. Armand Pilon**, M. Bertrand, Q.-M. Thai, L. Casiez, N. Bernier, H. Dansas, P. Gergaud, E. Delamadeleine, R. Khazaka, H. Sigg, J. Faist, A. Chelnokov, V. Reboud, J.-M. Hartmann and V. Calvo. GeSn lasers covering a wide wavelength range thanks to uniaxial tensile strain. *ACS Photonics* **6(10)**, 2462-2469 (2019).
2. D. Stange, N. von den Driesch, T. Zabel, **F. Armand Pilon**, D. Rainko, B. Marzban, P. Zaumseil, J.-M. Hartmann, Z. Ikonic, G. Capellini, S. Mantl, H. Sigg, J. Witzens and D. Grutzmacher. GeSn/SiGeSn heterostructure and multi quantum well lasers. *ACS Photonics* **5(11)**, 4628-4636 (2018).
3. V. Reboud, A. Gassenq, N. Pauc, J. Aubin, L. Milord, Q.-M. Thai, M. Bertrand, K. Guillo, D. Rouchon, J. Rothmann, T. Zabel, **F. Armand Pilon**, H. Sigg, A. Chelnokov, J.-M. Hartmann and V. Calvo. Optically pumped GeSn micro-disks with 16 % Sn lasing at 3.1 μm up to 180 K. *Applied Physics Letters* **111(9)**, (2017).

Oral presentations

1. **F.T. Armand Pilon**, Y.-M. Niquet, V. Reboud, V. Calvo, N. Pauc, J. Widiez, J.M. Hartmann, A. Chelnokov, J. Faist and H. Sigg. Continuous wave lasing in strained germanium microbridge. *IEEE, IPC Conference*, (virtual), September 2020.

2. **F.T. Armand Pilon**, A. Lyasota, Y.-M. Niquet, V. Reboud, V. Calvo, N. Pauc, J. Widiez, C. Bonzon, J.M. Hartmann, A. Chelnokov, J. Faist and H. Sigg. Strained germanium lasing in the Mid-Infrared. *IEEE, Group IV photonics conference*, Singapore, August 2019.
3. **F.T. Armand Pilon**, A. Lyasota, V. Reboud, V. Calvo, N. Pauc, J. Widiez, J.M. Hartmann, A. Chelnokov, J. Faist and H. Sigg. Single mode lasing in strained Ge microbridges. *SPIE Photonics West conference*, San Francisco (USA), February 2019.
4. **F.T. Armand Pilon**, A. Lyasota, Y.-M. Niquet, V. Reboud, V. Calvo, N. Pauc, J. Widiez, J.M. Hartmann, A. Chelnokov, J. Faist and H. Sigg. Lasing in highly strained Ge microbridges. *Paul Scherrer Institut Condensed matter retreat*, Dübendorf (Switzerland), December 2018.
5. **F.T. Armand Pilon**, N.Pauc, J. Widiez, V. Reboud, V. Calvo, J.M. Hartmann, A. Chelnokov, J. Faist and H. Sigg. Emerging optical gain in highly strained germanium. *OSA Advanced Photonics*, Zürich (Switzerland), July 2018.
6. **F.T. Armand Pilon**, T. Zabel, E. Marin, C. Bonzon, S. Tardiff, A. Gassenq, N.Pauc, V. Reboud, V. Calvo, J.M. Hartmann, J. Widiez, A. Chelnokov, J. Faist and H. Sigg. Cavity mode analysis of highly strained direct band gap germanium micro-bridge cavities. *IEEE, Group IV photonics conference*, Berlin (Germany), August 2017.

Poster presentation

1. **F.T. Armand Pilon**, A. Lyasota, Y.-M. Niquet, V. Reboud, V. Calvo, N. Pauc, J. Widiez, J.M. Hartmann, A. Chelnokov, J. Faist and H. Sigg. Towards the understanding of the dynamics and the Raman effect of strained germanium lasing. *Paul Scherrer Institut Condensed matter retreat*, Brugg (Switzerland), November 2019.

